INFORMATION TO USERS

This manuscript has been reproduced from the microfilm master. UMI films the text directly from the original or copy submitted. Thus, some thesis and dissertation copies are in typewriter face, while others may be from any type of computer printer.

The quality of this reproduction is dependent upon the quality of the copy submitted. Broken or indistinct print, colored or poor quality illustrations and photographs, print bleedthrough, substandard margins, and improper alignment can adversely affect reproduction.

In the unlikely event that the author did not send UMI a complete manuscript and there are missing pages, these will be noted. Also, if unauthorized copyright material had to be removed, a note will indicate the deletion.

Oversize materials (e.g., maps, drawings, charts) are reproduced by sectioning the original, beginning at the upper left-hand corner and continuing from left to right in equal sections with small overlaps.

University of Alberta

LIQUID-VAPOR CRITICAL BEHAVIOR IN SILICA AEROGEL

by

Tobias Kent Herman ©

A thesis submitted to the Faculty of Graduate Studies and Research in partial fulfillment of the requirements for the degree of **Doctor of Philosophy**.

Department of Physics

Edmonton, Alberta
Spring 2005

Abstract

Fluids in porous media provide a testing ground for the effects of disorder and confinement on phase transitions and critical phenomena. Specifically, highly porous silica aerogel with its tenuous solid structure has allowed low temperature physicists to probe the effect of dilute fixed impurities on both the ^{4}He superfluid transition and the ^{3}He superfluid transition. Both systems have yielded exciting results and work is ongoing, especially on ^{3}He in aerogel.

This thesis explores the effect of aerogel on another transition – the liquid-vapor transition near the liquid-vapor critical point. In dense porous media, the liquid-vapor transition is usually described as capillary condensation – a process which assigns surface tension a primary role in determining the thermodynamic state of the system. However, aerogels are often so diffuse (less than 5% silica by volume – the rest is open space) that it becomes difficult to speak of pore size and meniscus shape as one would in a denser porous medium. As one approaches the liquid-vapor critical point, thermal fluctuations within the fluid grow until they exceed the scale of the aerogel strands and pores themselves. In this regime one cannot expect surface tension to control the thermodynamics of the system – it is instead in a regime where thermal fluctuations may govern its behavior. In the past there were even suggestions that the addition of aerogel might shift the character of the transition into another universality class.

The following chapters present data collected on helium and neon in aerogel near their respective liquid-vapor critical points. While the behavior of the fluid at low temperatures is consistent with the pictures provided by capillary condensation, closer to the critical point they are incompatible and remain somewhat unexplained. Evidence for a shift in universality class was not found – in fact there was very little evidence for a macroscopic equilibrium transition of any type.

Acknowledgements

I cannot express all of my gratitude for the love, support and, especially, patience from Kristine Lui. Thank you for putting up with the painfully slow process which was my thesis composition. I am also eternally indebted for the help and support of my family: Tom, Kathy, and Giles. I would like to give heartfelt thanks to my grandparents Bill and Marie Fuller, who supported and encouraged me while I was deciding to attend graduate school and whose home was always welcoming when I needed a break.

I had great academic and technical support within the graduate program. My supervisory committee was always supportive and willing help: thank you Frank Marsiglio, Doug Schmitt and Andrzej Czarnecki and thanks to Janet Elliott for her input. I owe a great deal to my supervisor John Beamish for the many things he has taught me in the five years I have spent here, and appreciate the patience shown towards all my questions. His encouragement, both when experiments were working and when they weren't, kept me going even if the goal of the research sometimes seemed awfully far away. His talents as a teacher and mentor provide a powerful example to anyone who works in his laboratory, and his respect for, and from, others within the research community has taught me a great deal that I will carry forward.

While I encountered some tough challenges, especially as I began my program, Lynn Chandler helped greatly through her encouragement and seemingly limitless ability to navigate through the administrative complexities of helping graduate students not miss important opportunities, or deadlines. Thank you Lynn for your work and your friendship. I also couldn't have run any of these experiments as efficiently or as smoothly without the deep well of technical genius that resides in our department. I would especially like to thank Don Mullin for at least 1001 great ideas on everything from how to clean glass to how to design cryostats. There seemed to be no problem too big, or too small, to take to Don (for the price of a Guinness). When cell designs became complex, I always relied on the encyclopedic mind and great visualization of Gilbert Lachat to turn our basic cell sketches into a sensible design. Many components of the cells used in this thesis were constructed by the steady hands of Tony Walford or Boris Tomasevic – there was simply no substitute for such skilled machinists when the experimental cells were delicate. This work could never have been completed without the help of Yolande Peske, Steve Rogers and Nick Mys; not only were they indispensable in helping to find all the practical little things needed in the lab, they provided our lifeblood – liquid helium.

My fellow graduate students have also played a huge role in shaping my degree. It is impossible to mention everyone, but I would especially like to thank James Day for all of his help in the lab. And last but not least, thanks to everyone in the general office for their help through the last five years.

Table of Contents

List of Tables

List of Figures

Chapter 1

Introduction

This thesis summarizes our work on fluids near the liquid-vapour critical point in extremely porous silica glasses, known as aerogels. The motivation for this work was to search for novel critical behavior in fluids near their liquid-vapor critical points with fixed impurities, as suggested by theoretical predictions of the analogous system of binary fluids separating in a dilute polymer gel[1]. There have been dramatic changes elucidated for other fluid transitions in aerogel, including ^{3}He and ^{4}He superfluidity and ^{3}He-^{4}He phase separation. However, the behavior of fluids near their liquid-vapor critical points in aerogel was still a very open question when this thesis work began. There was a possibility that the liquid-vapor transition would show a dramatic qualitative change brought on by the inclusion of a dilute solid matrix, and early experimental work on helium in aerogel showed some truly bizarre behavior which needed further examination.

The superfluid transition in ^{4}He is in a different universality class than the liquid-vapor transition, belonging to the XY class rather than the Ising class. However, superfluidity of helium in aerogel is germane to our studies because it showed surprising behavior, different than seen in most dense porous glasses. In torsional resonator experiments on helium in Vycor, xerogel, and aerogel Chan *et al.* saw distinctly different critical exponents for the superfluid density, ζ [2]. While helium confined in Vycor has the same critical exponent as bulk helium, interestingly the exponent in aerogel was much larger[2, 3]. Heat capacity cusps at the superfluid transition also appeared fundamentally altered by the presence of aerogel[4]. The shape was incompatible with the bulk critical exponent for heat capacity – in fact a study of varying density aerogels showed that the critical exponent tended smoothly towards the bulk value as the aerogel density was decreased.

1

Superfluidity in bulk ^{3}He is very different from that in ^{4}He – while ^{4}He superfluidity occurs with incredibly small coherence lengths (close to atomic dimensions), in ^{3}He superfluidity arises from the pairing of ^{3}He atoms in a manner similar to Cooper pairing in superconductors. The resulting pair of ^{3}He atoms form a p-wave superfluid with a non-critical phase transition and having a coherence length which is highly dependent on pressure. The phase diagram for ^{3}He actually includes a number of superfluid phases which are stable under a variety of pressure-temperature-magnetic field conditions; for an introduction to bulk superfluidity in ^{3}He see reference [5]. In low density aerogel, the coherence length of superfluid ^{3}He is comparable to the spacing between aerogel strands, so aerogel can act as a homogenous or inhomogeneous impurity[6]. This also means that the exact structure of an aerogel sample has a large impact on the superfluid transition in ^{3}He. The effect of very porous aerogels on ^{3}He is currently a very large field of interest in low temperature physics, but its behavior is well enough understood now that phase diagrams can be described[7]. The effect on the superfluid transition is just as dramatic as in ^{4}He, and is another piece of evidence that one might expect interesting behavior at the liquid-vapor critical point in aerogels where coherence lengths approach the scale of the aerogel pores.

The two stable isotopes of helium (^{3}He and ^{4}He) separate into two partially miscible liquids below 1K. In bulk, this results in a characteristic phase diagram in which the phase separation and ^{4}He superfluid transition lines intersect in a tricritical point. When ^{3}He-^{4}He mixtures are confined to porous glasses, a thin film of ^{4}He forms along the wall of the pores, but beyond that shift the phase diagram remains unchanged by dense porous media such as Vycor[8]. On the other hand, helium mixtures in 98% aerogel show a fundamentally different phase diagram – the line of superfluid transitions is completely detached from the phase separation line[9]. In that case there is no longer a tricritical point.

With three examples of the dramatic effects of aerogel on fluid critical behavior, it seems reasonable to expect interesting behavior near the liquid-vapor critical point in such a dilute medium. Previous experimental work had been done on the liquid-vapor critical point in aerogels[10, 11] and binary fluid separation in wet gels[12, 13]; our study was designed to allow high resolution measurements of the coexistence curve that could complement some of the previous results while probing the condensation of helium in aerogel more deeply than previous studies. While earlier studies

2

often interpreted results in terms of equilibrium macroscopic coexistence like that seen in bulk fluids, recent work on helium adsorption in aerogels performed in France do not seem to show the straightforward liquid-vapor transition necessary for critical behavior. Their results point toward a more classical capillary condensation behavior[14, 15] controlled by the energetics of the liquid-vapor interface.

In order to place the work in this thesis within context, I begin the thesis with a review of critical phenomena, with an emphasis on fluid systems. Following this I introduce the random field Ising model, which has been suggested as a model for fluid separation in porous media. However, it is not obvious that the condensation of fluids in aerogels is best described within the framework of liquid-vapor critical phenomena at all. There is strong evidence that even quite close to the critical point of the fluid the condensation behavior is better described by capillary condensation – a phenomenon governed solely by surface tension. Therefore a section on capillary condensation follows the description of critical phenomena.

After this review of basic concepts, I review pertinent results from other researchers, both experimental and theoretical. As mentioned above, there have been a few studies of the liquid-vapor transition in aerogel, but there have also been investigations of fluids near their critical points in denser porous media and some of the most important of these will be addressed. Simulation is also starting to play a much larger role in soft condensed matter physics and physical chemistry than it used to play – as computing resources grow, simulations of large volumes of fluid are becoming possible. Simulation studies of fluid condensation in a variety of porous media have been published, and I will review the techniques and results of some applicable studies. Direct simulation of fluids in aerogel is difficult because the scale is so large – just a few years ago a single pore in an aerogel might have exceeded the size of an entire simulation volume. For this reason there have been relatively few studies of fluids in aerogel published. While this is not work that I have actively participated in, it is highly relevant to understanding fluids in aerogel.

In the next chapter I describe aerogels and how they are prepared. Unless otherwise indicated, all the samples used in my work were synthesized in house by me. We have performed our measurements on base catalyzed gels, similar to those used by most members of the low temperature community. However, gel structure depends on synthesis conditions and there remain questions about how important an effect the gel synthesis and drying conditions are to the behavior of adsorbed fluid.

3

Thus, this chapter includes some information about possible structural differences created during synthesis.

I will then discuss my experiments and results. Foremost will be a set of capacitively measured adsorption isotherms for helium in aerogel. We have a large set of data covering condensation of helium in 95% and 98% porous aerogels over temperatures ranging from 4.400K to above the liquid-vapor critical point. These isotherms show hysteretic behavior until close to the critical point, and shapes consistent with classical capillary condensation behavior. Next, the results of a series of low frequency acoustic experiments designed to measure the liquid-vapor coexistence curve in aerogel will be described. These studies included the condensation of neon in 95% porous aerogel and helium in both 95% and 98% porous aerogel. While not as straightforward to interpret as first hoped, these results allow us to make some interesting inferences about the transition.

Finally, on a somewhat unrelated note, I will discuss some recent results on the deformation of aerogel during filling with fluids at low temperatures. While the low surface tension of helium is usually not considered when designing experiments, aerogels turn out to be compressible enough that neglecting the helium surface tension can be damaging to high porosity aerogels if they contain any liquid-vapor interfaces. This study is interesting in its own right, but is equally important as a cautionary note to researchers using aerogel as a matrix for the study of disorder in fluids.

From all these studies we can finally conclude that the true behavior of near-critical helium in aerogel is not very well explained by approaching it as an example of critical behavior. However, neither is it well treated by the classical tools used in capillary condensation studies because the interface thickness can approach the scale of the aerogel strands and there is no well defined interface shape. Instead, helium in aerogel exhibits an interesting and complex melange of characteristics from these two models and depends sensitively on aerogel structure.

4

Chapter 2

Phase Transitions in Porous Media

This section introduces phase transitions with an emphasis on the behavior of fluids near the liquid-vapor critical point. The behavior of bulk fluids will be reviewed, and the possible implications of including "fixed" (or "quenched") disorder will be introduced. The second section of the chapter will address the phenomenon of capillary condensation of fluids in porous media. Finally some implications of capillary condensation of near-critical fluids will be explored.

2.1 Phase Transitions and Critical Phenomena

2.1.1 The Liquid-Vapor Phase Transition

The liquid-vapor transition is familiar to all of us – we transform liquid to vapor when we boil water on the stove-top, and we depend on water condensing to form clouds above us. The transition is characterized by a discontinuous change in density (from that of the liquid to that of the vapor or vice versa). As the temperature and pressure of the fluid are increased, the difference between the liquid and vapor densities shrinks continuously until there is no difference between liquid and vapor at all. That is the liquid-vapor critical point (LVCP).

A generic liquid-vapor phase diagram is shown in Fig. 2.1, with each panel showing the liquid-vapor transition in terms of different thermodynamic variables. The most familiar plot is in terms of Pressure and Temperature, with a "coexistence curve" separating the liquid and vapor regions of the phase diagram; this curve represents the values of pressure and temperature at which both liquid and vapor are stable phases. It can also be illuminating to display the coexistence curve in

5
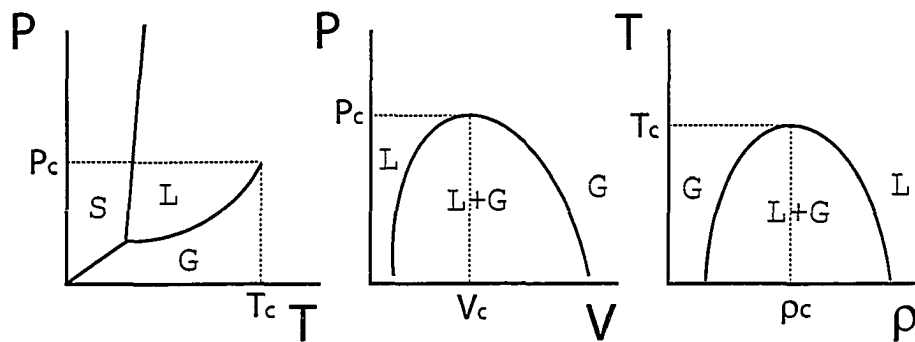
Figure 2.1: These are three representations of fluid phase equilibrium. Each axis is labelled with Pressure(P), Temperature(T), Volume(V), or density(ρ). The values of these parameters at the critical point are denoted by the subscript "c." Furthermore, each region of the phase diagrams is labelled by with the phase, or phases, present in that region: Solid(S), Liquid(L), Vapor(G, for "Gas").

terms of Pressure and Volume, Pressure and Density, or Temperature and Density. Examples of some of these curves are also included in Fig. 2.1 and, rather than as a line, each of these plots shows the coexistence curve as a region where liquid and vapor can coexist as a mixture.

To describe the form of a phase transition mathematically, an "order parameter" can be chosen to express the difference between the phases. In the case of the liquid-vapor transition the difference between the liquid and vapor densities ($\rho_l - \rho_v$) acts as the order parameter. The order parameter can be generalized to deal with many different fluids, with widely varying densities, using a reduced form such as:

$$\langle p(\mathbf{r}) \rangle = \left| \frac{\rho_l - \rho_v}{2(\rho_l + \rho_v)} \right|$$

Other phase transitions can be investigated using different order parameters such as magnetization (M) for ferromagnetic transitions, ψ for superconductivity, or superfluid density and phase (ρ_s) for superfluid ^{4}He.

2.1.2 Critical Points and Universality

As a sample approaches its critical point, thermal fluctuations in the order parameter become important. They grow as the sample approaches the critical point until, at the critical point, these fluctuations are macroscopic in size and may span the entire sample. In the case of fluids, these fluctuations manifest themselves as local density changes (i.e. regions of liquid appearing in the vapor phase and vice versa); as the

6

system approaches the critical point the fluctuations grow until they are even large enough to scatter light, leading to a characteristic known as critical opalescence.

As the scale of these fluctuations grows, other thermodynamic variables begin to behave in interesting ways as well – often tending towards zero or infinity at the critical point. This behavior is usually expressed in terms of power laws in temperature:

$$X = A \left| \frac{T - T_c}{T_c} \right|^a = A\epsilon^a \tag{2.1}$$

Here 'X' represents a thermodynamic variable such as susceptibility, heat capacity, or the size of density fluctuations (the "correlation length"), 'A' is a non-universal amplitude which depends on the system under investigation, 'T_c' is the critical temperature which also depends on the system and 'a' is referred to as the "critical exponent" which should be universal for all transitions in the Ising class. Note that the temperature here is scaled by the critical temperature and often expressed in reduced form ϵ to highlight the universality of the critical behavior.

There is a set of critical exponents for each phase transition which characterizes how each static thermodynamic variable behaves near the critical point. Scaling theory has gone on to show that in fact only two of these exponents are independent[16]. An early review of static phenomena in critical systems[17] gives a good summary and discussion of critical exponents and their interrelations. Table 2.1 defines some critical exponents for fluids and includes their up to date values as calculated by renormalization theory[18].

One of the amazing things about critical phenomena is that there are so few critical exponents. While different fluids may have vastly different critical temperatures and densities, they share the same critical exponents (see Table 2.2 which compares some experimental values for three different fluids). In fact, critical exponents turn out to be even more general. Not only do all fluids share the same exponents, all

Thermodynamic Variable	Exponent	Value
Isochoric Heat Capacity	α	0.109 ± 0.004
Density difference between phases	β	0.3258 ± 0.0014
Isothermal compressibility	γ	1.2396 ± 0.0013
Correlation length	ν	0.6304 ± 0.0013

Table 2.1: Critical exponents for the Ising universality class in three dimensions from [18]. The Ising universality class includes liquid-vapor critical behavior as well as that of uniaxial ferromagnets.

7

Fluid	$\rho_c(g/cm^3)$	β	γ
Ne (a)	0.484	0.327±0.002	1.250±0.015
N$_2$ (a)	0.314	0.327±0.002	1.233±0.010
^{3}He	0.0414 (b)	0.320±0.002 (c)	1.19±0.01 (c)

Table 2.2: Critical exponents for selected fluids. Modern experiments on critical fluids now tend to fix the critical exponents at their theoretical values and use their data to probe critical amplitudes and corrections to scaling. Earlier results (such as those shown here for ^{3}He) neglected some terms in their analysis which led to systematic deviations in their apparent critical parameters; when that data is replotted with more recent results it is completely consistent with the exponent values shown in Table 2.1. (a) from reference [19],(b) from reference [20], and (c) from reference [21].

three dimensional transitions with scalar order parameters show exactly the same behavior near the critical point (referred to as Ising behavior). Critical behavior turns out to depend exclusively on the form of the order parameter and the dimension of the system, allowing us to place all critical phenomena within a limited number of "universality classes." By analyzing a single system in a universality class we can make generalizations about the entire class of related transitions, including all the critical exponents.

The power law behavior of thermodynamic variables shown in Eq. 2.1 is only truly seen asymptotically close to the critical point; in real systems there are systematic deviations from Eq. 2.1 which must be accounted for as the distance from the critical point increases. For instance, asymptotically close to the critical point, the liquid-vapor coexistence curve should have the form:

$$\left| \frac{\rho_l - \rho_v}{2(\rho_l + \rho_v)} \right| = B_0 \left| \frac{T - T_c}{T_c} \right|^\beta = B_0 \epsilon^\beta$$

where B_0 is a non-universal amplitude which must be measured for each fluid. In reality, small corrections must be included so that the effective form of the coexistence curve becomes:

$$\left| \frac{\rho_l - \rho_v}{2(\rho_l + \rho_v)} \right| = B_0 \epsilon^\beta \left(1 + B_1 \epsilon^\Delta + B_2 \epsilon^{2\Delta} \right) \tag{2.2}$$

where β is the critical exponent, B_0, B_1, and B_2 are non-universal amplitudes and $\Delta = 0.5$ is the first correction to scaling exponent. If these corrections are not included, analysis of experimental data on fluids yields spuriously high values for β. Experimental measurements of critical exponents are challenging because, even using corrections to scaling, they must approach exceptionally close to the critical

8

point. When fitting the power law behavior, data must be collected over a few orders of magnitude in reduced temperature to achieve reasonably precise values for the critical exponents.

Theoretical determinations of the critical exponents are also highly challenging – the framework to compute them systematically was only developed in the late 1960's and early 1970's. Earlier calculations were limited to a few simple models and required a lot of work and ingenuity to produce what were fairly imprecise estimates of a few critical exponents. The sudden increase in the precision of the theoretical estimates was due to the development of renormalization group theory calculations of critical exponents by Kenneth Wilson[16]. This approach opened the possibility of calculating exponents to a high degree of precision fairly easily. Coupled with studies using other computational approaches, the values of the Ising critical exponents were well established by the 1980's and agree completely with experiments.

2.1.3 Ising Model and Random Field Ising Model

The liquid vapor phase transition falls into the Ising model universality class. The Ising model is most familiar in the context of ferromagnetic transitions – it represents the ordering of a uniaxial ferromagnet in a vanishing external field. The Hamiltonian of this system is:

$$H = -J \sum_{\langle i,j \rangle} S_i S_j \tag{2.3}$$

where J is the coupling constant between neighboring spins and S_i is a spin which can only have the values of ± 1.

The liquid-vapor transition becomes analogous to the Ising model at the critical point. Here the values of S_i can be 1 (liquid) or 0 (vapor). The separation of two immiscible liquids (sometimes referred to as liquid-liquid demixing) also belongs to the Ising class – in that case the "spins" represent the two liquid components ($S_i = +1$ if liquid A is present, $S_i = -1$ if liquid B is present). The system will tend to align all spins in one direction (for magnetic systems) or separate into two distinct phases (fluid systems) for all temperatures below T_c. The critical behavior of this type of system was addressed in the last section, including the critical exponents found for liquid-vapor and magnetic transitions.

The Ising model Hamiltonian can be slightly modified to include disorder in the form of random fields. The resulting Hamiltonian describes the random-field Ising

9

model (RFIM):

$$H = -J \sum_{\langle i,j \rangle} S_i S_j - \sum_i h_i S_i \qquad (2.4)$$

This expression is identical to Eq. 2.3 with the addition of a small field, h_i, which takes on a random value for each site i. For an introduction to the effects of randomness on magnetic transitions see reference [22]. The possibility of finding an analog in fluid systems was first explored by de Gennes[23, 1] in the context of binary fluid separation in a porous medium or gel.

When two immiscible liquids are imbided in a dilute porous medium, one phase will preferentially adsorb onto the walls or strands of that medium. The medium acts as a "fixed" or "quenched" impurity because it is fixed in space and non-mobile. Very dilute silica gels could therefore act as "random fields" with respect to the composition of the liquid in their vicinity. If the interface between the two liquids is well defined on a length scale less than the characteristic pore size of the gel, then one may see behaviors similar to those seen in random magnets. The separation of binary fluids in gels can be further generalized to the liquid-vapor transition in aerogels. In such a system the strands may act as a small random field which preferentially adsorbs liquid.

Part of the motivation for the studies in this thesis was to search for random field behavior of fluids in aerogels. To that end we mapped out coexistence curves so that the critical exponent β could be determined. A value far from that of the pure fluid ($\beta = 0.327$) would indicate a change in universality class, perhaps from that of the Ising model to that of the random-field Ising model. Calculations of the critical exponents for the random-field Ising model are nowhere near as well developed as those for the Ising model, but I have summarized some values Table 2.3. Note that β differs greatly from that of the Ising model – the shape of the coexistence curve should be a powerful indicator of any change in universality class.

2.2   Capillary Condensation

Far from the critical point, where pore size (R) is much larger than the correlation length of the fluid (ξ), much of the behavior of fluids in porous media is governed by the energetics of the liquid-solid, solid-vapor, and liquid-vapor interfaces, usually described as surface tension. This section will explore the role of surface tension in fluid-filled porous media and the effect that surface tension has on the liquid-vapor

10

Technique	Exponent	Value
Monte Carlo	ν	1.1 ± 0.2
[24]	η	0.50 ± 0.05
	β	0.00 ± 0.05
Migdal-Kadanoff	ν	2.25
renormalization group	α	-1.37
[25]	β	0.02

Table 2.3: Critical exponents for the random-field Ising model calculated by two different methods.

transition.

2.2.1 Surface Tension

Surface tension is another familiar phenomenon of everyday life – we take advantage of it every time we use a towel to dry ourselves off after a shower, we depend on it to hold paint to walls while it dries, and we manipulate it with chemicals to help wash greasy dishes.

It is an effect due wholly to the energetic cost of maintaining a boundary between two immiscible substances. If one imagines two materials in contact (during this discussion we will assume one is a vapor and the other a liquid, but they do not need to be) there exists a plane of molecules at each phase's surface in an unfavorable state. While molecules within the liquid are surrounded by identical molecules and are held in place with binding energy U, those at a liquid-vapor interface are only in contact with half the number of molecules and, hence, are held in place with binding energy $U/2$. Thus the interface has an energetic cost of $U/2$ per molecule, expressed as γ_{lv} (in units of J/m^2 or equivalently N/m) – γ is referred to as *surface tension* and the subscripts indicate that this particular interface exists between liquid and vapor phases. The interface will experience a force in whatever direction will minimize the energy of the system, so the liquid-vapor interface above will form the liquid into a spherical drop in order to minimize the surface area. Some implications of surface tension are explored in the next few sections – much of this discussion is adapted from the ideas in a wonderful book on the subject written by de Gennes, Brochard-Wyart, and Quéré[26].

11

Laplace Pressure

If one did work to change the size of the droplet described above by an infinitesimal amount, δR, then the energy involved would look like:

$$\delta W = -p_l dV_l - p_v dV_v + \gamma_{lv} dA_l$$

where δW is the work done to change the radius of the drop by δR, $-p_l$ and $-p_v$ are the pressures of the liquid and vapor, and $dV_l = -dV_v$ are the changes in the volumes of the liquid and vapor. For a sphere we know that $dV = 4\pi R^2 dR$ and $dA = 8\pi R dR$; in equilibrium we must have $\delta W = 0$ which leads us to the relation:

$$\Delta p = p_l - p_v = \frac{2\gamma}{R}$$

which is known as the *Laplace Pressure* and represents a pressure difference across the interface. For a more general curved interface this pressure is related to the curvature of the surface as:

$$\Delta p = \gamma C = \gamma \left(\frac{1}{R} + \frac{1}{R'} \right) \tag{2.5}$$

where R and R' are the radii of curvature of the surface. In the simple spherical example above $R = R'$ which leads to the simpler expression.

A few very important points should be made about Laplace pressure. First, it should be noted that the Laplace pressure can be positive or negative depending on the shape of the interface. Two examples are shown in Fig. 2.2. In the case of the droplet (Fig. 2.2a) discussed above we have an overpressure. In the case of liquid in a pore or a crack in a solid (Fig. 2.2b) the curvature is *negative* which leads to a lower pressure within the liquid. In such a situation liquid forms preferentially in the smallest cracks, corresponding to the least negative radii of curvature, and can be drawn out of a bulk reservoir to fill the porous medium. This type of behavior leads to capillary condensation, a topic addressed later in this chapter.

Three Phase Systems

In the case of liquid on a solid substrate the situation is not quite as simple as a free floating droplet, but it is much more interesting. The systems investigated in this thesis all involve a solid (silica aerogel) and a liquid (helium or neon) in coexistence with its vapor. Generally, to describe the behavior of such a system one needs to characterize three surface tensions:

12
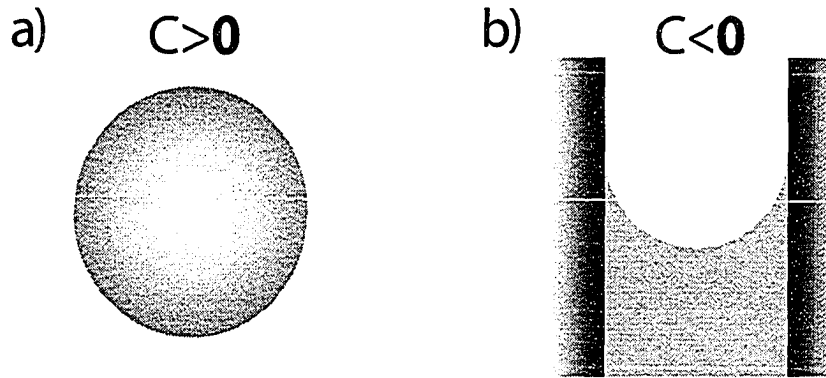
Figure 2.2: The two situations shown above illustrate conditions under which you can have positive (a) or negative (b) curvature of the liquid-vapor interface. In the case of the droplet (a) the liquid experiences an overpressure while in the case of liquid in a crack (b) the liquid is under-pressured.
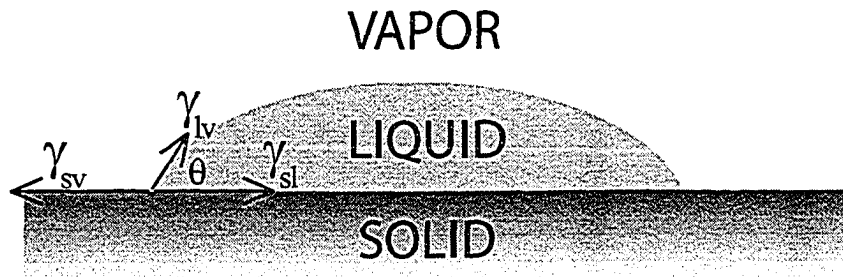
Figure 2.3: The triple line, where solid, liquid and vapor meet, experiences surface tension from each of the interfaces. If it is stable (i.e. not moving) these must balance. Note that while the horizontal component of γ_{lv} is balanced by the other two surface tensions, the vertical component is usually balanced by elastic stress on the solid.

γ_{sv} Surface tension along solid-vapor interface
γ_{sl} Surface tension along solid-liquid interface
γ_{lv} Surface tension along liquid-vapor interface

When a small area of the solid is covered with liquid there must exist a line along the edge where all three phases come into contact, known as the "triple line." If that line is stable, by Newton's second law, we must have $\Sigma \vec{F} = 0$ or, referring to Fig. 2.3:

$$\gamma_{sv} - \gamma_{sl} = \gamma_{lv} \cos(\theta) \tag{2.6}$$

13

In this equation θ represents the *wetting angle*, the angle that the surface of the liquid forms with the solid. In the systems within this thesis the solid is totally wetted by the liquid; in other words $\theta = 0$ and there is no triple line – any liquid present spreads out to cover the solid completely. This means that it is always energetically favorable to replace the single solid-vapor interface with two new interfaces with the same area: the solid-liquid and liquid-vapor interfaces. This simplifies analysis – all further discussion on behaviors due to surface tension assumes total wetting.

Thin Films

So far in this section we have treated everything macroscopically, but we must also consider microscopic liquid films if we are to apply any interpretation to fluids in aerogels. The characteristic scales of aerogel structure vary from about 2nm-200nm which is *not* large compared to the range of the van der Waals forces holding the liquid film to the aerogel surface. For films significantly thinner than 100nm on a flat substrate, the solid substrate can in some ways "sense" the vapor phase above the film[26], so we must include an additional energy term. The energy of the interface (per m^2) then becomes:

$$E = \gamma_{sl} + \gamma_{lv} + P(e)$$

for a film of thickness e. This extra energy term, $P(e)$, leads to another source of effective pressure within the film, the *disjoining pressure* ($\Pi(e)$), defined as:

$$\Pi(e) = -\frac{dP(e)}{de}$$

In a planar system governed solely by van der Waals forces these take on the values:

$$P(e) = \frac{A}{12\pi e^2} \qquad \Pi(e) = \frac{A}{6\pi e^3}$$

where "A," known as the Hamaker constant, varies from system to system and quantifies the strength of the interaction.

The most important question for us to ask is how such a thin film behaves on a rough surface, where there are competing forces: surface tension favors a film with a smooth surface that does not depend on the form of the substrate surface, while $P(e)$ favors a film of equal thickness covering the surface regardless of substrate profile. If the surface profile is changing slowly (Fig. 2.4a) then $P(e)$ wins out, resulting in a film of constant thickness. However, if the characteristic length of the variation is short (Fig. 2.4b), then the surface energy cost of creating a modulated film is too

14
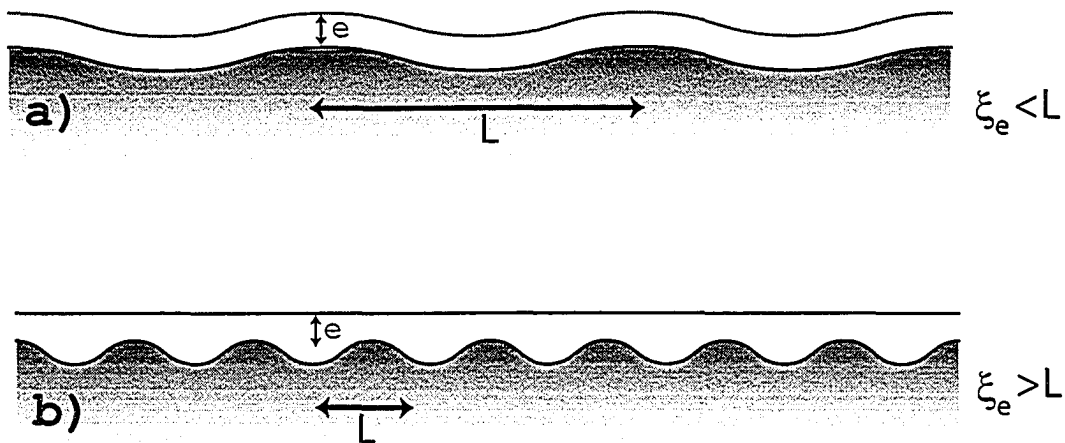
Figure 2.4: The behavior of thin films on rough surfaces. For modulations in the surface that occur on a scale greater than the healing length (ξ_e) the disjoining pressure ($\Pi(e)$), forces the film to follow the contours of the surface. For modulations that occur on scales shorter than the healing length, surface tension (and the associated Laplace Pressure) forces the film to adopt a flat profile.

great and the film has a flat profile. The length at which behavior crosses over from one picture to the other is given by the "healing length":

$$\xi_e = \left(\frac{\gamma_{lv}}{\frac{d^2 P(e)}{de^2}} \right)^{\frac{1}{2}}$$

While these derivations have been made assuming a planar substrate, it is interesting to use them to make an order of magnitude estimate for film behavior in aerogels. Aerogel consists of strands of silica which have roughness with a wavelength of about 5nm and relief of about 1nm (for more specifics on aerogel structure, see chapter 4). For a helium film on silica only van der Waals forces contribute to $\ddot{P}(e)$ so the healing length can be expressed as:

$$\xi_e = \left(\frac{\gamma_{lv} 2\pi e^4}{A} \right)^{\frac{1}{2}}$$

Using the fact that at 4K $\gamma_{lv} \approx 10^{-4} N/m$ [27] and $A(He - SiO_2) \approx 6 * 10^{-21} J$[28] we can calculate $\xi_e \approx 2 * 10^9 e^2$. Setting $\xi_e = 5nm$ to simulate the roughness of aerogel, there is a crossover in film structure at $e \approx 1.6nm$. For thinner films, the helium film tends to conform to the surface, covering all the areas equally. Thicker films will start to "fill in" irregularities in the strands and accumulate in joints where strands meet. While this is a very thin film, keep in mind that even at 1.6nm

15

thick, the surface area of aerogels is so large that this film occupies about 8% of the open volume in 95% porous aerogel. Thus, during adsorption a significant quantity of helium must be adsorbed before it will start to form three dimensional "blobs" anywhere. Since this behavior depends on the surface tension, which is temperature dependent, the "crossover" thickness of the film increases as temperature rises, albeit slowly ($e \propto \gamma_{lv}^{-\frac{1}{4}}$).

Instability of a Film on a Fibre

In the previous sections we've discussed the role of surface tension in smoothing out interfaces, but there exist situations in which surface tension can lead to *instability* of a smooth surface. For instance, a steady stream of water from a faucet will break up from a smooth cylinder to a stream of droplets (if given sufficient time) in an effort to minimize surface energy. An analogous process (the Plateau-Rayleigh instability) occurs along a fiber coated with a thin sheath of liquid. While the liquid sheath may begin as a cylindrical shell about the fiber, it will gradually destabilize into a wavy profile, and eventually separate into a chain of unconnected droplets. One could conceive of such a situation occurring along aerogel strands which are about 5nm thick and up to 100nm long – it behooves us to perform a few basic calculations to see if it does. All of these calculations have been performed using formulae from de Gennes *et al.*[26].

For a weakly modulated film surface the energy change of forming a modulation of wavelength λ and magnitude δe on a strand of radius b in *Joules/meter* is:

$$\Delta E = \frac{1}{4}\gamma\frac{\delta e^2}{R}2\pi(q^2 R^2 - 1)$$

where R is the outer radius of the film (i.e. $e_0 + b$), and q is the wavevector corresponding to λ ($q = \frac{2\pi}{\lambda}$). From this relation it can be seen that any modulation with $\lambda > 2\pi R$ is energetically favorable; this is shown pictorially in Figure 2.5.

For a very thin film, such as we might have on an aerogel strand, the energy gain of the modulation is going to be opposed by the energy loss of further thinning an already thin film. Assuming only van der Waals forces between helium and a planar substrate there will exist a film between droplets with thickness:

$$e = \left(\frac{bA}{6\pi\gamma_{lv}}\right)^{\frac{1}{3}}$$

For helium at about 4K on silica strands of diameter $\sim 5nm$ we can estimate $e \approx 2nm$, which, reassuringly, is slightly larger than the minimum film thickness

16
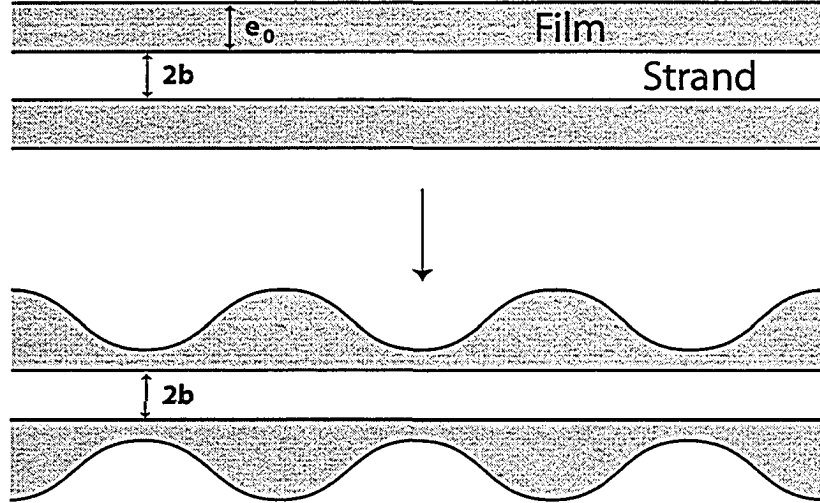
Figure 2.5: Under the right circumstances surface tension can lead to the instability of a smooth surface. Shown here is a cross-sectional view of a liquid film on a thin strand; the energetically favorable state is one which shows a modulating surface profile despite the smoothness of the underlying strand.

calculated earlier. If we take this as a lower bound on film thickness required to show the Plateau-Rayleigh instability, we find that the minimum unstable wavelength is about 30nm:

$$\lambda_{min} = 2\pi R = 2\pi(b + e_{min}) = 2\pi(2.5nm + 2nm) \approx 30nm$$

This is not much less than the average spacing between aerogel strand junctions; in fact, by the time a film thick enough to show significant modulation has formed the minimum wavelength has increased to about 50nm. In such a situation this instability is likely to be washed out by the inhomogeneity of the aerogel structure present on similar scales. In other words, droplets forming at the intersections of aerogel strands will dominate over any spontaneous formation along the strands themselves.

2.2.2 The Kelvin Equation and Capillary Condensation

We can combine knowledge of the thermodynamics of the liquid-vapor phase transition and the energetics of interfaces to derive the Kelvin equation, which gives us a relation between the surface tension of the adsorbed fluid and the depression of the condensation pressure during adsorption and desorption. To do so we need to

17

assume a certain shape for the interface (a hemisphere in this case) and a uniform size and shape for the pores. We will also assume that the liquid completely wets the pore walls. The details are contained in Appendix A, and the resulting relation is:

$$-RT \ln \frac{p_v}{p_0} = \frac{2v_l \gamma_{lv}}{r} + v_l(p_0 - p_v) \qquad (2.7)$$

Here R is the gas constant, T is temperature, v_l is the molar volume of the liquid, γ_{lv} is the surface tension along the liquid-vapor interface, p_v is the vapor pressure, p_0 is the bulk condensation pressure and r is the radius of the hemisphere. Thus the pressure at which the fluid condenses into the pore is reduced from the bulk condensation pressure in a way that depends sensitively on both surface tension and pore size.

In the case of isolated droplets (i.e. not within a porous medium) one has an overpressure within the droplet. Since this overpressure increases as droplet size decreases, liquid tends to evaporate from small drops and condense onto larger drops in a process known as Ostwald ripening.

2.2.3 Adsorption Isotherms

Capillary condensation in a porous medium is usually probed using adsorption isotherms of fluids (often liquid nitrogen) in that medium – an adsorption isotherm showing the capillary condensation of helium in aerogel is included as Fig. 2.6. The plot shows the quantity of helium adsorbed into a slice of aerogel as vapor pressure is increased from zero to the bulk saturated vapor pressure (p_0) and then cycled back well below p_0. The onset of capillary condensation is fairly abrupt, with the gel filling quickly with liquid over a small pressure range. The emptying of the gel is even more abrupt and usually occurs at a lower pressure than filling, leading to hysteresis.

The general prediction of the Kelvin equation is true – porous media with smaller pores show capillary condensation at lower pressures. However, capillary condensation does not occur in all pores at the same pressure. Instead, any real porous medium has a range of pore sizes and the adsorption and desorption branches both have a finite slope (whereas an ideal medium with uniform pores would exhibit an infinite slope). In fact, one can use the precise shape of the isotherm to estimate both the specific surface area of the sample and the range of pore sizes in the sample[29].
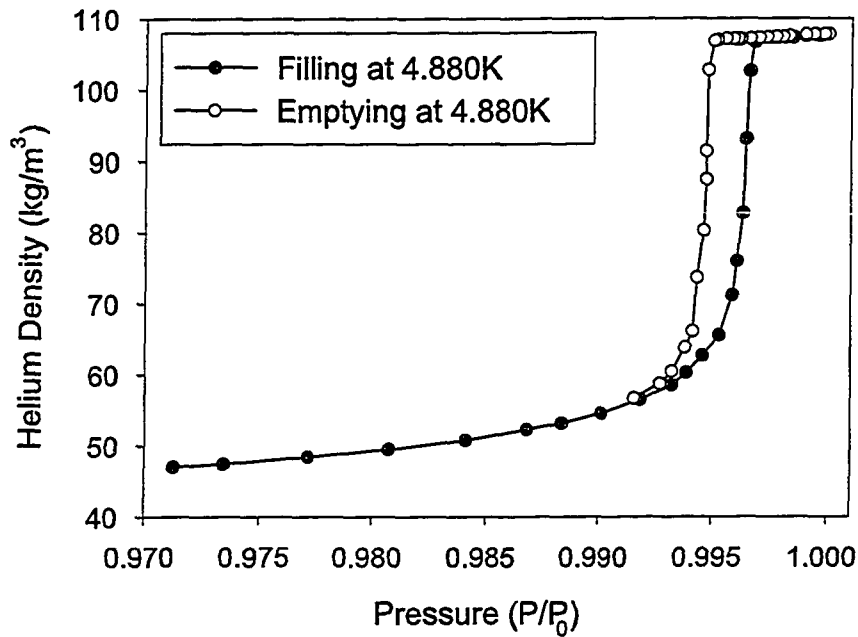
Figure 2.6: An adsorption isotherm for helium in 95% porous aerogel at 4.880K.

The fact that the adsorption and desorption branches of the isotherm occur at different pressures seems, at first, to contradict the simple history independent form of the Kelvin equation. However, a number of explanations for the origin of hysteresis have been advanced. One explanation asserts that there are two distinct sizes which govern capillary condensation in a porous medium — the (relatively larger) pore size and the (relatively smaller) neck size connecting the pores. During adsorption capillary condensation can occur in both the pores and necks, desorption is governed solely by the more restrictive necks. Thus adsorption and desorption probe two different size scales and the adsorption and desorption pressures differ.

Another explanation asserts that the shape of the menisci on the adsorption and desorption branches differ, affecting the Laplace pressure. If one envisions an ideal cylindrical pore, as the fluid is adsorbed onto the surface it forms a film over the walls of the cylinder. This film has a curvature with components parallel to the pore wall and perpendicular to it of:

$$C = \frac{1}{R_{\parallel}} + \frac{1}{R_{\perp}} = \frac{1}{\infty} + \frac{1}{R_{pore}} = \frac{1}{R_{pore}}$$

rather than the value $C = 2/R_{pore}$ that a hemisphere exhibits. As fluid is adsorbed the film thickens, but the shape remains cylindrical until the pore is almost full (when liquid bridges will form across the pore, completing the condensation). The

19

retreating meniscus (i.e. on the desorption branch), however, *does* have a hemi-spherical shape since the pore will empty from the end. As fluid is removed the meniscus retreats, keeping its hemispherical form. Since the curvature of the re-treating meniscus is twice that of the film formed along the adsorption branch, the Kelvin equation states that for cylindrical pores:

$$\ln\left(\frac{p_d}{p_0}\right) = 2\ln\left(\frac{p_a}{p_0}\right)$$

While aerogels do not contain perfect cylindrical pores, this general argument for hysteresis remains valid – *the shape of the meniscus during adsorption and desorption can be different, leading to a different capillary condensation pressure.*

Later in this thesis I will show some of our extensive data on adsorption isotherms for helium in silica aerogel, but most of the techniques for analyzing the shape of the adsorption isotherm quantitatively involve assumptions about pore shape that do not in any way reflect the structure of aerogel. The interested reader can track down further details on how adsorption isotherms can be used to determine pore size, shape and connectivity in the relevant references[29, 30, 31, 32].

2.2.4 Freezing in Real Pores

Freezing of liquids in small pores is affected in the same way that condensation is. The framework used to calculate the freezing point depression is included in Appendix A and gives:

$$\Delta T = \frac{2\gamma_{sl} v_s T_0}{r\,\Delta H}$$

where the volume used is now the volume of the solid, γ is the surface tension between solid and liquid, and ΔH is the heat of fusion. Studies show a convincing correlation between freezing point depression and $1/R$, even for pores with radii of 2nm[33]. Freezing of helium in small pores also shows a large depression of freezing temperature, or elevation of freezing pressure[34, 35] consistent with the Kelvin Equation.

If the interaction between the pore walls and the solid forming within the pores is strong enough, small pores can lead to *higher* freezing temperatures. This is because the interfacial energy favors the formation of the solid phase whereas usually an unfavorable interaction between solid and wall is assumed. Such elevations were seen in the freezing of carbon tetrachloride in the micropores of activated carbon fibers[36].

20

Solid helium in aerogel may provide an interesting model system for disorder in a solid, but its slow equilibration times and the fragility of the aerogel may make experiments prohibitively difficult.

2.2.5 Capillary Behavior in Near Critical Fluids

At the outset of the chapter I introduced critical phenomena in fluids with attention paid to the possible realization of the random-field Ising model by introducing aerogel (as a fixed impurity) into a fluid near its critical point. However, the last few sections have dealt solely with surface tension and adsorption of liquid films while completely neglecting the presence of fluctuations such as those that characterize the critical point. Indeed, far from T_c the picture provided by capillary condensation is powerfully predictive. However as the correlation length, ξ, approaches the strand thickness we may see something of a crossover from capillary condensation to fluid critical behavior as a system approaches the liquid-vapor critical point.

When ξ is small, fluctuations are not significant and we see behavior governed solely by capillary condensation. When ξ grows to the size of an average pore we would not expect capillary condensation to provide an adequate picture of fluid behavior in aerogel – capillary condensation requires that we define an interface between liquid and vapor but if $\xi > R_{pore}$ then we can't define any interface smaller than the size of the pore.

Correlation length follows the power law:

$$\xi = \xi_0 \epsilon^{-\nu} \left[1 + \xi_1 \epsilon^\Delta + ...\right] \tag{2.8}$$

where $\nu = 0.63$. To make a rough estimate of correlation length we can neglect the correction to scaling terms, although this means our estimates will not be very precise. For neon, $\xi_0^+ = 0.13nm$[37] while for ^{4}He $\xi_0^+ = 0.18nm$[38]. We are interested in the correlation lengths below T_c, so using $\xi_0^+/\xi_0^- \approx 2$ [39] we arrive at the correlation lengths shown in Table 2.2.5. From this table we can see that for $\epsilon > 10^{-2}$ the correlation length is less than the thickness of the silica strands and comparable to the healing length discussed earlier. For $\epsilon < 10^{-4}$ the correlation length exceeds the size of the pores and closer to the critical temperature the fluid can not sense the pores directly. If we see a crossover in behavior it should be in this region ($10^{-4} < \epsilon < 10^{-2}$). This is shown pictorially for helium in Figure 2.7, where the correlation length, and the associated liquid-vapor interface thickness,

21

ϵ	ξ(Ne)	$T - T_c$ (Ne)	ξ (^{4}He)	$T - T_c$ (^{4}He)
10^{-2}	1.2nm	445mK	1.6nm	52mK
10^{-3}	5.0nm	44.5mk	7.0nm	5.2mK
10^{-4}	22nm	4.5mK	30nm	0.5mK

Table 2.4: The correlation lengths in neon and helium near the critical point. As the temperature nears the critical temperature the correlation length grows to the size of the silica strands, and eventually to the size of the aerogel pores themselves.

are plotted as a function of temperature. The aerogel strand size (5nm diameter) and maximum pore size (50nm radius) are included so that one can easily see when the characteristic scales of the aerogel and the fluid fluctuations become comparable. Also included are the temperature regions explored by earlier work on helium liquid-vapor coexistence in 95% porous aerogel at Grenoble (shown as vertical lines at 4.88K and 5.14K) and at Penn State (shown as a shaded region from about 5.14K to 5.17K. These earlier studies are discussed in the next chapter; our work spans temperatures from 4.400K to above the critical point (T_c = 5.195K).

22
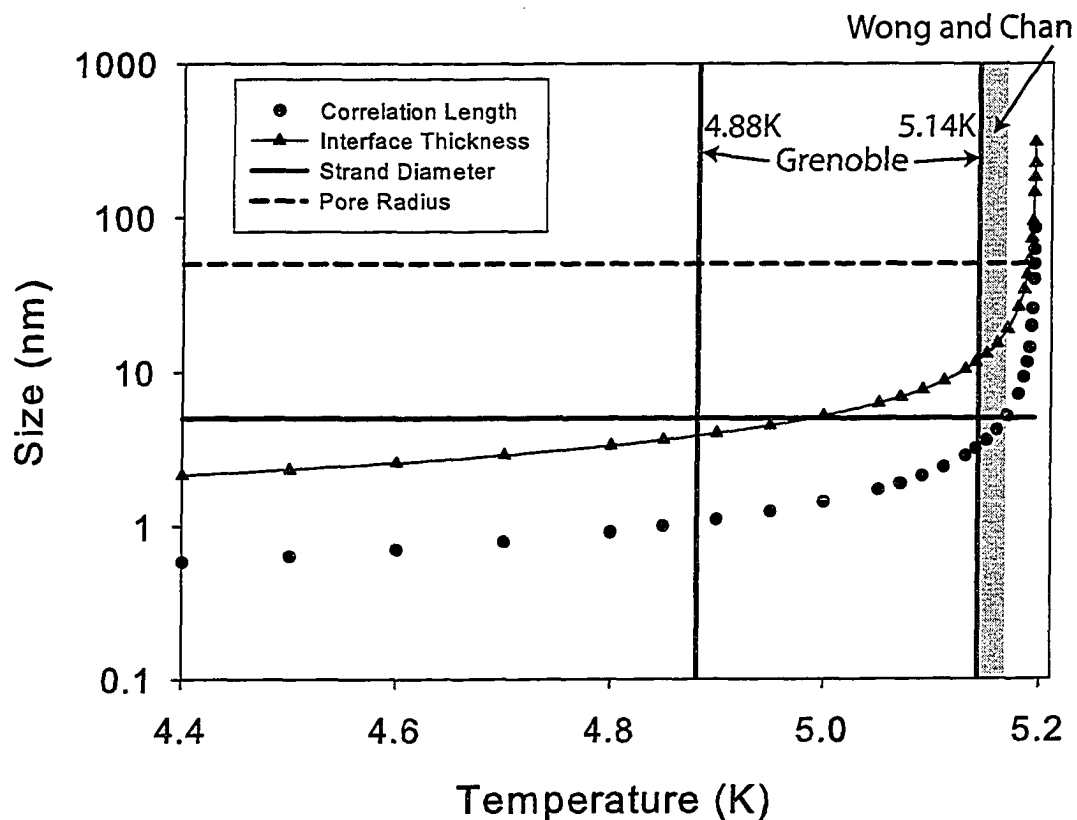
Figure 2.7: The average strand diameter of the aerogel, and an estimate of its maximum pore radius are plotted here and compared to characteristic lengths in the fluid. As the critical temperature is approached, the correlation length (and hence the liquid-vapor interface thickness) diverges – eventually exceeding the strand size and then even the maximum pore size. The temperature regions probed by earlier work in other groups are highlighted here – 4.88K and 5.14 by the Grenoble group[14] and about 5.14K to 5.165K by Wong and Chan[10].

23

Chapter 3

Relevant Results from the Literature

Experiments directly relevant to this thesis fall into two broad categories: those exploring capillary condensation in porous media and those exploring binary fluid separation ("liquid-liquid demixing") in dilute solid networks. In bulk systems, both the liquid-vapor transition and binary fluid separation belong to the Ising universality class, and ought to be affected in similar ways by the introduction of a dilute solid network. The solid might act as a random field, but for this to be the case the system under investigation must be in an equilibrium configuration, the strength of the fluid-solid interaction must be right and the scale of the solid network becomes very important. Researchers have been searching for a system in which all these factors cooperate to make a realization of the random-field Ising model for two decades.

The largest, and virtually universal, effect of a porous medium on the liquid-vapor transition or on liquid-liquid demixing is to slow the dynamics by orders of magnitude; in fact, the binary liquid in porous medium experiments can take months to equilibrate after a temperature step within the two-phase coexistence region of the phase diagram. In such situations it is very difficult to distinguish between equilibrium behavior and long lived metastable states. The following sections will review the attempts to elucidate the behavior of fluids near a critical point in porous media – a region whose interpretation requires a mix of capillary condensation and critical behavior.

Experimental work on near critical fluids in porous media has been complemented by some excellent theoretical and modelling work. A couple of powerful frameworks for the study of fluids in porous media have been developed in the last

24

two decades, and produce the depressed critical temperature and narrowed coexistence curve which is seen in experiments. Aerogel presents some difficulties beyond those experienced in modelling denser porous media, mainly because of the exceptionally large simulation volumes needed to give a realistic picture of the aerogel structure. However, in the last few years some exciting and intriguing simulations of adsorption of near critical fluids in aerogel provide a beautiful counterpoint to our experiments.

This chapter will try to touch on the most important published studies relevant to our work on neon and helium in aerogel. Some of the studies involve denser media than aerogel and provide a general picture of capillary condensation of near critical fluids, but whenever possible I have concentrated on studies involving aerogel. There is not room to discuss in detail the methods used (especially in the theoretical and simulation work) in most of these works but where possible I have tried to provide illuminating references which explain things much better than I could.

3.1 Capillary Condensation of Near Critical Single Component Fluids

The coexistence curve of a bulk fluid is well defined and easy to map out by locating the liquid-vapor transition along isotherms, isobars or isochores. However, when trying to define an analogue of the bulk coexistence curve in a porous medium there are some difficulties. First, one can sensibly ask if there even *are* direct analogues of the bulk liquid and vapor phases in porous media. As it turns out, there are reasonably distinct low and high density fluid phases ("pore vapor" and "pore liquid"), although the phase diagram can also include the complications of films, liquid bridges, and capsules forming in the pores [40]. However, even if there are two distinct pore-fluid phases, there is still difficulty defining a precise transition between the two.

In bulk the liquid-vapor transition appears as a sudden change in fluid density with no change in pressure or temperature – a region of zero slope on a density-pressure isotherm. Such an isotherm is shown in Figure 3.1 along with an isotherm for helium confined within 95% aerogel; both isotherms were taken at 5.194K, just below the bulk critical temperature. During capillary condensation there is no region with zero slope on a density-pressure isotherm, even at T=0. There is, however, a *plateau-like* region that is sometimes assigned the same significance as the actual
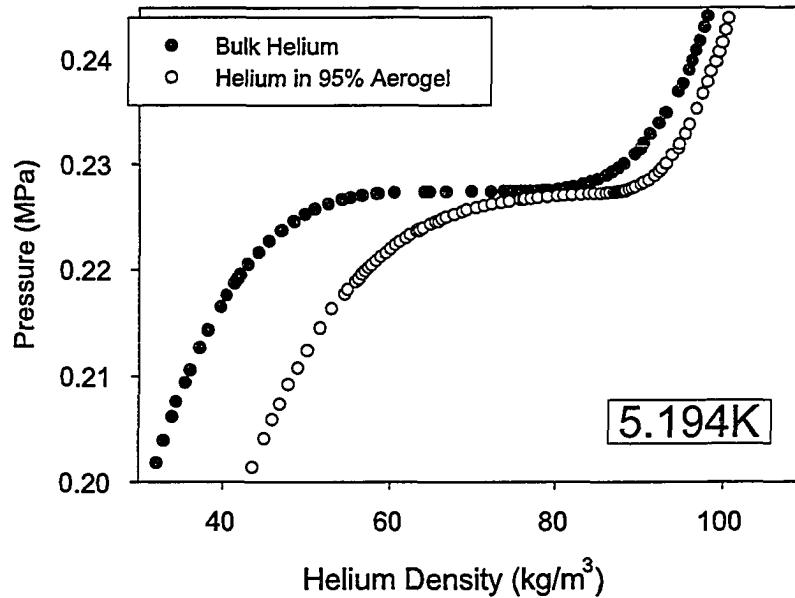
Figure 3.1: Bulk helium and helium in 95% aerogel (referred to as sample B110 later in this thesis) adsorption isotherms at 5.194K, just below the liquid-vapor critical point of helium. Note that helium is preferentially adsorbed in the aerogel shifting the isotherm to higher densities, especially on the lower density side where we can see the effect of a film of adsorbed helium on the strands of the aerogel. The bulk isotherm also exhibits a much wider and flatter plateau than the adsorption isotherm in aerogel and is more symmetric.

plateau seen in bulk fluids. The finite slope of adsorption and desorption isotherms is usually associated with the variety of adsorption environments – real porous media exhibit a range of pore sizes, with each pore exhibiting a phase transition at a slightly different point. In such a case the system is controlled by microscopic factors, precluding a true macroscopic transition. The largest barrier to interpreting capillary condensation in terms of liquid-vapor coexistence, however, is the existence of hysteresis in adsorption and desorption isotherms – hysteresis in isotherms tends to indicate a system out of equilibrium. The closure points of the hysteresis loop are sometimes used to mark liquid-vapor coexistence in pores, but that interpretation presents some difficulties.

Isotherms are not the only way to investigate the liquid-vapor transition in pores; alternatively measuring heat capacity, sound speed or light scattering along an iso-chore (i.e. constant density sample) can pinpoint transition temperatures which map out the "coexistence curve." However, the interpretation of such data has its own

26

pitfalls – without an accurate microscopic picture of the structure of the pore liquid and vapor phases, and in depth understanding of the transition, it is difficult to assign features of the isochore to the liquid-vapor transition. This was also a major problem with binary liquids in gels, where light scattering had an onset temperature consistent with the bulk demixing curve but which decayed slowly as the system equilibrated over weeks [41]. The true demixing curve of such systems cannot be precisely mapped out by light scattering because collecting the data might take decades.

The doubts about identifying a pore liquid-vapor transition expressed above do not imply that we are completely in the dark about the process of capillary condensation. In fact, condensation in simple, model, pores is well understood and is well explained by the Kelvin equation. However, near to the critical point things become fuzzier and the assumptions made in the derivation of the Kelvin equation begin to dissolve. In this situation it behooves us to express what information we hope to extract from a pore liquid-vapor coexistence curve, however we choose to map out that curve. We may unambiguously define a temperature, T_{ch}, above which hysteresis in the adsorption isotherms disappears. T_{ch} should be less than the bulk critical temperature T_c, since above T_c there should not be any liquid-vapor transition at all. We may also try to define the "pore critical temperature" T_{cp} which may or may not be equal to T_{ch} or T_c. T_{cp} is analogous to T_c in bulk – it is the temperature at which distinct liquid and vapor phases cease to exist.

Many people have assumed that $T_{ch} = T_{cp}$, but since there is no agreement on the precise origin of hysteresis during adsorption and desorption it is somewhat dangerous to use the presence or absence of hysteresis as a marker for the physical state of the system. One possible approach is to define T_{cp} as the point at which the slope of the adsorption isotherm (i.e. the isothermal compressibility) changes abruptly. In bulk fluids the slope of the isotherm (measured at the critical density) changes from zero for $T < T_c$ to a finite positive value which increases with temperature for $T > T_c$; in capillary condensation the change would not appear quite so abrupt but there are examples where a kink in the isotherm slope is seen at a temperature far above the disappearance of hysteresis[42]; such a plot for argon in MCM-41 is included as Figure 3.2.

27
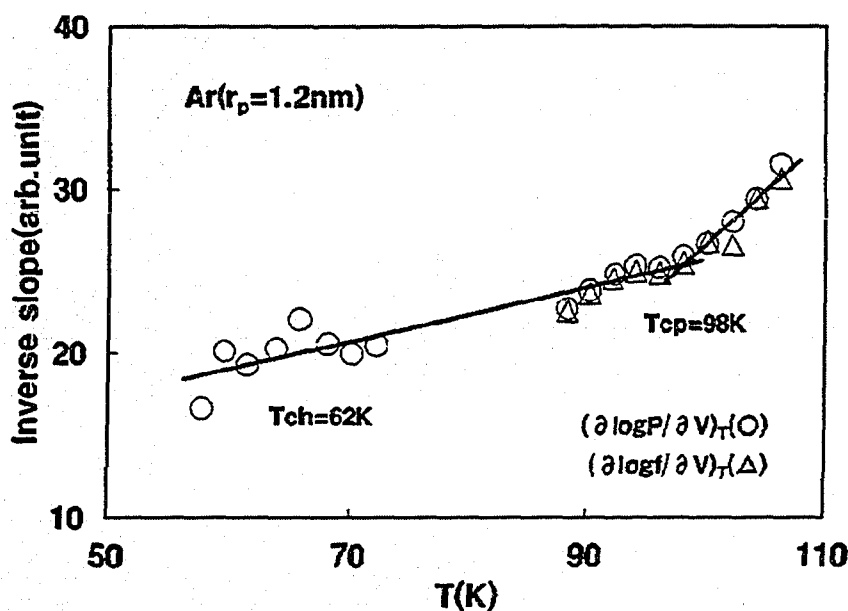
Figure 3.2: Determination of pore critical temperature of Argon in MCM-41. The inverse slope of the adsorption isotherm is plotted versus temperature for a series of isotherms of Argon condensing in MCM-41 with a pore diameter of 1.2nm. While hysteresis disappears from isotherms above 62K, the pore critical temperature is assigned to the kink in this graph at 98K which is still well below the bulk T_c of 151K. Note that 'inverse slope' is plotted here because their adsorption isotherms are plotted in a different manner than ours. From reference [42].

3.1.1 Capillary Condensation in Dense Porous Glasses

The general picture of capillary condensation during filling of porous media consists of gradual adsorption of fluid as a thin film along the pore cavities followed by a sudden filling of the pore bodies once the film reaches some critical thickness. Huber and Knorr have published a nice study of capillary condensation of Argon in porous glass[43] using several techniques to provide complementary information on the process. Although none of their data were taken in the critical region, they elucidate the process of condensation as the growth of a film followed by condensation of the film into a liquid which fills the pores. This picture is also consistent with studies of condensation within aerogel, as discussed later in this chapter.

There have been a small number of studies of capillary condensation in dense porous glasses near the critical point of the adsorbed liquid. Most studies assume that there exists some pore critical temperature which is the analog of the bulk liquid-vapor critical point, however not everyone accepts that such a point must

exist. If it does, then such properties as surface tension must disappear as T approaches T_{cp}, and there does not seem to be enough evidence one way or the other to state unequivocally whether this is the case.

William Machin has performed studies of a number of fluids near their critical points in controlled pore glasses[44], mapping out "coexistence curves" defined by the size of the adsorption isotherm hysteresis loop. This coexistence curve shows a fairly large depression of the critical point, but the "capillary critical point" is no longer identified with the disappearance of well defined fluid phases; instead Machin shows evidence that those well defined fluid phases exist to much higher temperatures, and his capillary critical point, T_{cp}, is the temperature at which the capillary condensation behavior of liquid in pores switches from being well described by capillary condensation to being better described by homogenous nucleation. The work supports a picture of capillary condensation in which the presence of the porous medium has no effect on the intrinsic properties of the fluids, instead only shifting the chemical potential of the fluid and affecting its ability to reach an equilibrium state (and the path taken to that state).

At temperatures above the disappearance of hysteresis Machin's adsorption isotherms continued to exhibit the same general shape as those that exhibited hysteresis, with the porous medium filling with fluid at some pressure below saturated vapor pressure (P_0). As an interesting side note, there is evidence for "critical depletion" at temperatures just above T_c; this is a phenomenon in which the density of fluid inside the porous medium actually *drops* as the temperature is lowered into a narrow region just above the critical temperature. This is in stark contrast to all other temperature and density conditions in which the density within the pores is enhanced over that in the bulk phase and increases as the temperature is lowered. Some studies have shown some evidence of this effect, while others have not seen such an effect.

Studies of capillary condensation within arrays of single cylindrical pores (MCM-41 and related structures) have the advantage of almost uniform pores[45, 42]. Again there is some confusion about what constitutes the "pore critical point," although it certainly appears that $T_{cp} > T_{ch}$ (see Figure 3.2). These media have small pore sizes so that the temperature depression of the critical point is much larger than any seen in porous media like aerogels.

A series of papers by Findenegg *et al.* investigated the adsorption of SF$_6$ near

29
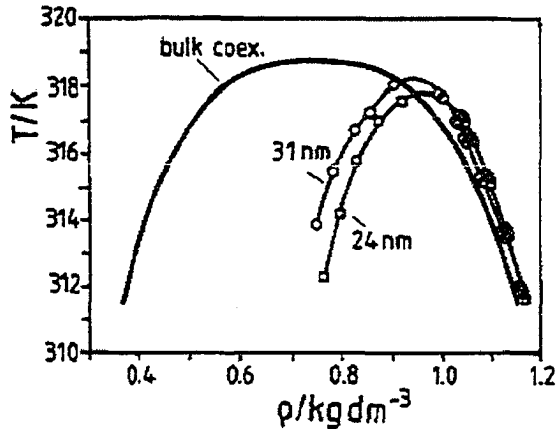
Figure 3.3: Findenegg SF_6 diagram. These are coexistence curves for sulphur hexafluoride confined in two different controlled pore glasses. Each curve is constructed by noting the onset and cessation of condensation into the porous glass. The bulk coexistence curve is included for reference. The confined curves are narrower than bulk, and shifted to lower temperatures and higher densities, but the shape of the curves is not dramatically different than bulk. From reference [46].

its critical point[47, 46, 48] in controlled pore glasses. They mapped out a coexistence curve (Figure 3.3) by keeping the bulk fluid density in their cell constant and monitoring the excess fluid adsorbed by the porous medium as the temperature is lowered from $T > T_c$. At some temperature below T_c fluid condenses within the pores. They have shown a depression of the critical temperature and narrowing of the coexistence curve, but a shape that is consistent with a bulk liquid-vapor transition (i.e. $\beta = 0.35$). Furthermore, they also found evidence for critical depletion in the porous media – at temperatures and densities near the critical point some fluid appeared to spontaneously *leave* the pores. Their computational work to explain this occurrence was later shown to be flawed[49], and the precise origin, or even the existence, of critical depletion is still an area of active interest.

On the topic of critical depletion, the adsorption of nitrous oxide in a dense porous silica shows depletion of density within the pores for temperatures within the range of $T_c < T < 1.015T_c$ [50]. This system differs from the two studies mentioned above in both the porous medium and the adsorbed fluid, which lends a note of generality to the phenomenon. However, there is still no simulation evidence for such behavior in model pores (see, for example, reference [51]), and the analysis used to quantify the critical depletion in the experiment is complex (which may lead to errors). We have seen no evidence for critical depletion in our helium adsorption isotherms in aerogel.

30

3.1.2 Capillary Condensation in Aerogel

Little work has been done on the condensation of fluids in aerogel near the liquid-vapor critical point other than our measurements – published work on condensation in aerogels near the critical point has only come from the labs of Moses Chan at Pennsylvania State University and Laurent Puech and Pierre-Etienne Wolf at the Centre de Recherche sur les Très Basses Températures in Grenoble. However, other work has been performed on fluid adsorption and phase separation in aerogel. Most applicable of these is a study of the structure of liquid films and droplets during condensation of helium in aerogel at low temperatures which has been undertaken at the Advanced Photon Source (APS) of Argonne National Laboratory (ANL). Finally, a short study of carbon dioxide near its critical point in aerogel has been made using neutron scattering.

X-ray scattering during helium adsorption in aerogel

A study of helium adsorption by Lurio *et al.* in 98% aerogel used X-ray scattering to determine exactly how the helium is adsorbed at 3.5K[52]. A similar study is also underway on the low temperature ^{3}He-^{4}He phase separation by Mulders, Paetkau, and Lurio[53]. X-ray scattering can shed little light on the macroscopic distribution of fluid within the sample, but is a powerful tool which can extract a length scale characteristic of the thickness of the aerogel strands or the largest filled pores in the sample. Below 3.5K helium has an appreciable surface tension, so critical density fluctuations do not need to be considered. Not surprisingly the helium is at first adsorbed as a thin film along the strands of the gel, up to a thickness of about 2.5nm. As more helium is added "blobs" form, draining fluid from the film, and grow until their size exceeds the resolution of the instrument. Upon emptying, the reverse process occurs with one main difference: during filling the characteristic length scale remains small until the gel is about 80% full while upon emptying the length scale remains unresolvably large until the gel is only about 40% full. This implies that during filling there are many nucleation sites for condensation of liquid within the aerogel, but during emptying the liquid remains in fewer, larger domains. This is reinforced by the patchiness seen in Wolf's optical experiments which will be described in this section.

It is worth noting that in this paper the adsorption isotherm shown is assumed to exhibit a vertical step in density during condensation, when in fact the isotherm

shown clearly exhibits a large but finite slope. This is a common feature in papers on capillary condensation in aerogels – the steepness of the isotherm is greater than in most porous media but it is *not* infinite.

Heat capacity and light scattering data from the Penn State group

Apollo Wong and Moses Chan studied the condensation of pure helium and pure nitrogen in 95% and 84% aerogel[10, 11, 54]. They published some isotherm data, but the majority of the published data is based on heat capacity (for helium) or light scattering (for nitrogen) along isochores. Each data set showed a narrowed coexistence curve shifted to lower temperatures than bulk. Later some high precision adsorption isotherms for helium in 98% aerogel were collected[55]. Their surprising results for helium in 95% aerogel spurred on research in both our lab and at Grenoble.

The heat capacity data for helium in aerogel were taken along isochores as shown in Figure 3.4. There were up to three significant features in each heat capacity scan: at bulk T_c there was a sharp peak assigned to the transition in any bulk fluid present in the cell, just below bulk T_c there was a peak assigned to the liquid-vapor transition in aerogel if it was present, and at lower temperatures there was a broad maximum in heat capacity which remains somewhat unexplained. Using the position of the cusp ("A" in Figure 3.4), an extremely narrow coexistence curve was mapped out, shown in Figure 3.5. A similar treatment using the position of the lower temperature broad maximum in heat capacity led to a wider phase diagram, shown in Figure 3.6.

The precise origin of the two peaks in heat capacity is not entirely obvious, and the whole picture is complicated by the presence of some bulk fluid surrounding the aerogel. Since the sample used in this experiment was a thin disc machined from a large block of aerogel, and aerogel is a difficult material to machine smoothly, there was an estimated 8% of the total cell volume unoccupied by the aerogel sample. While this volume is not large enough to completely overpower the signal from the aerogel, it is large enough to significantly affect the density of helium in the aerogel. Since helium near its critical point is incredibly compressible, it is entirely plausible that the density of fluid in the gel is not really that close to the average density of fluid in the cell, especially considering the fact that any bulk in the cell will be phase separated. With no way of knowing exactly how the helium is distributed

32
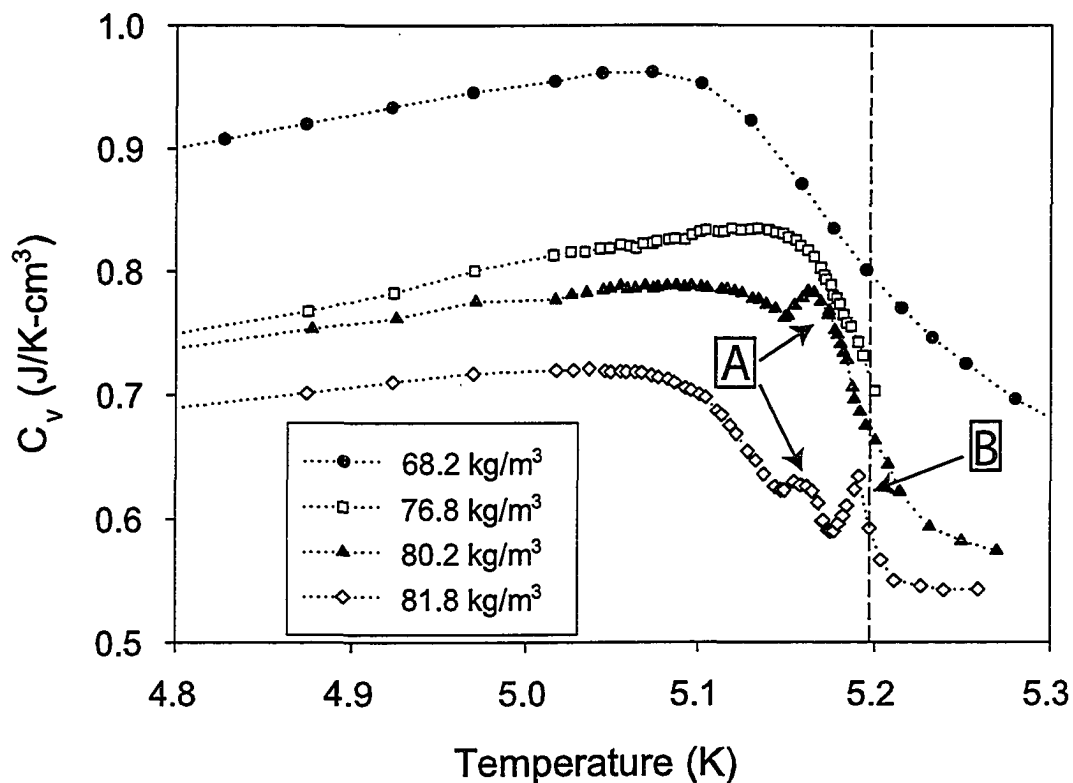
Figure 3.4: Wong and Chan's helium heat capacity cusps in 95% aerogel. This figure includes four constant density scans: I($\bullet$)=68.2, II($\square$)=76.8, III($\blacktriangle$)=80.2, and IV($\Diamond$)=81.8 kg/m^3). The dashed curve shows the critical temperature of bulk helium. The lowest density curves only exhibit a broad maximum at $\sim 5.05K$, but as density is increased (curve III) a sharp smaller cusp appears below T_c which is assigned to the liquid-vapor transition within the aerogel (cusp labelled "A" in curves III and IV). At the highest density shown here a third peak appears very close to the bulk T_c and is labelled "B"; this is interpreted as a signature of bulk helium collecting in the space around the aerogel sample. Data extracted from reference [54].
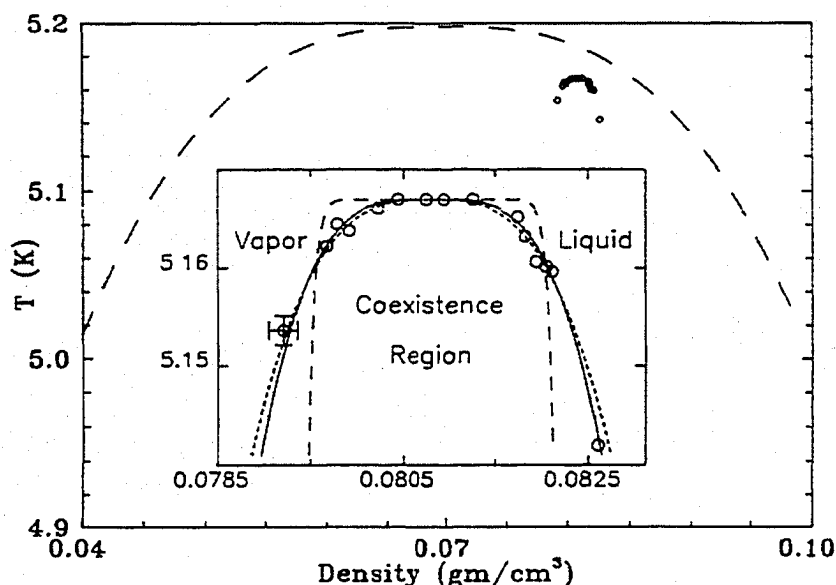
Figure 3.5: Wong and Chan's helium in 95% aerogel coexistence curve. The position of the cusp ("A" in Figure 3.4 in heat capacity is plotted here as a function of average density in the cell. The coexistence curve described by these transitions is extremely narrow and somewhat shifted in both temperature and density – the coexistence curve of bulk helium is included as a long dashed line for comparison. A magnified view of the experimental data is provided as an inset – although the coexistence curve is changed dramatically, its shape is consistent with a critical exponent identical to bulk. The dotted line is an unrestricted best fit giving $\beta = 0.28$ while the solid and dashed lines are best fits when restricting β to 0.325 (Ising model) and 0.05 (random field Ising model) respectively. From reference [10].

within the cell during the experiment, assignment of peaks "A" and "B" may be a little ambiguous. Since the amplitude of the cusp assigned to the transition of fluid within the aerogel is quite small, it is conceivable that the cusp is related to some sort of redistribution of fluid. The origin of the lower temperature heat capacity maximum is even more unclear, but may reflect the confinement within individual pores, as opposed to the higher temperature peaks which could include the pore connectivity. Since this data was all collected using an AC heat capacity method, one must also consider the time constants for thermal equilibration within the sample. Our samples are of similar size and have thermal time constants much slower than the AC heating frequency used in this study, so it seems implausible that the sample used in this heat capacity study was actually in equilibrium.

While the results of their experiments on liquid-vapor critical behavior in 95% aerogel are well known, little is mentioned about their results for helium in 84%

34
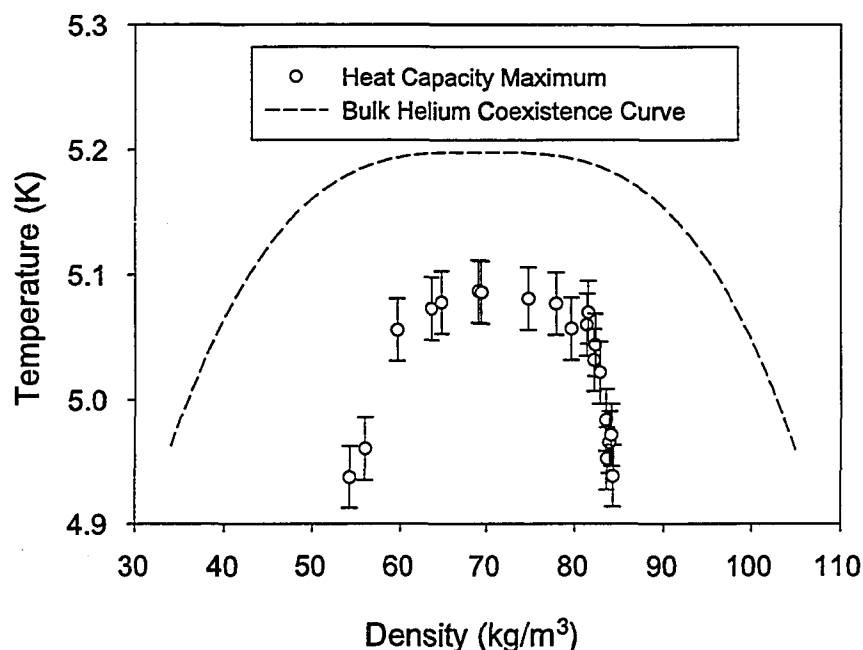
Figure 3.6: Wong and Chan's broad heat capacity anomaly for helium aerogel. If the position of the broad maximum in heat capacity is plotted as a function of average helium density in cell, a much wider curve results than from the small sharp peaks. Data extracted from reference [54].

gel. In fact they saw the same sort of heat capacity signatures for the liquid-vapor transition in the denser aerogel. Using the location of the sharp peaks to map out the coexistence curve as they did in the 95% gel resulted in a coexistence curve for helium in 84% porous aerogel about *50 times* narrower than the bulk curve. It is fairly well accepted that the behavior of fluids in aerogels with $\phi < 90\%$ is analogous to the behavior of fluids in dense porous glasses and such a narrow coexistence curve has never been seen in those glasses. So that leads one to wonder exactly what the sharp heat capacity features are, and if they exist in a system that is believed to be governed by metastable states (i.e. helium in 84% aerogel), can the same peaks truly be used to map out an equilibrium phase diagram in another system? For easy comparison, the "coexistence curves" of helium in bulk, 95% aerogel, and 84% aerogel are plotted together in Figure 3.7.

Despite these uncertainties the helium in aerogel work of Wong and Chan hints at some very interesting behavior of fluids in aerogel, which was at the time a very novel system. With a view to generalize their results they undertook a second set of measurements, using optical scattering to investigate the critical behavior of nitrogen

35
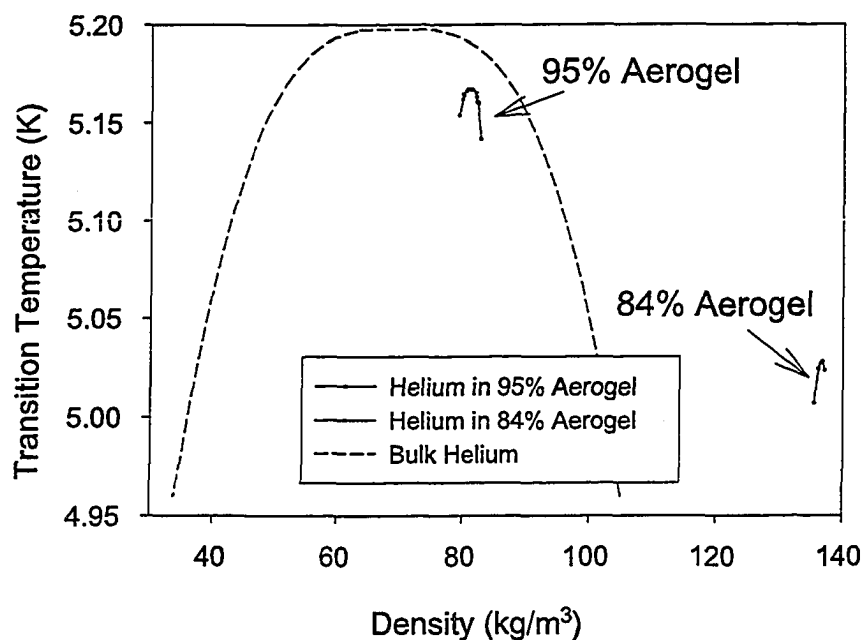
Figure 3.7: Wong and Chan's helium in aerogel coexistence curves. The data for helium in 95% aerogel is identical to that shown in Figure 3.5, but is included again to highlight the differences in the 95% aerogel and 84% aerogel data sets. The bulk helium coexistence curve is included for reference as a dashed line. Data extracted from reference [54].

in aerogel[54]. Light should be strongly scattered in the two-phase region, so the onset of scattering was used to map the coexistence curve. The universal nature of critical points leads one to expect similar critical behavior in different fluids confined in aerogels – thus the coexistence curve of nitrogen should be narrowed in a manner similar to that of helium. The optical data also allowed them to monitor the relaxation of the system after temperature changes.

The coexistence curve of nitrogen in 95% gel as mapped out by light scattering is included as Figure 3.8. It is narrowed with respect to bulk nitrogen, and shifted to slightly lower temperatures and to slightly higher densities. There is a large difference between these results and the helium results, however. The degree of narrowing is very different for nitrogen – the coexistence curve is about half as wide as in bulk whereas the helium curve is much, much narrower. The narrowing of the nitrogen coexistence curve is comparable to that seen in fluids in other porous media. If one assumes that the coexistence curve as plotted represents a true equilibrium phase transition then the exponent describing its shape, $\beta = 0.35 \pm 0.05$, agrees roughly with that of the bulk transition. However, if the transition is more closely

36
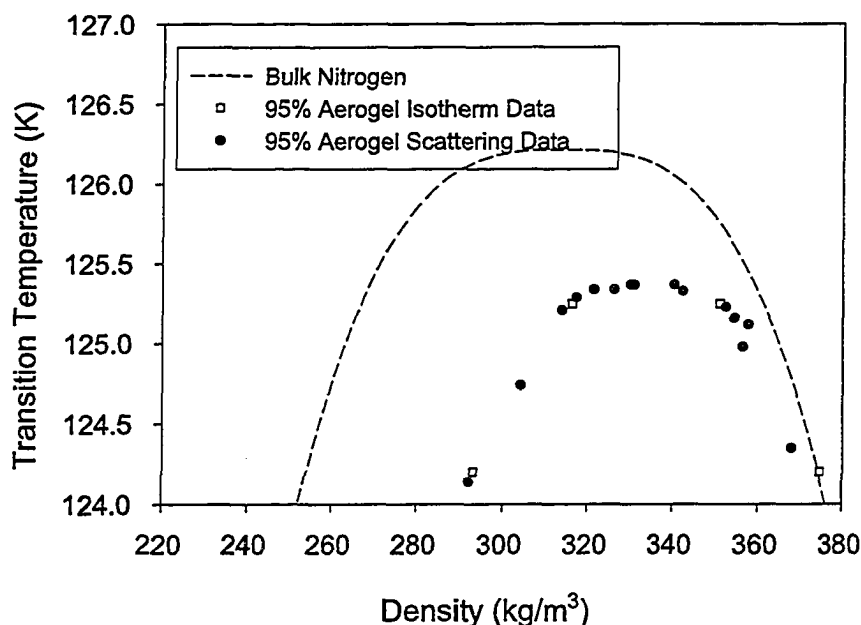
Figure 3.8: Wong and Chan's nitrogen coexistence curve. The graph includes points derived from scattering results along isochores (•) and from pressure-density isotherms (□). Error bars and power law fits have been omitted so as not to obscure the data. The bulk coexistence curve for nitrogen has been included for reference as a dashed line. Data extracted from reference [54].

akin to capillary condensation it is not at all obvious what information can be extracted from the curve shape or if a power law fit is appropriate.

The optical scattering data were backed up by a series of isotherms aimed at approaching the transition by adjusting a different thermodynamic variable. Flat sections in the adsorption isotherms were interpreted as coexistence regions for nitrogen within the aerogel and these points along the coexistence curve agreed with the data from the scattering experiments. However, the precision of the isotherms was not high and assigning endpoints to the "flat section" is difficult. The advantage of including both isotherm data and scattering data is that one approaches the coexistence curve from two directions – the scattering data was taken by setting the density (i.e. an isochore) and adjusting the temperature while the isotherms held temperature constant while adjusting the fluid density. Thus, in the density-temperature plane the two methods approach the coexistence curve vertically and horizontally, respectively. We have taken a similar approach in our work, studying both density along helium adsorption isotherms and compressibility (which has a critical divergence governed by heat capacity) along isochores.

37
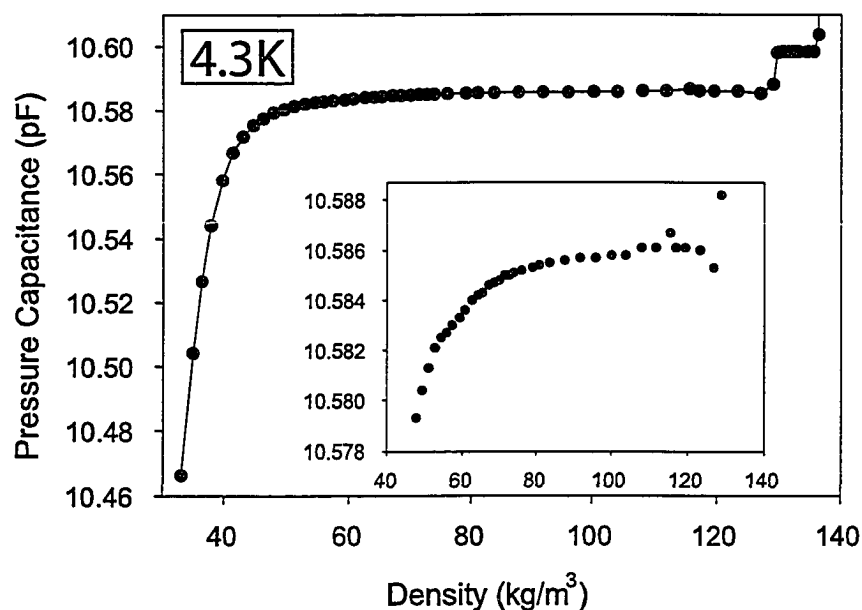
Figure 3.9: A low temperature (4.3K) adsorption isotherm for helium in 98% silica aerogel. The inset is a blow-up of the capillary condensation region. Note that while helium condenses over a very narrow pressure range, it does exhibit a finite slope. From unpublished results provided by Moses Chan [55].

The bulk fluid volume in the scattering cell was less than that in the heat capacity cell and appears to have been easier to estimate. In addition, the scattering signal is large and not affected by small patches of bulk like the heat capacity data may have been.

Adsorption of helium in aerogel was revisited in the Penn State laboratory later, using a cell with a high precision *in situ* pressure gauge to take careful adsorption isotherms in 98% aerogel[56]. These isotherms show that helium condenses in aerogel over a very narrow pressure range, but there is no unambiguous marker for a liquid-vapor phase transition. An example of one of the low temperature isotherms is included as Figure 3.9; it clearly shows that helium capillary condenses over a very narrow pressure range, and that the condensation pressure is depressed slightly from bulk saturation pressure. Only one branch of the isotherm is shown; it would appear that only one branch was collected, perhaps because they saw no hysteresis in their earlier isotherms. Hence we cannot evaluate the width of the hysteresis loop that was probably present. At higher temperatures, data were only collected on the high density portion of the isotherm since this is where the liquid-vapor coexistence region was expected. Two of the higher temperature isotherms are shown in Figure 3.10.

38
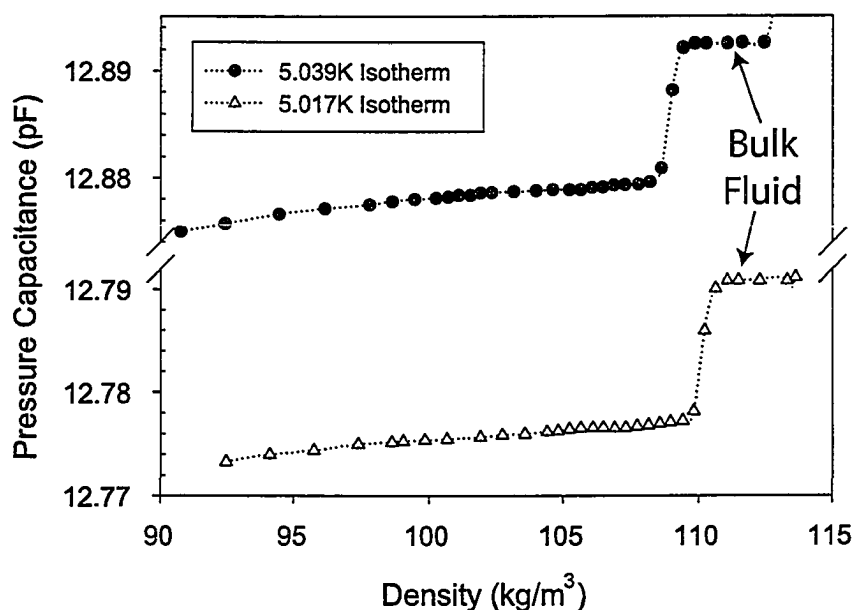
Figure 3.10: Two higher temperature (5.017K and 5.039K) adsorption isotherms for helium in 98% silica aerogel. As seen in the 4.3K isotherm, neither of these isotherms is flat. From unpublished results provided by Moses Chan [55].

They do not seem to show any distinct plateaus that would indicate an equilibrium liquid-vapor coexistence region.

Furthermore, if the system did exhibit hysteretic behavior then the dosing method used along these isotherms may not be the best choice; with each burst of helium added the aerogel-fluid system is thrown well out of equilibrium. There is no guarantee that it relaxes to a state along the adsorption or desorption branches – it may be stuck in a metastable state within the hysteresis loop.

Isothermal data from the Grenoble lab

More recently there was a creative experiment that searched for critical behavior around the liquid-vapor critical point of helium in 95% aerogel using a very low frequency resonance technique to measure the density of helium adsorbed into the gel[15, 14]. Performed as part of the PhD project of C. Gabay, the experiment monitored the period of a pendulum consisting of a cylinder of aerogel suspended on thin wires, shown in Figure 3.11. The aerogel was a large cylindrical monolith that included thin copper mesh throughout the sample to assist in thermal equilibration across the sample. The large size of the samples (3.2cm by 1.5cm) required the copper filaments to avoid ten hour equilibration times seen in their preliminary

39
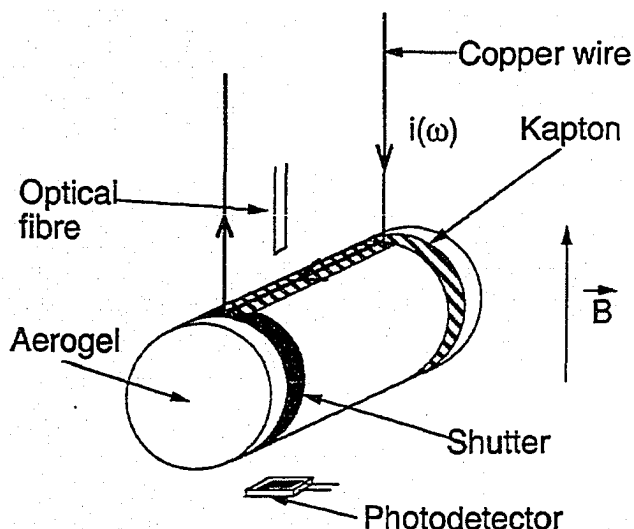
Figure 3.11: The low frequency pendulum for the Grenoble lab's helium in aerogel work. A monolithic cylinder of aerogel was suspended by two wires and its position monitored by a photodiode. The period of oscillation of the pendulum depends on the mass of the pendulum, its size, shape, and the density of the fluid through which it swings. From reference [57].

experiments with pure silica aerogel. Even with the incorporation of these high conductivity paths, the thermal equilibration of the sample limited the time scale of the experiments. Since this method assumes that the pendulum is oscillating in a single fluid phase, measurements cannot be performed when there is bulk two-phase coexistence.

A series of isotherms were performed at temperatures close to, but below, the critical temperature (some are shown in Figure 3.12). Below about 5.15K they showed hysteresis loops, without any distinctly flat coexistence region. The onset of condensation is characterized by a rounded corner in the adsorption isotherm, matched by a similarly rounded feature at the low density end of the desorption isotherm. Thus there is no easy feature that may be assigned to the transition on the low density side. The features on the high density side of the coexistence curve are much more distinct, but the finite slope of the isotherms does not support the interpretation of the transition in terms of true liquid-vapor coexistence. Isotherms at a lower temperature (4.88K) took so long to equilibrate that rate dependence was obvious in runs taking two days or more. Equilibration nearer to the critical point was somewhat faster; this slow equilibration is consistent with our experience using aerogel samples in experiments. There was some difficulty with the density calibration for helium in the pendulum, although this was corrected in later analysis.

The key results from Claude Gabay's work on helium in aerogel near the liquid-vapor critical point are that there is hysteresis present even close to the critical temperature, and the isotherms do not show the sharp corners and vertical steps we associate with liquid-vapor coexistence. In fact, all evidence from this study points

40
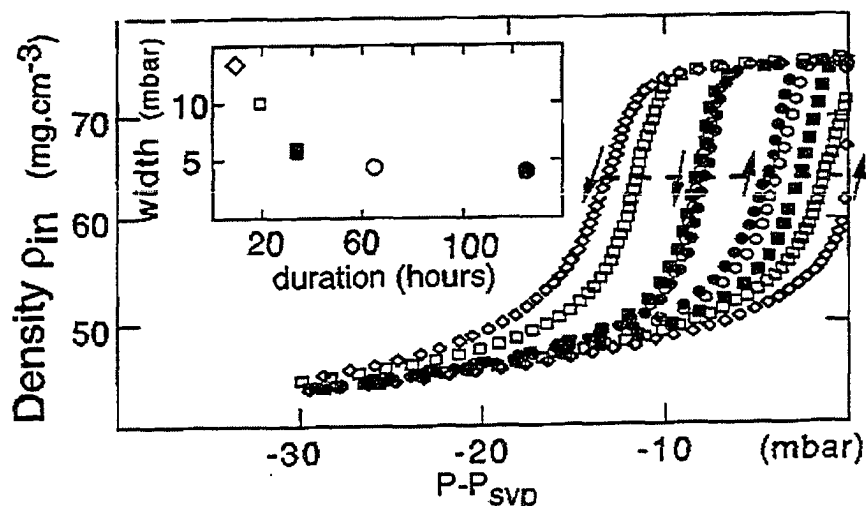
Figure 3.12: Adsorption isotherms for helium in aerogel collected using the pendulum shown in Figure 3.11. These isotherms were taken at 4.88K and illustrate the rate dependence of the hysteresis loop. Then isotherms have a finite slope during condensation and exhibit a hysteresis loop which tends toward a small but finite width as the filling and emptying time is increased to many days. From reference [14].

toward a more traditional capillary condensation picture of adsorption in a porous medium. The isotherms show much wider "coexistence" regions (as determined from the closure points of the hysteresis loops) than the isotherms taken by Wong and Chan, and they do not show evidence of any sharp transition.

The pendulum results were followed by a study of optical light scattering from helium condensing in a slice of 95% porous aerogel[58]. This study was designed to allow visual inspection of the sample as well as quantitative measurement of light scattering from the sample. During condensation within the aerogel, strong light scattering was observed – consistent with the appearance of microscopic domains of liquid and vapor within the gel. Furthermore, the sample appeared patchy to the eye during filling and even patchier during emptying. This implies that the aerogel sample may have large scale inhomogeneities favoring the retention of liquid in some regions of the gel over others, and there is no reason to think that any other aerogel samples used in studies of capillary condensation are more homogenous. It could also be consistent with macroscopic coexistence.

More recently the Grenoble group has measured a series of adsorption isotherms for helium in neutrally catalyzed aerogel; these exhibit a shape different from isotherms

41

in the base catalyzed aerogel.

Neutron scattering from CO_2 in aerogel near its LVCP

Recently a study has been published in which small angle neutron scattering (SANS) was used to directly measure the size of density fluctuations in CO_2 near its critical point, and what effect the aerogel might have on those fluctuations[59]. While fluctuations in the bulk fluid diverged near the critical point, as expected, there was no such divergence in the confined fluid. It appears that the addition of aerogel quenched the density fluctuations, so that while there is a jump in size near the liquid-vapor transition the fluctuations never exceed the approximate pore size. While the data set is somewhat sparse, and has the appearance of a preliminary investigation, it is precise enough to say that critical density fluctuations in a fluid-aerogel system are unlikely to dominate its behavior.

3.2 Binary Fluid Separation in Silica gels

Extensive studies of binary fluid separation in dilute silica gels have been carried out by Dr. Cannell's group and by Dr. Frisken[12, 60, 61, 13, 62, 41]. These studies have used neutron scattering and light scattering to detect phase separation within the gel and monitor the rate at which domains of separated fluid grow or shrink. Much of the work highlights the similarities between the slow equilibration and domain dynamics of the binary fluids with those of random-field antiferromagnets. The analysis developed by this group was also used by Lurio *et al.* to extract domain sizes from the the X-ray scattering data on helium condensing in aerogel discussed in the previous section.

Studies included 2,6-lutidine–water mixtures and isobutyric acid (IBA)–water mixtures in silica gels with $\phi \geq 98\%$. Both systems were quenched from temperatures at which the fluid system was a single homogenous phase to temperatures where phase separation produced strong light scattering. Even before the samples entered the true two-phase region of the bulk mixtures, the samples exhibited scattering consistent with the formation of domains rich in one of the components or the other. These domains disappeared over a time scale orders of magnitude longer than in binary mixtures without silica gel, and were reminiscent of the slow dynamics near a transition in a magnet which includes small random fields.
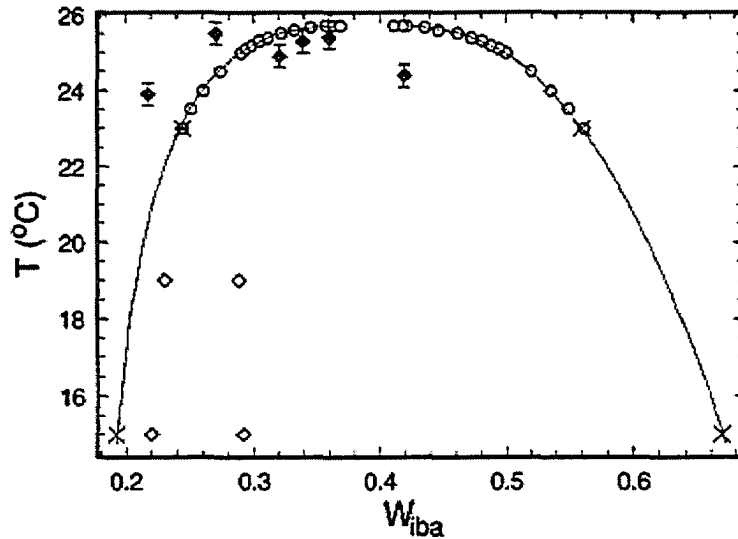
Figure 3.13: IBA-water phase diagram in a dilute silica gel. The solid line is the liquid-liquid demixing curve for isobutyric acid and water with no impurities. Open circles and crosses (O,X) are experimentally determined points along that line. Closed diamonds (♦) mark the onset of strong light scattering in the binary fluid-gel system during cooling, while open diamonds(◊) mark the region of constant chemical potential (i.e. two phase coexistence) along isotherms. From reference [41]

While these studies shed a great deal of light on the growth of domains and fluctuations within silica gels, they raise the question of whether the onset of scattering can be used to pinpoint the onset of coexistence as has been assumed for the optical scattering work on single fluid coexistence in aerogel. In fact, in a study of IBA-water mixtures it was shown that the onset of scattering occurred at temperatures much higher than plateaus in the chemical potential of the system (i.e. the true two-phase coexistence region within the gel), as shown in Figure 3.13. It is unlikely that this impugns the interpretation of single-component fluids in aerogels, but it means that scattering from binary fluids in silica gels can not practically be used to probe the binary fluid demixing critical point, even if one exists.

3.3 Simulations of the Liquid-Vapor Transition in Pores

Theoretical and computational approaches to the liquid-vapor transition have a long and illustrious history dating back to the van der Waals equation of state. Early approaches reproduced the basic thermodynamic behavior of fluids, but missed many of the subtleties of true fluids. In particular they do not produce the correct behav-

43

ior near the liquid-vapor critical point – the critical exponents often possess mean field values rather than Ising values. Recently more accurate parametric models produce sensible behavior in the critical region, but the easiest approach to studying near critical fluids is through computer simulation rather than analytically. In particular, several Monte Carlo approaches have proven very efficient in calculating certain equilibrium fluid properties, such as density, near the critical point. For an instructive introduction to some techniques used for pure fluids, see reference [63]. Our interest is in studies of fluids confined within porous media, specifically aerogels. This adds a significant complication, and the remainder of this chapter will be devoted to how to circumvent this difficulty as well as results.

3.3.1 General Methods and Challenges for Calculating Fluid Properties in Porous Media

The presence of a solid matrix greatly complicates the simulations. First, one must generate the matrix, deciding on the size and distribution of particles of which the matrix is composed. Fluids are very sensitive to the structure of the matrix as well as its density, so careful attention must be paid to what final matrix structure is chosen. While pure fluids can be simulated using a relatively small number of particles except very close to the critical point, the volume of the porous medium simulation must be large to incorporate a wide enough range of adsorption environments. Small simulation volumes can lead to spurious results arising from a single adsorption site in disordered media. Aerogels are especially difficult to model since the density of the matrix is so low that small simulation volumes may only contain a single strand; far from representative of the true structure of the gel. To be reproducible, studies may need to average over a large number of runs in different matrix realizations.

3.3.2 Simple Geometries and Model Pores

Simulations of fluids in model pores (e.g. cylindrical pores, slit pores, or ink-bottle pores) have different challenges and very interesting results relevant to capillary condensation far from the critical point. By their very construction they preclude the effects of connectivity seen in real porous media so, while instructive in probing fluid behavior far from the liquid-vapor critical point, papers directly relevant to the liquid-vapor transition near the liquid-vapor critical point in aerogel all use some form of disordered matrix.

44
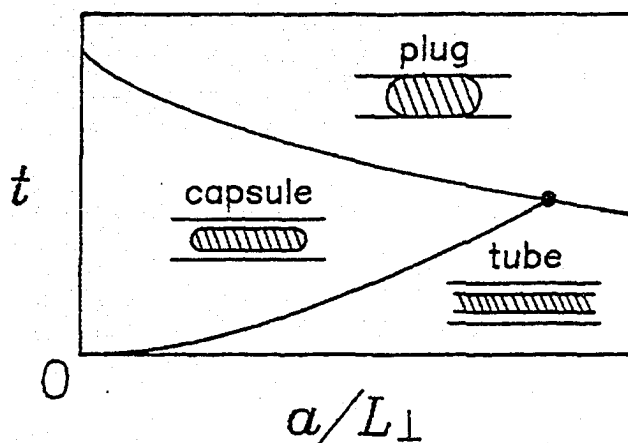
Figure 3.14: The phase diagram for a binary fluid in a cylindrical single pore as a function of temperature(t) and pore diameter($a/L_\perp$). From reference [66]
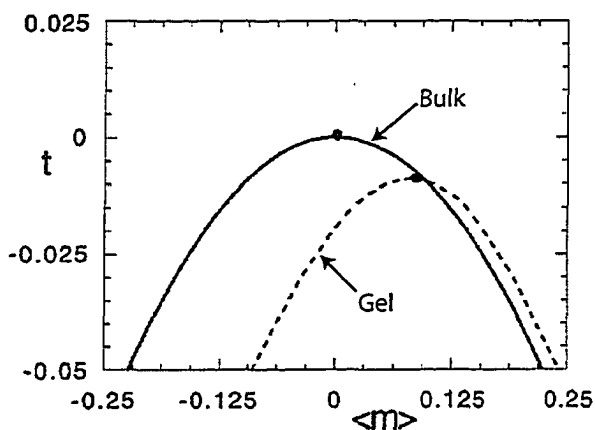
Figure 3.15: The coexistence curve of a single component near its liquid-vapor critical point, confined in a periodic "gel." Note that this curve has been calculated using mean field theory, and its shape is therefore described by mean field critical exponents. From reference [67]

However, even in the simplest geometries some very rich phase behavior can surface. In studies of adsorption in a simple array of cylinders Gatica *et al.* outlined a phase diagram including film and necking states in addition to filling completely with condensed liquid[64]. Studies of binary fluid separation in cylindrical pores show similar phase behavior, with three distinct phases that depend on the temperature and pore radius as seen in Figure 3.14 [65, 66]. A study of near critical (but mean field) fluids in very dilute gels (modelled as a periodic array of cylinders) showed a narrowed coexistence curve in their simplest calculations (Figure 3.15). When a model which allowed for thermal fluctuations was used, the phase diagram showed two transitions, terminating in two critical points, shown in Figure 3.16 [67]. While the coexistence curve does not closely resemble experimental curves, it does share some tantalizing details with the curves from the simulations outlined in the next section.

45
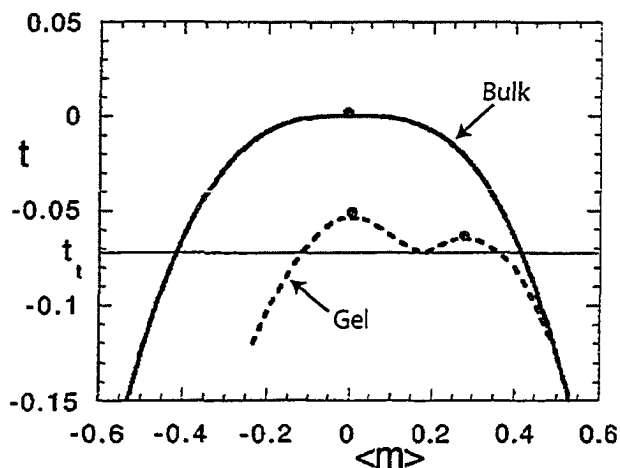
Figure 3.16: The coexistence curve of a single component fluid near its liquid-vapor critical point in a periodic gel calculated using a parametric model. This curve shows the presence of two critical points. From reference [67]

3.3.3 Techniques and Results for Simulations in Dense Porous Media

Important results for the adsorption of fluid in small pores up to about 1990 were summarized in a review by Evans[68]. Advances in models, techniques, and computational power since then make any additional review of early works unnecessary with the exception of introducing the formalism of Madden and Glandt[69]. They defined a set of Ornstein-Zernicke equations that treated the fluid-matrix system as a two phase fluid system with one phase fixed in space. This method was extended to arbitrary matrices by later work[70]; combined with a mean field approach to the fluid interaction, coexistence curves for the confined fluids were mapped out[71]. The curves were slightly narrowed and depressed in temperature. Using a similar approach Pitard *et al.* showed similarities between the model of fluid adsorbed in a matrix and the random field Ising model[72].

As the 1990's progressed, simulations grew in number and complexity. Monson and coworkers performed a series of increasingly complex simulations of a system first designed to mimic the adsorption of methane in silica xerogel[73, 74, 75]. The coexistence curve was narrowed and shifted to lower temperatures. When a randomly arranged matrix was used there appeared to be two separate transitions, assigned tentatively to complications with liquid bridges forming. However, an ordered (fcc) lattice only showed evidence of a single transition[73]. Later, averaging over a number of realizations of random matrices, the two distinct transitions disappeared, merging into a single coexistence curve[74]. The appearance of the "second transition" in some realizations of the random matrix shows how sensitive these

46

studies are to small changes in microscopic structure – if the simulation volume is small, averaging may not be sufficient to smooth out small perturbations in fluid behavior. It is interesting to note, however, that the model of dilute gels used by Donley and Liu[67] mentioned in the previous section also produced a coexistence curve with two transitions despite the lack of randomness in their model.

Later, Monson and Sarkisov developed a lattice model to increase the efficiency of these simulations further[75], and this combined with mean-field density functional theory calculations were used to explore the thermodynamic states present inside the adsorption isotherm hysteresis loops. Their results supported an earlier study by Kierlik *et al.* which studied the adsorption of fluid in a disordered porous medium using mean-field density functional theory of a lattice-gas model[76]. The most germane results from these papers were the conclusions about the relationship between the hysteresis loops in adsorption isotherms and the underlying liquid-vapor transition, or rather the lack of relationship. Their results show that for different matrix-fluid interaction strengths there may or may not be an equilibrium transition, however the existence of hysteresis in the adsorption isotherms for the system *does not* depend on the existence of an equilibrium transition.

As more clever tricks and techniques are applied to these simulations, the variety of matrices and fluids grows. Adapting Gibbs-ensemble Monte Carlo to fluid adsorption, Brennen and Dong were able to complete a large number of calculations exploring the effects of porosity and the nature of the fluid-matrix interaction[77]. Their high porosity matrix was similar in density to 95% aerogel, although their matrix model was not particularly aerogel like. Some of the resultant coexistence curves showed the existence of a second transition, as seen above. All the simulations showed narrowing of the coexistence curve and significant depression of the critical temperature. Rzysko *et al.* measured the critical exponents of fluid in a 95% porous matrix and showed that they did not agree with the bulk fluid values[78].

One final note on simulations in dense porous media concerns the effect of the matrix structure on the fluid coexistence curve. It should surprise no one that a matrix of random unconnected spheres should not affect fluid in the same manner as a physically realistic model of interpenetrating networks of pore-space and solid. To quantify the sort of differences one could see Zhang *et al.*[79] performed a series of simulations using solid matrices that had identical porosity but whose structure differed. As expected there were large differences, with the more physically realistic
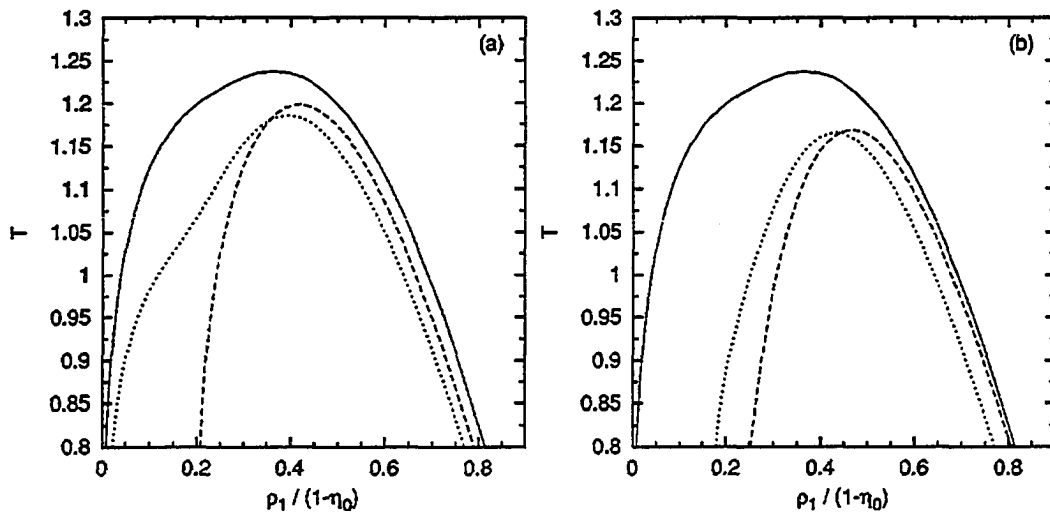
Figure 3.17: These are coexistence curves for fluid confined to 95% aerogel, calculated using the integral equation approach originated by Madden and Glandt. The two panes show different matrix-fluid interaction strengths; the left hand pane, (a), shows the phase diagram for a fluid which interacts more weakly with the matrix, while the right-hand pane, (b), shows the phase diagram for a more strongly interacting system. In each pane the solid line shows bulk fluid behavior, the dotted line shows behavior in a random distribution of spherical matrix particles, while the dashed line show the phase diagram in the presence of a correlated matrix structure which resembles aerogel. The curves are narrowed and shifted to higher densities as expected. From reference [81]

'template directed' matrices affecting the fluid less dramatically than completely random matrices.

3.3.4 Techniques and Results for Simulations in Aerogel

Lopatnikova and Berker[80] studied ^{3}He-^{4}He phase separation in $\sim$95% aerogel using renormalization group theory and reproduced the detached phase diagram seen in experiments. Adsorption of fluid in aerogel was also studied using the formalism of Madden and Glandt while incorporating the aerogel structure factor into the Ornstein-Zernicke equations[81]. This produced the expected narrowed coexistence curve shifted to lower temperature, and showed the effect of the aerogel structure by comparing results from calculations using matrices with the same porosity but no correlated structure (see Figure 3.17).

Simulated adsorption isotherms in aerogel have been calculated using local mean field theory by Tarjus and coworkers [83, 82]. The work used a model on a coarse lattice to reduce the computational complexity to a manageable size, but for the high

48
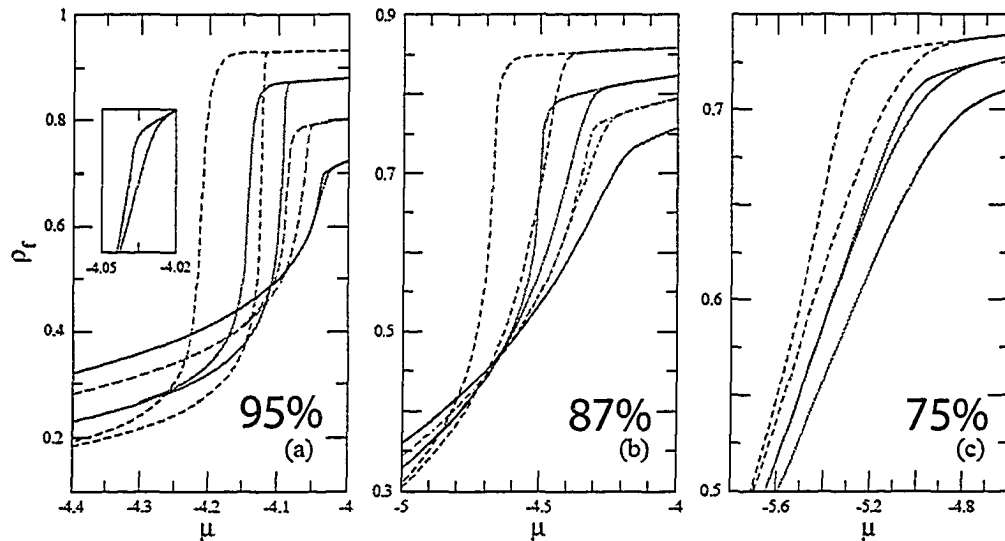
Figure 3.18: Isotherms for fluid adsorption in three porosities of aerogel calculated using density functional theory on a coarse grained lattice model of aerogel. In each pane, the isotherms move to higher temperatures as you move from left to right; that is, as temperature is raised, the hysteresis loop shifts to higher chemical potential (pressure) and shrinks in size. The temperatures (in this system, $T_c=2.0$) shown are: (a) T=1,1.4,1.7,1.9 (b) T=1,1.4,1.6,1.8 (c) T=1,1.2,1.4. From reference [82]

porosity aerogels even this approach requires significant computation resources. The aerogel structure was produced using a diffusion limited cluster-cluster aggregation algorithm which has been widely accepted as producing structure similar to real base catalyzed aerogels. In order to avoid spurious effects from particular microstructure present in any single realization of the aerogel matrix, all results were averaged over a number of independent realizations of the matrix. The number of realizations used depended on the size of the lattice, which in turn depended on the porosity of the matrix. For aerogels with $\phi = 0.95$ the lattice needed to be large in order to include enough matrix to be representative of an aerogel, so only a couple hundred different matrix realizations were used. For smaller lattice sizes, more realizations could be calculated.

The main drawback of the method is its exclusion of thermal fluctuations, thus invalidating any results near the liquid-vapor critical point (since they would reflect mean-field behavior rather than the true fluid behavior). However, far below T_c the mean field results should reflect the true behavior of the system. The simulations produce isotherms that closely resemble those seen in the experiments in

49
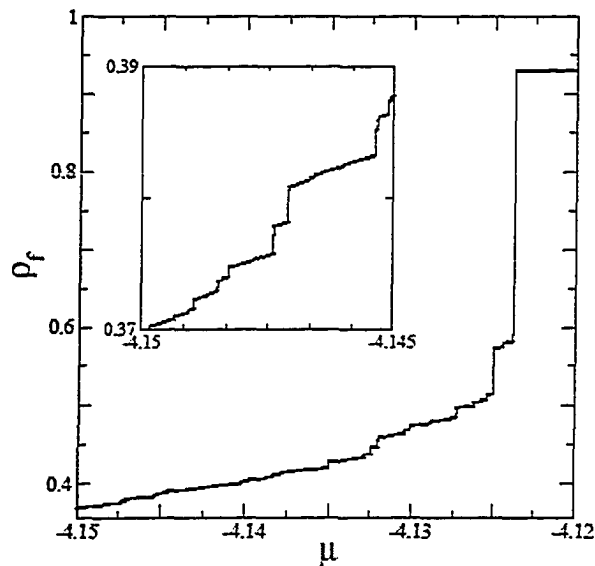
Figure 3.19: Isotherm for filling in a single realization of 95% aerogel at T=1. The smooth shape of the isotherms in Figure 3.18 results from averaging over about 100 realizations of each lattice, with randomly generated aerogel structure. Each individual realization exhibits a series of small jumps in density corresponding to avalanches of fluid into the aerogel. From reference [82]

our lab and in Grenoble. Since the mean-field calculations neglect thermal fluctuations, the isotherms calculated should correspond to the rate-independent hysteresis loops seen in very slow experimental data collection – they cannot be compared to dynamic hysteresis in samples which have not reached thermal equilibrium (rate independent loops are composed of states where all the thermally activated relaxation processes have already occurred and remaining hysteresis will not disappear simply by waiting).

The isotherms produced by averaging over all the realizations of the matrix are smooth (Figure 3.18), but individual isotherms (i.e. for a single realization of the matrix) are not at all smooth – Figure 3.19 shows an isotherm for a single realization of a 95% porous aerogel. They are instead characterized by a series of jumps in fluid density corresponding to avalanches into, or out of, the aerogel. For the lower porosity aerogels, adsorption is characterized by a large number of relatively small avalanche events, while the higher porosity aerogels are characterized by a number of small avalanche events followed by a single large avalanche which fills the remaining pore space with fluid.

In addition to isotherm shapes, snapshots of the system (for example Figure 3.20) can provide insight into the structure of the adsorbed fluid. As expected fluid is first adsorbed as a film covering all the matrix surfaces, followed by filling of the smallest "pores" and finally by filling the large voids. At no point does there appear to be a well defined interface with a constant curvature which could be used to interpret
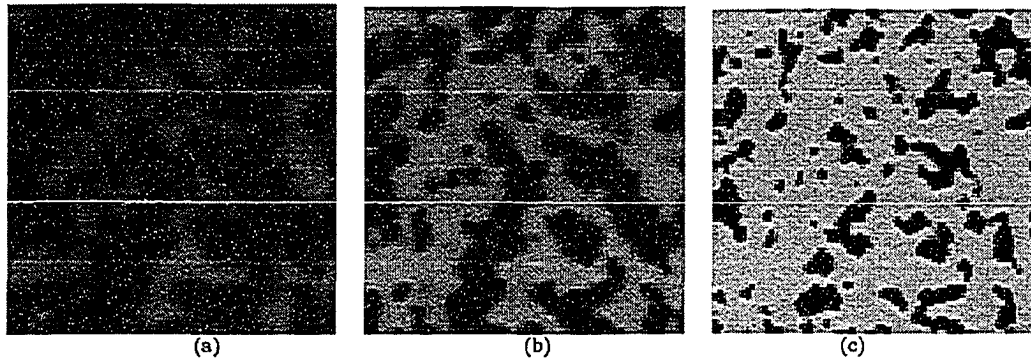
Figure 3.20: Distribution of fluid during capillary condensation in 95% porous aerogel at three different temperatures (T=1.9, 1.7, and 1 from left to right); in this system $T_c = 2$. Note that as the temperature falls the interface between phases becomes more distinct. Each pane consists of a two dimensional slice through the three dimensional model. From reference [82]

the condensation in terms of the Kelvin equation.

Information about the mechanisms of adsorption and desorption can be gleaned from a careful study of the isotherms and maps of fluid distribution. In short, adsorption can occur as a reversible process, a series of microscopic avalanches, or as a single macroscopic avalanche depending on porosity and temperature. The onset of desorption can appear as a macroscopic depletion or reversible process as one can infer from the adsorption behavior, but in a region between these two options one can see behavior governed by either cavitation of percolation depending on conditions.

51

Chapter 4

Aerogels

There are a huge variety of well characterized porous media (for an overview of some of these media, see Appendix B), and their effect on phase transitions in fluids has been an area of active interest in the Low Temperature and Statistical Physics communities for thirty years or more. Aerogel has become a popular material for such studies in the last fifteen years because it provides a pseudo-random arrangement of pores and an unparalleled openness of structure. This means that fluids within aerogel are only slightly perturbed by the silica matrix, and much of their bulk behavior is preserved.

The key to producing high porosity aerogels is the use of a supercritical drying process. While supercritical drying was used by S. Kistler[84] over seventy years ago to create aerogels with very high porosities (and consequently very low densities), it was not until decades later that aerogels received widespread interest. Kistler focussed on synthesizing aerogels from a wide variety of materials to gain insight into the structure of gels – still a very open question when he started his work. After his work, aerogels faded from the scientific literature.

Interest in aerogels was renewed in the late 1960's, with the advent of a fast and efficient synthetic route[85]. High-energy physics experiments began to use it as a radiator in Cherenkov counters[86] since aerogel's tunable density results in a tunable refractive index. In the 1980's the use of sol-gel processing to obtain high purity glasses sparked interest in the chemistry that underlies gelation of silica, and since then aerogels have been synthesized in many laboratories for many different reasons. They are even used as a sculpting material[87].

The synthesis of silica aerogels has been reviewed a number of times; more recent aerogel research has focused on applications, and on simplifying the drying

52

process[88, 89, 90, 91]. For instance, with their high surface areas aerogels are an attractive material for catalyst support, but their development is hampered by their low physical strength. Interest in aerogels has tended to focus on their very low thermal conductivity, and consequently their value as thermal insulators. Other uses are more esoteric, such as their use in low temperature physics studies of fluids and as cosmic dust collectors in NASA missions such as "Stardust"[92].

4.1 General Aerogel Synthesis

4.1.1 Wet Chemistry

Silica aerogels are the most easily synthesized, although similar synthetic routes can be used to construct aerogels from a variety of oxides[93] and organic materials[94]. The process is a simple gelation of a silica source followed by careful drying. The silica source is usually tetramethyl orthosilicate (TMOS) or tetraethyl orthosilicate (TEOS), although sodium silicate ("water glass") can also be used. Small amounts of base or acid and water are added to encourage polymerization of the silicate. In the acid catalyzed reaction, the silicate is completely hydrolyzed quite quickly and then polymerizes in a slower reaction. In the base catalyzed reaction the hydrolysis and polymerization occur on similar time scales[95]. Thus, much of the microscopic structure of the gel is governed by the catalyst – acid catalysis leads to gels composed of long thin interconnected strands of silica while base catalysis leads to agglomerations of small silica spheres. The exact concentration of basic catalyst (i.e. the pH of the gelling solution) is important in determining the final microscopic structure of the aerogel[96]. A schematic of the silica condensation reaction is included as Fig. 4.1.

The density of the aerogel, and therefore its porosity, can be controlled by diluting the reactant mixture. Even if the reaction is run without solvent, four moles of alcohol are produced for each mole of silica in TMOS and TEOS, resulting in a gel which is only about 14% silica by volume. This wet gel is referred to as an "alcogel." When dried, the "aerogel" retains the physical structure of the alcogel, resulting in a porous monolith with a porosity (ϕ) of 86%.

Alcogels can not be synthesized with a lower porosity, although they can be dried under subcritical conditions[97] or treated afterwards in such a way as to compress them, lowering the final porosity of the aerogel through sintering[98] or isostatic

53

$$
\begin{array}{c}
\text{OCH}_3 \\
|
\end{array}
\quad
\text{H}_3\text{CO}-\!\!\!\overset{\displaystyle \text{OCH}_3}{\underset{\displaystyle \text{OCH}_3}{\text{Si}}}\!\!\!-\text{OCH}_3
\quad
\xrightarrow[\text{H}_2\text{O}]{[\text{OH}^-]}
\quad
{}^-\text{O}-\!\!\!\overset{\displaystyle \text{OCH}_3}{\underset{\displaystyle \text{OCH}_3}{\text{Si}}}\!\!\!-\text{OCH}_3 + \text{CH}_3\text{OH}
$$

$$
\xrightarrow{\text{H}_2\text{O}}
\left(\!\!\text{O}-\!\!\overset{\displaystyle \text{O}-}{\underset{\displaystyle \text{O}-}{\text{Si}}}\!\!-\text{O}\!\!\right)_{\!n}
\quad etc.
$$
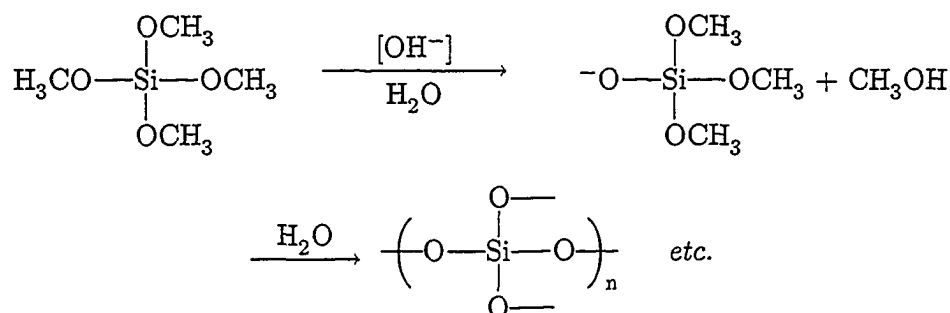
Figure 4.1: Aerogel is synthesized by polymerizing a silica source, such as tetramethyl orthosilicate (TMOS) shown here. The reaction also requires water and a catalyst: either base, as shown here, or acid. The relative rates of hydrolysis and polymerization depend on the catalyst – the oligomers produced can be linear or highly branched depending on the pH of the reactant solution. These oligomers continue to condense and cross-link – when the reaction is complete a continuous skeleton of SiO_2 has formed, liberating 4 moles of methanol for each mole of TMOS used.

compression[99]. On the other hand, higher porosities are easily obtained. Since an aerogel retains the macroscopic form of the alcogel, one needs only to dilute the reactant mixture to obtain higher porosity aerogels($0.86 < \phi < 0.98$). Unfortunately it is difficult to get the most dilute solutions to gel – in these dilute solutions the silica moieties are re-hydrolyzed at a rate comparable to their condensation – to make aerogels with $\phi > 0.98$ a two-step process must be used[100]. In this process, the silica is first hydrolyzed in an acidic solution with a sub-stoichiometric quantity of water to form silica dimers, trimers, and other oligomers but not the large polymers necessary for gelation. The solvent is then distilled off leaving the silica oligomers as an oil. This oil is subsequently dissolved in a different, aprotic, solvent with a stoichiometric quantity of water and a basic catalyst and set aside to gel. In this manner aerogels with porosities up to 99.8% ($\phi = 0.998$) have been synthesized.

The alcogel forms as soon as polymers reach a size comparable to the macroscopic size of the sample. However, this does not imply that the silica source is completely exhausted. For this reason the alcogels are often allowed to age for a week once they have gelled. Aging in a high pH solution can cause "ripening" of the gel – dissolution of some silica and redeposition into the smallest pores or sharpest corners[95]. If an alcogel is not left to age long enough, it has a greater chance of cracking during the drying process[101]. Once aged for a week or so, the gels are ready to dry.

54

4.1.2 Supercritical Drying of Aerogels

If the alcogels are removed from the sealed containers in which they were synthesized, then as the solvent evaporates, the liquid meniscus retracts through the gel. The surface tension along that meniscus is more than sufficient to collapse the tenuous structure that makes up the alcogel. As the solvent is removed the larger pores collapse and the sample will crack and fracture.

While this sort of collapse destroys much of the structure of the gel, the smaller pores are unaffected by the surface tension of the solvent because they have much more silica backbone than open space. In fact, if the rate of evaporation is carefully controlled then the monolithic nature of the samples can be preserved, and the resulting glass is referred to as a "xerogel" [93]. This drying process may take months, whereas supercritical drying of aerogels takes only hours. Xerogels have a much narrower distribution of pore sizes, since the small pores remain virtually unchanged while all the larger pores shrink as the silica skeleton collapses.

To completely retain the structure of the alcogel, the solvent must be removed without allowing a meniscus to form within the gel. This can be done be raising the temperature and pressure of the solvent above the liquid-vapor critical point[102, 103]. The gel is sealed within an autoclave and heated slowly. Once the temperature exceeds the critical point of the solvent, the pressure of the system is gradually reduced until no alcohol remains in the gel. The aerogel is then cooled and removed. Stress developed during the process can still break the aerogel, and even with careful handling it is common to observe some shrinkage of the aerogel upon drying.

High temperatures can be avoided during the drying process if one replaces the alcohol with another solvent which has a lower critical point. The most convenient substitution is with CO_2, which has a much lower critical point ($T_c = 31°C$ and $P_c = 72.9atm$)[27]. Once the alcohol has been exchanged for CO_2 the gel can be supercritically dried, as above, but at a much more reasonable temperature. This can avoid the structural changes that may occur at higher temperatures because of redistribution of silica[104], and also makes the drying environment much less restrictive. Materials may be incorporated into the gel that would be destroyed, or destroy the gel, under the conditions present during supercritical drying with alcohol – this process allowed the inclusion of copper mesh in the Grenoble aerogel

55

Porosity ϕ	Density kg/m^3	Gelation Time	TMOS		$NH_4OH_{(aq)}$		Methanol	
			mL	moles	mL	moles H_2O	mL	moles
97.5%	51	a few days	3mL	0.019	0.73mL^a	0.040	24mL	0.60
95%	110	a few hours	3mL	0.019	0.73mL^b	0.040	7.3mL	0.18

Table 4.1: Recipes for aerogels with densities/porosities used in this thesis. Gelation time is highly variable – some of the batches meant for low density gels never gelled at all. The number of moles listed under the aqueous solution of ammonium hydroxide are for the *water* added. 0.030Molar NH_4OH was used in order to speed gelation in the higher porosity aerogel (marked "a") while 0.015M NH_4OH was used for all denser aerogels, including the 95% porous gels used in this thesis (marked "b") .

pendulum discussed in chapter 3. There are even processes that allow the gel to be synthesized *in* CO_2 directly[105]. Systematic studies of the effect of supercritical drying parameters (and of gel aging before drying) have shown that the structure of the aerogel does change during the drying stage and have investigated the conditions under which one is most likely to obtain a monolithic aerogel[106, 107]. To be consistent with the aerogels studied in most low temperature experiments, all of our gels have been dried in supercritical alcohol.

4.2 My Aerogels

4.2.1 Wet Chemistry

All the aerogels used in my studies were synthesized from TMOS using the one step, base catalyzed, process. Thus my samples were restricted to porosities between 86% and 98%. Some proportions for synthesizing aerogels are shown in Table 4.1. Once combined, the reactants were mixed quickly with a Pasteur pipette and then poured into molds. The molds were then placed in sealed Nalgene or glass bottles with some additional methanol added to the bottom of the bottle to maintain saturated vapor pressure. After gelation, the gels were completely covered in methanol and left to age at least a day, usually 1-4 weeks.

4.2.2 Supercritical Drying of Aerogels

Equipment/Setup

The drying system is shown schematically in Figure 4.2; it was built to allow for the high temperatures (270°C) and pressures (1600psi $\approx$ 120atm) necessary to extract methanol as a supercritical fluid ($T_c = 240$°C and $P_c = 78.5atm$)[27]. The aerogel is sealed within a drying cell and heated inside a tube furnace. The gas handling
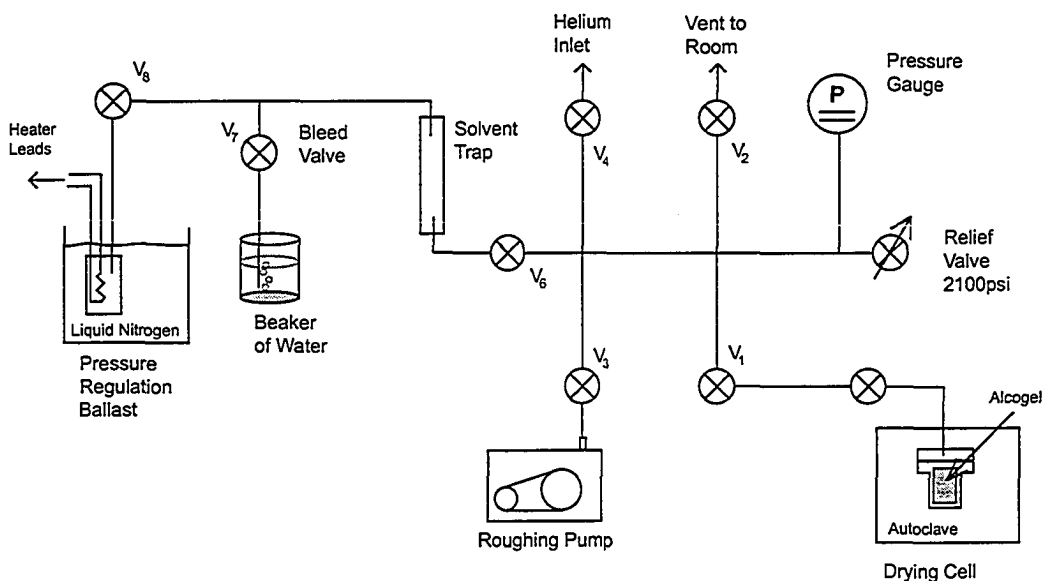
Figure 4.2: This is a schematic of the system used to dry the alcogels into aerogels. The alcogel is sealed in the drying cell and placed in an autoclave or tube furnace. Helium is admitted into the system until the pressure reaches about 1600psi and kept constant by the pressure regulation ballast during heating. As the cell temperature rises, the solvent expands into the gas handling system – the solvent trap is required to keep the solvent safely away from the pressure regulation ballast where it might cause a plug. Once the final cell temperature has been reached, the bleed valve and pressure regulation ballast are used to slowly depressurize the system. Finally, at low pressures the pressure regulation ballast is closed and the roughing pump is used to remove any remaining solvent in the system.

system is equipped with a Setra capacitive pressure gauge (0-5000psi), a helium cylinder with high pressure regulator, a belt-drive roughing pump, a solvent trap and a pressure regulation ballast; all connections in the gas handling system are made by 0.060" OD (0.025" ID) stainless steel Hi-P tubing. This system allows for the pressurization and depressurization of the cell under carefully controlled conditions.

Drying Cell The alcogel is sealed within a stainless steel cell equipped with a 1.33" CF flange. A thermocouple temperature gauge is attached directly to the stainless steel cell, and they are further encased within an aluminum cylinder. The aluminum cylinder acts as a thermal mass to help smooth out local variations in temperature since thermal gradients in the gel may result in damage to the structure during warming. This entire assembly is placed within a Thermolyne tube furnace

57

and temperature is controlled by an Omega CN6081 Ramp and Soak Temperature Controller connected to the thermocouple bolted to the cell.

The stainless steel cell is welded together – solder is avoided for two reasons. First, any accidental overheating of the cell while pressurized could lead to a disastrous explosion; if the solder was to weaken enough to allow the methanol vapor to escape then the heat of the autoclave might ignite it. In 1984 the only commercial producer of aerogel (a Swedish company by the name of Airglass) suffered a methanol explosion[108]. A gasket used to seal the pressure vessel failed, causing the supercritical methanol to escape, then ignite. The entire building was destroyed and three employees injured – this cautionary tale underscores the need to be safety conscious when drying aerogels. The second reason solder is avoided is that impurities must be kept to a minimum; supercritical methanol is a very good solvent and impurities in the solder may dissolve in the methanol and then react with the silica gel. This can result is significant damage to the final aerogel.

Some later aerogel samples were too large for the drying cell above, so those samples were dried in a larger cell sealed with 2.125" CF flanges.

Pressure Regulation Ballast The pressure in the gas handling system can be controlled by the pressure regulation ballast. This consists of a power resistor encased in a sealed stainless steel reservoir ($V \sim 50 cm^3$) which is immersed in a liquid nitrogen bath. Pressure is regulated by a LakeShore Cryotronics DRC 82C Temperature Controller with the voltage output from the Setra capacitive pressure gauge used as the input for the controller and the heater output routed through the power resistor within the pressure regulation ballast. Power supplied to the heater creates a local warming within the pressure regulation ballast, resulting in an increase in pressure in the gas handling system. While the pressure can only be changed by about 10% using the controller, it ably performs its main purpose which is to smooth out any abrupt changes in pressure and maintain a steady rate of depressurization during the degassing stage.

Solvent Trap Since methanol is being removed from the alcogel, it enters the gas handling system and makes it difficult to control the rate of flow through valves. It can also form blocks by freezing in the inlet tubing of the pressure regulation ballast. To counteract these problems a simple solvent trap was installed between the drying

58
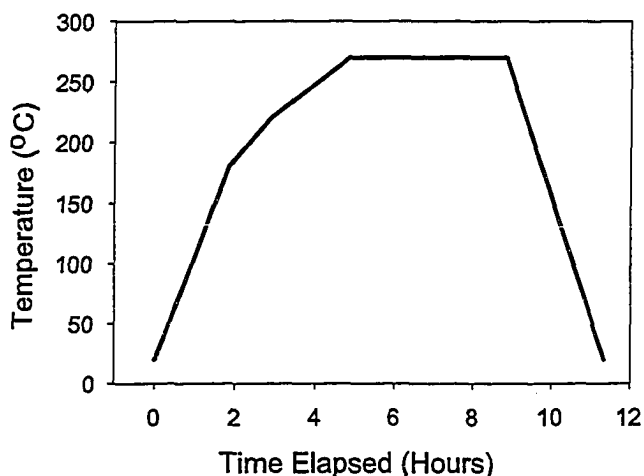
Figure 4.3: The drying program for my aerogels. Once the gel has reached 270°C the supercritical methanol is slowly released. Some longer gels (as used in the LVDT work described later) forced the solvent to follow a longer path to leave the sample – they were heated using a similar program, but only half as quickly.

cell and the bleed valve. The trap consists of a vertical steel tube (V~5cm^3) – the helium/methanol mixture in the GHS enters through an inlet in the bottom of the cylinder and an outlet from the top of the cylinder leads to the bleed valve and pressure regulation ballast. Gravity retains the methanol in the bottom of the trap and it can be removed by evacuating the gas handling system.

Bleed Valve The bleed valve is a standard Hi-P valve, but the gas is vented through a piece of 0.020" O.D. capillary tubing which is immersed in a beaker of deionized water. This allows for visual estimation of the degassing rate.

Drying Procedure

The mold containing the alcogel is immersed in methanol within the drying cell and the cell sealed with a copper gasket. The cell and gas handling system are pressurized with helium gas to about 1550psi, above the critical pressure of methanol (1100psi). The pressure regulation ballast is then used to ramp the pressure up to about 1600psi while the gel is still at room temperature. The pressure is maintained at 1600psi as the gel is heated according to the temperature program shown in Figure 4.3.

Once the gel has equilibrated at 270°C, gas is slowly released through the bleed valve into the beaker of water while the pressure is ramped down at a rate of 20-25psi/min. By careful adjustment of the bleed valve and use of the pressure regulation ballast it is possible to maintain a constant rate of degassing even though it is difficult to maintain a constant rate by adjusting the bleed valve alone. However, even with the pressure regulation ballast it is still common to have small dips in pressure as the bleed valve is adjusted. These may be only a couple of psi in most

59

cases, but it is common for a run to have a 5-10psi dip in just a couple of seconds.

Once the pressure has been reduced to 15psi, the system is evacuated with a roughing pump until all liquid in the gas handling system has evaporated. The gel is then flushed with air two to three times and left under vacuum while it cools to room temperature. Once cooled, the cell can be vented, opened and the aerogel and vial removed.

Condition of dried aerogels

All gels prepared in the above manner retained most of their volume, and most were monolithic. However, slight shrinkage of the gels, a rounding of the top and cracks through the sample were common. About half of all gels prepared were free of cracks and not subject to much shrinkage. The curvature of the top could be minimized by filling the alcogel molds just to the top edge with the gelling solution – there was no meniscus, positive or negative. James Day discovered that placing the vials containing the alcogels into the drying cell *upside-down* led to reduced curvature of the aerogel as well.

The presence of cracks indicates that too much stress developed at some point during the drying process. This may be due to improper aging[107], quick heating, quick degassing, or sudden changes in pressure while degassing. Despite careful record keeping, it is not obvious which factors are playing the largest role in the damage. Recently, careful work has been done in other labs on the development of stress during aerogel drying[109]; using these results it may be possible to design a more reliable drying program.

We find that a slight shrinkage is actually desirable since it pulls the the aerogel away from the walls of the mould. On occasions when the gel did not shrink radially it was very difficult to remove from its mould. To assist in removing these aerogels one can use "vacuum tweezers," shown schematically in Fig. 4.4, which consist of a metal tube terminating in a perforated disc and backed by a roughing pump. The perforations are small enough that the pump does not damage the gel, so a stubborn aerogel can be moved without handling it directly with your fingers.

60
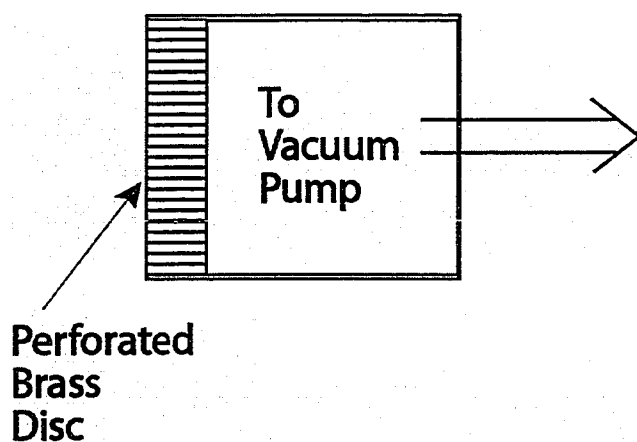
Figure 4.4: Vacuum Tweezers – made by soldering a perforated metal disc into a copper tube, which in turn can be connected to a roughing pump through plastic tubing. The resultant gentle suction can safely manipulate aerogels without cracking or contaminating them. These tweezers were used to extract aerogels from moulds without handling them directly.

4.3 Aerogel Structure and Properties

4.3.1 Microscopic Structure

The microscopic structure of aerogels depends on the silica source, the catalyst used and on the drying conditions. Gelation can be catalyzed by acid or base: acid catalyzed gels have a wide distribution of pore sizes from micropores ($< 2nm$) to macropores ($> 50nm$) while base catalyzed gels do not exhibit microporosity – they appear as agglomerations of small silica particles. I have stuck to the techniques and silica source used to make most of the silica aerogels in the low temperature physics community – base catalyzed condensation of TMOS followed by supercritical drying in methanol.

Microscopy Most aerogel features are smaller than 100nm. As such, they are not well suited to scanning electron microscopy (SEM), although it is possible to distinguish basic textural differences between different aerogels. To obtain high quality images of aerogels one must employ transmission electron microscopy (TEM). Base catalyzed aerogels appear as a network of strands and clumps composed of small (5-10nm diameter) roughly spherical silica particles. The particles appear smooth and that supposition is supported by the lack of micropores indicated by adsorption isotherms, and by scattering data addressed below. A TEM micrograph of one of my aerogels is included as Fig 4.5.

Careful preparation is needed for systematic investigations of aerogel by electron microscopy due to sample charging – a simple thin film of carbon is not always enough to protect the aerogel. A study of very high porosity aerogels using stereoscopic images from TEM[110] used aerogels which were coated with platinum and

61
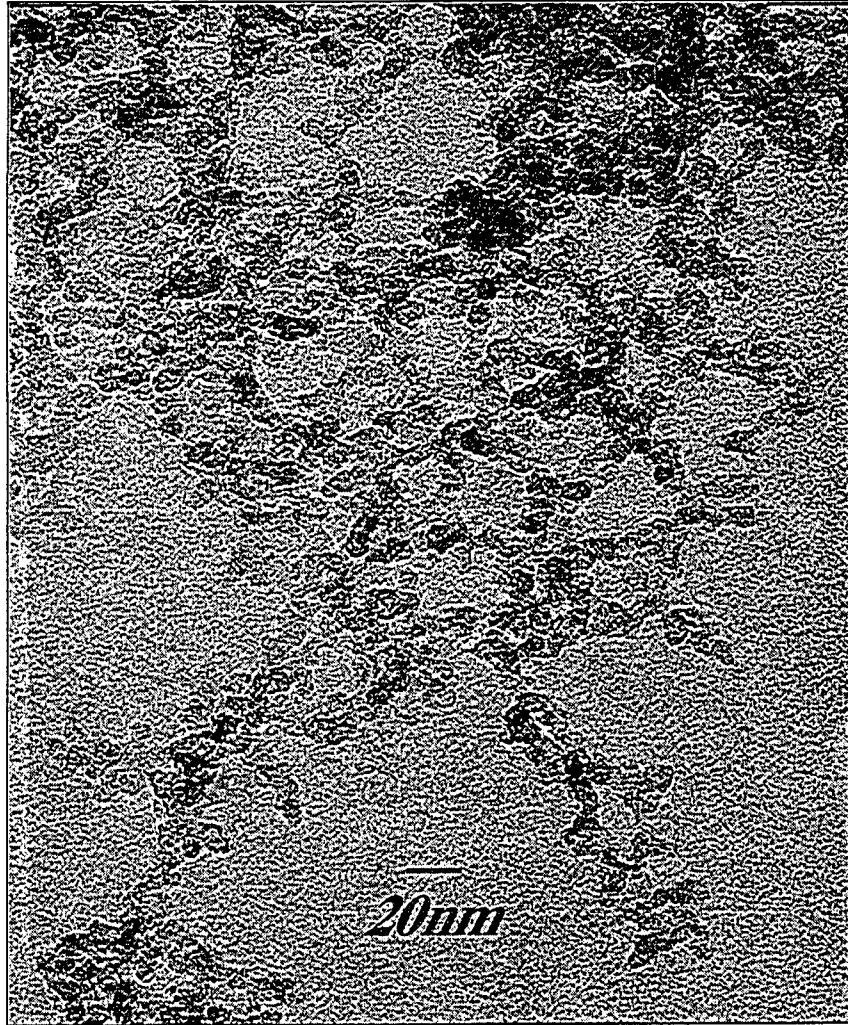
Figure 4.5: TEM micrograph (JEOL-2010) of a 95% aerogel (B110) synthesized in-house.

62
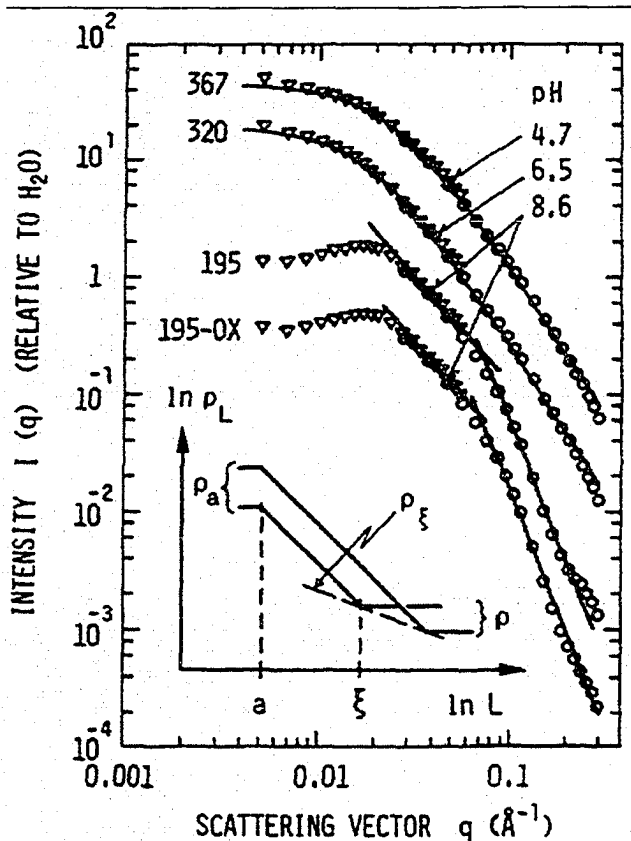
Figure 4.6: Small Angle Neutron Scattering (SANS) from acid and base catalyzed aerogels. The curves are labelled with the pH of the gelling solution. These data show the crossover from fractal to surface behavior present in the base catalyzed gels, but not present in the acid catalyzed gels. The slope of the curves for the base catalyzed gels correspond to a fractal dimension of D=1.9 for small q and surface scattering for large q. This figure is reproduced from reference [111].

carbon followed by removal of the silica. The images were then used to tabulate the distribution of pore sizes and strand sizes.

SAXS and SANS Small angle X-ray scattering (SAXS) and small angle neutron scattering (SANS) data can provide detailed information about the mass correlations within a solid. When a beam of incoming X-rays (SAXS) or neutrons (SANS) interacts with a porous solid, it is scattered by the solid matrix in a way that depends sensitively on the structural correlations within the media. For instance, scattering intensity from a flat interface will have a certain dependence on scattering wave-vector, while scattering from a mass fractal will show a completely different dependence. By careful analysis of scattering results, especially when interpreted through the use of models and simulated scattering curves, a great deal of information can be inferred about the microscopic structure of aerogels.

SAXS and SANS studies of aerogels show how aerogel structure changes over different length scales. In base catalyzed gels, short range correlations appear surface-like. This implies that the constituent particles of silica have smooth surfaces. But at longer scales this behavior changes to become that of a mass fractal with di-

63
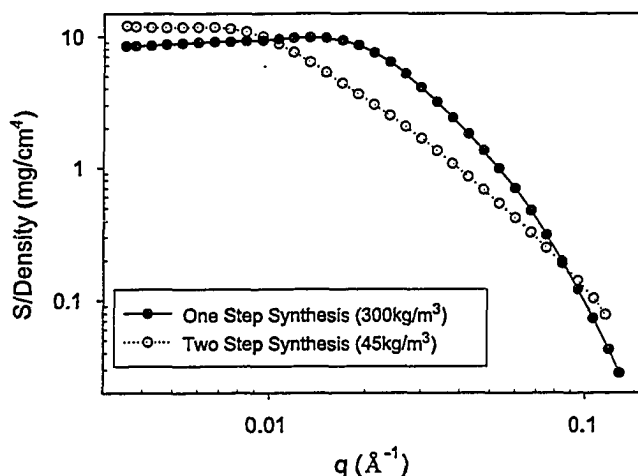
Figure 4.7: Small angle X-ray scattering from aerogels synthesized using one-step and two-step processes. Each curve has been scaled by the aerogel density – if the structures were identical except for density, the two curves would collapse to a single curve once divided by density. The fact they do not points to some small differences in the microscopic structure.[53].

mension close to 2. At longer distances the scattering intensity reaches a maximum and then decreases[112]. The region with fractal characteristics is no larger than an order of magnitude, and corresponds roughly to the dimensions of the pores ($\sim 5 - 50nm$). An example is included as Figure 4.6, along with results from a set of acid catalyzed gels which exhibit a slightly different structure. In Figure 4.7 scattering data from two base catalyzed gels are compared – a one-step synthesis gel and a two-step synthesis gel. The two gels show some similarities, but there are differences as well; the slopes of the scattering curves are different in the region of "q" which represents the most important size scales (1nm to 50nm).

Studies on aerogels prepared under neutral conditions and gels prepared from colloidal aggregations of silica particles show similar results[113, 111]; studies of acid catalyzed gels show no crossover from fractal to smooth surface behavior – they exhibit fractal structure down to the atomic scale[111] but with a larger fractal dimension than base catalyzed gels. As an interesting side note, NMR can also be used to probe the fractal structure of aerogels; Devreux et al. used NMR to measure the fractal dimension of acid catalyzed aerogels[114] and found that the dimensions agreed, roughly, with those from SAXS. Finally, light scattering from a series of very dilute wet silica gels by Ferri et al.[115] shows a similar crossover from fractal structure to a homogenous structure above some crossover distance ξ. They saw no crossover to surface structure at small scales, but their technique did not allow them to probe such small scales.

Adsorption Isotherms Interpretation of N_2 adsorption isotherms can give a quantitative measure of the specific surface area and pore size distribution within

64

the sample[32] but this is not appropriate for aerogels. The compliant nature of the gels leads to structural changes during adsorption that bias all the results and can permanently damage the sample. While many studies of aerogels include these results, they should be taken with a grain of salt – I have not performed these measurements on my samples because of the unreliability of these techniques.

4.3.2 Macroscopic Properties

Elastic Properties

The elastic properties of aerogels are unlike those of denser silica glasses. The reason for this is quite simple – since aerogels are such tenuous structures, their behavior is governed more by the connectivity of the constituent silica than by the elastic properties of the silica itself. One of the most successful models of aerogel elastic properties[116] relies completely on describing the structure of aerogels as interconnecting strands of silica with sharp bends, or "knees," responsible for the compression and re-expansion of the aerogel. Studies have looked at sound speed in aerogels with a wide range of densities at various frequencies[117, 116, 118]. Other studies have looked at static compression, using a flexural technique[119], a mercury "porosimetry" technique[120, 121], and using micro-indentation[122].

All these methods allow one to analyze the effect of aerogel density on elasticity parameters such as the bulk modulus or Young's modulus. Young's modulus for aerogels follows a power law dependence on density as:

$$E = E_0 \rho^m$$

with $m \approx 3 - 3.6$[122, 120].

Sound velocity and attenuation Sound speeds within aerogel are among the lowest in any solid – high porosity gels exhibit sound speeds of 100m/s or less[116]. High porosity aerogels are also very sensitive to the presence of gas in their pores because the density of gas becomes comparable to the density of the aerogel. Gels with $\phi > 98\%$ (i.e. $\rho < 50 kg/m^3$) exhibit lower sound speeds when evacuated than when measured in air, with differences of up to a factor of five for the most porous gels. Because of aerogels' diffuse structure, along with these low sound speeds come very high attenuations – especially at ultrasonic frequencies[118]. A study by Daughton *et al.*[123] used a resonance technique to measure sound speed in aerogels over a wide

temperature range; they found that the shear modulus increased linearly at high temperatures (above 100K). This type of behavior is associated with systems such as rubber, whose elastic moduli include a large entropic contribution. High porosity aerogels (or alcogels) have a low enough bulk modulus that the compressibility of any fluid (even air) in their pores greatly affects sound propagation in the gel. The theoretical framework developed by Biot[124, 125] to deal with sound propagation in fluid filled porous media has been adapted to aerogels by Forest *et al.*[126].

Thermal Properties

High porosity aerogel has one of the lowest thermal conductivities measured. The low conductivities ($\lambda < 0.1 Wm^{-1}K-1$) are due to the form of the silica strands. Since the individual strands are only a few nanometers in diameter and a path across the aerogel sample must be extremely tortuous, heat conduction along the strands is very limited. Any air in the aerogel pores can conduct heat, but the individual pores are small and any path across the aerogel will be just as tortuous for air as it is along the silica strands. Finally, radiative heat transfer is restricted by the large number of absorbing and emitting surfaces in the aerogel. The major contribution to thermal conductivity comes from the air in its pores, so evacuated high porosity aerogels show the lowest thermal conductivities. The behavior of the thermal conductivity at low temperatures can also give information on the elementary excitations in the aerogel which carry heat along the silica strands[127, 128].

Aerogel's low thermal conductivity has led to speculations about using it commercially as an insulator[88]; however, its high cost and fragility make it unlikely to have many applications. In our experiments, however, this low thermal conductivity makes life miserable. It can lead to exceptionally long equilibration times, sometimes requiring more than a day to equilibrate for a single data point. We work around this by using the smallest possible samples, but experiments still require many minutes to hours to equilibrate.

Chapter 5

Capacitive Measurements of Helium Condensation in Aerogel

We have performed a series of high precision measurements of helium density in silica aerogels along adsorption isotherms near the liquid-vapor critical point of helium. To achieve high precision we made several refinements of our sample cell and measurement technique over the course of this investigation. All measurements were taken capacitively except for temperature, which was measured resistively – the precision of our final results was in fact set by the uncertainty in cell temperature ($\pm 50\mu K$) and by a comparable drift in the stability of our temperature controller. Adsorption isotherms were collected for helium condensation in three aerogel samples, with porosities between 95% and 98%. These isotherms show that for temperatures much below the bulk liquid-vapor critical temperature, helium condensation in aerogel exhibits hysteresis, and that adsorption isotherms have finite slopes – not the zero slope one would expect from a true liquid-vapor coexistence. Closer to T_c, the shape of the isotherms gradually changes and hysteresis disappears. There is no single obvious "pore critical" temperature.

This chapter describes the experimental systems used to measure adsorption isotherms in aerogel and our results. It also includes results from very simple model calculations used to design the cells and interpret our capacitive results. The samples used in this study are described here, but for details of their synthesis one should consult Chapter 4.

67

5.1 Experiment Design

5.1.1 Aerogel samples

Our final results were collected for three different aerogels. Two of them were synthesized in our lab using the standard one-step base catalyzed method described in Chapter 4. These two aerogels had densities of $110\frac{kg}{m^3}$ and $51\frac{kg}{m^3}$ corresponding to porosities of about 95% and 98% respectively; they are referred to as aerogels "B110" and "B51." The third sample described in this chapter was not synthesized in our lab, and we therefore do not know as much about its structure and composition; its provenance has been lost, due to incorrect labelling at some point years before I began my degree, so it is referred to as "Aerogel X."

Our original concept for measuring the density of fluid in aerogel called for a coaxial capacitor which would measure the dielectric constant of the fluid between the inner and outer electrodes. The aerogel sample was grown *in situ* between coaxial sections of stainless steel tubing with Macor (machinable ceramic) spacers separating the tubes. The gel was grown normally in a 0.5" diameter glass vial with the coaxial capacitor immersed in the gelling solution; it was dried supercritically in methanol without any apparent cracks or shrinkage. The final capacitor is shown in Figure 5.1. However, while this capacitor was very sensitive to helium density, the equilibration times during data collection proved to be prohibitively long (many hours for any point within the coexistence region). The long equilibration times were due to the exceptional thermal insulating qualities of the aerogel coupled with the release of latent heat as fluid condensed within the aerogel. The large aerogel volume ($\sim 2cm^3$ inside and surrounding the capacitor) needed to be eliminated. The size of the sample was dramatically reduced by moving to a capacitor which consisted of a thin disc of aerogel with parallel plate electrodes deposited directly onto the sample (Figure 5.2). Both of these arrangements eliminate possible bulk regions in the gap between electrodes and aerogel.

The aerogel discs were cross sections cut from aerogel cylinders about 0.490" in diameter and ~1" long (the general size and shape used in the resonator experiments) using a Foredom high speed grinder (Micro Motor handpiece Model #MH-135) fit with a Horico SuperDiaflex diamond coated saw blade. Cutting the aerogel is a painstaking process which requires a great deal of patience – cutting too fast will destroy the fragile solid. It takes about forty-five minutes to cut a
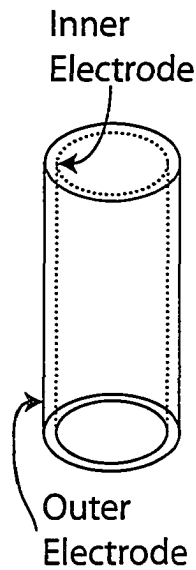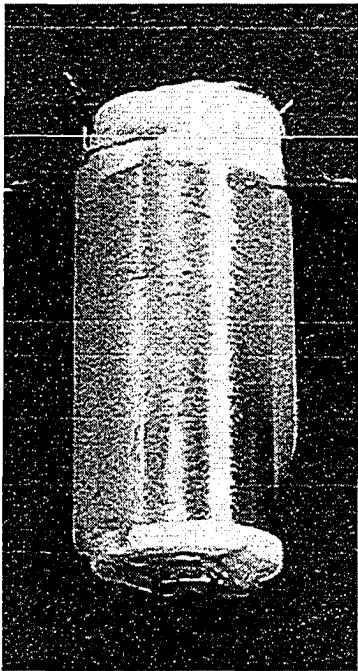
Figure 5.1: This is a photo of a sample of aerogel B110 grown between coaxial capacitor plates. The inner and outer electrodes are lengths of stainless steel thin-wall tubing held apart by ceramic spacers. The aerogel fills the capacitor, and is visible coating the outside as well (although some has chipped off).

Inner Electrode

Outer Electrode
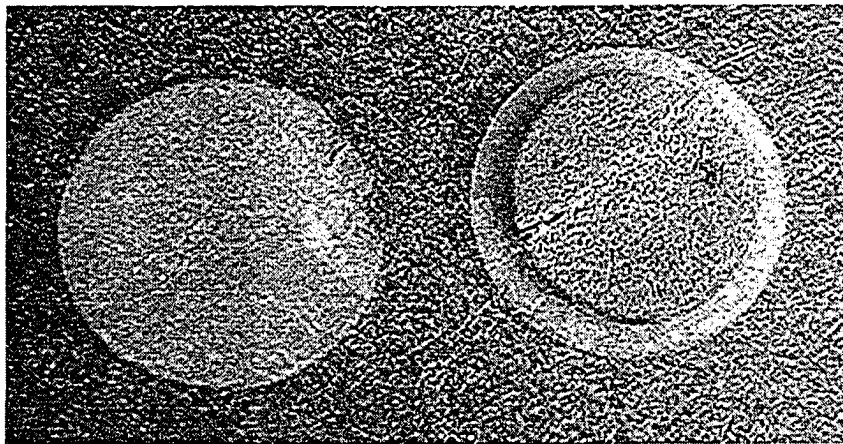
Figure 5.2: This is a photo of a sample of aerogel B51 with and without capacitor plates evaporated onto the two faces. The unplated sample on the left shows some chipping caused during cutting, probably when the disc separated from the cylinder and fell into the collecting tray. The copper electrode was electrically continuous, confirmed by measuring resistance across the face of the sample. The poor contrast in the image is due in part to the transparent nature of aerogel and the thinness of the samples.

69

0.020" (0.5mm) thick disc from the 0.5" diameter cylinder of aerogel and, once cut, that disc is difficult to catch or to find if it is dropped. About half of the discs are destroyed or lost during cutting.

The capacitor plates were copper thick films deposited directly on the aerogel disc by thermal evaporation (deposited at $\sim$ 3-4 Å/sec to a thickness of $200 \pm 20nm$, as monitored by quartz crystal microbalance). Empirically, metal does not seem to penetrate significantly into the aerogel and the copper film does not plug the pores as is would for a denser porous medium. This is consistent with the open structure of the aerogel surface and with mean free paths of 80nm and 200nm calculated for 95% and 98% porous aerogels by a group at Northwestern [129]. The metal film acts as a continuous electrode, confirmed by electrical conductivity measurements; modelling it as a flat plate in capacitance calculations gives values consistent with experimental results.

While it would be nice if the samples actually acted as infinite parallel plate capacitors, unfortunately the real geometry of the samples leads to some significant effects from fringe fields (electric field lines which project from the edges of the capacitor). Some of these field lines go through the aerogel slice, but others exist past the edges of the aerogel slice and go through the bulk volume in the cell. The fields that might be present in a real parallel plate capacitor are shown schematically in Figure 5.3. Since the measured capacitance depends on the details of all the electric field lines, it is sensitive to the environment outside the aerogel as well as the environment inside the aerogel. This effect can be seen in the experiment and in the model, with good agreement between the two described later in this chapter. For a free floating slice of aerogel of the dimensions shown in Figure 5.2 fringe fields cause the capacitance to deviate from the ideal parallel plate capacitance by about 10%.

Early results from Grenoble[15] showed a significant difference between the density of liquid helium in aerogel and that of bulk liquid helium at P_{SVP}. After our initial run had proven to us the effectiveness of our technique, and with that uncertainty in absolute helium density in mind, we wanted to move to a geometry that allowed a more absolute determination of helium density in the aerogel. In order to reduce fringe effects a slightly different electrode geometry was designed, incorporating a "guard ring" while leaving the aerogel dimensions unchanged. A guard ring is an electrode which is held at ground, so that field lines originating at one electrode

70
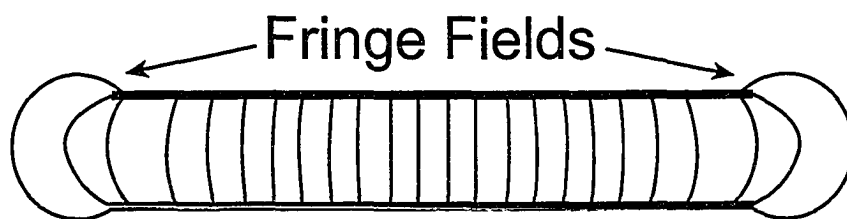
Figure 5.3: A finite sized parallel plate capacitor does not exhibit uniform electric field between the plates as an infinite capacitor would. As shown schematically in this cross-sectional view, fringe fields protrude out the side of a finite parallel plate capacitor. This causes its actual capacitance to deviate from the ideal value and the final value depends on the dielectric surrounding the capacitor as well as the dielectric directly between the plates.

cannot stray off to the side. This technique has historically been used to study surface potentials, and a number of designs have been created for electrodes guarded by a grounded electrode (see for example reference [130]). Modelling showed that in our case the guard ring should reduce the effects of the fringing fields to a few percent. Results from calculations on both the original and guard ring geometries are discussed in Section 5.4.

For samples incorporating the guard ring, the guard ring and electrode are deposited simultaneously by masking the sample with a thin ring of steel. The ring was about 0.300" in diameter, with a radial width of about 0.015" and was held in place during deposition by a magnet behind the sample. The setup is shown schematically in Figure 5.4. We have made samples with guard rings, but have not yet used any in our studies.

5.1.2 Cell Construction

These measurements were performed in two cells. As mentioned, the original concept for this experiment involved a coaxial capacitor with aerogel as the dielectric between the plates, but did not produce usable data. This cell was then refitted to measure a disc of aerogel with capacitor plates on the two flat faces. This first cell was a simple design which incorporated an *in situ* Straty-Adams pressure gauge, a coaxial capacitor to measure bulk fluid density, and a clamp arrangement to hold a thin slice of aerogel. This cell is shown in Figure 5.5 with a disc of aerogel as the sample. Whenever possible, components were machined from oxygen-free high conductivity copper. All epoxy used was BIPAX Tra-Bond BA-2151, which has proven to provide
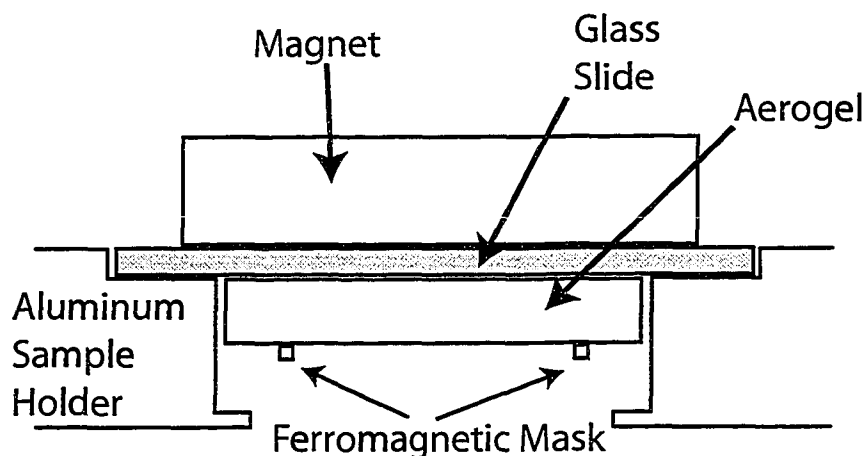
Figure 5.4: This is a schematic of how the aerogel slices were held during the deposition of the copper electrodes. The aluminum sample holder was mounted in a thermal evaporation system, and about 200nm of copper were deposited at a rate of about 0.2nm/sec. In order to deposit the central electrode and the guard ring simultaneously, a ring of ferromagnetic steel was held onto the face of the aerogel as a mask. This ring was held in place by a magnet mounted behind the sample; in order to remove the magnet without holding onto the aerogel, the magnet was glued to the back of a glass microscope slide. To deposit an electrode with no guard ring, the aerogel sample was allowed to rest on the rim at the bottom of the holder, with no magnet behind it.

reliable contact even upon repeated thermal cycling between room temperature and 4K; furthermore it is an aesthetically pleasing shade of blue.

The *in situ* pressure gauge was necessary to obtain the degree of precision and reproducibility seen in our experiments. The gauges were constructed after the design of Straty and Adams[131], and consisted of a thin beryllium-copper diaphragm whose deflection influences the separation of two parallel brass plates. Thus, the deflection can be measured to very high precision by monitoring the capacitance between the parallel plates – well assembled gauges have resolutions of $10^{-5} bar$ or better.

The second experimental cell was designed so that we could reduce stress on the aerogel and limit the effect of fringe fields on the capacitance measurement, but retain the good properties of the previous cell. The new cell reduces the compressive force on the aerogel by holding it in place by thin flexible mesh soldered to a thin flexible wire instead of the relatively stiff beryllium-copper arms. This feature is required for working with weaker, high porosity, aerogels. The cell also allows us to reduce the fringe fields by incorporating a guard ring into the electrode design

72
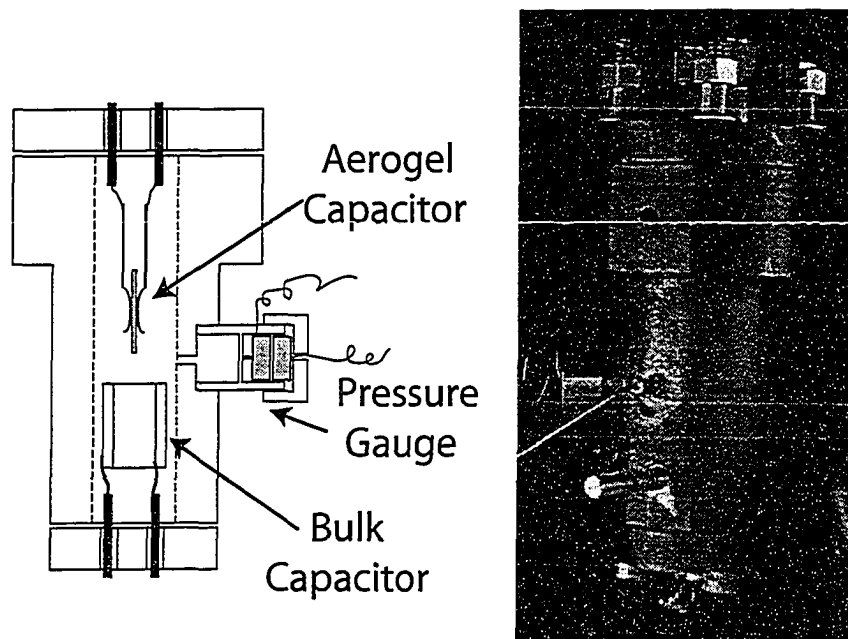
Figure 5.5: This is the first capacitance cell used to investigate adsorption isotherms of helium in 95% silica aerogel (B110). The aerogel is a ~ 0.025" thick disc $\sim \frac{1}{2}$" in diameter with copper electrodes deposited on the two parallel faces. It is held in place with two beryllium-copper arms which also provide electrical contact. The bulk density capacitor is coaxial, consisting of two concentric stainless steel tubes with outer diameters of 0.250" and 0.375" held apart by small dabs of epoxy. The pressure is monitored *in situ* by a Straty-Adams type capacitive pressure gauge.

(discussed below), although that feature has not yet been used.

The complete layout of the unassembled cell is shown in Figure 5.6. There are three distinct modules to the cell (parts 1,3 and 4 in Figure 5.6), each with a single measurement function – a central piece and two endcaps. The center includes an inlet capillary through which fluid can be admitted and the Straty-Adams pressure gauge. One endcap measures bulk fluid density using a coaxial cylindrical capacitor where the bulk fluid acts as a dielectric between the plates. The second endcap is used to hold the aerogel sample for measurements of fluid density within the gel. Cross-sectional views of the two endcaps are included in Figure 5.7.

The aerogel lies in a shallow copper cup which makes contact with the bottom electrode on the aerogel slice and is electrically connected with one isolated feed-through soldered into the cell. Contact to the top electrode is made by a patch of fine metal mesh – the patch acts as a very weak spring, holding the slice in place while ensuring good contact. The mesh is in turn soldered to a coiled length of

73
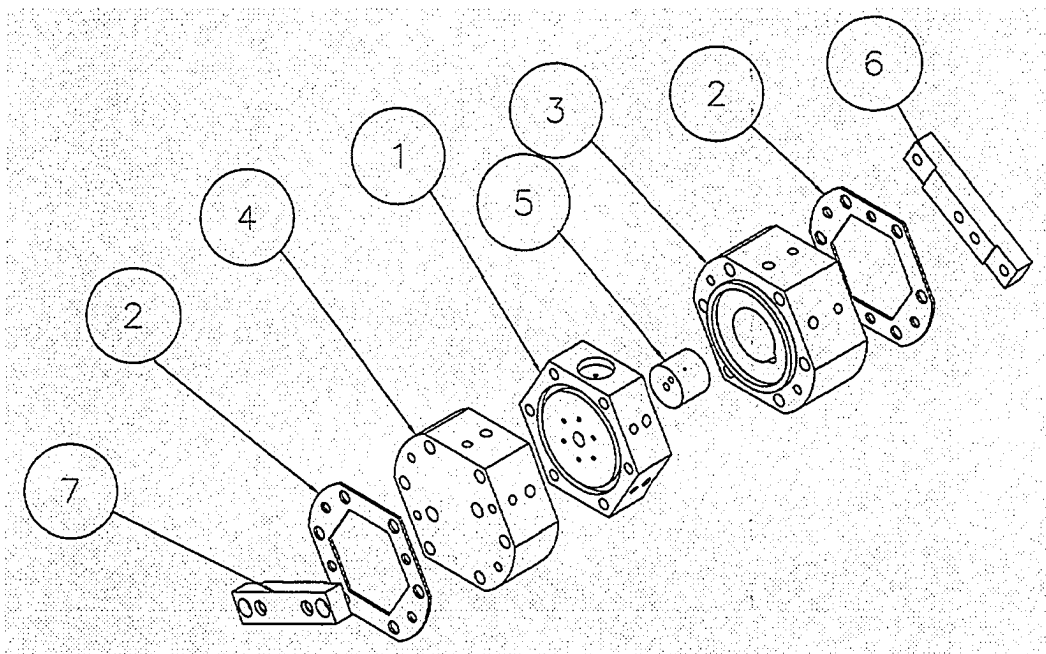
1 - Center Piece with Pressure Gauge and Fluid Inlet

4 - Aerogel Density Capacitor Endcap

3 - Bulk Density Capacitor Endcap

5 - Inner Electrode for Bulk Capacitor

2, 6, 7 - Exterior Pieces to Support Nuts and Coaxial Connectors

Figure 5.6: This is the second capacitance cell used to investigate adsorption isotherms of helium in various porosities of silica aerogel. The cell was designed to be modular and versatile; the two endcaps were designed to measure helium density in the bulk phase and in an aerogel slice respectively. These could be used for any fluid, at a wide range of pressures and temperatures. The center piece included the fluid inlet capillary and the *in situ* pressure gauge; this portion of the cell could be constructed to suit the pressure range of the fluid under investigation. Our experiments used a center which held a Straty-Adams gauge with a 0.008" thick flexible diaphragm calibrated to work well near the critical pressure of helium, but if one wished to repeat these experiments with neon it would be a simple matter to swap this center piece for another which held a thicker diaphragm Straty-Adams gauge.

74

Aerogel Density Capacitor

Bulk Density Capactior
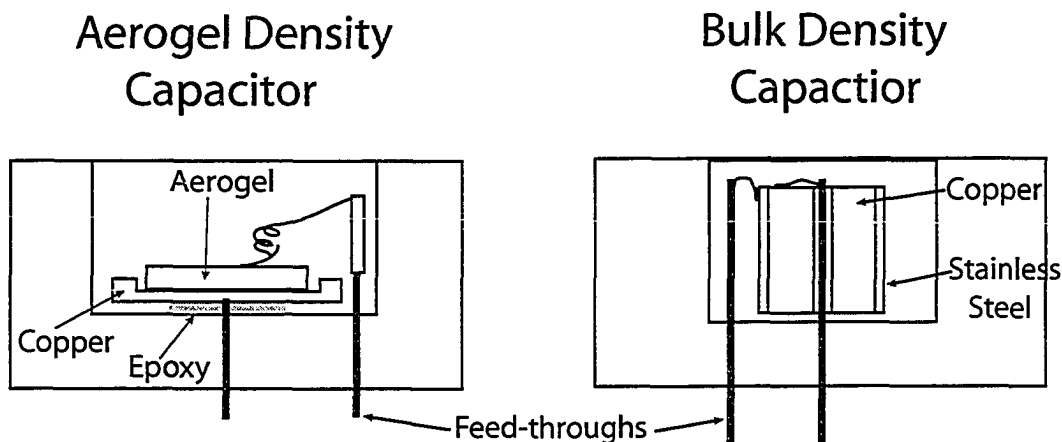
Figure 5.7: These are schematics of the endcaps from the second generation cell used to investigate adsorption isotherms of helium in various porosities of silica aerogel. The aerogel capacitor uses a copper cup to support the aerogel slice. Contact to the top electrode on the aerogel is made with a thin patch of metal mesh soldered to the end of a thin piece of coiled wire. This arrangement minimizes the local stress on the aerogel while assuring good electrical contact. A second pin, not shown here, is soldered directly into the cell and can be used to make contact to the guard ring in the same manner as contact is made to the top electrode. The bulk capacitor consists of a copper cylinder as the inner electrode and a piece of coaxial thin wall stainless steel tubing as the outer electrode. The plates are separated by small dabs of epoxy.

fine wire which acts as a slightly stronger spring. Finally that wire is soldered to a female pin which may be slipped over the other isolated electrical feed-through soldered into the cell. A male pin is also soldered directly into the cell body so that a second female pin/wire/mesh connector can be used to anchor a guard ring to electrical ground. A typical aerogel sample has a capacitance of $C_{gel} \sim 2pF$. The bulk density capacitor, with a plate separation of about 0.003", has a capacitance of $C_{bulk} \sim 35pF$.

5.2 Measurement Technique and Resolution

5.2.1 Temperature Control

Temperature was controlled by a Neocera LTC21 temperature controller, using a Germanium resistive thermometer and 200Ω thick film resistive heater mounted directly on the cell body. Cooling power was provided by a small quantity of helium exchange gas in the vacuum can of a liquid helium cryostat. The cell was mounted inside a radiation shield which also acted to reduce the heat link between the cell

75

and the helium bath. Thermometer resolution was 0.1mK, with very little noise, implying that the cell temperature was probably controlled to $\pm 50 \mu K$. Temperature controller drift over hours was also about $\pm 50 \mu K$. This was our resolution limiting factor in the work on aerogel B51.

5.2.2   Electronics

The capacitances were all read using a bridge technique. The early data sets were obtained using a manually balanced capacitance bridge (General Radio model 1615-A) with a 1kHz excitation frequency. This provided high quality data but was very labor intensive – it required the full attention of a person for over a day to finish any significant portion of an isotherm. Additionally, the bridge's resolution and drift, while not bad, limited the experimental resolution to about 1 part in 10^5. The data collection process was greatly facilitated by the acquisition of an automated, high resolution, Andeen-Hagerling capacitance bridge (model AH2550A), also operating at 1kHz excitation frequency. This bridge, coupled with in-house LabVIEW data acquisition software, allowed almost complete automation of the data collection process. This, in turn, allowed a higher density of data points along an isotherm, with higher precision, without increasing the time required to acquire a complete isotherm. A schematic of the measurement electronics is included as Figure 5.8.

5.2.3   Gas Handling

Helium was admitted to the cell using two very different methods. Originally helium was directly admitted to the cell from a room temperature gas handling system. The rate at which helium was added was controlled by a mass flow controller (MKS Instruments PR4000); the entire gas handling system is shown in Figure 5.9. The flow controller ensured a continuous flow into the cell at a well controlled rate, but even the slowest rate of flow was too fast to allow for relaxation within the aerogel. Thus to allow enough time for the helium and aerogel to relax to whatever metastable, or equilibrium, state they were going to reach, the flow controller had to be shut off and the cell allowed to equilibrate at each point without any additional mass input.

Later a second method was used by mounting a low temperature ballast volume just above the cell; the setup is shown schematically in Fig 5.10. The ballast temperature was controlled independently of the cell temperature. It could be maintained

76
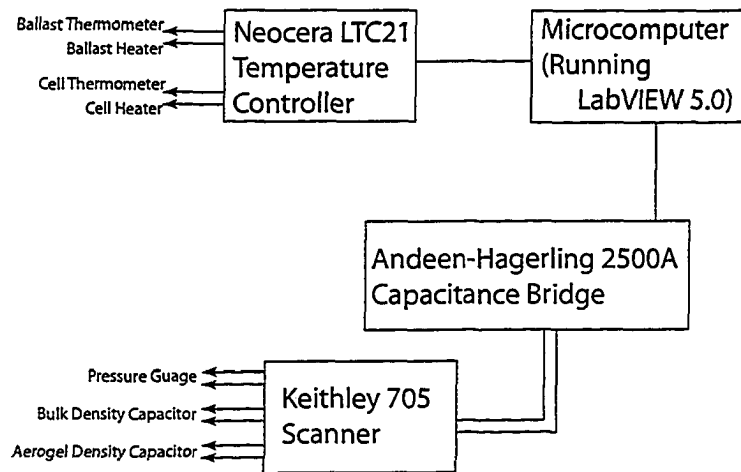
Figure 5.8: A schematic of the electronics used to measure aerogel capacitance during adsorption isotherms of helium in silica aerogel. Temperature of ballast and cell were controlled independently by a Neocera LTC21 temperature controller to about $\pm 50\mu K$. Coaxial cables ran from each of the three capacitors in the cell to a Keithley 705 Scanner, which passed on the selected signal to an Andeen-Hagerling 2500A capacitance bridge for measurement. The two temperatures and three capacitances were monitored using custom software programmed within the LabVIEW 5.0 environment. For data taken on aerogel B110 before the automated AH2500A bridge was available, capacitance was measured with a General Radio 1615-A Capacitance bridge using a 1kHz excitation frequency.
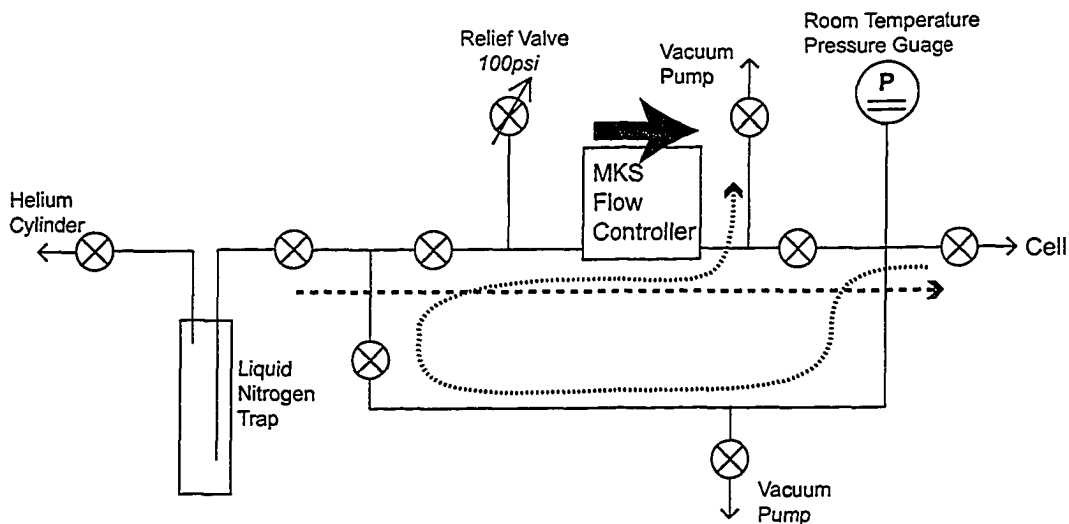
Figure 5.9: A schematic of the room temperature gas handling system used for admitting helium for the adsorption isotherms in silica aerogel. The flow controller allowed control of filling and emptying rate, with the flow path used for filling illustrated by a dashed line and the emptying path shown by the dotted line. (Note that each "$\otimes$" represents a valve.)

at a temperature above the cell temperature so that it only contained vapor and helium could be added or removed using the room temperature gas handling system as before, or it could be held at a temperature below the cell temperature so that liquid and gaseous helium coexisted within the ballast. When the ballast held co-existing liquid and vapor a small step in the ballast temperature would change the equilibrium vapor pressure of the helium in the ballast, and consequently change the pressure in the sample cell without affecting the temperature of the sample cell. Thus, small pressure steps along the adsorption isotherm could be automated and required no additional helium input from the gas handling system outside the cryostat. This technique has an advantage over adding measured doses of helium into the cell because it ensures that the temperature of the system remains very stable – when helium is added as shots there is no guarantee that the temperature throughout the sample will remain unchanged. Unfortunately, while our technique works well for isotherms which exhibit finite slopes, it only produces a few points along very flat isotherms whereas the dosing technique allows a higher density of points. For the denser samples we measured there was no problem obtaining enough points along the hysteresis loop of the isotherm, but for the less dense sample the isotherms were so flat that they would fill or empty completely over a pressure range spanned by only two or three data points.

5.2.4 Resolution

The resolution and drift of the manual capacitance bridge was the limiting factor in the first data runs, but the resolution of the AH2500A capacitance bridge is about $10^{-7}pF$, at least an order of magnitude better than the noise seen in our setup. Much more attention would need to be paid to the construction and mounting of the cell if one was to try to reduce this noise – for instance, some of the coaxial cables used to measure signals end in small lengths of unshielded wire. However, for all signals involved the inherent noise of the signal is small to insignificant when compared to the absolute uncertainty and temperature drift of the signals – for example, there is little need to increase density resolution to $0.001\frac{kg}{m^3}$ when data points are separated by density jumps of $10\frac{kg}{m^3}$ and when two data runs may return density values that differ by $1\frac{kg}{m^3}$ (as shown later in this chapter).

Pressure resolution is set by the temperature control on the ballast rather than the pressure gauge itself and is about $0.02mbar$ but with a strong temperature de-
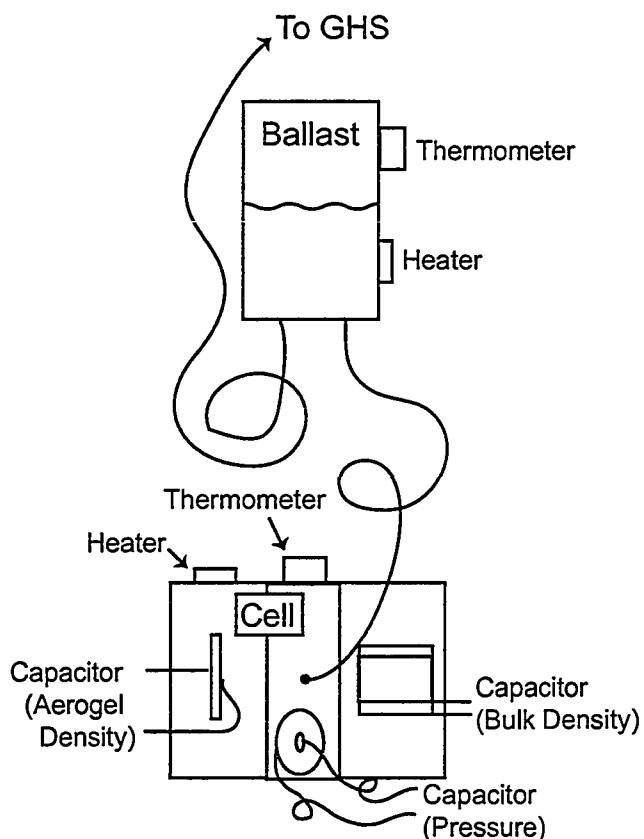
Figure 5.10: A schematic of the low temperature portion of the setup used to measure aerogel capacitance during adsorption isotherms of helium in silica aerogel. The pressure of the system was set by closing off the room temperature gas handling system and controlling the temperature of a ballast volume containing coexisting helium liquid and vapor. The ballast and cell were connected by a length of $\sim 0.015''$ CuNi capillary and their temperatures controlled independently.

pendence; the pressure gauge has a resolution of about $\pm 0.01 mbar$ but this could easily be increased by a factor of two or three with longer averaging times. The resolution of the bulk density capacitor is about $\pm 3 \cdot 10^{-3} \frac{kg}{m^3}$. The aerogel density resolution is sample dependent, but always much better than $\pm 1 \frac{kg}{m^3}$ and sometimes as good as $\pm 10^{-2} \frac{kg}{m^3}$. Both the bulk and aerogel density capacitances show greater shifts with temperature or thermal cycling than their inherent noise, and the simplistic method for extracting density from capacitance also shows errors on the order of those seen from electrical noise. Also, note that the pressure head across the sample as it was mounted was on the order of 0.05mbar; to greatly improve the resolution of this experiment the sample must be mounted horizontally, and should be much thinner (on the order of 50μm).

Temperature could be controlled in increments of 0.1mK or greater and this limitation affects our ability to control pressure, since cell pressure is equal to the saturated vapor pressure of the helium in the ballast. To improve the resolution of the adsorption isotherms, temperature control for the ballast must be drastically improved. It is the temperature controller which limits the precision of the tem-

79

perature control, but even with resolution of only 0.1mK smaller jumps should be possible by having the set point oscillate (e.g. to attain a temperature of about 5.09995K one could have the temperature set point oscillate between 5.0999K and 5.1000K). Alternatively one could control using the raw resistance measured from the thermometer. However, any increase in ballast temperature resolution must be accompanied by a comparable improvement in cell temperature control and the temperature controller environment must be carefully controlled to prevent drift.

In most data collected there are regular dips in pressure about every eighty minutes. These correspond to dips in the pressure in our helium recovery system, which result in cooling of the helium bath in our cryostat. Because our cooling power comes from exchange gas in the vacuum can, this slight cooling of the helium bath causes a ~ 0.2mK dip in ballast temperature which is then passed on to the cell as a dip in pressure. The least noisy data were collected by taking the cryostat off of helium recovery, but even then it pays to remember that by using exchange gas we are coupling out cell thermally to the outside world and this puts a limit on our stability.

5.3 Interpretation of Capacitance

Interpretation of our capacitance results requires that we assume a linear relationship between capacitance and fluid density. Since capacitance depends linearly on dielectric constant, this assumption reduces to an assumption that ϵ depends linearly on fluid density. While in uniform bulk fluids this is an excellent assumption (certainly to the level of precision used in our experiments), there may be geometric effects which add a non-linear component to the response of fluids in aerogel.

Since aerogel is a dilute impurity, it turns out that it has very little effect on the linear relationship between density and capacitance. The details of the calculations are included in Appendix C. The calculations are done for a uniform fluid in aerogel and for a phase separated fluid in aerogel. The calculations for the uniform fluid show that there is a nonlinear term proportional to $(1 - \phi) * (\epsilon_{He} - 1)$. Since we are using 95% and 98% porous gels, and the dielectric constant of helium does not get above 1.05 in our experiments, we remain in a regime where we can assume a linear dependence on density. The calculations involving phase separated liquid and vapor inside aerogel are more involved and require a few more assumptions, but in the end they show that there is likely no more than a 3% deviation from linearity in

80

the relationship between average helium density and capacitance. This is not worse than the experimental variations between runs, or errors introduced by incomplete equilibration of the system between data points.

In the capacitance modelling done in the following chapter, dielectric constants were calculated by taking a simple volume weighted average of silica dielectric constant and helium dielectric constant. In turn, the dielectric constant of helium was calculated from its density.

5.4 Computational Modelling

While our helium adsorption isotherms were relatively straightforward to interpret, there was a large jump in capacitance (after the gel appeared to be completely filled with liquid helium) as the bulk liquid level rose to cover the sample. We ascribe this jump to the capacitor fringe fields sensing the formation of bulk liquid helium in the space surrounding the aerogel sample. With a view to justifying the magnitude of this jump we undertook an extensive series of capacitance calculations. Furthermore, those calculations were used to aid in the design of the second experimental cell.

When interpreting the modelling data it is important to remember that precise measurement of the physical dimensions of the experimental samples are difficult, and absolute values from the modelling results should not be compared directly to experimental results. For this reason, when not necessary, I have not included the precise dimensions used in the calculations – it is the trends that are important. Every result involving fringe fields has been converted to a percentage of total signal so that results can be compared between models and runs without worrying about absolute magnitudes.

5.4.1 Modelling Technique

The aerogel capacitor was modelled using a variety of electrostatic modelling programs; the most complete results were obtained using the student version of the package "Maxwell© 2D" produced by Ansoft Corporation [132]. This software uses an iterative process to calculate the electric fields on a finite element mesh.

Models are constructed of a variety of materials with known conductivities and permittivities, voltage sources are specified and the fields are solved self-consistently. Once the estimated uncertainty in total system energy has reached a small enough value the calculation is halted and the system capacitance can be calculated.

81

5.4.2 Model Geometry

The modelling fell into two distinct categories: that done to check results for the aerogel slices used in the early experiments, and that done to design a new cell to reduce fringe effects. The models used in the computer program must be built on a cartesian grid; the grid I used had increments of 0.001". For instance, although the capacitor plates are effectively two dimensional, they appear in the model as slabs 0.001" thick. The models are shown in Figure 5.11. Once a model geometry was laid out the program solved for the electric fields self-consistently; it was allowed to run through sufficient iterations for the capacitance to converge to a constant value (within the resolution of the program).

Free Aerogel Slice

The first geometry modelled was that of the freely suspended aerogel slice, which was the geometry of the first experiments. The model as input into Maxwell© 2D is included as the top model in Figure 5.11. This is a cross-sectional view of the rotationally symmetric cylindrical slice. The left-hand side of the figure is treated as an axis of rotation for the computations, which allows us to model the three dimensional behavior of the capacitor using the two dimensional computational techniques of Maxwell© 2D.

The thickness of the aerogel slices used in the experiment is difficult to determine very precisely. Estimates can be made from how they were cut, and measurements using a travelling microscope can also give approximate values for the thickness. However, these values are only reliable to within a few percent. For this reason, the thickness of the simulation was sometimes adjusted arbitrarily so that the values of capacitance in the simulation more closely match those of the experiment – calculations were performed on slabs 0.020" to 0.024" thick.

Since the plates protrude from the surface of the aerogel in the first model shown in Figure 5.11, a second set of calculations was run with the plates recessed into the aerogel rather than sitting atop it (the second model shown in Figure 5.11). Within this general model, the electrode diameter was also allowed to vary to see what, if any, effect that would have on the fringing fields. If by varying the plate size, the fringe effects changed significantly then it would be possible to minimize the fringe effects by simply changing the copper deposition process rather than re-engineering the entire experimental cell. This proved not to be the case – the effect of the fringe

82

Exterior

Recessed

Cup

Exterior with
Guard Ring
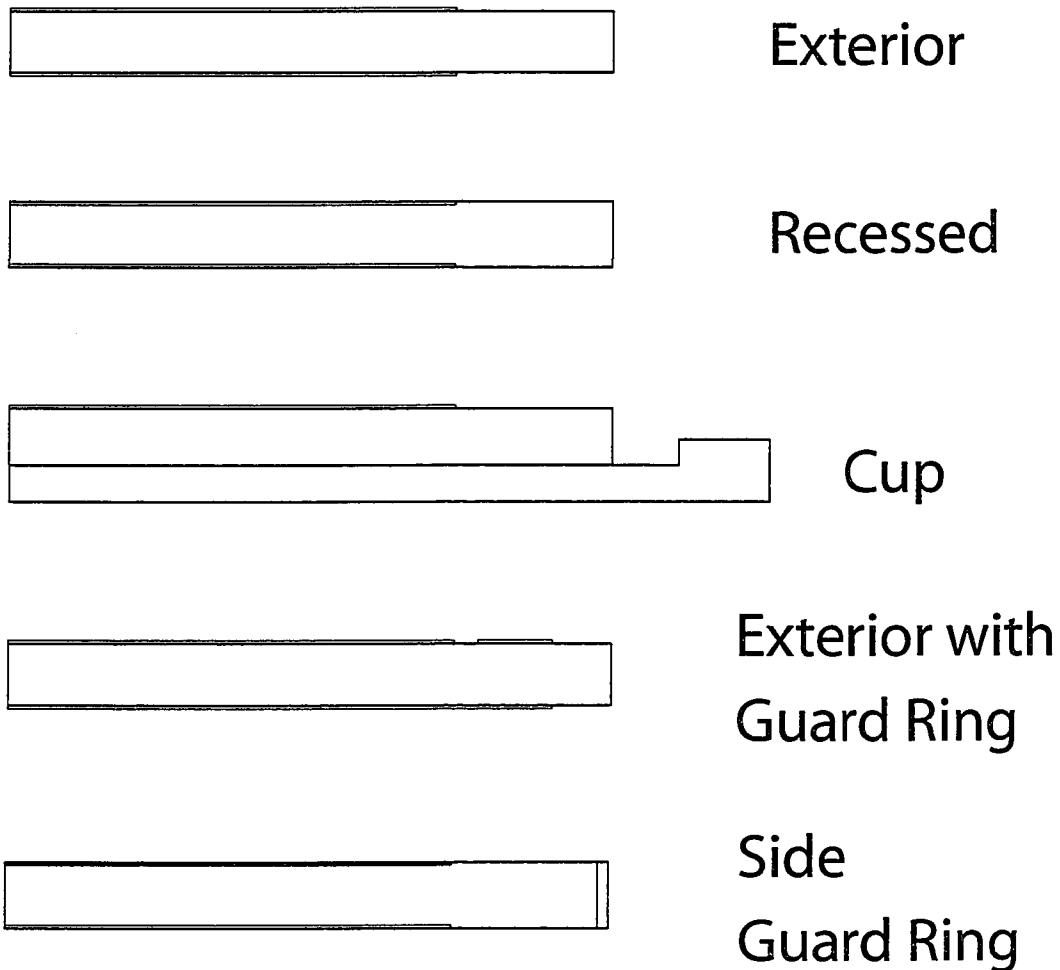
Side
Guard Ring

Figure 5.11: These are examples of some of the geometries used in capacitance calculations. All are rotationally symmetric about the left-hand side. There are four examples which assume a free floating gel slice, while one imposes a geometry that conforms closely to that actually present in the experimental cell ("Cup"). There was no easy way to model the very thin copper electrodes – the geometries "Exterior" and "Recessed" were used to gauge the seriousness of this flaw. The only difference between these geometries is whether the 0.001" electrodes are sunken into aerogel or floating on top of them.

83

fields was almost independent of the diameter of the copper electrode relative to the aerogel disc.

Aerogel in "Cup" Electrode

A second set of models was used to evaluate new geometries which would avoid fringe field effects as seen in the first set of geometries. These all used a "cup" shaped bottom electrode, not because of any inherent value of that shape as an electrode, but because it provided an easy way to anchor the aerogel slice in the experimental cell. The general geometry is shown in Figure 5.11 as "Cup". This geometry was varied to include a small or large guard ring, or no guard ring at all. The cup was used as the bottom electrode while the top electrode and the guard ring were modelled as 0.001" thick plates (the same as in the "free aerogel" model described above).

The aerogel slice modelled in these cases would be held in the cup by spring contacts to the top electrode and the guard ring. The results from the model *without* the guard ring are important because subsequent measurements were all made without guard rings. As it turns out, the experimental hassle of preparing and mounting a sample with a guard ring outweighed the advantage of the increased accuracy gained by using such a sample in the experiment. Note that while in the model calculations the cup acted as the bottom electrode, in the experiment there was still an electrode patterned directly onto the aerogel slice so that bulk fluid could not penetrate between the electrode and the sample.

5.4.3 Model Results

To evaluate the sensitivity of the capacitance technique and the effect of fringing fields, capacitances were computed for a number of states of the aerogel-helium system, which are summarized in Table 5.1. By computing the change in capacitance between these states one gains knowledge about the sensitivity of the capacitor to the density of helium within the aerogel, and its sensitivity to the helium *surrounding* the capacitor.

In order to calculate these capacitances in the model, assumptions must be made about the dielectric constant of the aerogel sample. For all these calculations the density of liquid helium within the pores of the aerogel is assumed to be the same as the density of bulk helium at that temperature, without the aerogel. There are

State	Abbreviation	Aerogel Pores	Surrounding Space
1	C_1	Vacuum	Vacuum
2	C_2	Liquid	Vacuum
3	C_3	Liquid	Vapor
4	C_4	Liquid	Liquid

Table 5.1: This table shows the states for which capacitances were calculated. The difference between states 1 and 2 indicates how sensitive the measurement is to the density of helium in the aerogel, while the difference between states 2 and 4 give a measure of how significant the effects of fringing fields are in an experiment.

no calculations involving aerogel slices filled with helium vapor (i.e. the capacitance of the sample near the low density side of the coexistence curve) because it is not at all obvious what helium density would be appropriate to use in that case.

The results that follow include raw calculations, and a series of differences; the abbreviations used in the results are contained in Table 5.1. The difference $C_i - C_1$ shows the effect of having helium present in and around the sample, and will vary between states i=2, 3, and 4. The difference $C_i - C_2$ is a measure of how large an effect the helium outside the aerogel will have on the measured capacitance and can be thought of as the "fringe" effect. To represent the importance of the fringe effect we can express it as a percentage of the capacitance difference when the gel and the surrounding space are both filled with liquid, i.e. $(C_4 - C_2)/(C_4 - C_1)$. Finally, by comparing the fringe effect present when the surroundings are filled with vapor with that present when the aerogel is surrounded by liquid helium $(C_4 - C_3)$ we can predict the apparent "jump" in density as the cell body fills with bulk liquid. This number can be directly compared with experiment.

Free Aerogel Slice

A series of calculations were performed for a slab of aerogel in space. The geometry differs from the experimental setup which had the gel suspended in a finite, grounded, copper cavity much larger than the gel; this would affect the measured capacitances systematically but should leave capacitance differences virtually unchanged. The purpose of these calculations was two-fold. First of all, these were an attempt to justify the jump in experimentally measured aerogel capacitance as the cell filled with bulk liquid. Secondly, they provided a way to relate the effects of fringe fields (presumably responsible for the jump in capacitance) to various sample parameters such as electrode size and position. The next few paragraphs describe

the more important calculations performed.

First of all we should rule out spurious effects due to the artificial sample geometry in the model; it is possible that the position of the electrode may affect the results if the field is exceptionally strong at their edges. To evaluate that possibility calculations were made for two systems – one of which had 0.001" thick electrodes atop either side of the gel sample and one of which had the same plate separation but with the plates sunk *into* the gel sample ("Exterior" and "Recessed" in Figure 5.11). Data for these two cases are shown in Table 5.2 and Table 5.3. For comparison, the capacitance calculated assuming a perfect parallel plate capacitor of the same dimensions gives C=1.129pF. Thus fringe fields contribute an extra 11% to the total capacitance calculated by the modelling program.

At this point it should be pointed out that all the data tables share the same basic format. The left-hand column may be used to describe the geometry used in the model, or left blank if the geometry remains unchanged for all the data. Next, the temperature is listed; for each given temperature a series of calculations are performed to calculate the capacitance (**C**) for each of the four states described in Table 5.1. These states represent an incremental filling of the experimental volume with fluid. From these calculations a change in capacitance due to the fluid is calculated (**C-C₁**); this also gives a measurement of how sensitive the experiment is to changes in fluid density. Next the contribution of fluid *outside* the aerogel is calculated by subtracting the contribution of the fluid inside the gel from the total capacitance (**C-C₂**). These numbers can be converted to percentages of the total capacitance change seen (**% Fringe**), so that the effects of the fringe fields can be compared between models with different geometries. Finally, the jump in capacitance seen as the cell fills with bulk liquid can be calculated (**% Jump**) for comparison to experiment.

There are two main points which should be taken from these data tables. The first is that the slight change in electrode geometry had very little effect on the results. The individual capacitances shifted only slightly due to the extra aerogel present, and the effects of the fringe fields were changed by less than 1%. The second point is that while the signal is dominated by the behavior of the fluid in the aerogel, fringe effects *do* contribute significantly to the measured capacitance.

It is also worth discussing the agreement between simulation and experiment, summarized in Table 5.4. As can be easily seen in the table, the predicted jump

Free Aerogel Slice With Exterior Electrodes						
T(K)	State	C(pF)	C-C_1(pF)	C-C_2(pF)	% Fringe	% Jump
4.4	1	1.2725				
	2	1.3159	0.0434			
	3	1.3166	0.0441	0.0007	1.5	
	4	1.3204	0.0479	0.0045	9.4	7.9
5.0	1	1.2725				
	2	1.3086	0.0361			
	3	1.3100	0.0375	0.0014	3.5	
	4	1.3124	0.0399	0.0038	9.5	6.0
5.1	1	1.2725				
	2	1.3059	0.0334			
	3	1.3076	0.0351	0.0017	4.6	
	4	1.3094	0.0369	0.0035	9.5	4.9

Table 5.2: This table gives a summary of the calculations for free aerogel with *exterior* plates as shown in Figure 5.11. The "states" referred to in the second column are defined above, in Table 5.1.

Free Aerogel Slice With Recessed Electrodes						
T(K)	State	C(pF)	C-C_1(pF)	C-C_2(pF)	% Fringe	% Jump
4.4	1	1.2746				
	2	1.3185	0.0439			
	3	1.3191	0.0445	0.0006	1.3	
	4	1.3225	0.0479	0.0040	8.4	7.1
5.0	1	1.2746				
	2	1.3111	0.0365			
	3	1.3124	0.0378	0.0013	3.3	
	4	1.3145	0.0399	0.0034	8.5	5.3
5.1	1	1.2746				
	2	1.3084	0.0338			
	3	1.3099	0.0353	0.0015	4.1	
	4	1.3116	0.0370	0.0032	8.6	4.6

Table 5.3: This table gives a summary of the calculations for free aerogel with *recessed* plates

87

Free Aerogel Slice, Experimental Data						
T(K)	State	C(pF)	C-C$_1$(pF)	C-C$_3$(pF)	% Fringe	% Jump
4.4	1	1.6602				
	3	1.7223	0.0621			
	4	1.72615	0.06595	0.00385		5.8
5.0	1	1.6602				
	3	1.7138	0.0536			
	4	1.7168	0.0566	0.0030		5.3
Free Aerogel Slice, Model Calculations						
4.4	1	1.2746				
	2	1.3185	0.0439			
	3	1.3191	0.0445		1.3	
	4	1.3225	0.0479	0.0034	8.4	7.1
5.0	1	1.2746				
	2	1.3111	0.0365			
	3	1.3124	0.0378		3.3	
	4	1.3145	0.0399	0.0021	8.5	5.3

Table 5.4: This is a table comparing experimental data to calculations for free aerogel with recessed plates. Since "State 2" (where liquid in the pores coexists with vacuum in the surrounding space) cannot physically exist, it is impossible to calculate the percentage of the signal which comes from fringe fields in the experiment, however the jump in capacitance as the cell fills with bulk liquid is still directly comparable between experiment and calculation.

(e.g. 5.3% at 5.0K) in capacitance agrees with the observed jump (5.3% at 5.0K). The degree of agreement is deceptively good at 5.0K – more than one should ask for from such a primitive model with so many assumptions used in the calculations. However, the very small temperature dependance of the jump in the experimental capacitance is somewhat disconcerting. One would expect that if this jump was due solely to fringe fields outside the aerogel then it should scale with the density difference between the two bulk phases, $\rho_{(liq)} - \rho_{(vap)}$. This difference increases by 60% from 5.0K and 4.4K, while the capacitance jump only increases from 0.0030pF to 0.00385pF. The explanation for this is probably that taking data manually made it difficult to tell exactly when the gel was full and how much bulk was in the cell. Both the 4.4K and 5.0K data agree reasonably well with calculations, and the discrepancies may be taken as an indication of the reproducibility of the data taking technique.

Finally, while still discussing the freely suspended aerogel slice, effects of changing the patterned electrodes were explored. Two approaches were taken to try to

Free Aerogel Slice With Exterior Electrodes							
Geometry	T(K)	State	C(pF)	C-C$_1$(pF)	C-C$_2$(pF)	% Fringe	% Jump
Large Exterior Electrodes	4.4	1	1.9319				
		2	1.9981	0.0662			
		3	1.9991	0.0672	0.0010	1.4	
		4	2.0043	0.0724	0.0062	8.6	7.2
	5.0	1	1.9319				
		2	1.9870	0.0551			
		3	1.9889	0.0570	0.0019	3.2	
		4	1.9921	0.0602	0.0051	8.5	5.3
Top Guard Ring	4.4	1	0.70911				
		2	0.73406	0.0250			
		3	0.73422	0.0251	0.0016	0.6	
		4	0.73503	0.0259	0.0097	3.9	3.2
	5.0	1	0.70911				
		2	0.72987	0.0208			
		3	0.73018	0.0211	0.0031	1.5	
		4	0.73068	0.0216	0.0081	3.9	2.4
Side Guard Ring	4.4	1	1.1585				
		2	1.1996	0.0411			
		3	1.1997	0.0412	0.0001	0.2	
		4	1.2006	0.0421	0.0010	2.4	2.2
	5.0	1	1.1585				
		2	1.1927	0.0342			
		3	1.1930	0.0345	0.0003	0.9	
		4	1.1935	0.0350	0.0008	2.3	1.5

Table 5.5: These calculations show examples of possible geometries to reduce the effect of fringe fields on aerogel capacitance. The geometries are explained in the text – the "top guard ring" geometry is what was settled on as the most easily realized measure to reduce fringe effects.

89

reduce the effects of fringe fields. The first was to expand the size of the electrodes and the second was to add a grounded guard ring; the results are shown in Table 5.5. As the diameter of the electrodes increases the capacitor should become more similar to the infinite parallel plate capacitor (where fringe fields have a negligible effect). Unfortunately, the size of the electrodes can not be increased significantly because of the finite sample diameter, but calculations were made for the largest electrodes that could be sensibly patterned onto the aerogel (0.440" diameter instead of the 0.375" diameter electrodes used in the experiment). The calculations show only a slight change in the fringe effects. The second approach to reducing the effects of fringe fields (adding a guard ring near one of the electrodes on the aerogel) was more successful. In one arrangement there was a single large electrode on the bottom of the gel, and a smaller top electrode surrounded by a guard ring. In another arrangement a grounded ring was added all around the outside of the gel, simulating a grounded conductive coating around the curved outside of the aerogel disc. While this model produced promising results, it would be experimentally difficult to realize.

Aerogel in "Cup" Electrode

Moving to an arrangement where the aerogel is supported in a cup which acts as the bottom electrode has a few experimental advantages. It provides even support for very fragile samples (such as the higher porosity aerogels), it allows for very gentle handling while mounting the sample (compared to the spring clamps used to hold the freely suspended aerogel slices), and it holds the sample in place while multiple connections can be made to electrodes patterned on the top of the sample. The aerogel sample itself must still have an electrode patterned on the bottom since any surface unevenness could lead to significant bulk fluid existing between the cup and the bottom of the aerogel sample. However, with the bottom electrode patterned directly onto the aerogel slice, the cup merely acts as a large electrical contact for that electrode.

The top of the aerogel slice may be patterned in a variety of ways. The calculations included here show the effect of patterning a simple circular electrode as used in the previous experiments, or a smaller circular electrode surrounded by a concentric guard ring, grounded to the cell body. The relative sizes of the electrode and guard ring were varied and a check for the effect of the gap between the electrode

90

Geometry	Electrode Radius	Gap	Guard Ring Width
No Guard Ring	0.177"	N/A	N/A
Narrow Guard Ring	0.145"	0.005"	0.080"
Larger Gap	0.140"	0.015"	0.075"
Wide Guard Ring	0.050"	0.005"	0.165"

Table 5.6: Geometries used in the calculations for aerogel samples in a copper cup electrode. The results of the calculations are summarized in Table 5.7.

and the guard ring was performed. The geometries are defined in Table 5.6 and the capacitance results are summarized in Table 5.7. They show that the use of the cup shaped electrode leads to larger fringe effects; however, the addition of a guard ring does greatly reduce those effects.

The relative sizes of the top electrode and guard ring proved not to be terribly important, so the larger electrode is preferable (because of its higher sensitivity). The widening of the gap between electrode and guard ring does lead to larger fringe fields – the last section of the table shows the effect on widening the gap between the electrode and a small guard ring from 0.005" to 0.015". While the fringe fields are not much worse with a larger gap, when patterning the electrode it is worth every effort to minimize the gap

Despite all these careful computations, by the time we were ready to prepare samples for the new cell it was generally agreed that the discontinuous jump in pore liquid density at P_{SVP} published earlier was spurious. Thus we did not feel the need to reduce the magnitude of the fringe fields and have been satisfied using samples without guard rings – the fringe effects have been manually subtracted. The simpler geometry of the samples without guard rings makes it easier to mount the gels and presents fewer opportunities for things to go wrong. At some point in the future, if measurements with smaller fringe effects are necessary they will be easy to perform in the cell we have built.

5.5 Bulk Helium Measurements

Since we collected data on the helium density in the bulk volume of our cell while measuring the density of helium in our aerogel samples, we can use the bulk data to illustrate how data in general was collected as well as to get a feeling for the accuracy and precision of the techniques. From our simultaneous measurements of pressure,

Aerogel Slice in Copper Cup Electrode							
Geometry	T(K)	State	C(pF)	C-C_1(pF)	C-C_2(pF)	% Fringe	% Jump
No Guard Ring	4.4	1	1.4797				
		2	1.5262	0.0465			
		3	1.5278	0.0481	0.0016	2.8	
		4	1.5362	0.0565	0.0100	17.7	14.9
	5.0	1	1.4797				
		2	1.5184	0.0387			
		3	1.5215	0.0418	0.0031	6.6	
		4	1.5267	0.0470	0.0083	17.7	11.1
	5.1	1	1.4797				
		2	1.5155	0.0358			
		3	1.5193	0.0396	0.0038	8.7	
		4	1.5232	0.0435	0.0077	17.7	9.0
Narrow Guard Ring	4.4	1	0.97585				
		2	1.0096	0.03375			
		3	1.0100	0.03415	0.0004	1.1	
		4	1.0118	0.03595	0.0022	6.1	5.0
	5.0	1	0.97585				
		2	1.0040	0.02815			
		3	1.0046	0.02875	0.0006	2.0	
		4	1.0058	0.02995	0.0018	6.0	4.0
	5.1	1	0.97585				
		2	1.0019	0.02605			
		3	1.0027	0.02685	0.0008	2.9	
		4	1.0036	0.02775	0.0017	6.1	3.2
Larger Gap	4.4	1	0.96091				
		2	0.99399	0.03308			
		3	0.99438	0.03447	0.00039	1.1	
		4	0.99636	0.03545	0.00237	6.7	5.6
Wide Guard Ring	4.4	1	0.10259				
		2	0.10614	0.00355			
		3	0.10618	0.00359	0.00004	1.1	
		4	0.10638	0.00379	0.00024	6.3	5.3

Table 5.7: This table shows calculations for aerogel samples in the copper cup. It includes calculations for the geometries described in Table 5.6.
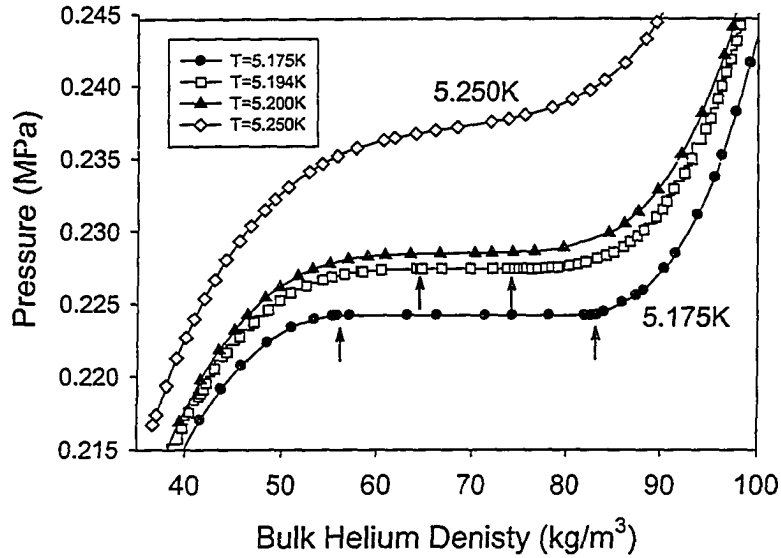
Figure 5.12: These are four isotherms for bulk helium taken just below and just above the critical temperature of 5.1952K. Below T_c there exists a region of two-phase coexistence where the isotherm is completely flat. This region is indicated by the arrows along the isotherms at 5.175K and 5.194K. Above T_c this flat region is replaced by an inflection point.

density and temperature we can map out the bulk helium coexistence curve and also measure the compressibility. Both the width of the coexistence curve and the isothermal compressibility exhibit power law behavior near the critical point, so our data can be used to extract critical exponents.

Data on capillary condensation of helium in aerogel were taken along isotherms, so it is illustrative to begin with examples of bulk isotherms taken just below and just above the critical point (which was empirically determined to be 5.1952K on our thermometer calibration). Four isotherms are shown in Figure 5.12, two below T_c and two above it. For the lower isotherms there are three distinct regions as the cell fills with helium: at low density we have a vapor phase whose density increases with pressure, then we have a coexistence region where liquid begins to condense and the average density increases with no change in pressure, finally, at high density, the cell is completely filled with liquid whose density increases with pressure once again. The width of the two-phase coexistence region shrinks as the critical temperature is approached; above T_c there is no coexistence and isotherms are single smooth curves with an inflection point near the critical density.

93
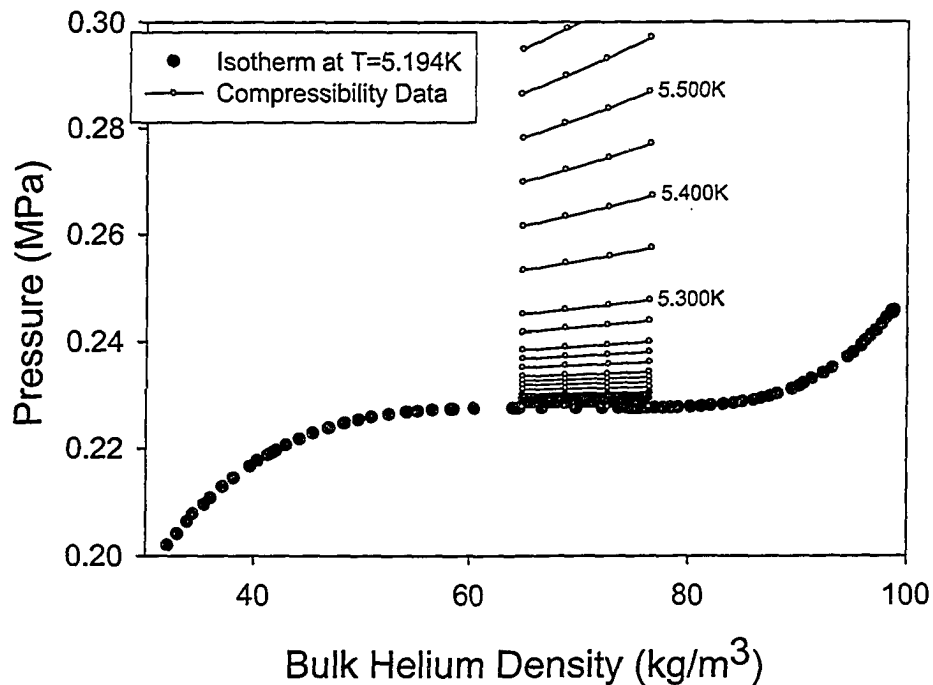
Figure 5.13: Pressure-density data just above T_c can be used to calculate compressibility as a function of temperature. The data shown here were used to calculate compressibilities for temperatures from 5.195K to 5.700K.

The slope of the isotherm is a measure of isothermal compressibility, and a series of isotherms can be used to explore the temperature dependence of compressibility. Data taken over the range from T_c to 5.700K are shown in Figure 5.13; compressibilities extracted from these data are plotted in Figure 5.14. The compressibility data closely follow a power law in temperature with an exponent of $\gamma_{exp} = 1.26$, close to the Ising model value of $\gamma_{Ising} = 1.24$.

Our direct measure of the helium density allows a very precise mapping of the coexistence curve. Rather than taking a series of isotherms and using the onset of the zero slope region to determine vapor and liquid densities, it is easier to fill the cell completely with vapor or liquid and take a series of measurements as temperature is changed. As long as there is a small amount of the coexisting phase we are guaranteed to be measuring density at saturated vapor pressure. The densities were calculated from measured capacitances using a conversion given in the next section. The final coexistence curve is shown in Figure 5.15; notice that the data spans three orders of magnitude in reduced temperature. The shape of the coexistence curve
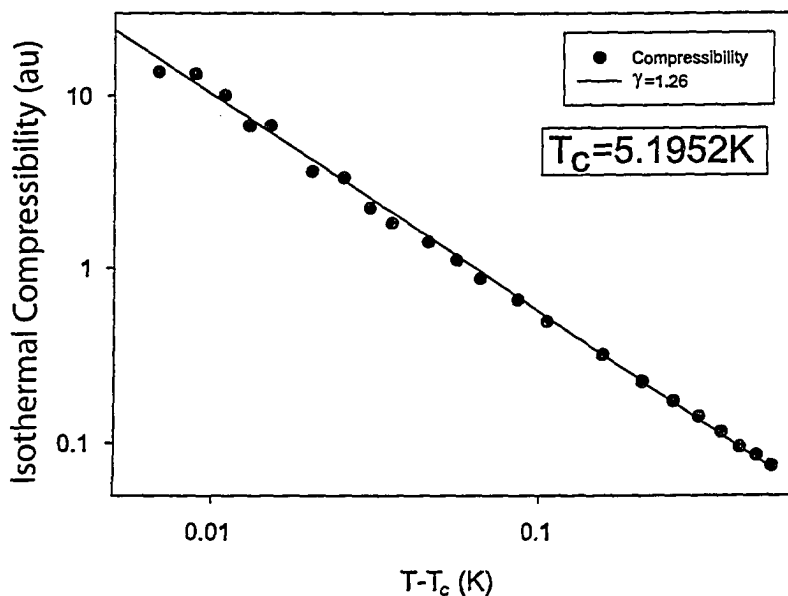
Figure 5.14: Compressibilities calculated from Figure 5.13 can be used to extract γ, the critical exponent for compressibility. The straight line shows that our data are consistent with an exponent of $\gamma_{exp} = 1.26$, very close to the accepted value for the Ising model of $\gamma_{Ising} = 1.24$; this degree of agreement is surprisingly good considering how far from T_c many of the data were collected.

near the critical point can be described, as mentioned in previous chapters, by the exponent β where $\rho_l - \rho_v \propto \epsilon^\beta$. Hence β can be extracted from the log-log plot shown in Figure 5.16. The data support a value of $\beta \approx 0.35$ which is reasonable since data taken further than a few millikelvin from T_c tend to drive the value above that expected from pure Ising behavior; these data are very similar to the data on bulk neon that follows in chapter 6.

Finally, it is instructive to show one more plot, taken from the compressibility data already shown in Figure 5.13. By plotting the slope of the isotherm against temperature it is possible to get an (imprecise) estimate of T_c. While this particular plot is not of much use in analyzing bulk data, it is the analog of a plot shown later for helium in aerogel. There is the possibility of identifying a pore critical point which is independent of the disappearance of hysteresis but shows up as a kink in a plot of the slope of the adsorption isotherms versus temperature[42]. In the case of bulk helium this kink appears as a distinct transition from a zero slope below T_c to a finite slope above T_c. This technique is only capable of providing a rough estimate – from the plot shown in Figure 5.17 we would estimate the T_c of bulk helium to be about $5.20K$ – 5mK too high.

95
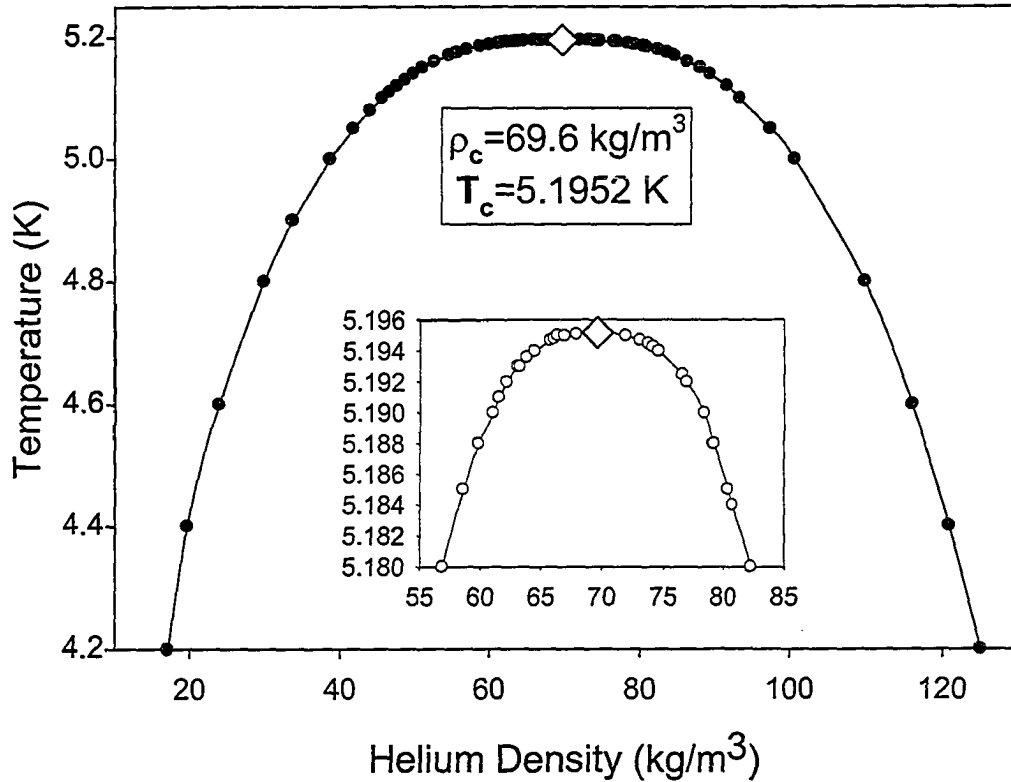
Figure 5.15: This is the experimentally determined bulk helium coexistence curve. The critical point is indicated by the diamond at $\rho_c = 69.6\frac{kg}{m^3}$ and $T_c = 5.1952\text{K}$, determined empirically. The inset is a magnified view of data near T_c.
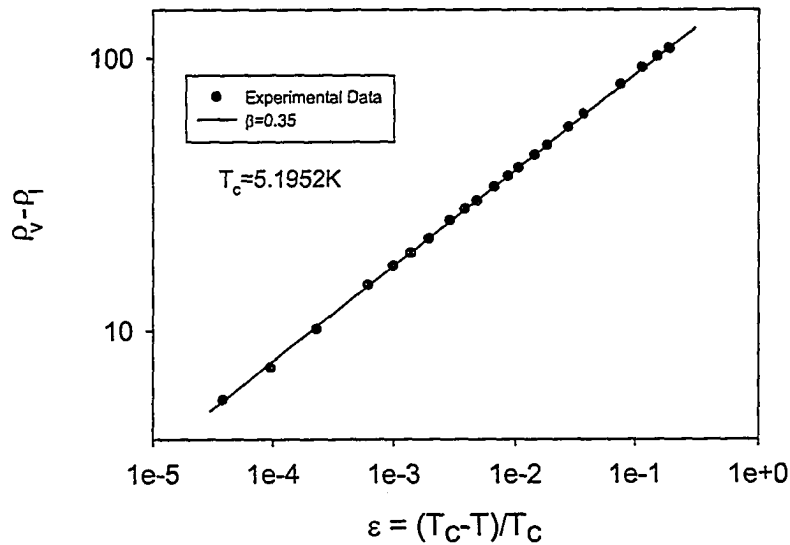
Figure 5.16: Plotting the density difference between coexisting fluid phases allows us to extract the critical exponent β and determine T_c. Note that $\beta_{eff} = 0.35$, higher than its true asymptotic value because our data include relatively large values of ϵ.

96
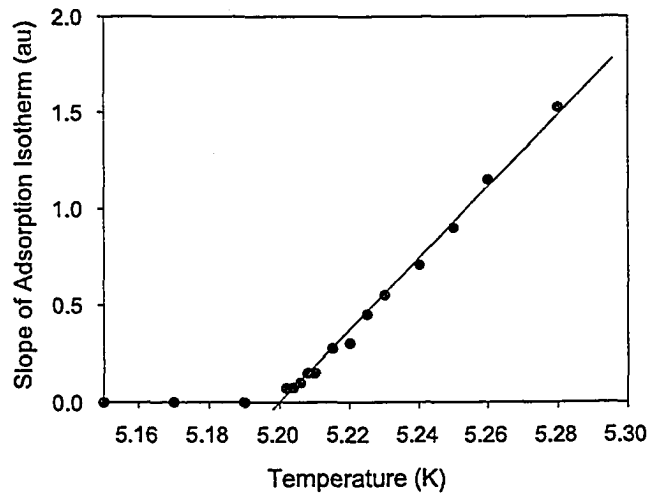
Figure 5.17: The slope of adsorption isotherms at the critical density decreases as the temperature approaches T_c and is identically *zero* for $T < T_c$, as described in Figure 5.12. A similar plot for isotherms in a porous medium would not show a decrease to zero at T_c(pore) but might show a kink similar to, but less dramatic than, that shown here for bulk helium.

97

5.6 Helium in Aerogel B110

The first data we collected on capillary condensation in silica aerogel were on a sample with a density of $110\frac{kg}{m^3}$ (sample "B110"). This sample had a porosity of about $\phi \approx 0.95$ and was identical to the samples used in the first two resonator experiments described in the next chapter. As well, this was close to the porosity used by Wong and Chan in their work on the liquid-vapor critical point in aerogel[10]. The data for sample B110 was taken in the first cell described in this chapter (Figure 5.5), with the slice of aerogel held by two beryllium-copper spring arms. Most of the data were collected manually, with only two capacitors measured simultaneously (i.e. [C_p and C_{gel}] or [C_p and C_{bulk}] but not all three at once) and with lower resolution than provided by the AH2500 capacitance bridge (only five significant figures).

5.6.1 Density Calibrations

Bulk Helium Density

The bulk capacitor was calibrated by using literature values[133] for the density of helium at 4.4K, and adding a small term to compensate for the background temperature variance of the capacitor. The values for density at 4.400K were used to fit the density to an expression of the form: $\rho = A(C - C_0^{eff})$. The capacitance of the bulk capacitor has a slight temperature dependence, with or without fluid. Therefore, an empirical temperature correction of the form $D(T - 4.500K)$ was added later to minimize deviations from literature values at higher temperatures. The resulting expression for bulk density in terms of capacitance was:

$$\rho_{bulk} = 962.6(C_{bulk} - 4.0335pF) + 0.97(T - 4.500K) \tag{5.1}$$

A comparison between densities calculated from experimental data and some literature values extracted from the NIST Chemistry WebBook[133] is shown in Figure 5.18.

Helium Density in Aerogel

The density of helium in the aerogel sample is computed as described in Section 5.3. An isotherm taken at low temperature (4.400K) is shown in Figure 5.19. The capacitance of the aerogel was measured when empty, when full with liquid but surrounded by bulk vapor (point A in Figure 5.19), and when full with liquid and surrounded by bulk liquid (point B in Figure 5.19). There are three contributions to the measured

98
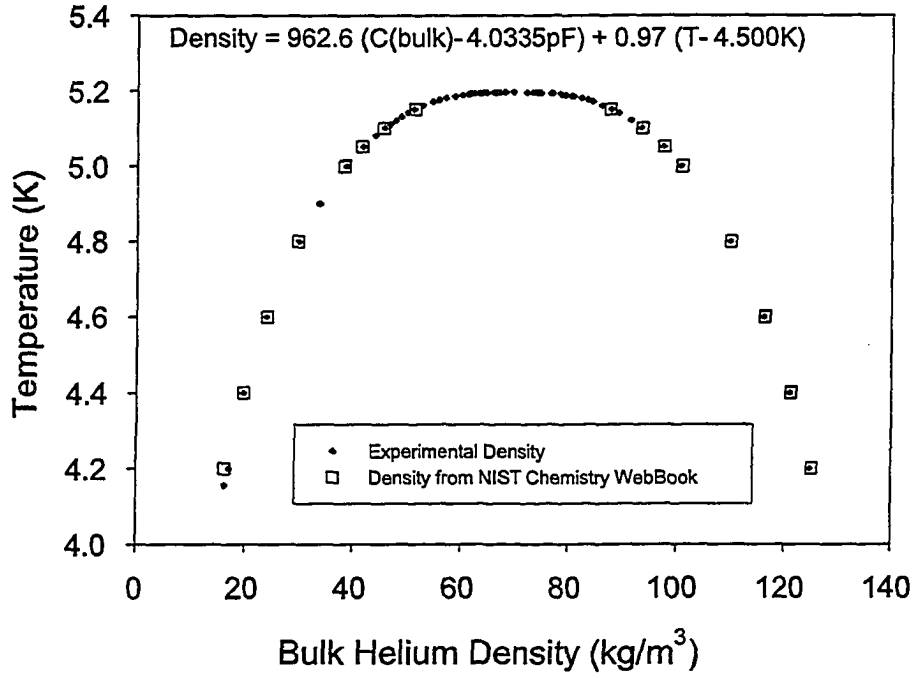
Figure 5.18: The bulk helium coexistence curve determined from experimental points using Equation 5.1 compared with literature values from NIST[133].

capacitance: the geometric capacitance (in vacuum), the capacitance added by the density of helium in the aerogel, and the capacitance added by the bulk helium density in the fringe fields:

$$C_{total} = C_0 + C_{gel}^{He} + C_{bulk}^{He}$$

Using the three points in Figure 5.19 (C_0, C_A, C_B), and assuming that helium density at 4.400K in aerogel is identical to bulk helium density at 4.400K, it is possible to fit the density of the helium to an expression of the form:

$$\rho_{gel}^{He} = D \left(C_{gel} - C_{gel}(0) - \frac{\rho_{bulk}}{E} \right)$$

where "D" represents the sensitivity of the capacitor to the density of helium in the aerogel and "E" represents the effects of the fringe fields (i.e. the influence of the environment surrounding the gel, which must be subtracted from the signal to extract the actual density within the gel). For this sample we find

$$\rho_{gel}^{He} = 1972.7 \left(C_{gel} - 1.6602pF - \frac{\rho_{bulk}}{26234} \right) \qquad (June\ 2002) \qquad (5.2)$$

99

for the initial data run (which included almost all the data described in this section) and

$$\rho_{gel}^{He} = 1980 \left(C_{gel} - 1.65933pF - \frac{\rho_{bulk}}{25900} \right) \quad (February \ 2003) \quad (5.3)$$

for a second data run, which included the isotherm shown in Figure 5.19, as well as isotherms at 5.100K (to show equilibration times) and at temperatures above the disappearance of hysteresis. This second run used the newly arrived AH2500 capacitance bridge. When bulk capacitance and aerogel capacitance were measured simultaneously it is easy to subtract the fringe effects, however when bulk data were not available an approximate bulk density was used: for $T < T_c$ the density for helium vapor at SVP was used, for $T > T_c$ it was assumed that $\rho_{gel} \approx \rho_{bulk}$ which causes Eq. 5.2 to reduce to:

$$\rho_{gel}^{He} = 1834.7 \left(C_{gel} - 1.6602pF \right) \quad (June \ 2002, \ T > T_c)$$

5.6.2 Thermal Equilibration

As mentioned numerous times in earlier chapters, and also earlier in this very chapter, aerogels are truly phenomenal thermal insulators. In their role as experimental samples that means that waiting for thermal equilibration could try the patience of a saint, and not too many of us physicists would qualify as saints. By moving to samples which are only a few hundred micrometers thick we greatly increased the speed of thermal equilibration, but even so there was a very large rate dependence in our adsorption isotherms. To give an impression of how slowly the samples equilibrated Figure 5.20 and Figure 5.21 show the response of sample B110 to a change of 1mK in ballast temperature. As described earlier, and shown schematically in Figure 5.10, our system is designed so that a small step in ballast temperature results in a small step in the vapor pressure in the ballast and cell. The data in Figures 5.20 and 5.21 show that while the step in ballast temperature is effectively instantaneous and the cell pressure and bulk helium respond completely within a few minutes, the density of helium in the aerogel sample takes hours to equilibrate. This is probably due to slow thermal equilibrium within the aerogel, although it may be related to slow mass distribution within the helium film adsorbed on the aerogel strands.

100
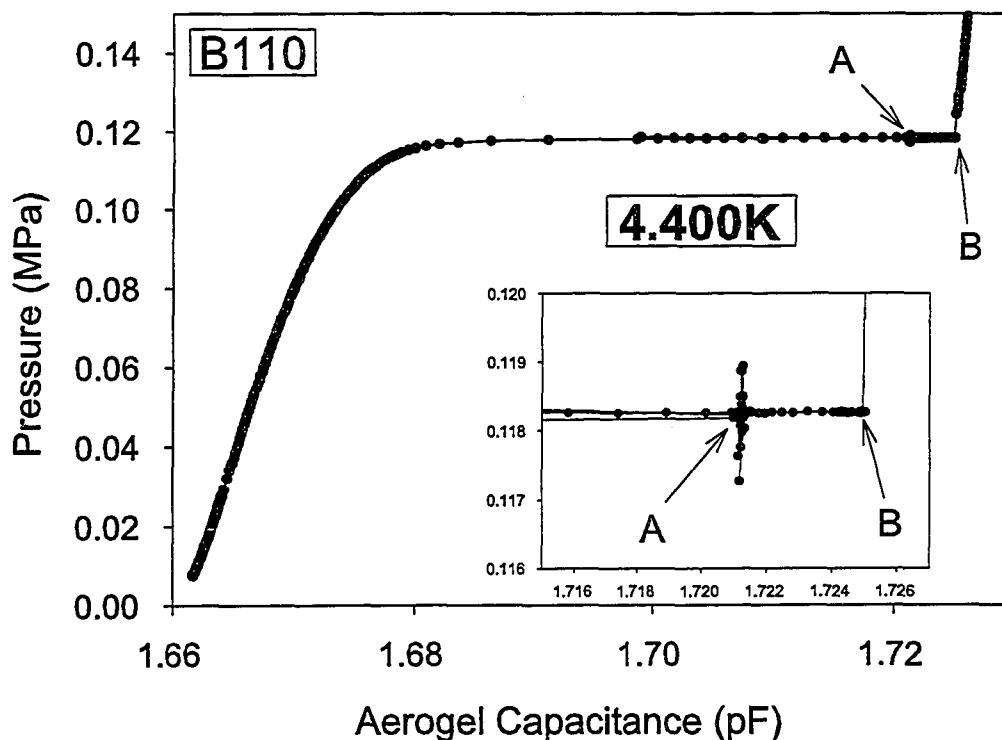
Figure 5.19: An adsorption isotherm for filling sample B110 with helium at 4.400K. Point "A" corresponds to the aerogel being full of liquid coexisting with bulk vapor outside the gel. Point "B" corresponds to a full gel surrounded by bulk liquid helium. The spike of noise in pressure at point A is probably due to momentary temperature control problems in the cell as bulk liquid begins to condense, suddenly starting to dump significant latent heat into the cell. As the bulk liquid meniscus moves up over the aerogel sample (i.e. between points "A" and "B") C_{gel} increases due to fringe fields in the bulk helium, not due to any change in the helium density within the sample. By quantifying these fringe effects it is possible to subtract them from all the capacitance data and compare data from different isotherms without worrying about spurious shifts in apparent helium density. These data were collected using the AH2500 bridge rather than the manual General Radio bridge.

101
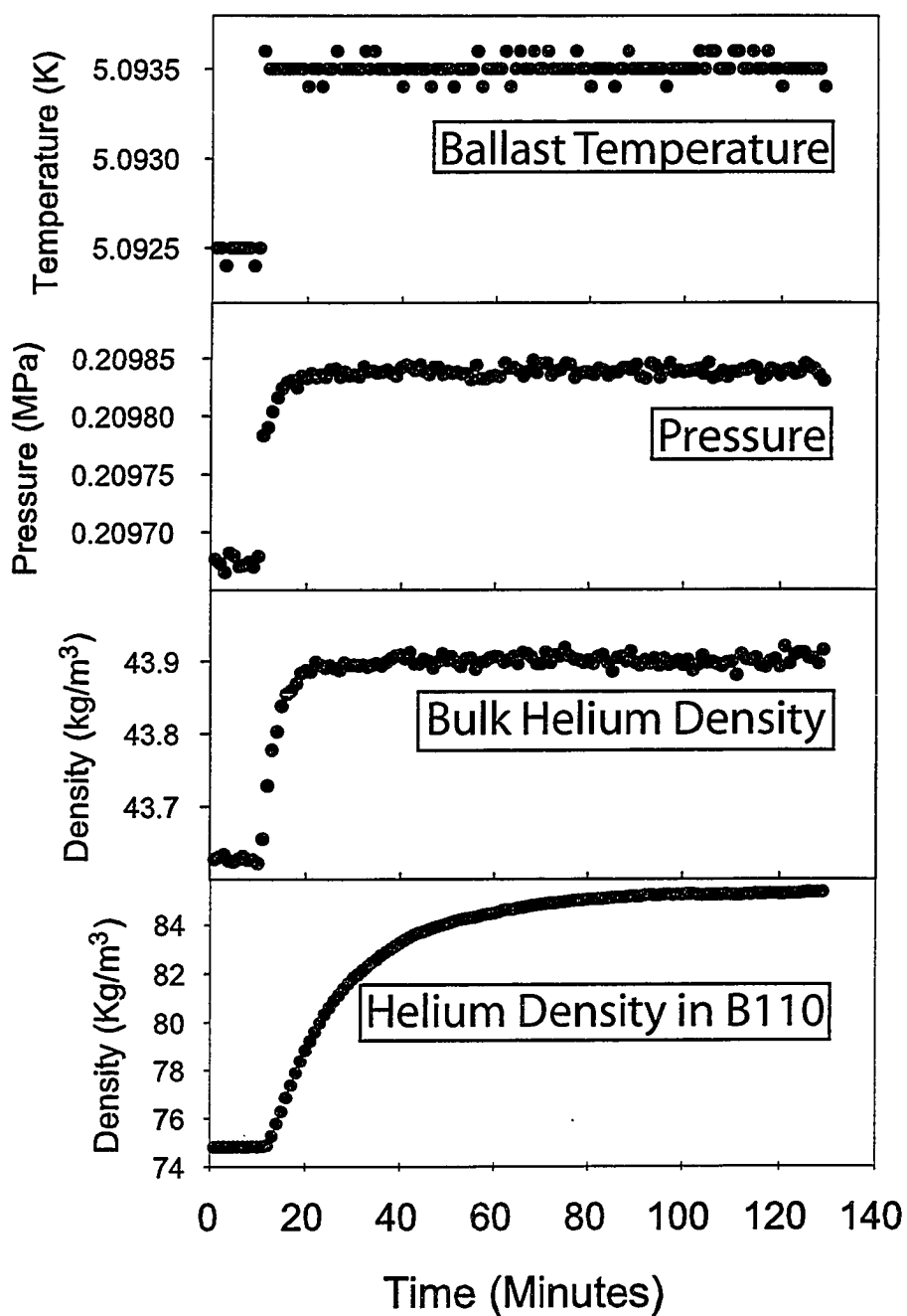
Figure 5.20: Equilibration during cell filling at 5.100K. Notice that while the ballast temperature equilibrates at a new value within a minute, and the cell pressure and the density of the bulk helium in the cell equilibrate within a few minutes, the aerogel sample takes two *hours* to settle on its final value.

102
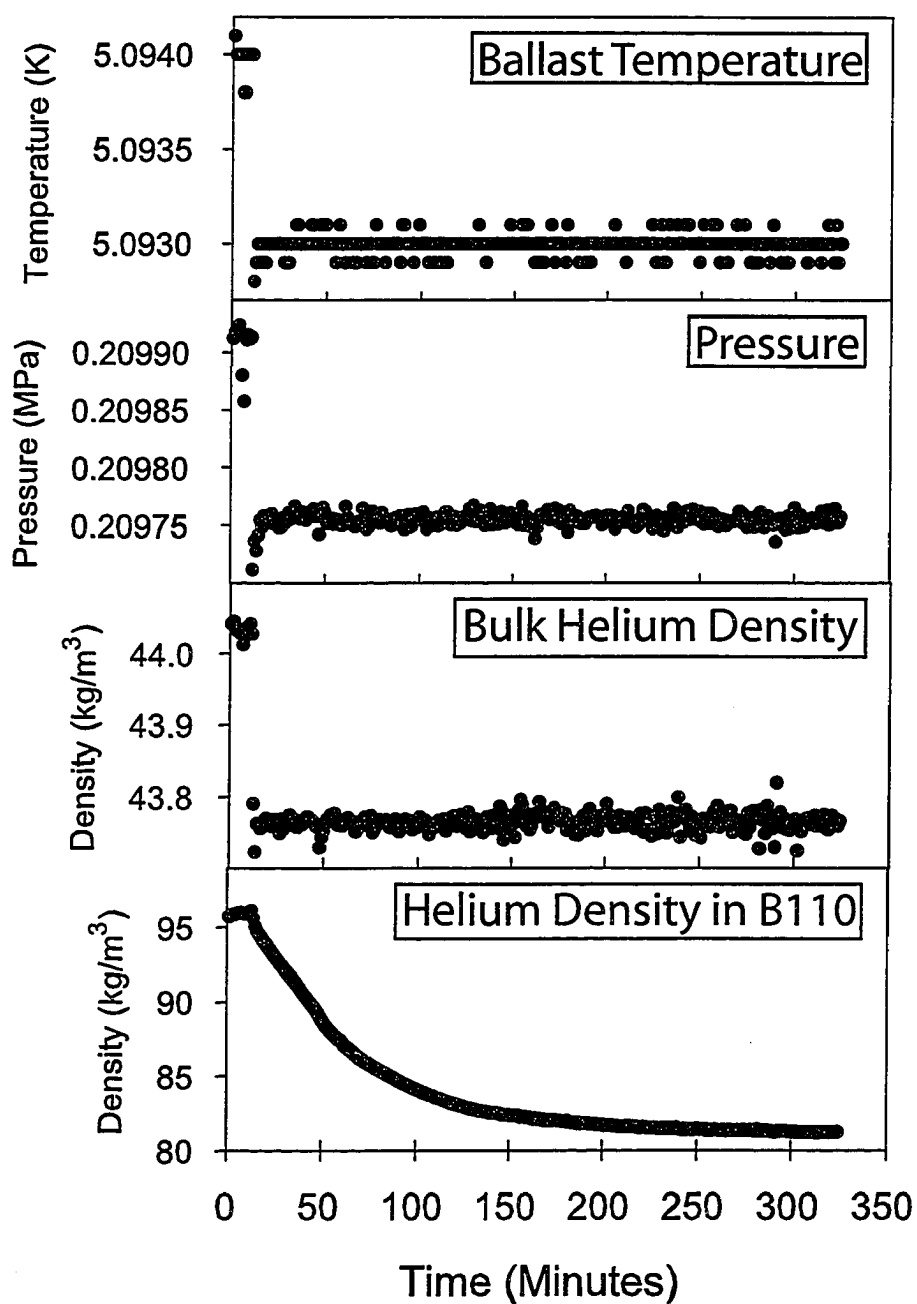
Figure 5.21: Equilibration during cell emptying at 5.100K; this is identical to the previous figure, but corresponding to a 1mK step down in ballast temperature rather than a step up in ballast temperature. Under these circumstances the change in density is almost twice as large as that in Figure 5.20 and it takes about *five hours* for the value of C_{gel} to settle.

103

5.6.3 Rate Dependence of Hysteresis

As one would expect, given the data on equilibration times shown in Figures 5.20 and 5.21, adsorption isotherms exhibited a significant dependence on filling rates. Even at the slowest filling rates, continuous flow adsorption isotherms did not allow for thermal equilibration at low cell temperatures; equilibrated points along these isotherms were taken by admitting a set amount of helium, then stopping the flow controller and waiting for equilibrium. Later data sets (for the other samples) were collected by controlling the ballast temperature below the cell temperature, but that technique had not been perfected while collecting this data. The effects of filling rate are illustrated in Figures 5.22 and 5.23 for isotherms taken at 4.880K and 5.140K respectively. The flow rates are given in "sccm" or "standard cubic centimeters per minute," a measure of mass flow rate used by the flow controller. However, the controller is *not* calibrated for helium, nor is it designed for flow below 2sccm, so the flow rates indicated in the figures should only be used as relative indicators of flow rate.

The effect of filling rate is greater for the lower temperature isotherms, possibly because of a greater degree of latent heat deposited into the sample, or possibly because of how the helium is distributed within the gel at different temperatures. Above bulk T_c equilibration is faster and there is no problem with using continuous flow measurements (which is fortunate since controlling the temperature of the ballast only works below T_c where there is a well defined P_{SVP}).

5.6.4 Adsorption Isotherms for B110

We have well resolved adsorption isotherms for helium in sample B110 for temperatures from 4.88K to above 5.2K. At low temperatures these isotherms show a large hysteresis loop, which gradually shrinks as the temperature is raised, until (at about 5.155K) it finally disappears. The hysteresis loops cover a large density range – much wider than the coexistence curve mapped out by Wong and Chan[10] – but are narrower than the bulk helium coexistence curve. The loops all exhibit a finite slope; there are no adsorption isotherms that exhibit the flat coexistence regions seen in bulk helium.

Adsorption isotherms at fairly low temperature (Figure 5.24) have a somewhat rectangular shape, with a very sharp and distinct high density kink. However, the lower density closure of the loop is much less distinct and occurs in a gradual curve of
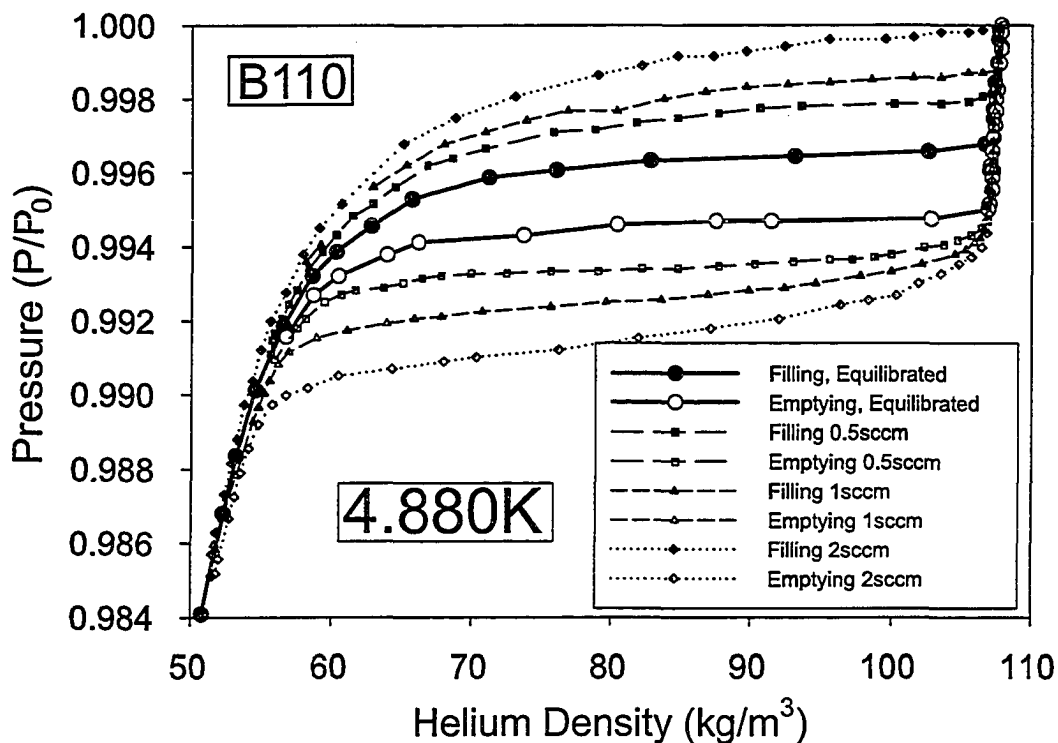
Figure 5.22: Isotherms for helium adsorption in aerogel B110 at 4.880K showing three continuous filling rates and also equilibrated points. The size of the hysteresis loop decreases as the rate of filling is slowed. Filling at "0.5sccm" corresponds to about two hours for each branch of the hysteresis loop (i.e. filling and emptying) while the limiting hysteresis loop corresponds to a full day to fill and another full day to empty.

the isotherm that makes it difficult to equate any particular point with a transition from a pore-vapor phase to a two-phase coexistence region.

As the temperature is raised, the hysteresis loop gradually shrinks. The high density end of the loop remains well defined, especially along the desorption branch, but the hysteresis loop becomes less and less distinct at the low density end. The loop transforms from a roughly rectangular shape to a squashed triangle with one drawn-out corner (Figure 5.25). Finally, at higher temperatures the hysteresis loop completely disappears (Figure 5.26). While the hysteresis loop is still distinct at 5.150K, by 5.155K the loop is too small to resolve. By 5.165K there is no hint of hysteresis.

As the temperature is raised further, the shape of the isotherm begins to change; at $T \gtrsim 5.150K$ the adsorption isotherms still show a fairly distinct corner at a density above ρ_c. Figure 5.27 shows some isotherms for $5.150K < T < T_c$; at about

105
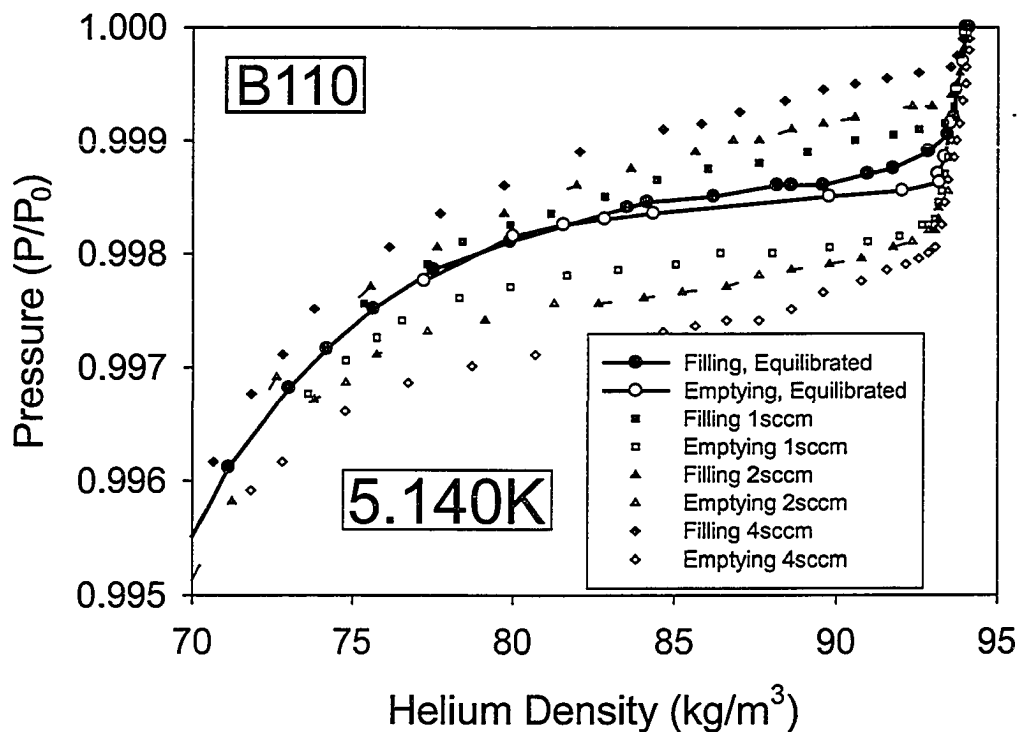
Figure 5.23: Isotherms for helium adsorption in aerogel B110 at 5.140K showing three continuous filling rates and also equilibrated points. Equilibration is faster than at 4.880K (probably due to less latent heat), but the slowest continuous fill rates are still too fast to allow for thermal equilibration within the sample.

5.180K the fairly distinct corner is replaced by a much more gradual curve. This transformation is highlighted by an enlargement of that area of the isotherm in Figure 5.28, with more isotherms included.

So far we have concentrated on the shape of the hysteresis loops and the disappearance of those loops as the temperature is raised above 5.150K. However, as mentioned in Chapter 2, the disappearance of a hysteresis loop need not imply the disappearance of distinct pore liquid and pore vapor phases. Perhaps the disappearance of the sharp corner in the high density region of the adsorption isotherm may be an indication of the disappearance of a distinct "pore liquid" phase at some temperature above the disappearance of hysteresis but below the bulk critical temperature. The slope of the adsorption isotherms also contains information about the phase(s) present in the aerogel sample, although exactly what sort of information is not entirely clear. However, one would expect different behavior from aerogel

106
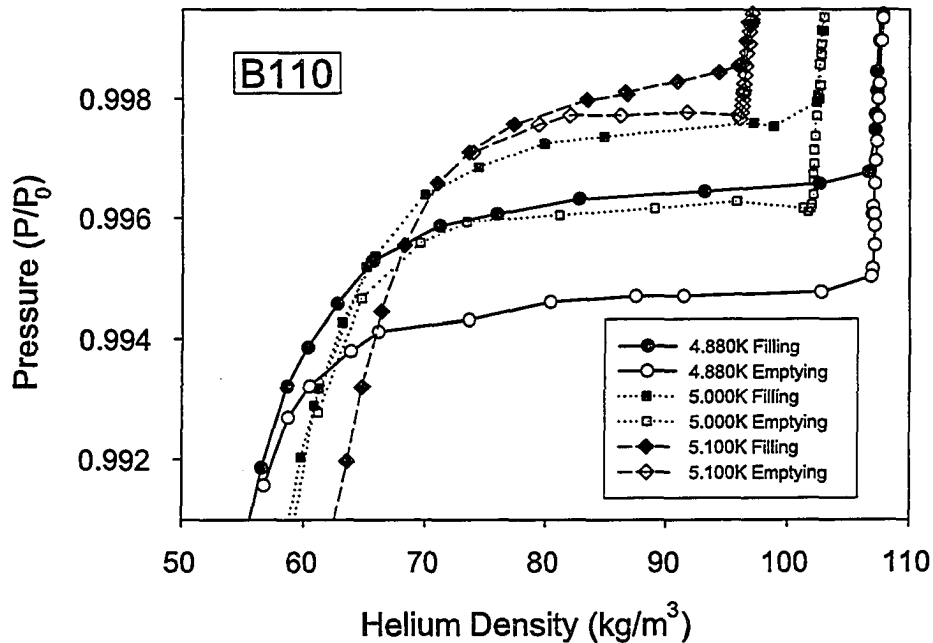
Figure 5.24: Three adsorption isotherm for helium in sample B110. These three isotherms correspond to the lowest temperatures for which we have equilibrium data. Notice that although the high density side of the hysteresis loop is distinct, the low density side is curved and closes gradually. Also, all these isotherms exhibit finite slopes over the width of the hysteresis loop rather than the flat regions one would expect from true liquid-vapor coexistence.

filled with two coexisting phases and aerogel filled with a single fluid phase. In a two phase system the isotherm slope should be shallower since a small change in pressure can cause a large shift in density by favoring one phase over another; any density shift in a single phase system must come from the compressibility of that phase. We have isotherms collected over a large range of temperatures both below and above bulk T_c, a few are shown in Figure 5.29 and those close to T_c are shown in Figure 5.30.

By picking a single density and measuring the slope of these isotherms at that density we can plot the isotherm slope as a function of temperature. The isotherm slopes calculated at $\rho = 84 \frac{kg}{m^3}$ are shown in Figure 5.31; that density was chosen because it intersects all the hysteresis loops at lower temperatures and the inflection point of the higher temperature isotherms. The figure includes two different temperature scales, with straight lines as guides to the eye for both. If one concentrates on

107
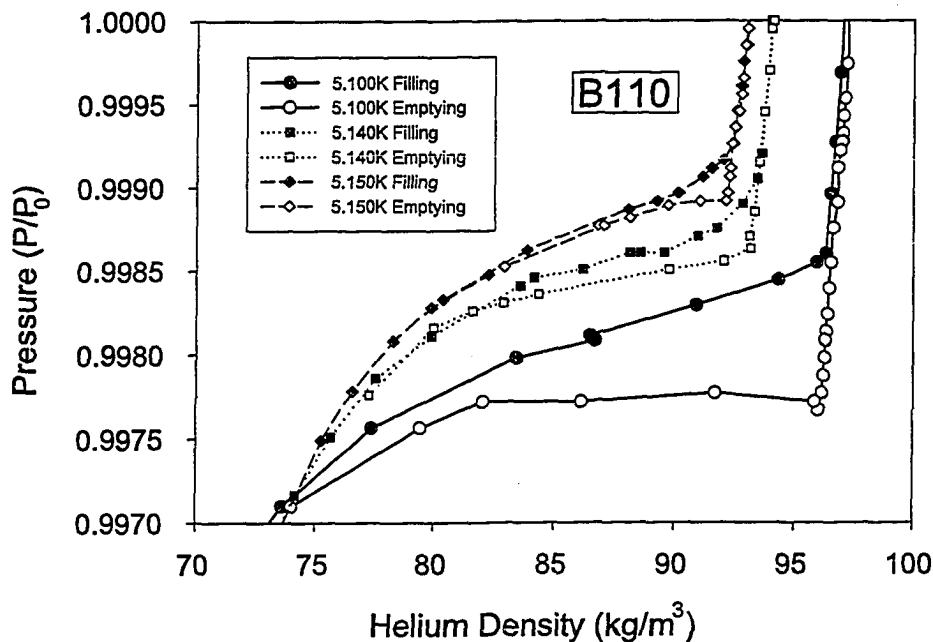
Figure 5.25: Three adsorption isotherm for helium in sample B110; these isotherms show hysteresis loops at intermediate temperatures. The hysteresis loop is distinct in each of these isotherms, but is gradually shrinking as the temperature is raised.

the data below bulk T_c the guide lines intersect at $T \approx 5.155K$, as shown in the inset: below $T \approx 5.155K$ the isotherm slope is small and approximately constant and above $T \approx 5.155K$ the slope increases quickly. This is significant because $5.155K$ is the temperature at which hysteresis disappears. Over a larger temperature scale however, the two guide lines intersect at about $5.185K$. Interestingly, this is approximately the temperature at which the "corner" in the adsorption isotherms disappears. The ambiguity of this type analysis when there appear to be three distinct regions in the graph ($T<5.155K$, $5.155K<T<5.195K$ and $T>5.195K$) makes it difficult to identify a single temperature which may act as the pore critical temperature.

108
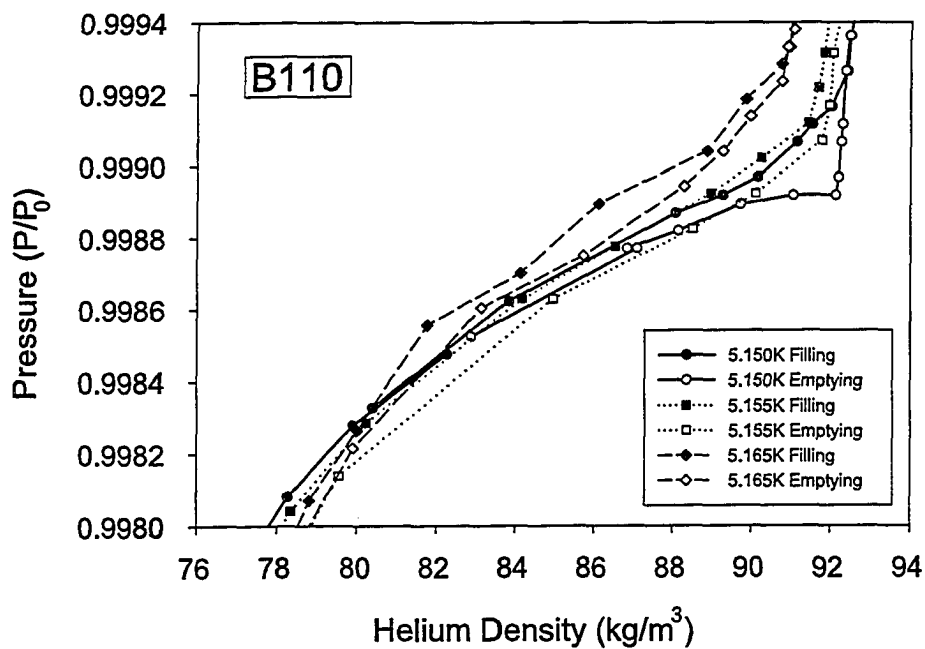
Figure 5.26: Three adsorption isotherms for helium in sample B110; these isotherms show the disappearance of the hysteresis loop at high temperatures. The isotherm taken at 5.150K clearly shows hysteresis while that at 5.165K clearly shows no hysteresis. The isotherm at 5.155K does not appear to show hysteresis, although there may be a very small loop which we failed to resolve. We can therefore take the temperature at which hysteresis disappears to be about 5.155K ± 0.005K

109
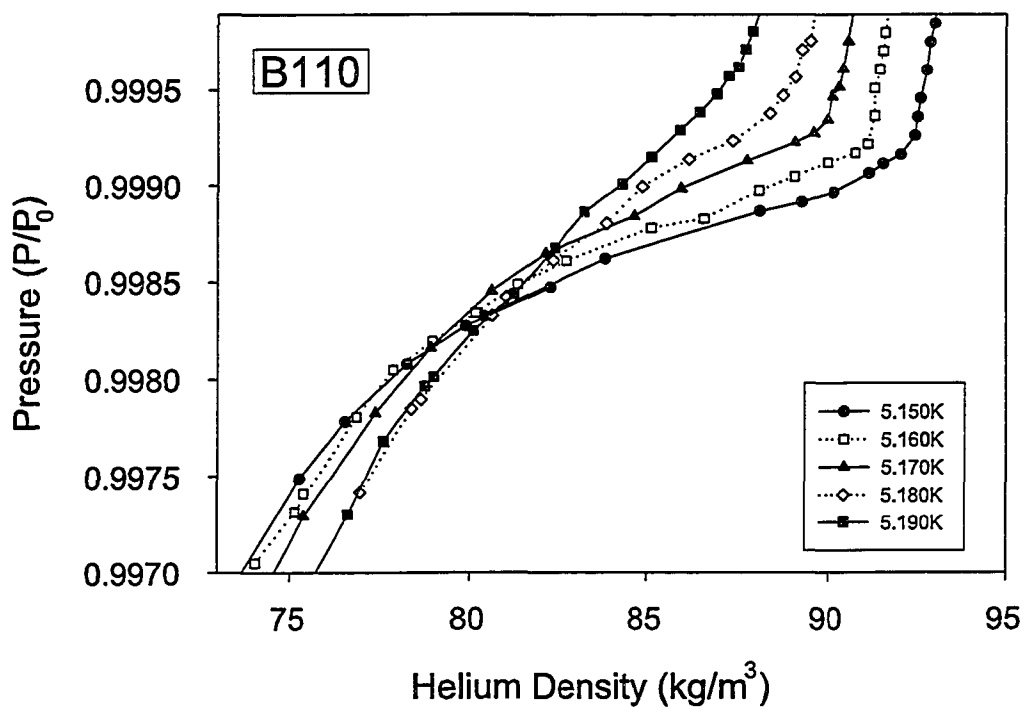
Figure 5.27: Adsorption isotherms for helium in B110 during filling for temperatures spanning the range from the disappearance of hysteresis to bulk T_c. As the temperature is raised the isotherms become steeper and the distinct corner at high density gradually disappears.

110
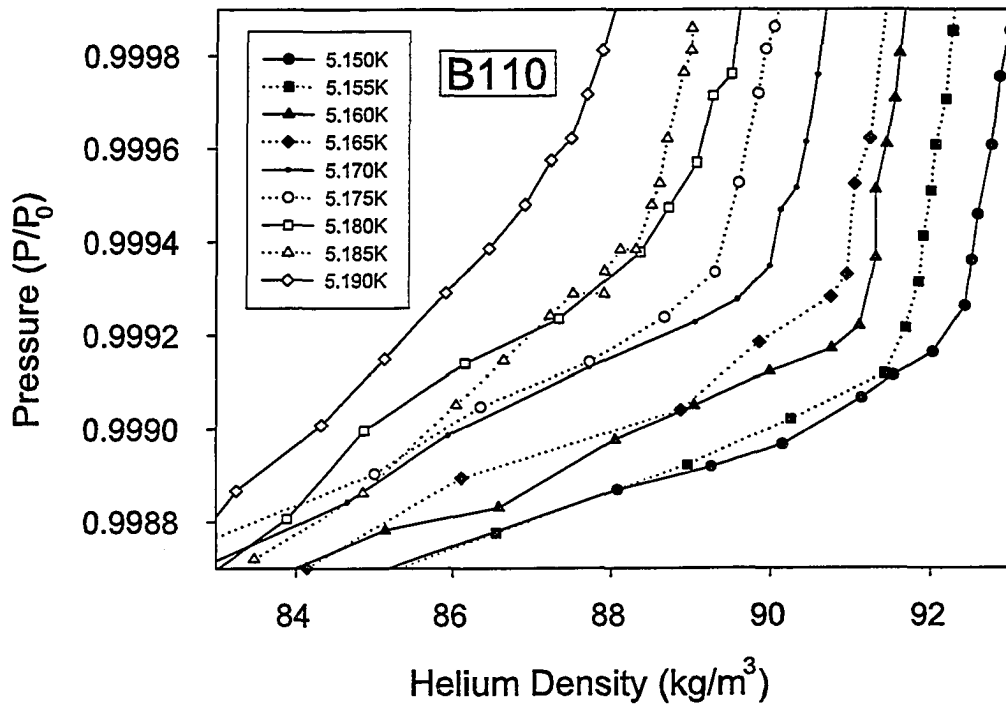
Figure 5.28: Adsorption isotherms for helium in B110 during filling for temperatures spanning the range from the disappearance of hysteresis to bulk T_c. This figure contains the data in Figure 5.27 as well as additional data for intermediate temperatures. By zooming in on the high density corner of the isotherm, we can see that there is distinct kink below 5.170K but that it has smoothed out by 5.180K.

111
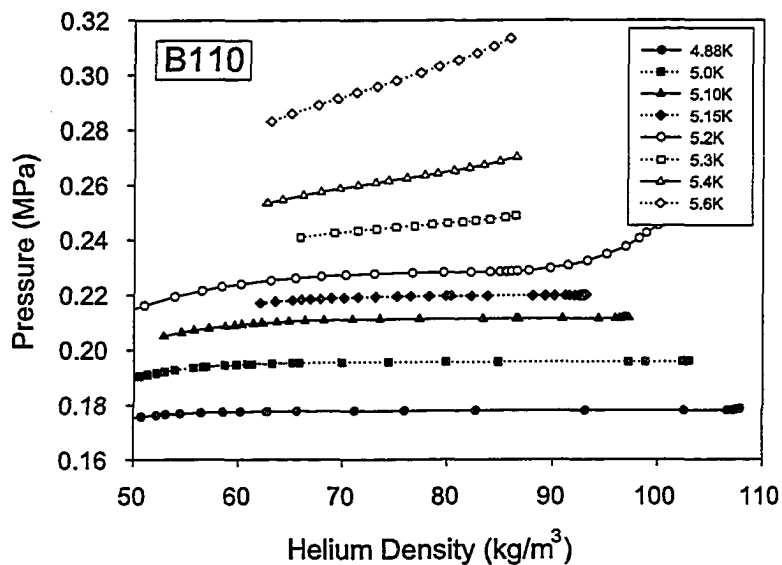
Figure 5.29: The filling branches of adsorption isotherms for helium in B110 spanning all available temperatures. On this compressed scale, only isotherms above bulk T_c show any discernable slope, but in fact all of the isotherms shown exhibit non-zero slopes.
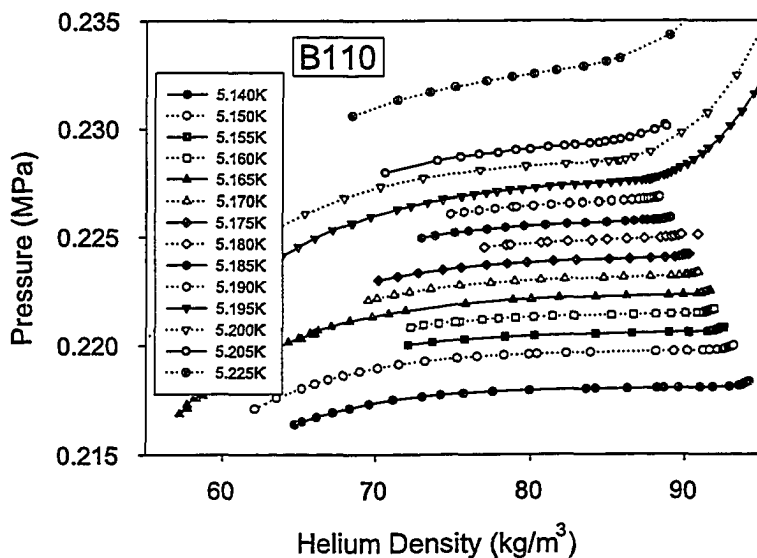
Figure 5.30: The filling branches of adsorption isotherms for helium in B110 near to bulk T_c. Our greatest concentration of data spans the range of $5.140K<T<5.225K$, all of which are included here. Data outside of the range shown in this figure are more sparsely distributed in temperature and were all shown in Figure 5.29.

112
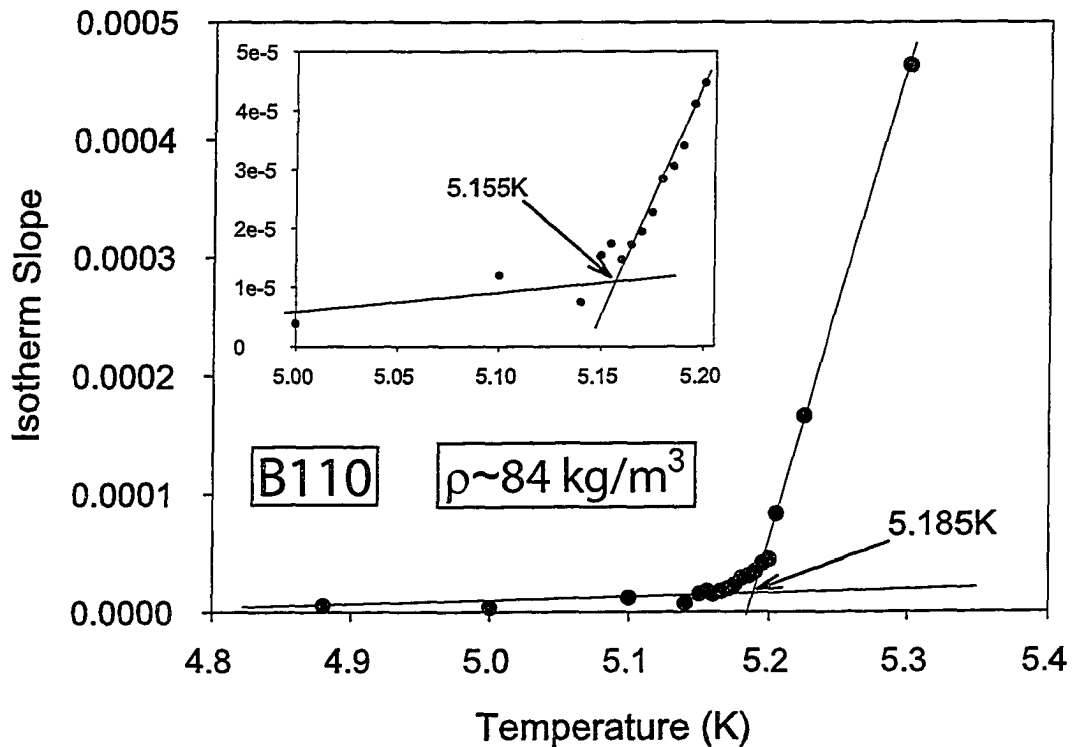
Figure 5.31: The slope of adsorption isotherms for helium in B110 as a function of temperature. These slopes were calculated at the $\rho \approx 84 \frac{kg}{m^3}$ point of the isotherms. The inset displays the same data shown in the larger figure, but displayed over a more limited temperature range. Straight lines are included as guides to the eye, and their intersection may indicate a pore critical point. However, since the figures contains three distinct regions it is not entirely obvious which intersection temperature is the significant one.

113

5.7 Helium in Aerogel X

Having collected a data set for an aerogel with a porosity of about 95%, we wished to compare to adsorption in a more porous aerogel. Adsorption isotherms at low temperatures in more porous aerogels show much sharper capillary condensation with very little rounding of the corners at low temperature[134]. With that in mind James Day cut and plated a second sample which we believed to be approximately 98% porous aerogel, synthesized using a two-step process as described in Chapter 4. Unfortunately, as we collected our results it began to look as if we had accidentally remounted a sample of 95% aerogel. This turned out not to be the case, but the sample was certainly *not* 98% porous. Because of the small size of the samples, a direct measurement of density is difficult but it looks as if the sample is about 96% porous (a density of $\sim 86\frac{kg}{m^3} \pm 20\%$). While the gel was clearly labelled, the label was incorrect and it has since proved impossible to track down its exact provenance. Since we can not be sure of this sample's density it is referred to as "**Aerogel X**."

While we may not be able to use this data to comment on the effect of porosity on helium adsorption, it is still possible to learn a great deal about our system from this extra data set. A series of isotherms was taken over the same temperature range as the previous sample, but the data was collected in the second generation experimental cell (Figure 5.6). The sample was prepared without guard rings, so fringe fields were still a large correction to the aerogel signal. Also, the sample was warmed to room temperature between two short data runs, allowing us to evaluate the consistency and repeatability of our setup. This sample happened to be slightly thinner than the previous one (a fact reflected in its larger capacitance) which may have allowed slightly quicker thermal equilibration.

5.7.1 Density Calibrations
Bulk Helium Density

During the first data run, in July 2003, the bulk density capacitor short circuited during cool down, so the bulk density was not measured for the those isotherms. During the second run, in August and September 2003, the bulk capacitor was working however, and by assuming NIST values for helium density at 4.400K, bulk density was calculated from the capacitance using:

$$\rho_{bulk} = 98.898 \left(C_{bulk} - 35.165 pF \right) \tag{5.4}$$

114
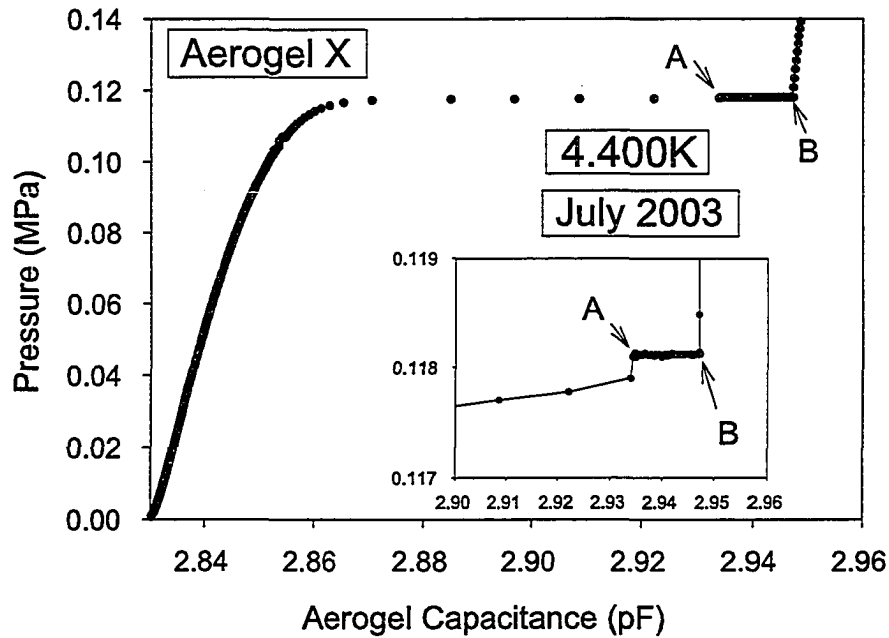
Figure 5.32: The filling branch of the helium adsorption isotherm for Aerogel X at 4.400K taken during the July 2003 data run. This isotherm is used to calculate the effects of fringe fields and obtain a calibration for helium density within the aerogel. Compared to Figure 5.19 fringe fields contribute more to the signal in Aerogel X than in aerogel B110, reflected by the greater distance between points A and B in this figure, because it is mounted in the cup shaped electrode of the second experimental cell.

The new cell incorporated a bulk capacitor with a much smaller gap, and a correspondingly larger capacitance. There is no temperature correction included in this calibration because the magnitude of such a correction was always less than $1\frac{kg}{m^3}$; since the only role the bulk density played in this data set was as a fringe effect such a small correction to the bulk density calibration was unnecessary.

Helium Density in Aerogel

The calibration for helium density in aerogel shifted slightly between data runs, but by less than a percent. The two density calibrations are shown below, and were calculated from the adsorption isotherms shown in Figure 5.32 and Figure 5.33 respectively.

$$\rho_{gel}^{He} = 1136 \left(C_{gel} - 2.825302pF - \frac{\rho_{bulk}}{7924} \right) \quad (July2003) \quad (5.5)$$

$$\rho_{gel}^{He} = 1141 \left(C_{gel} - 2.799407pF - \frac{\rho_{bulk}}{8139} \right) \quad (August2003) \quad (5.6)$$

115
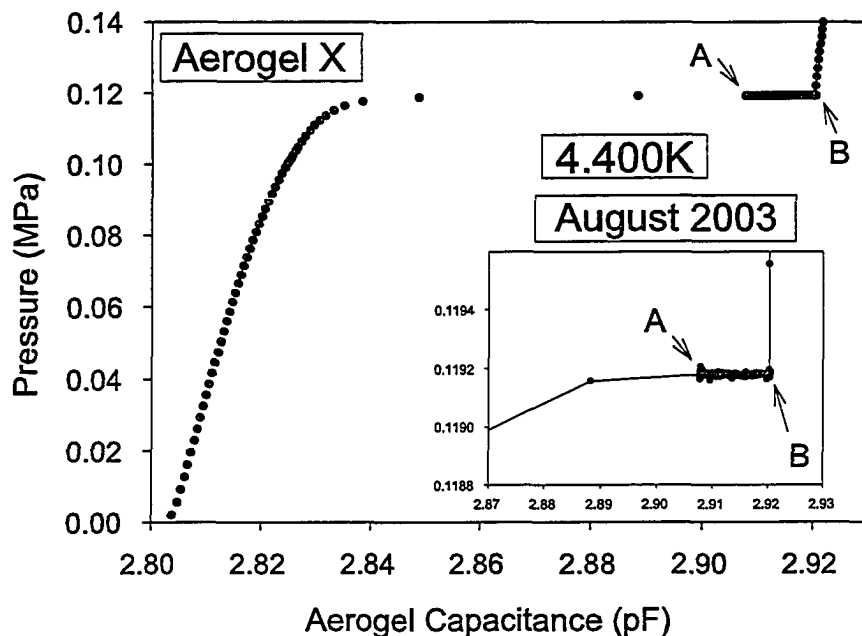
Figure 5.33: The filling branch of the helium adsorption isotherm for Aerogel X at 4.400K taken during the August 2003 data run. The values for the aerogel capacitance are slightly shifted from Figure 5.32, which is taken into account in the helium density calibration. There is also a small offset in bulk condensation pressure, which is an artifact of the pressure gauge calibration – while pressure changes can be resolved very well, the absolute pressure calibration in this pressure range is not perfect.

5.7.2 Comparison between Runs

The density calibration is recalculated for each data run, so the two separate data runs on this one sample allowed us to make a direct comparison between data collected for exactly the same system on two different occasions. Isotherms for adsorption at 5.165K are shown in Figure 5.34 for both data runs. They should be identical – any difference indicates a deficiency in our calibration. Notice that the shape of the isotherm remains virtually unchanged – the only noticeable difference is a shift of about $1\frac{kg}{m^3}$ in density. This good agreement between data runs is despite the complete lack of bulk density measurements for the July data (remember that the aerogel density calibration includes subtracting out about 15% fringe field). However, the shift in density means that we must be careful not to claim too much accuracy when interpreting absolute density measurements for helium in our aerogel samples.

116
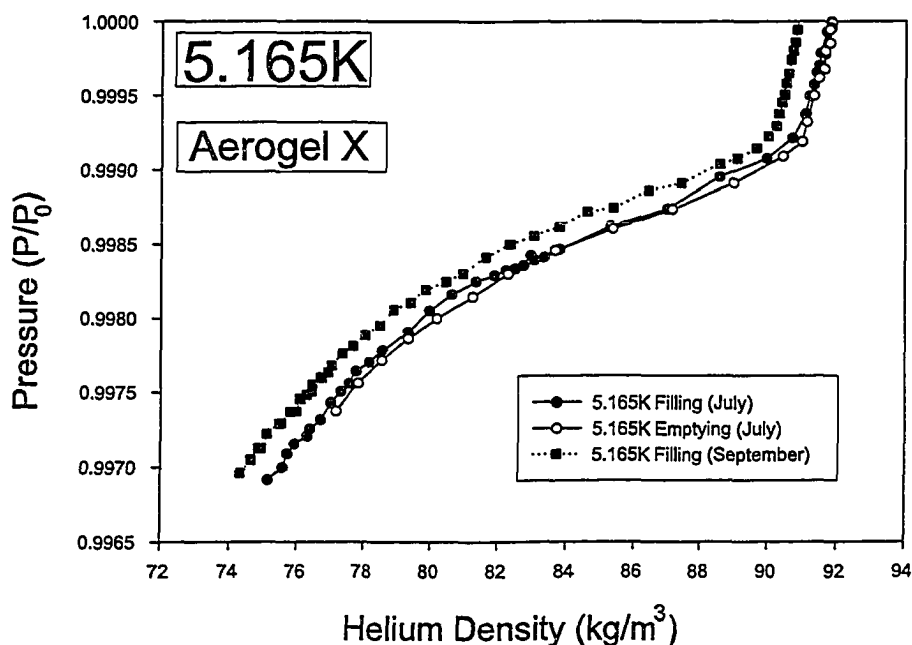
Figure 5.34: Adsorption isotherms for helium in Aerogel X at 5.165K taken during two different data runs. The density of helium in the aerogel differs by about $1\frac{kg}{m^3}$ between the runs. The data from July did not include direct bulk density measurements, which may have contributed to differences in calculated densities.

5.7.3   Rate Dependence of Hysteresis

Adsorption isotherms in this sample were almost all collected by controlling the ballast temperature; continuous flow into the cell could not be controlled at a slow enough rate to allow equilibration. A sample isotherm showing how sensitive the system is to filling rate is included as Figure 5.35; this behavior is very similar to sample B110.

5.7.4   Adsorption Isotherms for Aerogel X

The shape, and the temperature evolution of the shape, of adsorption isotherms in this sample is very similar to those seen in sample B110. Included in Figure 5.36, Figure 5.37, and Figure 5.38 are a series of isotherms spanning the temperature range from 4.880K to the disappearance of hysteresis at 5.155K.

At higher temperatures (above 5.155K) we do not have precise enough saturated vapor pressure values to plot all isotherms in terms of P/P_0 so Figure 5.39 shows higher temperature adsorption isotherms in terms of density and absolute pressure. These three isotherms show that while hysteresis may be present at 5.155K, it is gone

117
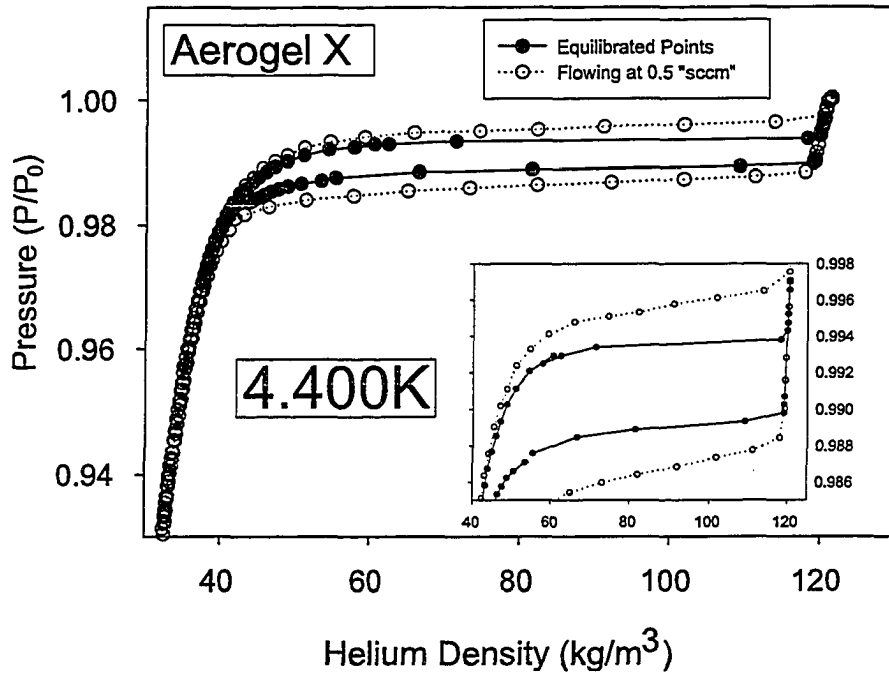
Figure 5.35: Adsorption isotherm for helium in Aerogel X at 4.400K. Equilibrated points define an inner loop, while points taken during continuous filling and emptying form a much wider loop. Notice that even at the slowest possible filling rate (0.5sccm) the hysteresis loop deviates considerably from its equilibrium shape.
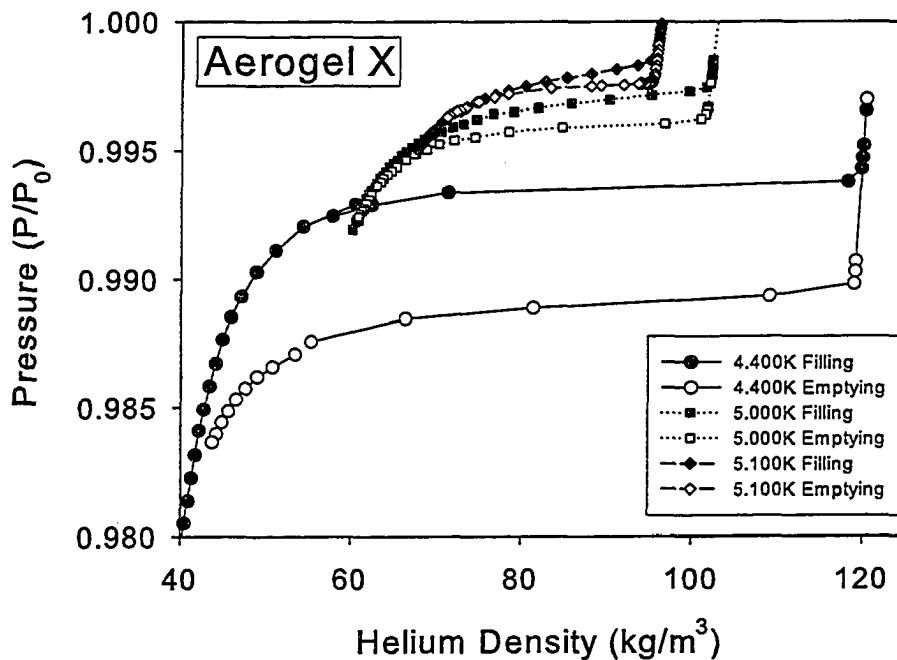
Figure 5.36: Adsorption isotherms for helium in Aerogel X. All these low temperature isotherms show distinct hysteresis loops very similar to those seen in sample B110 (Figure 5.24).

118
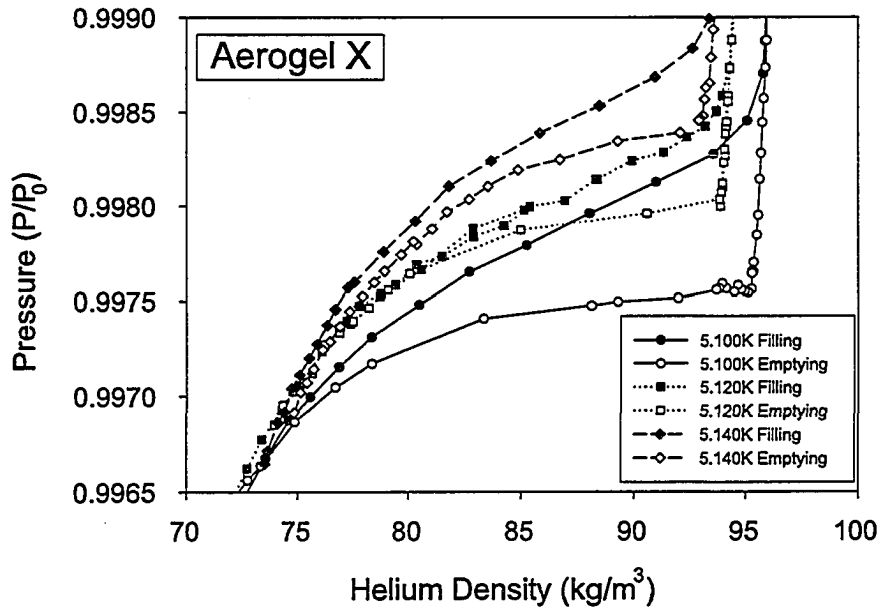
Figure 5.37: Adsorption isotherms for helium in Aerogel X. These slightly higher temperature isotherms show the hysteresis loop shrinking and the low density side of the loop becoming less distinct.
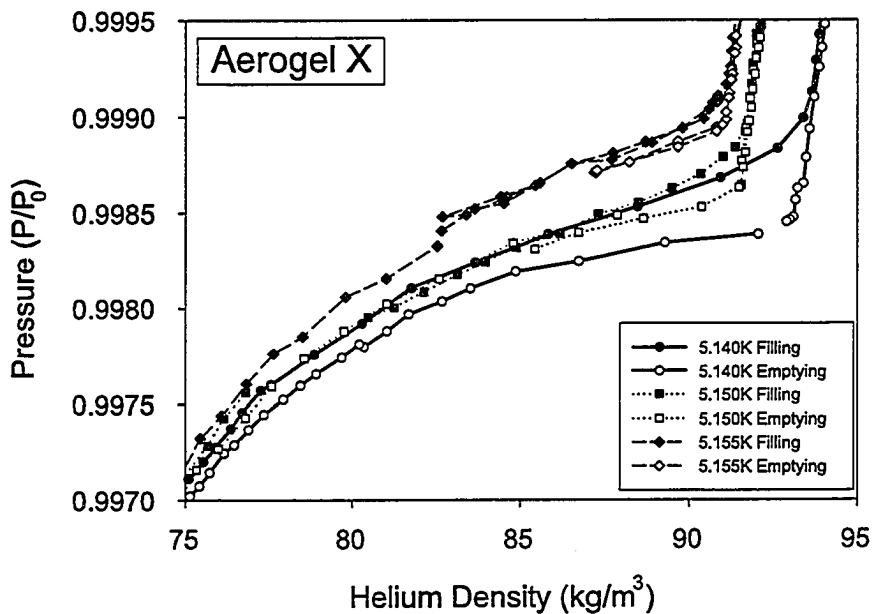
Figure 5.38: Adsorption isotherms for helium in Aerogel X. These higher temperature isotherms show the gradual disappearance of the hysteresis loop – by 5.155K it just barely resolvable.

119
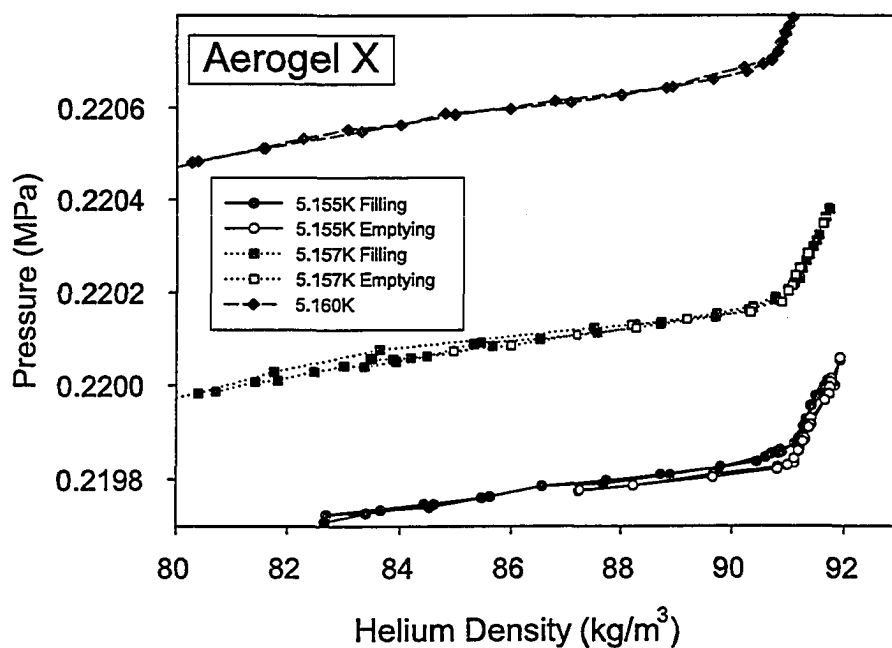
Figure 5.39: Adsorption isotherms for helium in Aerogel X. These isotherms show that while a small hysteresis loop is visible in the 5.155K isotherm, above 5.155K hysteresis has completely disappeared. These isotherms are plotted in terms of absolute pressure because of unreliable bulk saturated vapor pressure data in this temperature range.

by 5.157K. This is within a few millikelvin of the temperature at which hysteresis disappeared in sample B110.

Figure 5.40 shows many adsorption isotherms over a range of temperatures from the disappearance of hysteresis to the bulk critical temperature. While the high density "corner" of the isotherm is not well highlighted in such a plot, one can see that it smooths out near 5.175K or 5.180K as it did in sample B110.

120
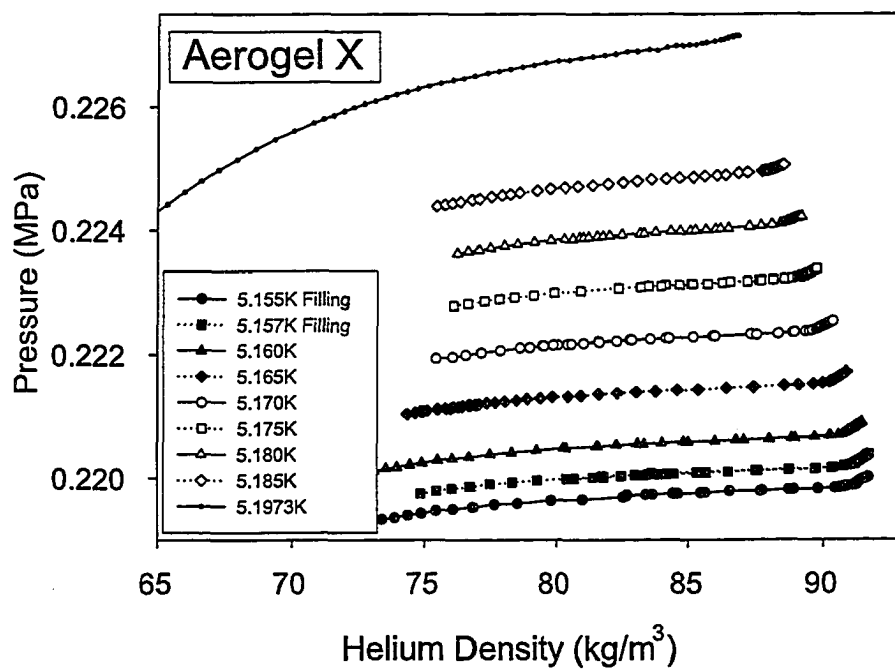
Figure 5.40: Adsorption isotherms for helium in Aerogel X, for temperatures from the disappearance of hysteresis at 5.155K to bulk T_c. For the lower temperature isotherms only the filling branch is shown; for the higher temperature isotherms there is no hysteresis and filling and emptying branches are equivalent.

5.8 Helium in Aerogel B51

Our third sample in this study of capillary condensation of helium in silica aerogel was a slice of $\sim 98\%$ aerogel with a density of $51\frac{kg}{m^3}$ referred to as "B51." This sample was synthesized in-house using the same one-step process used to synthesize B110, so the microstructure of the gel should be very similar. The sample was cut and plated in the same manner as the first two samples.

5.8.1 Density Calibrations
Bulk Helium Density

The bulk density calibration for this data run was again set by assuming literature values for the density of helium vapor and liquid at 4.400K. The calibration is very close to that seen from the August 2003 run, which is reassuring. A temperature correction term is included, but again it is not very significant (never more than $0.4\frac{kg}{m^3}$).

$$\rho_{bulk} = 98.712 \left(C_{bulk} - 35.188676pF - 0.00183 \left(T_{cell} - 4.400K \right) \right) \qquad (5.7)$$

Helium Density in Aerogel

The aerogel capacitor calibration is again computed from the adsorption isotherm at 4.400K, including fringe effects (see Figure 5.41).

$$\rho_{gel}^{He} = 2261 \left(C_{gel} - 1.44848pF - \frac{\rho_{bulk}}{11517} \right) \qquad (5.8)$$

5.8.2 Adsorption Isotherms for Aerogel B51

Adsorption isotherms in aerogel B51 differ from those in the previous two samples. Capillary condensation does not occur until slightly higher relative pressures than in the denser gels and when it does occur the gel fills (or empties) over an exceptionally narrow pressure range. Two isotherms are shown in detail: one at low temperature (Figure 5.42) and one closer to T_c (Figure 5.44). In both figures any point which has not quite equilibrated is marked by an asterisk. With so many points out of equilibrium, it is hard to assign a width to the hysteresis loop, but for the 4.880K isotherm the width must be in the range: $0.00045P/P_0 < Width < 0.00125P/P_0$, about half the width of the same isotherm in B110.

Also of interest in the 4.880K isotherm is the *decrease* in apparent density of helium after the gel has filled and the pressure is increased towards bulk saturation

122
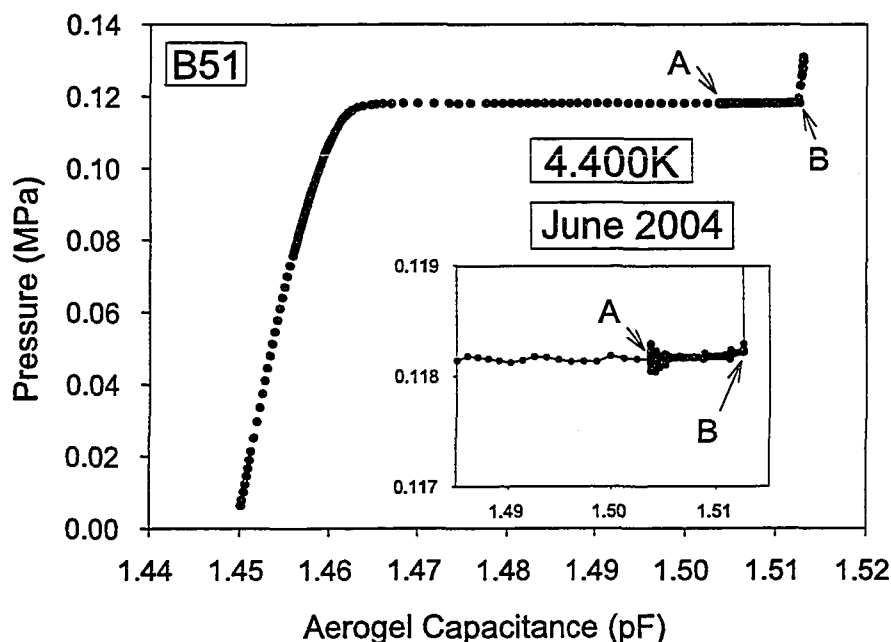
Figure 5.41: Adsorption isotherm for helium in sample B51 at 4.400K. Again, the positions of points A and B are used to determine the helium density calibration used throughout this data set (Equation 5.8)

pressure. In this regime the gel is full of liquid, but bulk liquid has not formed in the cell yet. There is an interfacial energy associated with this liquid-vapor interface which acts to deform the aerogel; the decrease in capacitance is probably not due to an actual decrease in the helium density, but is in fact due to a geometric change in the capacitor. If we assume an isotropic compression of the aerogel an increase in capacitance is actually expected, since $C \propto \frac{Area}{Thickness}$. In fact, within about 30%, we would expect:

$$\frac{\Delta L}{L} = \frac{\Delta C}{C}$$

which means that capacitance should increase with pressure if the effect of aerogel is isotropic. Figure 5.43 shows the desorption branch of the 4.880K isotherm in aerogel B51, plotted in terms of raw capacitance. By extending the data near the closure of the hysteresis loop along straight lines we can estimate the change in capacitance – about $-1.6fF$. This corresponds to a change in capacitance of about 0.1%, much less than the $\sim 1\%$ change in length expected from the results in chapter 7 in addition to being of the wrong sign. Thus, the capacitance we are measuring must be more complicated than we first assumed. Perhaps the deposition of the electrodes

123
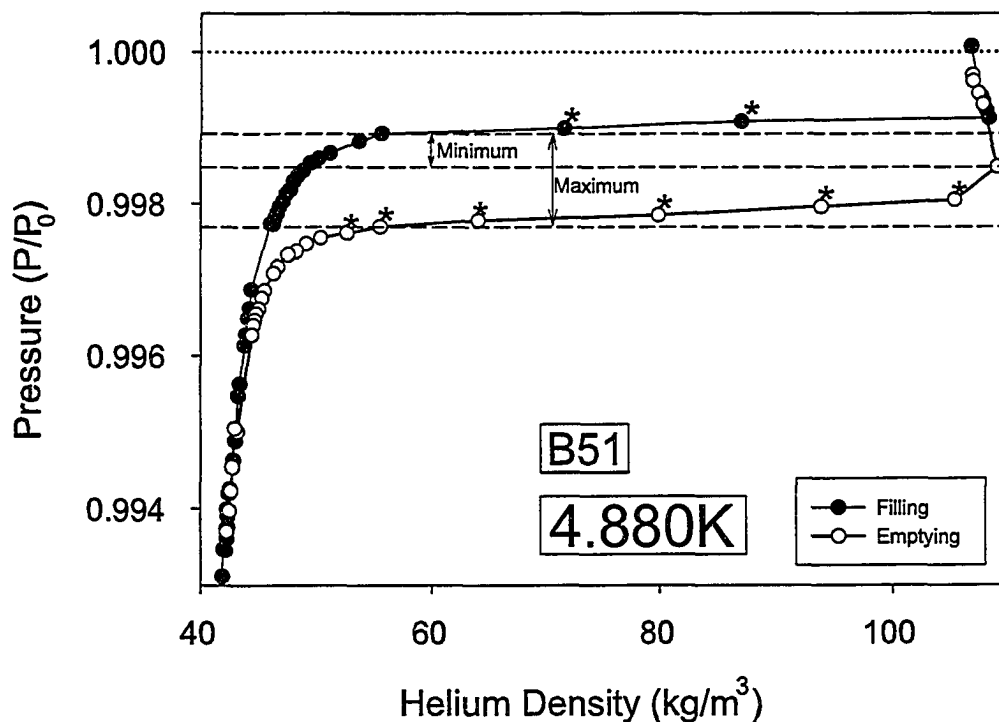
Figure 5.42: Adsorption isotherm for helium in B51 at 4.880K. While most points are equilibrated, some have not completely settled and are indicated by an asterisk (*) near the point. The minimum and maximum widths of the hysteresis loop are indicated. The minimum is set by the highest pressure equilibrated filling point on the low density side of the loop and the lowest pressure equilibrated emptying point on the high density side of the loop. The maximum width is set by the difference between the equilibrated filling point and the unequilibrated emptying point at the same density. Also note the apparent decrease in helium density *after* the sample is full – this is probably indicative of deformation of the sample caused by the helium's surface tension, the topic of another chapter in this thesis.

124
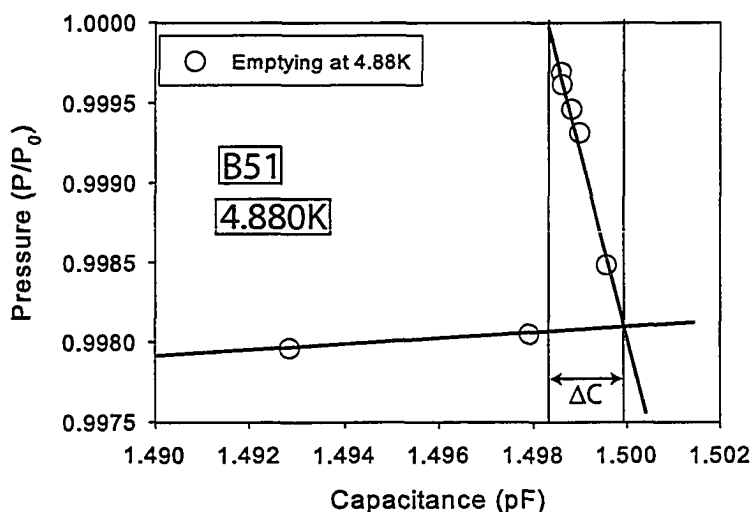
Figure 5.43: Desorption branch of isotherm at 4.880K in aerogel B51. It is plotted in capacitance so that the degree of deformation of the aerogel can be calculated.

alters the aerogel structure on the large faces of the slice, or the deformation of the aerogel is affected in some way by the manner in which it is mounted in the cell. A closer examination of the sample may be necessary to completely understand this behavior; until then it is dangerous to try to extract information about the physical deformation of the aerogel from any capacitive measurement involving electrodes deposited directly on the aerogel.

Hysteresis is still easily resolved in the 5.150K isotherm (Figure 5.44), which also happens to be the best equilibrated hysteretic isotherm we have for sample B51. This hysteresis loop extends over a large range of densities but drains almost entirely in a single pressure step.

Figures 5.45 to 5.47 show the evolution of the adsorption isotherms with temperature. Hysteresis is still resolvable in the isotherm at 5.170K, although the precision of our pressure control is barely good enough (a few parts in 10^5) to see the loop. At 5.180K and above no hysteresis was seen; however, a number of points along the higher temperature isotherms showed a slow random drift. This drift in density was sometimes small, and sometimes a significant part of the density change seen during that isotherm's step. This is probably an indication that at such temperatures the isotherms are *very* sensitive to cell temperature and pressure and we have reached the limits of our ability to control the system well enough.

5.8.3 Thermal Equilibration

The thermal equilibration of aerogel B51 during fluid adsorption resembles that of B110 in that is is slow and although cell pressure and bulk density equilibrate quickly

125
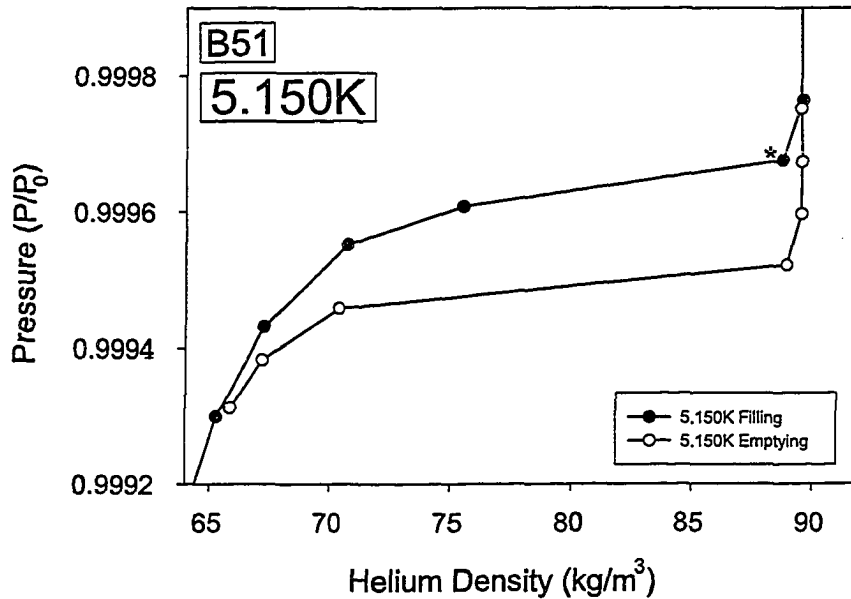
Figure 5.44: Adsorption isotherm for helium in B51 at 5.150K. This isotherm is very well equilibrated, and the hysteresis loop is very distinct. However, the (pressure) width of the loop is only about two steps in ballast temperature. The loop is much wider in terms of density and flatter than high temperature loops in the other two samples. The only point in the plot which does not represent a fully relaxed state is indicated by the asterisk('*'). Note that this loop is only a few times wider than our resolution – in fact, within resolution, the emptying branch of this isotherm is flat.

after a step in ballast temperature, the helium density in the aerogel slice lags far behind. Figures 5.48 and 5.49 show the response of aerogel B51 to a small step in ballast temperature within the hysteretic region of the 5.150K adsorption isotherm. These are exactly the same form as those shown for aerogel B110 (Figures 5.20 and 5.21), except that the upper pane (T_B) has been removed. This is because the step in T_B used here was not resolvable within thermometer noise – each step along this isotherm corresponded to a change in T_B of only 0.1mK, as opposed to the 1.0mK change shown for aerogel B110 in a previous section.

The relaxation of helium density in aerogel B51 seems slower than in aerogel B110, which is probably related to the much smaller change in system pressure along the step. A direct comparison of the two is shown in the next section. There is also an important observation to make about system response from these figures – there is long term drift in bulk density. This drift is probably caused by drift

126
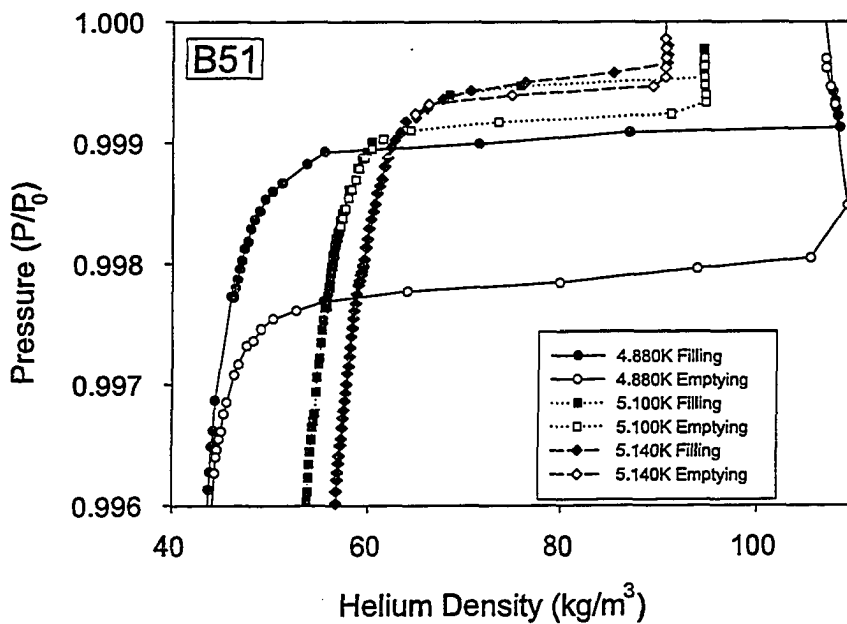
Figure 5.45: Adsorption isotherms for helium in B51. These three isotherms were collected at lower temperatures, where the hysteresis loop is fairly wide and well defined.
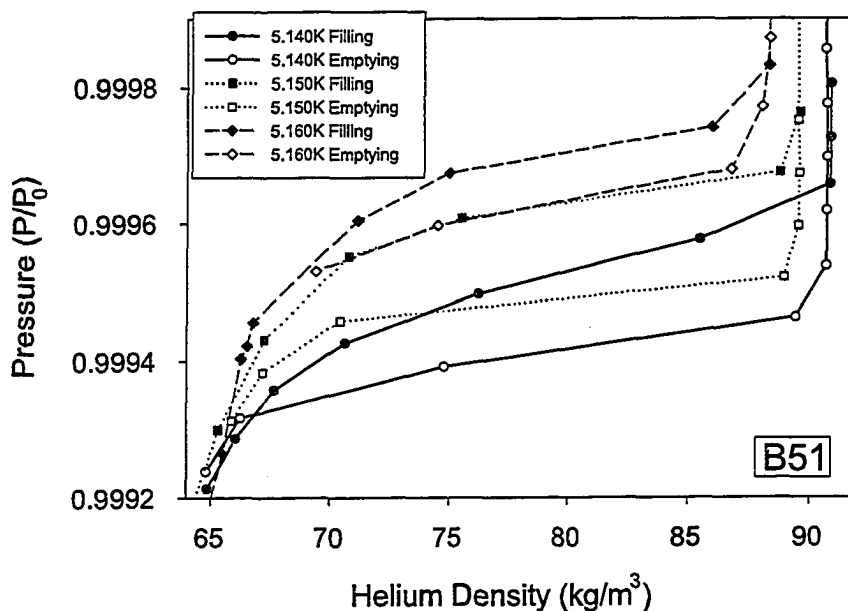
Figure 5.46: Adsorption isotherms for helium in aerogel B51. Hysteresis disappeared over this temperature range in aerogel B110 and Aerogel X, but in B51 the hysteresis loops remain well defined, although over a very narrow pressure range.

127
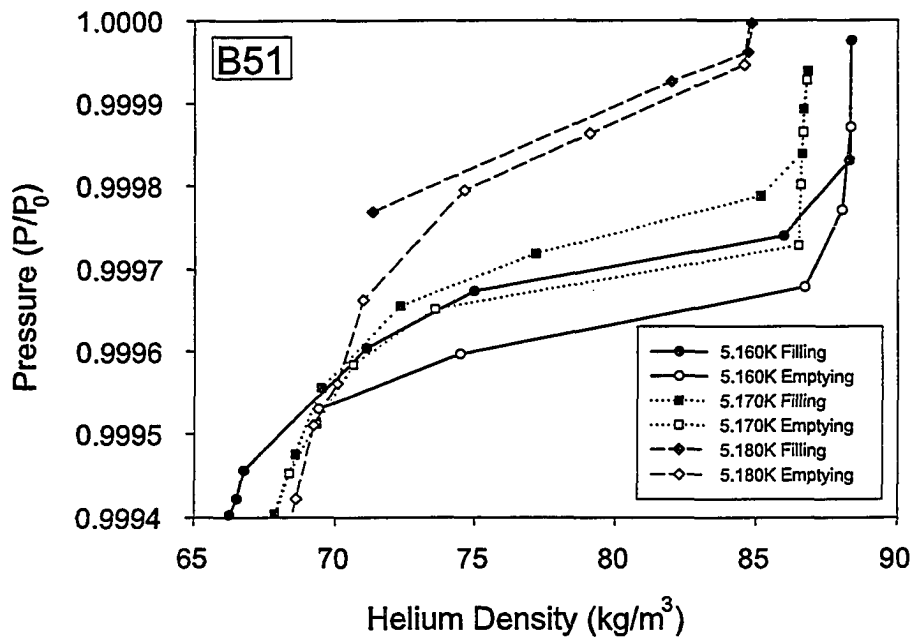
Figure 5.47: Adsorption isotherms for helium in B51. These higher temperature adsorption isotherms show the disappearance of the hysteresis loop somewhere between 5.170K and 5.180K. The isotherm at 5.180K included points which appeared to drift over time; these points have been removed from the figure and probably indicate that we are operating at the limit of resolution for this system.

of the cell pressure, although the noise on the pressure signal makes that difficult to distinguish. If the drift is also present in the cell pressure, then it is probably related to temperature drift in the ballast (which, after all, controls cell pressure). The temperature controller specifies an accuracy of 0.1%, which would correspond to ± 5mK in this system. While the controller actually provides very stable and reproducible readings down to fractions of a milliKelvin in this temperature range, it must be expected to drift somewhat on the scale of 100μK since that is two orders of magnitude beyond specifications. A drift in cell pressure will also turn up as a drift in aerogel density. Since the drift in density is still a fraction of the total step caused by stepping the ballast temperature we can still sensibly interpret the adsorption isotherms, but there were times when the drift was too large and those points needed to be removed from the data files.

Cell temperature is controlled in the same manner as ballast temperature, so a drift in cell temperature could also account for drift in bulk density, although in this case there will be no accompanying drift in cell pressure. In either case, we have reached the limit of resolution for our present system – temperature control will

128
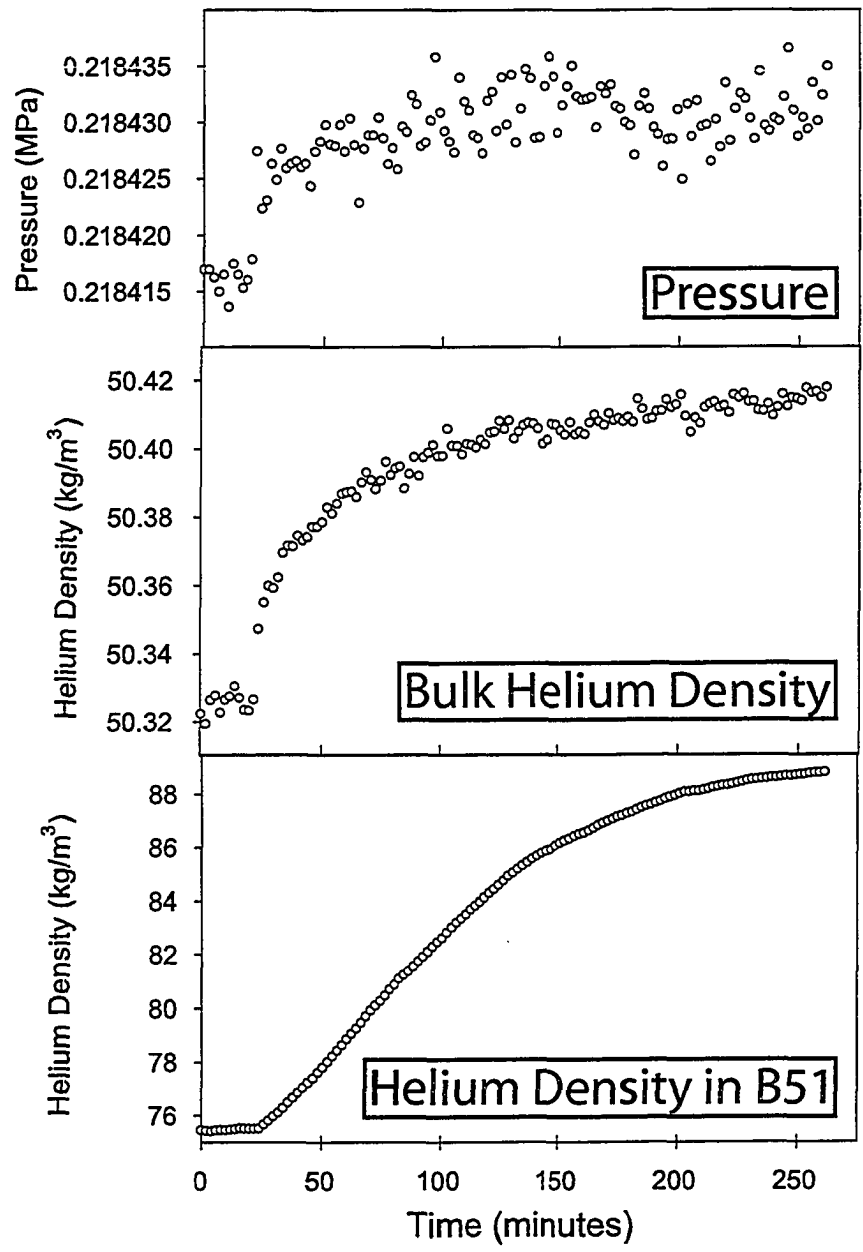
Figure 5.48: Equilibration during cell filling at 5.150K. The ballast temperature is not included because the step in T_B was only +0.1mK – not resolvable from noise. There is a slight drift in bulk density and in cell pressure, probably due to drift in ballast temperature.

129
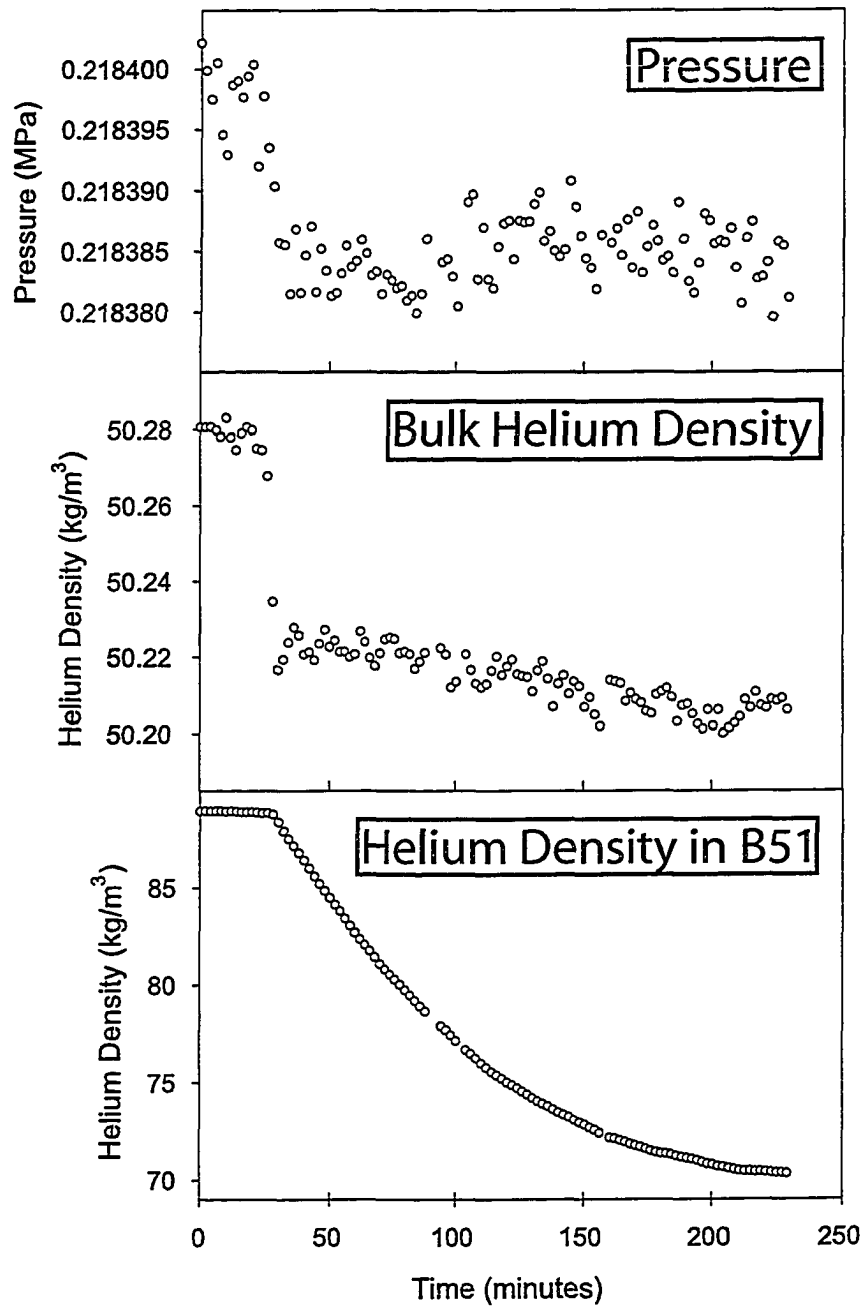
Figure 5.49: Equilibration during cell emptying at 5.150K. This figure is identical
to the previous one, but corresponds to a temperature step of $\Delta T_B = -0.1\text{mK}$

130

need to be improved if anyone wants to investigate these isotherms more closely, or work with less dense aerogels in this system.

5.8.4 Absence of Critical Depletion in Aerogel B51

Since our setup allowed simultaneous measurement of helium density in the bulk cell space and in the aerogel sample, we could easily check for critical depletion. As mentioned in chapter 3 there have been a few instances which would suggest that close to the bulk critical point fluid leaves the pores of certain porous materials as the temperature is lowered.

If such a process occurred in the aerogel sample, then a plot of helium density in the gel along a series of isotherms should show crossing of the isotherms when the bulk helium density is near its critical value. All of these isotherms were taken above the critical point, over a range of temperatures from 5.1952K to 5.600K ($\epsilon \approx 10^{-1} - 10^{-4}$). In an experiment on the adsorption of nitrous oxide in a dense silica gel[50], researchers saw evidence for critical depletion for reduced temperatures below about 10^{-2} – a range covered well in our data. Isotherms for helium adsorbed in aerogel B51 are shown in Figure 5.50 and clearly show no evidence for critical depletion. This figure can be directly compared to Figures 3 and 4 in reference [50] – we see no crossing of isotherms in the range where they clearly see crossing. It would be interesting to use our system to investigate critical depletion in denser glasses since the data analysis allows for very quick interpretation of raw data – although we saw nothing in the very porous aerogel sample, there might be interesting behavior in the denser porous glasses such as Vycor.

131
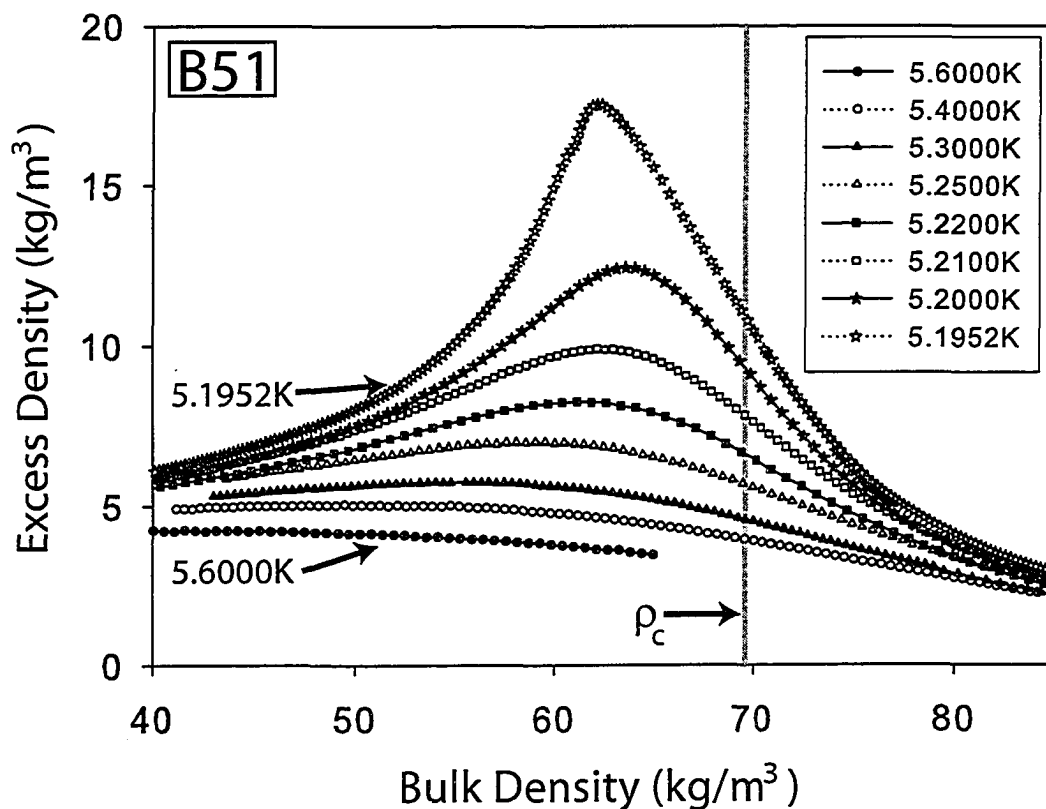
Figure 5.50: Isotherms in aerogel B51 at temperatures above the bulk critical temperature. Critical depletion would show up as a crossing of these isotherms near the bulk critical density. Clearly there is no such crossing in these data. The isotherms span a wide range in reduced temperature, with the highest temperatures showing little excess adsorbed helium as the bulk density is swept over a wide range and the lowest temperatures showing a significant (i.e. $\sim$ 20%) density enhancement. The lowest and highest temperature isotherms are directly labelled on the plot, and the bulk critical density is shown by a vertical grey line.

132

5.9 Comparison Between Samples

5.9.1 B110 and Aerogel X

There is every indication that these two samples have very similar structures and porosities. All the helium adsorption isotherms collected indicate that hysteresis in these two samples occurs in the same temperature range and that the hysteresis loops cover similar density and pressure ranges (Figures 5.51, 5.52, and 5.53). The only differences are near the low density closure of the hysteresis loop – in Aerogel X the closure is somewhat more gradual than in B110. This part of the isotherm corresponds to the initial stages of capillary condensation, when small spaces within the aerogel begin to fill with liquid. The differences between the two samples may indicate a slightly different structure on the smallest length scales, consistent with slightly different catalysis during synthesis or drying program. However, overall the differences are quite minor, especially on the higher density side of hysteresis loop.

At 5.165K, after the hysteresis loop has disappeared, the isotherms in B110 and Aerogel X are practically indistinguishable (Figure 5.53). In fact, the two isotherms show better agreement than the two separate data runs on Aerogel X.
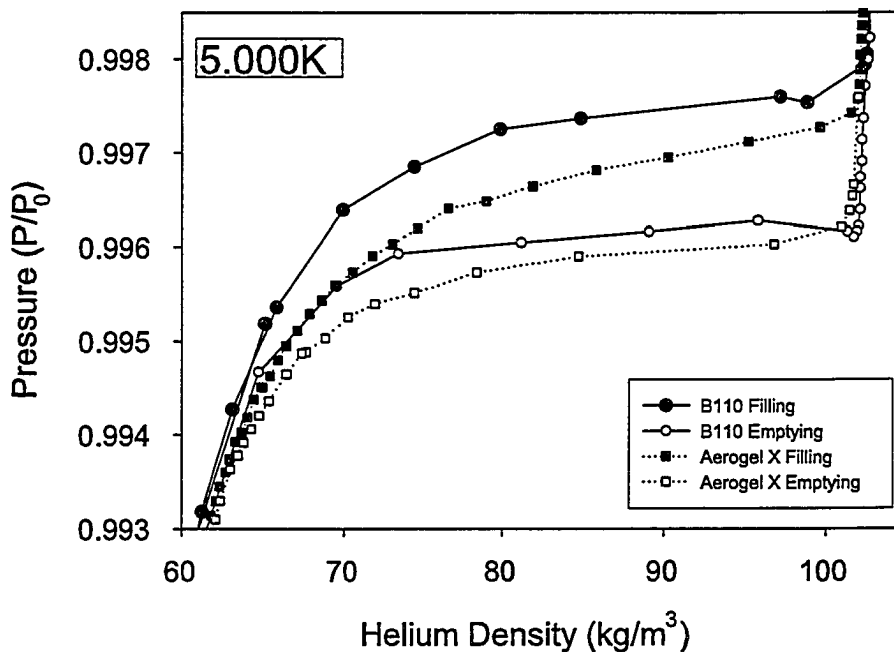
Figure 5.51: Adsorption isotherms of helium at 5.000K in aerogel B110 and Aerogel X. The two isotherms are remarkably similar, showing only slight differences in slope, width, and curvature on the low density side of the hysteresis loop.

133
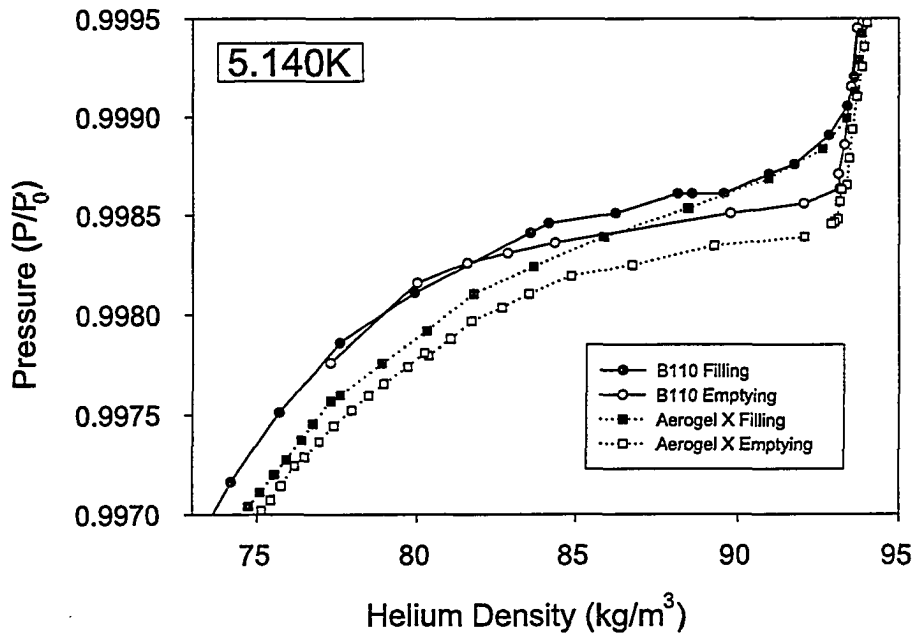
Figure 5.52: Adsorption isotherms of helium at 5.140K in aerogel B110 and Aerogel X. Again the isotherms are very similar, although the slight differences are highlighted because the hysteresis loops have become so narrow at this temperature.
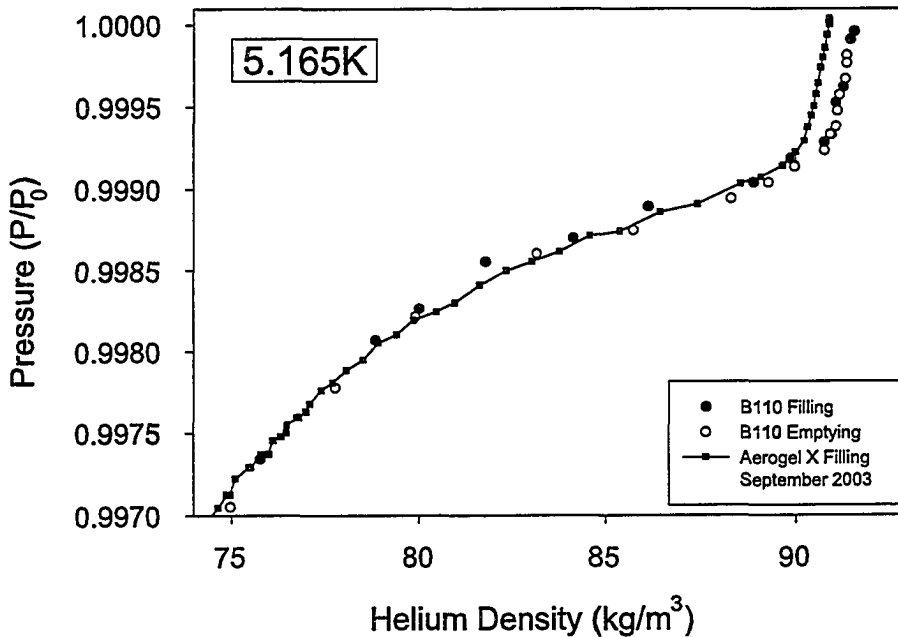
Figure 5.53: Adsorption isotherms of helium at 5.165K in aerogel B110 and Aerogel X. The two samples are virtually indistinguishable at this temperature. In fact the agreement is as good or better than the agreement between the two data runs with Aerogel X shown in Figure 5.34.

134

5.9.2 B110 and B51

There are much more significant differences between adsorption isotherms in the 95% and 98% porous aerogels (B110 and B51). In fact the shape of the adsorption isotherms is fundamentally different, as emphasized in Figures 5.54 and 5.55 for T=4.880K and T=5.150K respectively. In aerogel B51 the hysteresis loops occur much closer to saturated vapor pressure and cover a larger range of densities. The low density portion of the adsorption isotherms in B51 shows less density enhancement before the onset of capillary condensation, consistent with a lower surface area per volume – the less dense medium perturbs the density less from its bulk value. Similarly, the density enhancement when the gel is full (at 5.150K) is smaller in B51, as expected.
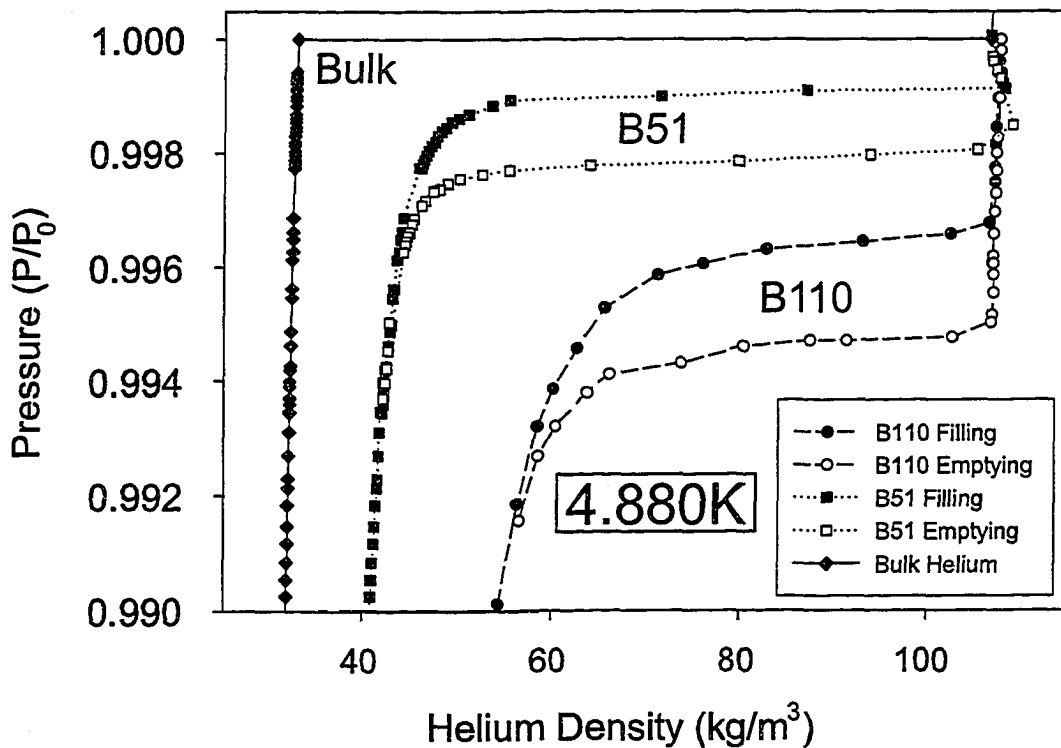
Figure 5.54: Adsorption isotherms of helium at 4.880K in aerogels B110 and B51. While the liquid density in the aerogel remains virtually unchanged, every other characteristic of the adsorption isotherm has changed. Compared to B110, the low pressure corner of the isotherm has been shifted to lower helium density for B51, the capillary condensation pressure has shifted upwards, and the slope of the isotherm during capillary condensation is much flatter. The hysteresis loop is about half-way between the bulk density curve and the B110 loop, a fact consistent with the ratio of sample densities – one would expect a gel that is half as dense to perturb the condensation of helium much less.

135
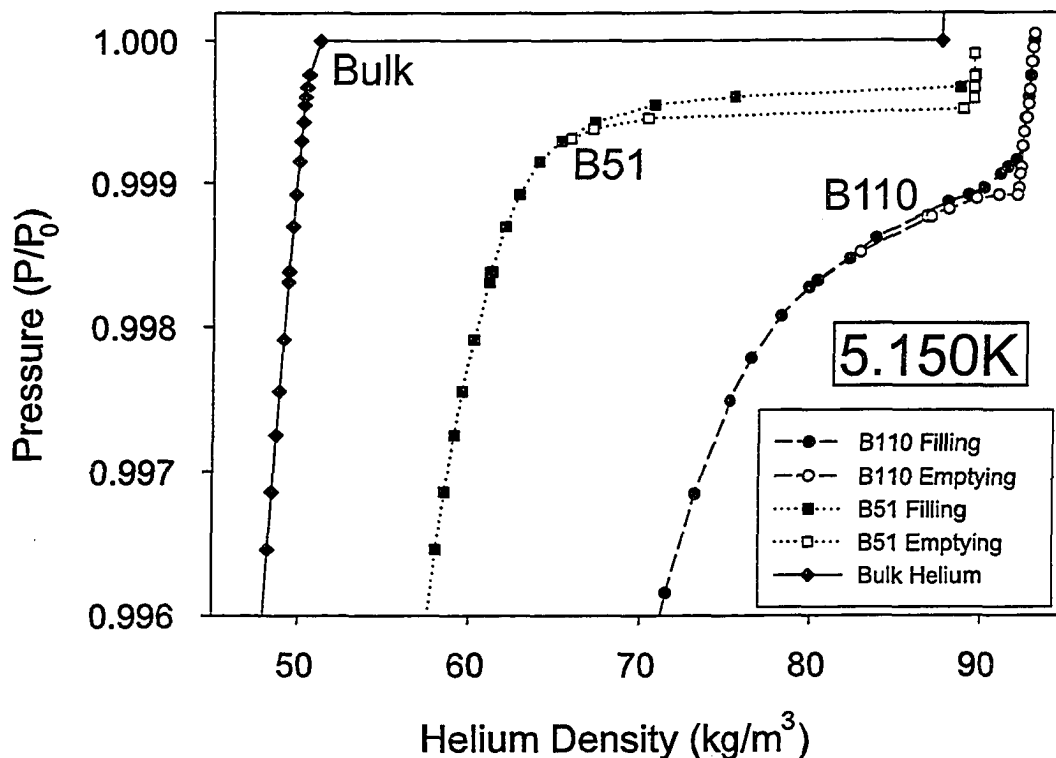
Figure 5.55: Adsorption isotherms of helium at 5.150K in aerogel B110 and B51. The statements made in the caption of Figure 5.54 apply here as well, and the difference in hysteresis loop shapes is more obvious here. By this temperature hysteresis has almost disappeared in B110, and the remaining loop is just a small triangle; in B51 the loop remains distinct and much more rectangular.

The disappearance of the hysteresis loop with temperature is also very different in these two samples. In B110 the loop disappears between 5.150K and 5.160K ($\sim$40mK below T_c), while in B51 it disappears between 5.170K and 5.180K ($\sim$20mK below T_c). Thus, the hysteresis loop closes at a temperature below T_c which is roughly proportional to the aerogel density. However, perhaps more significant is the manner in which the loop closes. The hysteresis loop in sample B51 covers smaller and smaller pressure ranges as the temperature is raised, but its shape does not change drastically as it shrinks. Sample B110, on the other hand, exhibits a hysteresis loop that almost seems to "zip" closed as the temperature is raised; while the high density side of the adsorption isotherm does not change drastically as the temperature is raised, the closure of the loop on the low density side moves to higher and higher densities until nothing is left but a small triangular loop nestled up against the corner of the emptying branch of the isotherm. While at high tem-

136

peratures the B51 loops do adopt a more triangular form than at low temperatures, they never become as triangular as the B110 loops.

Equilibration of helium density in aerogels B110 and B51

It is interesting to compare the behavior of aerogels B51 and B110 in terms of thermal equilibration during fluid adsorption, shown in Figures 5.56 and 5.57. The relaxation of both these samples as they are filled and emptied has been discussed in each sample's respective section; here the time dependence of the adsorbed helium density is directly compared for the two samples at $T_{cell} = 5.100K$. Equilibration appears to be somewhat slower in aerogel B51, but this may have something to do with the lower ballast temperature step. A smaller temperature step creates a smaller pressure change which in turn prevents much latent heat from being deposited into the gel at once (since any latent heat would cause local heating, pushing the local pressure above that of the rest of system). While in the denser gel, most of the latent heat of condensation may be liberated as soon as the pressure is changed, and the sample need only conduct the heat away, in B51 perhaps the slower response indicates that in addition to the smaller gradient across the sample, there is a longer process of condensation occurring. Also, aerogel B51 appears to not have equilibrated by the end of the data shown here – this is in fact the case. Neither of the points shown for B51 were given sufficient time for the adsorbed helium density to reach its limiting value.

137
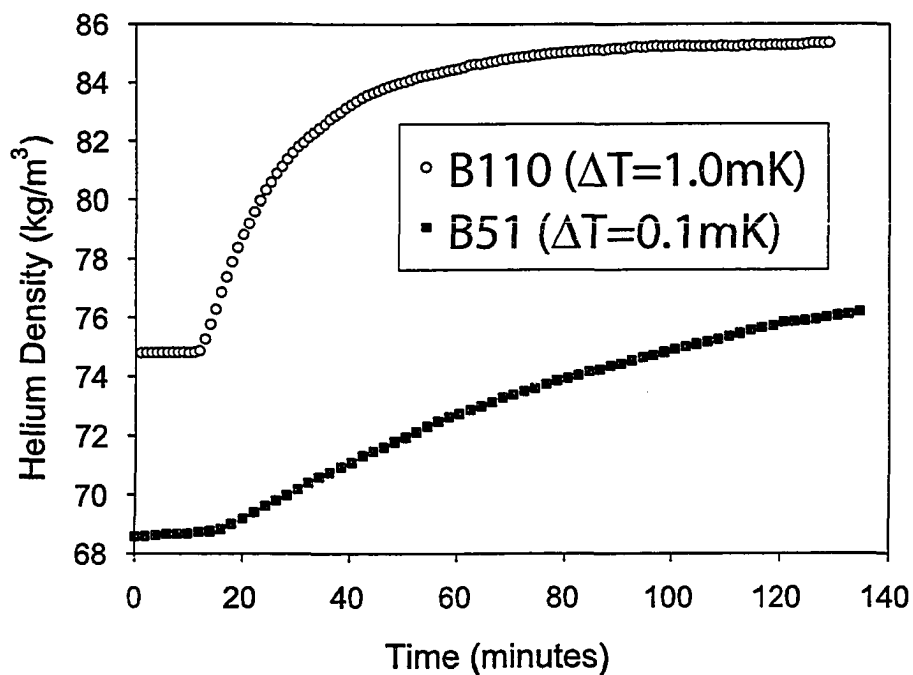
Figure 5.56: A comparison between the equilibration of adsorbed helium density in aerogels B110 and B51 during filling at $T_{cell} = 5.100K$. Both samples show very slow relaxation, with the B51 sample appearing proportionally slower. Note the much smaller pressure (i.e. T_B) step necessary to cause a large density change in aerogel B51.
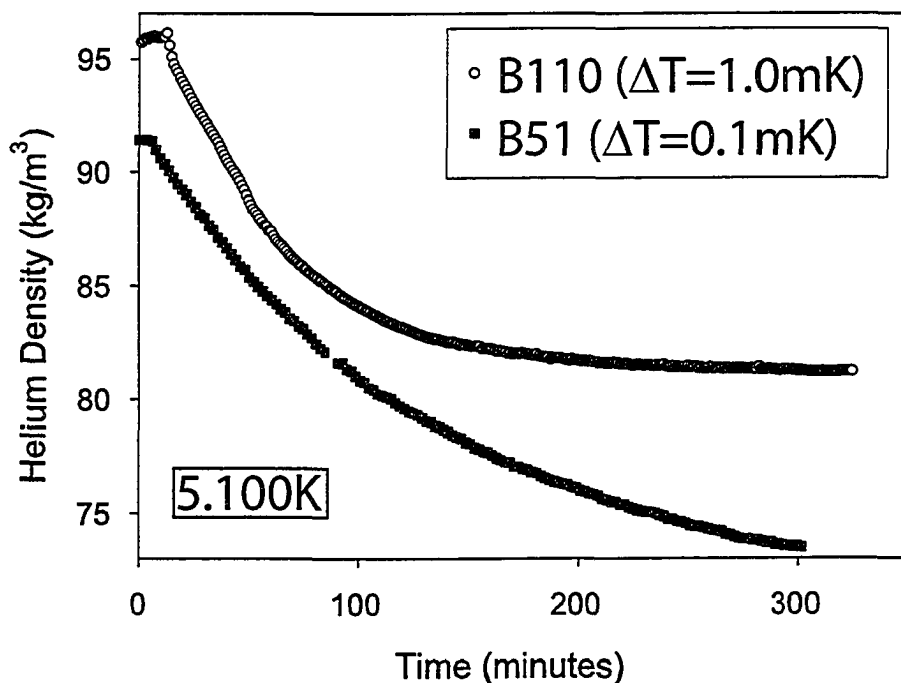
Figure 5.57: A comparison between the equilibration of adsorbed helium density in aerogels B110 and B51 during emptying at $T_{cell} = 5.100K$.

138

5.10 Density Calibrations for Resonator Experiments

The density calibrations for helium in the two aerogel resonators described in the next chapter were constructed from capacitive measurements like those shown throughout this chapter. Both helium resonators were filled at $T_{cell} = 5.700K$, so calibrations were made by fitting the density determined capacitively from isotherms at 5.700K to a polynomial in pressure. Density calibration isotherms and polynomial fits are shown in Figure 5.58 for gel B110 and Figure 5.59 for gel B51.

The density calibration used for the neon resonator results, on the other hand, was constructed by dosing the cell with gas at a known pressure in a known volume. This calibration is discussed in detail in chapter 6.

$$Density = -1.31835*10^{-5}P^6 + 3.780511*10^{-3}P^5 - 0.4486281\,P^4$$
$$+ 28.18813\,P^3 - 988.7216\,P^2 + 18355.65\,P - 140895.9$$
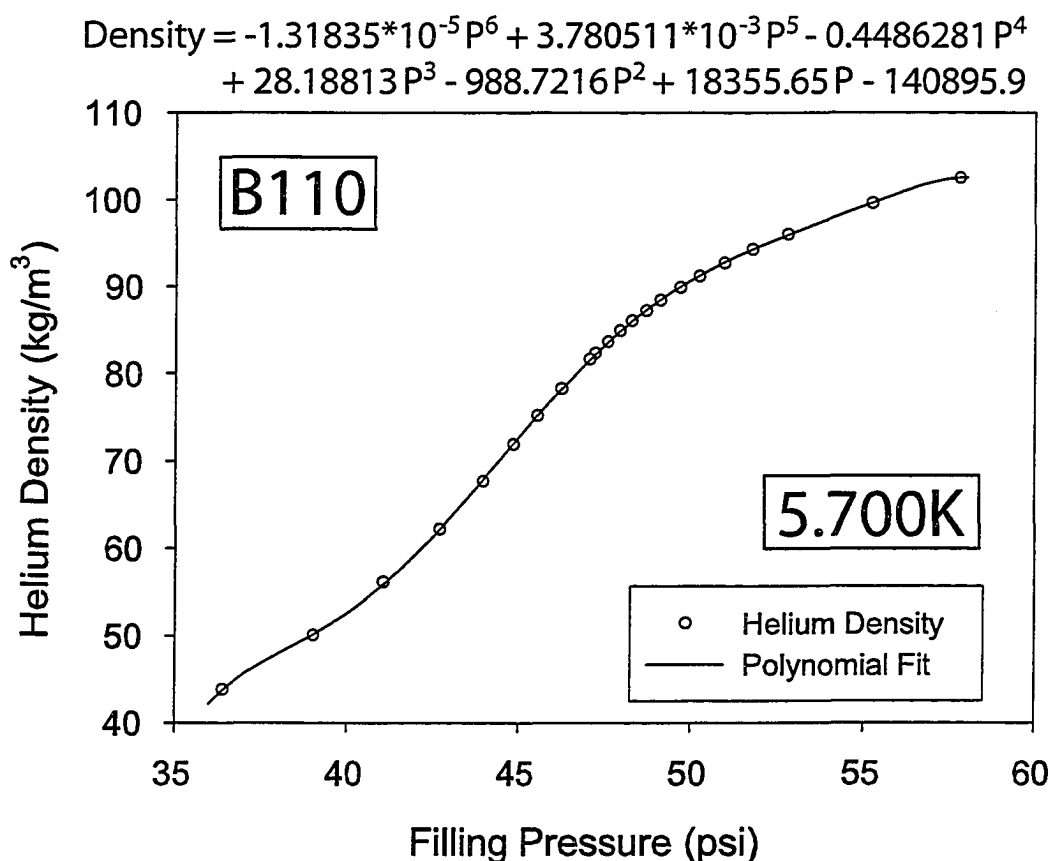
Figure 5.58: This is the density calibration for helium in aerogel B110 at 5.700K. The polynomial fit is given at the top of the figure. This calibration was used in the resonator experiments described in the next chapter.

$$\text{Density} = -1.4351410 * 10^{-5} P^6 + 4.1882100 * 10^{-3} P^5 - 0.50573883 P^4$$
$$+ 32.333459 P^3 - 1154.0517 P^2 + 21803.604 P - 1703543.6$$
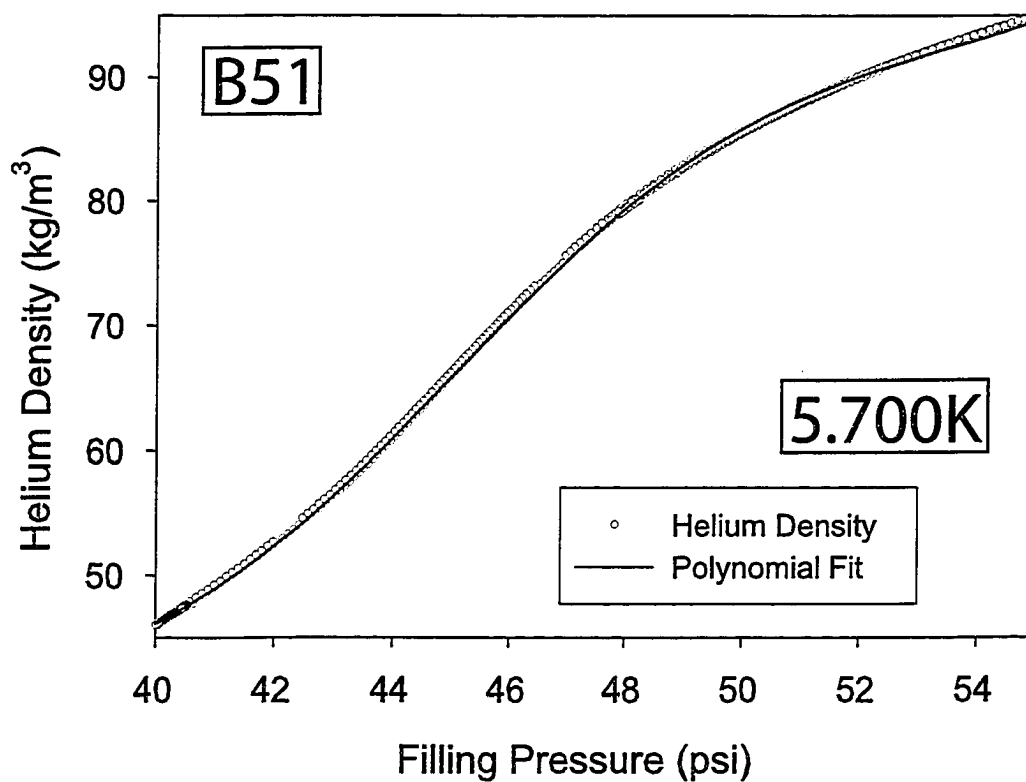
Figure 5.59: This is the density calibration for helium in aerogel B51 at 5.700K. The polynomial fit is given at the top of the figure. This calibration was used in the resonator experiments described in the next chapter.

Chapter 6

Acoustic Investigation of Fluids in Aerogel

I completed three experiments using a low frequency acoustic resonance technique to sense the phase separation of fluids in aerogels by locating a sudden change in elastic properties of the fluid-aerogel system. While this technique promised the possibility of pinpointing precise temperatures for the liquid-vapor transition in aerogel, details of the transition and of the mechanical behavior of aerogel complicated matters. In the following sections I will give an overview of why we chose to try a resonance measurement of the coexistence curve, what sort of acoustic response we saw, and what can be inferred from that response.

6.1 Acoustic Resonance Experiments

The resonant frequencies of a body depend on its elastic properties, so that by measuring those frequencies it is possible to reconstruct the elastic constants governing the body. This principle is used in techniques such as resonant ultrasound spectroscopy[135] and, in simple systems, a single measurement can allow you to extract elastic moduli, such as Daughton *et al.* obtained from monolithic pieces of aerogel[123]. The use of acoustic resonators to detect fluid phase transitions goes back decades (for example, see [136]), and is still used today. Even if absolute values for elastic constants (or, for fluids, compressibility) are not extracted, resonance measurements can be used to locate phase transitions – simply locating the temperature at which the elastic properties change suffices to pinpoint the location of the transition.

Early work on the thermodynamics of critical fluids near the liquid-vapor critical

141

point used the acoustic resonance in cylinders to map the sound speed in a fluid along isochores (scans whose overall density remained constant while temperature was varied)[136]. Sound speed dipped sharply as the critical point was approached, and the location of the minimum could be used to map out a coexistence curve while at the same time providing information on the critical behavior of the compressibility. Since sound is adiabatic, the sound speed is related to the adiabatic (κ_S) and isothermal (κ_T) compressibilities by Equation 6.1:

$$v^2(0) = \frac{1}{\rho\kappa_S} = \frac{1}{\rho\kappa_T} + \frac{T\left(\frac{\partial P}{\partial T}\right)_v^2}{\rho^2 C_v} \tag{6.1}$$

A disadvantage of this resonance technique is the large sample volume involved – more precise measurements of the coexistence curve have been made using other techniques (such as capacitive measurements of dielectric constants[19]) because gravity-induced density gradients across the sample become significant near the critical point. However, when a fluid is confined within a porous medium such as aerogel the density stratification is not expected to be a problem since interactions with the medium should dominate any gravitational force.

6.2 Cell Design and Cryostats

The cells were constructed to be simple cylindrical resonance chambers. When filled with single phase fluid the resonance frequencies are simply those of a closed pipe of length L:

$$f_n = v\left(\frac{n}{2L}\right)$$

where v is the speed of sound in the fluid and n is any integer. The cells were constructed to fit a monolithic cylinder of aerogel snugly while minimizing the volume of bulk fluid around the aerogel. Therefore, the resonant frequencies of the cylindrical cavity depended on a mixture of the elastic properties of the aerogel backbone and the compressibility of the fluid within the aerogel. To extract the actual fluid compressibility from this data requires a more detailed analysis which takes into account both the solid backbone of the porous medium and the fluid within the medium. Analysis tools were pioneered by Biot for this type of calculation[124, 125, 126]. However my results showed rounded transitions; thus very little information about the critical behavior of the compressibility was likely to be extracted. Hence, I have

142
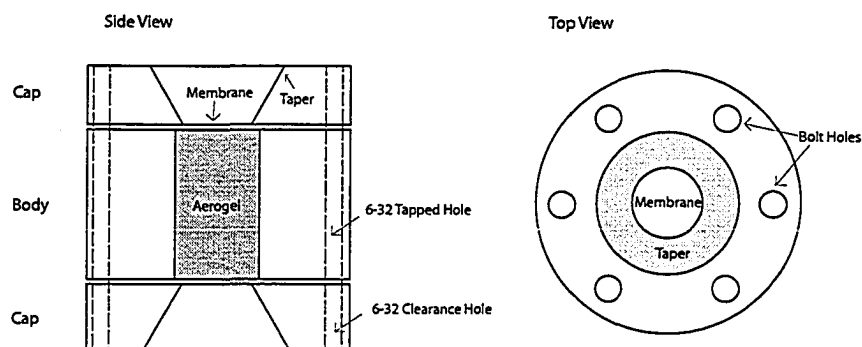
Figure 6.1: This is the cell used to investigate neon in aerogel B110 (95% porous). The body of the cell incorporated a six-bolt circle of tapped 6-32 holes to hold 6-32 steel threaded rod; the caps were then fixed on with nuts. The aerogel cavity was machined to fit the aerogel sample snugly, and had a very slight taper to match a slight shrinkage in one end of that particular aerogel sample. Discs of 0.0105" thick PZT were soldered directly onto the outside of the thin membrane in each cap. The cap-body seal was provided by indium wire.

used the features of the resonant frequency along isochores solely to map out the coexistence curve.

6.2.1 Cell Construction

The resonance cells were machined from copper rod stock and capped by two thin membranes. The cavities were machined to fit the precise dimensions of the aerogels, once dried – it was much easier to machine the resonators to fit individual gels than to manufacture gels to fit the resonance cavities. Schematics of the sample cells are included as Figures 6.1 and 6.2. A number of earlier data runs used similar cells, but the data is not included due to poor signal quality (because of poor sensitivity), the presence of too much bulk fluid, or the explosion of the sample cell (not caused by me) before proper calibrations could be made.

The caps were sealed with indium for the neon resonator, and the membranes could withstand pressures up to $\sim 700psi$ before deforming enough to damage the brittle PZT ceramic transducers. The caps on the helium resonators were sealed and held in place using blue Bipax Tra-Bond (BA-2151) epoxy; the pressure was kept below $\sim 65psi$ to avoid cell damage.

143
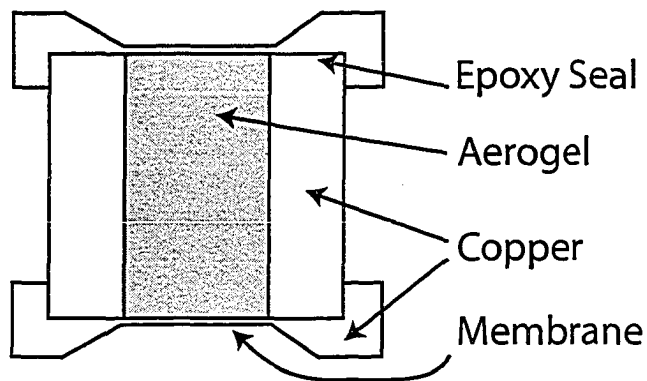
Figure 6.2: This is a schematic of the cells used to investigate helium in silica aerogels B110 and B51 (95% and 98% porous, respectively). These cells were very similar to the neon cell described in Figure 6.1, but were held together by epoxy, obviating the bolts.

6.2.2 Signal Generation and Detection

A thin piezoelectric transducer (0.0105" thick PZT disc with silver electrodes) was soldered onto the outside face of each acoustic membrane, electrical contact to the top face of the transducer was made by directly soldering a thin copper wire to the transducer. The intrinsic resonance of these transducers was in the MHz range, far from interfering with the fluid resonances. One transducer was excited by a sinusoidal signal from a digitized function generator (Stanford Research SR345) while the signal from the other transducer was fed into aa lock-in amplifier (Stanford Research SR530); a schematic is shown in Fig 6.3. The sinusoidal excitation signal had an amplitude of 2 volts, peak-to-peak. The excitation frequency was swept over a range that included the fundamental resonant frequency of the closed pipe system and usually the second harmonic frequency of the cavity. Occasionally other resonances interfered with the signal (e.g. mechanical resonances of the membranes themselves), especially at higher frequencies. The absolute magnitude of the lock-in response was not used in any analysis – the maximum in the response was used solely to locate the resonant frequency of the cavity. Examples of output from the resonators are included in Section 6.4, along with explanations of how they were interpreted.

6.2.3 Cryostats and Temperature Control

The neon resonator was mounted on a "CTI Cryocooler 8" closed cycle refrigerator. The cell was suspended on a braided copper cable to adsorb the vibrations caused by the fridge's piston; cooling was provided through another braided copper cable connected to the baseplate of the cryostat. Temperature was controlled using a Neocera LTC-21 temperature controller reading a 100Ω Platinum resistance ther-

144
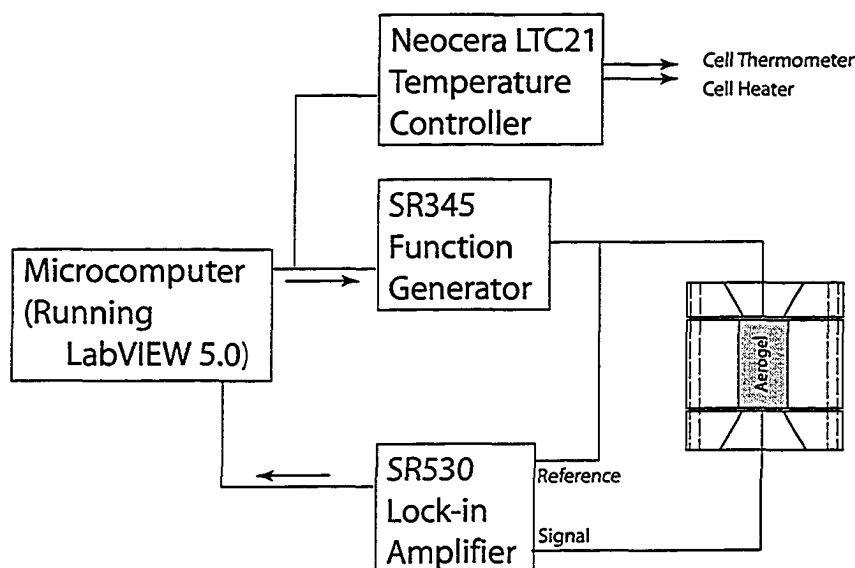
Figure 6.3: This is a schematic of the electronics for measuring acoustic response. All parts of data collection were performed by custom made LabVIEW data acquisition software. The response from the lock-in amplifier was recorded as the excitation frequency was swept over the frequency range of interest. The resultant spectrum was also analyzed using our own LabVIEW data analysis programs.

mometer and controlling via a 200Ω thick film resistor both mounted on the cell body. The calibration of the thermometer proved to be in error by over 100mK, an issue addressed in section 6.2.4.

The helium resonators were mounted below the 1K pot of a dilution refrigerator, although the dilution fridge was not run during data collection. Again temperature was controlled by the Neocera LTC-21 bridge using a resistive thermometer and 200Ω thick film heater; in this case a calibrated Germanium thermometer (LakeShore Serial Number #21017) was used. The B110 resonator was cooled by admitting a few mbar of exchange gas into the vacuum can, while the B51 resonator was cooled through a brass mounting block acting as a weak thermal link to the pot.

6.2.4 Thermometer Calibrations

All thermometers used in this work came with manufacturer's calibrations. However, the platinum resistance thermometer used for the neon experiments showed signs of a large deviation ($\sim 0.2\%$) from that calibration. To address this, a short experiment was performed to map out the bulk neon coexistence curve and use the critical

145
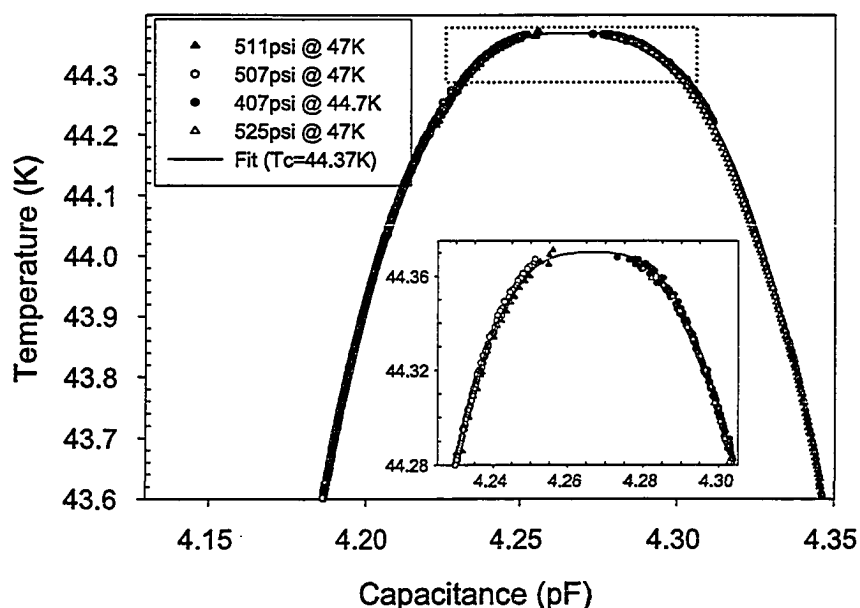
Figure 6.4: The coexistence curve of neon, measured by the capacitance of a cylindrical capacitor with neon as the dielectric between the plates. The inset is a blow-up of the region near the critical temperature. The solid line is a fit to the form of Eq. 6.2. The T_c used in the fit indicates the offset in the thermometer calibration.

temperature as a fixed point to adjust the thermometer readings.

As we did in chapter 5, the bulk coexistence curve was mapped out using a coaxial capacitor with fluid as the dielectric between capacitor plates. The results are included as Figures 6.4 and 6.5. The capacitor was mounted in a large cavity in a copper experimental cell, pressurized at temperatures above the critical point of 44.48K, sealed, and slowly cooled along these isochores.

The filling pressure controlled the average density of the neon within the cell, and consequently the position of the meniscus once the neon began to separate into liquid and vapor. Four filling densities are shown in Figure 6.4, each with a different range of temperature and density that could be probed before the meniscus reached the level of the capacitor. Once the meniscus reaches the capacitor, the capacitance depends on the position of the meniscus as well as the dielectric constant of both the liquid and vapor phases, making this data more difficult to interpret.

To a first approximation capacitance is directly proportional to fluid density (i.e. $\rho_{neon} \propto C - C_0$). The data have not been converted to absolute densities, since the critical temperature and critical exponent β can be extracted without the task

146
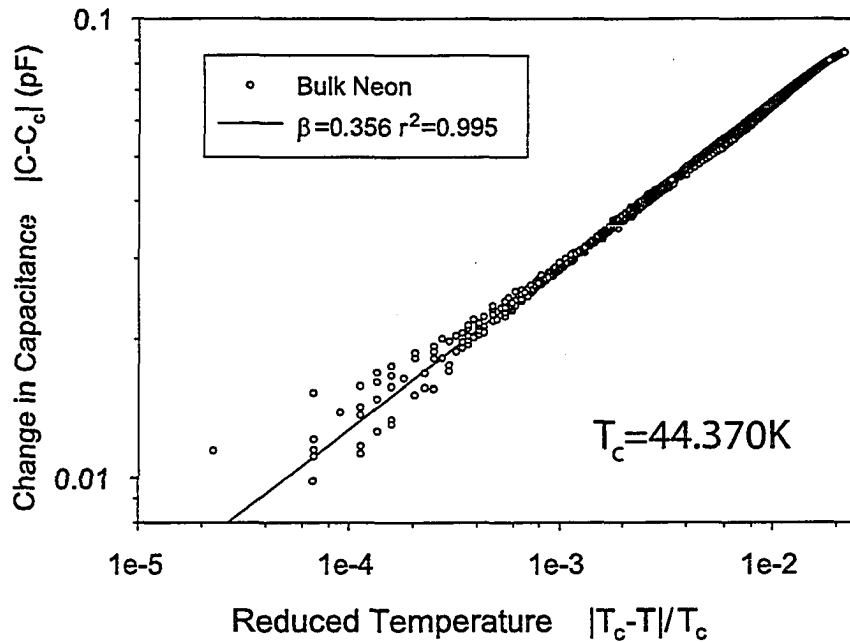
Figure 6.5: The data from Figure 6.4 plotted in terms of reduced variables. The slope of the line of best fit gives an approximate value for β, although the presence of non-asymptotic correction terms (i.e. B_1, B_2) leads to a value ($\beta = 0.356$) above that seen asymptotically close to the critical point ($\beta = 0.327[19]$)

of calibrating density. The fit included in Figure 6.4 is of the form

$$\left| \frac{\rho_c - \rho}{\rho_c} \right| = B_0 \epsilon^\beta \left(1 + B_1 \epsilon^{\frac{1}{2}} + B_2 \epsilon \right) \qquad (6.2)$$

where $\beta, B_0, B_1,$ and B_2 are taken from the data of Pestak and Chan[19]. The only parameters that were adjusted were the critical temperature, T_c, and the reference capacitance, C_0. The fit is excellent and the log-log plot shows no marked deviation from linearity, but it requires us to assume a critical temperature of 44.370K. This deviates from the accepted value of 44.479K[19] by 109mK. This calibration was performed soon after finishing the final resonator run and, if the thermometer calibration drift is slow, this data should reflect the thermometer error in that run.

The bulk neon resonator results shown later and the capacitive measurements shown in Figure 6.4 show that the thermometer calibration must be shifted by between 80mK-145mK. Signs of the thermometer calibration being off are evident in other work using this thermometer as well; in Hong Wee Tan's work[137] in this lab on neon in aerogel the thermometer already exhibited an offset. In Figure 3.11 of that work the apparent critical temperature of bulk neon is 44.400K, indicating an error of about 80mK in the thermometer. All this variation indicates that the

147
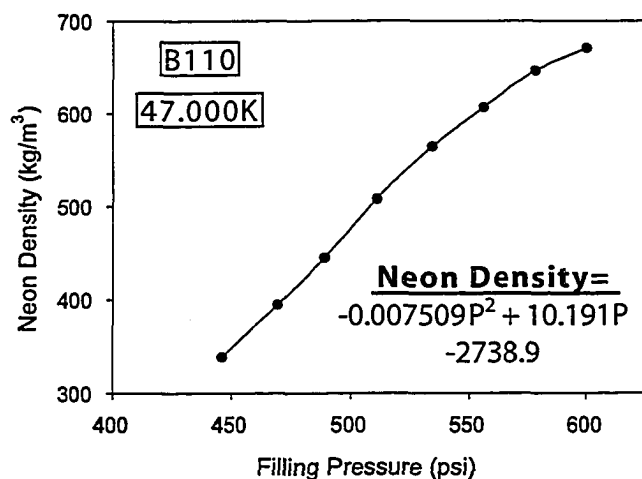
Figure 6.6: The density calibration for neon in aerogel B110 at 47.000K. This was constructed by adding known quantities of neon to (and removing neon from) the cell and allowing the pressure to come to equilibrium.

calibration of the platinum resistive thermometer is not stable (over years) to better than 100mK. The capacitive measurement of the neon coexistence curve discussed above was taken soon after the neon in 95% resonator data run, so it is reasonable to use it to calculate a correction to the measured temperatures (+109mK), but even this correction must be treated with some skepticism.

6.2.5 Density Calibration for Neon in B110

The density of neon in our experiment was calibrated by dosing the cell with neon from a gas handling system of known volume. The resultant calibration curve relates pressure at $T_{cell} = 47K$ to the density of neon in the cell and is shown in Figure 6.6.

6.3 Software and Data Collection

All data acquisition was performed with software written within the National Instruments LabVIEW programming environment. The programs, also referred to as "virtual instruments" (VI's), were all written by me or adapted from VI's written by Dr. Beamish and have also been adapted to control other experiments in the lab. The electronics used for acoustics and for temperature control were all controlled through the VI's, allowing for completely automated data collection.

The VI's set the sample temperature, evaluated when the temperature had stabilized and waited a prescribed "equilibration time" while the sample's internal temperature settled. They would then collect a full spectrum and proceed to the next data point. The VIs also tracked and logged the resonant frequency as a function of time, although this method could not be completely trusted since it had trouble dealing with the spurious resonances and odd peak shapes. The log files

148

were valuable in showing how quickly the cell equilibrated, but the final data have all been taken from the full spectrum data files.

The only factor that was not automated was the filling and emptying of the sample. Filling and emptying were performed well above the critical point (at 47K in neon and at 5.7K in helium) and had to be done manually, usually once per day. There was no direct measure of sample density available, so the neon density was calibrated by dosing the cell from a GHS of known volume (see Figure 6.6); the helium densities were taken from capacitive isotherms described in Section 5.10.

6.4 Form of Results

The goal of these experiments was to precisely map out the liquid-vapor coexistence curves of helium and of neon in their critical regions, when they are confined to highly porous silica aerogel. This goal required hundreds of data points for each system and, coupled to the very long equilibration times for the samples, this translated into weeks of data collection for each sample. This short section is devoted to describing the form of the data, illustrated with examples from a simpler bulk neon experiment done to test the technique.

Each coexistence curve is constructed by locating the transition temperature along each of a series of isochores. If one has observed true liquid-vapor coexistence, plotting the transition temperatures against the fluid density should produce a curve which is approximated by the equation:

$$|\rho - \rho_c| \propto \left| \frac{T - T_c}{T_c} \right|^{\beta}$$

The exponent β can then be determined from a fit to the data, and this will shed light on which universality class contains the phase transition. Each isochore requires a day or so to collect, and produces a single $(T - \rho)$ point for the coexistence curve – at least a dozen of these points are necessary for the complete curve.

Each isochore, in turn, is constructed from a series of a few dozen data acoustic spectra taken as the temperature is varied. Thus, each isochore results in a graph of resonant frequency against temperature. A phase change can be seen where a sharp feature appears in the isochore – usually a dip or a kink. This is often accompanied by a sharp feature in the resonance amplitude as well. Although the form of the feature is well defined (and very obvious) in bulk fluid experiments, it is not as straightforward in the aerogel results. In fact, the form of the feature changes

149
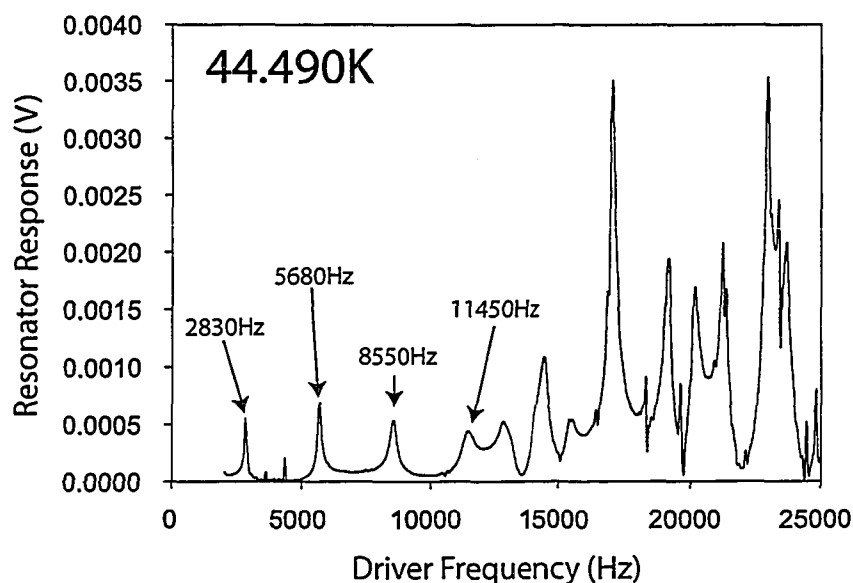
Figure 6.7: This is a spectrum of bulk neon ($\rho \approx 475\frac{kg}{m^3}$) in a cylindrical resonator at T=44.490K, just above its liquid-vapor critical point. Notice the harmonics of a simple closed end cylinder become obscured at higher frequencies by the mechanical resonances of the endcaps and membranes.

significantly as the density changes – isochores from the low and high density sides of the coexistence curve look quite dissimilar. Whatever form the feature takes, its location is recorded (i.e. T, ρ) and plotted on the coexistence curve.

The resonant frequency plotted for each temperature along the isochore is itself determined from a plot of response against frequency for each temperature and density point. These spectra are the actual raw data recorded in the experiment and take two to five minutes to collect, after the cell has equilibrated at each temperature.

6.4.1 Bulk Neon

An example of a spectrum, taken with bulk neon (i.e. no aerogel) near the liquid-vapor critical point is included as Figure 6.7. The fundamental and first three harmonics are labelled, and the higher frequency signal is swamped by interference from other modes. The frequency of the fundamental resonance is recorded and a series of these spectra can be combined to form an isochore, the shape of which can vary depending on the density, as shown in Figure 6.8. At the critical density the isothermal compressibility diverges at the transition, but this is not the case far from the critical point. Thus, the phase transition appears as a very sharp dip when $\rho \sim \rho_c$ but appears as a kink far from ρ_c.

150
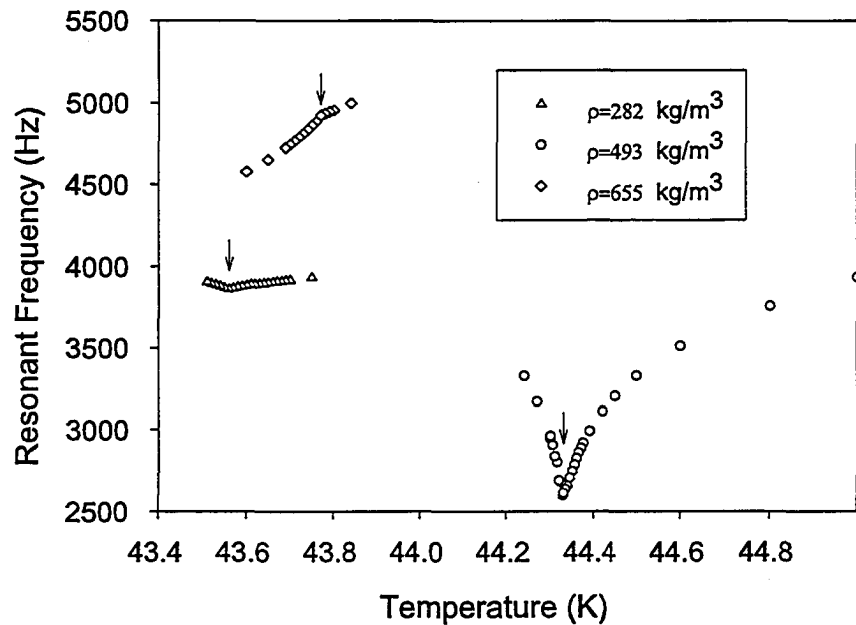
Figure 6.8: These are three isochores for bulk neon, constructed by plotting the position of the first peak in spectra such as Figure 6.7 as the temperature is varied. Near the critical density, the phase transition appears as a sharp dip while farther away it becomes more subtle (but still easily identifiable). Along each isochore the transition temperature is indicated by a vertical arrow.

The position of the resonant peaks can be used to calculate the speed of sound in neon as a function of temperature along an isochore. The fundamental and first harmonic should give identical values for sound speed in a perfect cylindrical resonator. In our case the two peaks give very similar values for sound speed in the one phase region, but the apparent sound speeds differ in the two phase region. This is because the existence of an inhomogeneous fluid distribution, with the appearance of a liquid-vapor meniscus, wrecks the cylindrical symmetry of the resonator and the second resonant frequency is no longer a simple harmonic of the fundamental frequency. Sound speed along an isochore is plotted for $\rho_{neon} = 670\frac{kg}{m^3}$ in Figure 6.9 – below 43.620K the sound speeds change dramatically, marking the entrance into two-phase coexistence. Even when the resonant frequency does not show a large change, sometimes comparing sound speeds calculated from the first two resonant frequencies allows a more precise determination of the transition temperatures.

Combining the data from isochores, one can construct a coexistence curve, as shown in Figure 6.10. Notice that the data must be shifted by 145mK to agree with literature – this error in the thermometer calibration does not agree with that
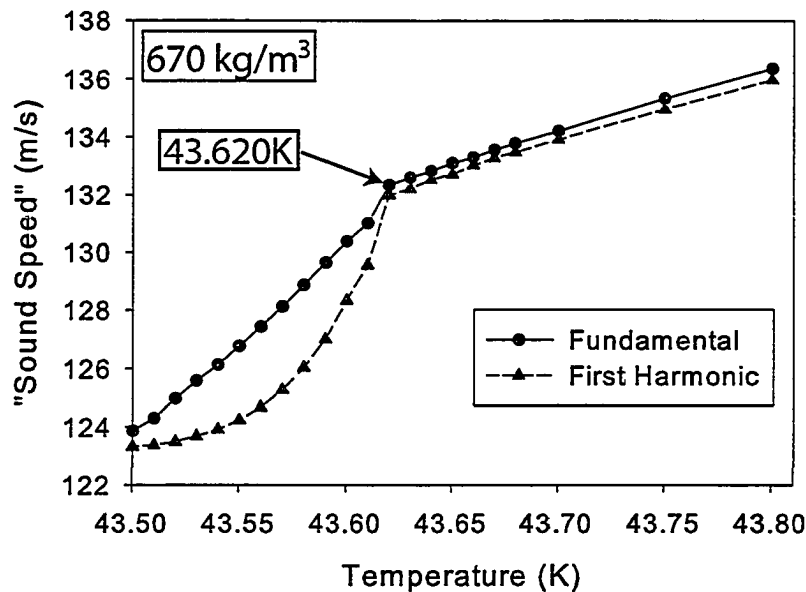
Figure 6.9: Sound speed in neon ($\rho = 670\frac{kg}{m^3}$) as a function of temperature. Above 43.620K the first and second resonance peaks track well and give very similar values for the sound speed, but below 43.620K the two peaks behave differently. This more complicated behavior is an indication of the appearance of a meniscus in the neon which destroys the cylindrical symmetry of the resonance cavity.

determined in Section 6.2.4 and may indicate that the thermometer calibration is not incredibly stable. These data were taken during summer 2002.

Data from the bulk neon resonator were only meant as a quick check and therefore the points are rather sparse and a bit scattered – they illustrate the general shape of the coexistence curve but they do not make it possible to determine critical parameters. The capacitive measurements in section 6.2.4 are much more suited for that sort of analysis. These data also point out the limitations of our density calibration – since density is determined by incremental filling of the cell, the absolute error grows as density increases. This may be seen in the deviation of the high density points from the literature curve.

6.4.2   Fluids in Aerogels

Resonator results for the aerogel cells are of the same form as the bulk neon results discussed above, but with a few complications. The data points along an isochore were necessarily sparse because of long equilibration times (which will be discussed in Section 6.8). At temperatures above the two-phase region, equilibration times of half an hour were usually sufficient to reach equilibrium, while on many runs it

152
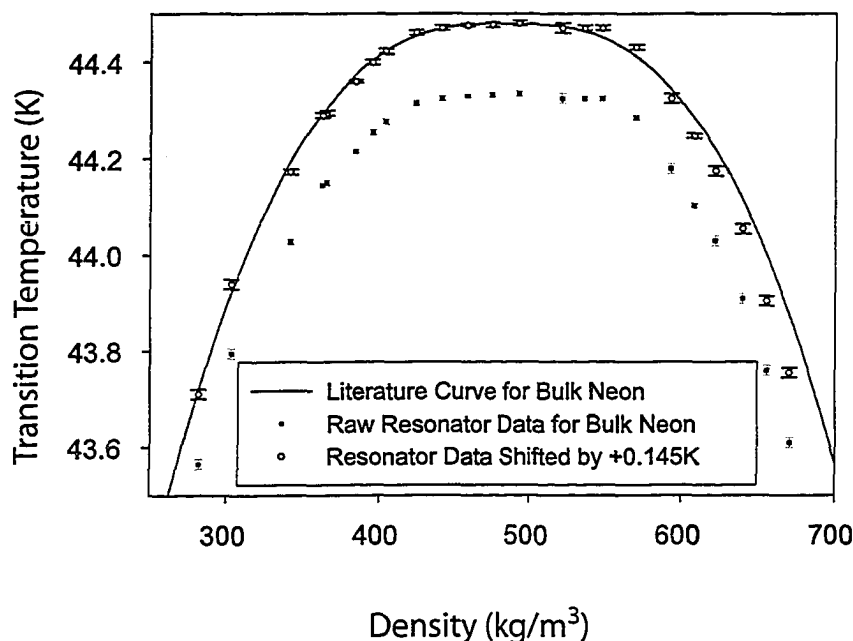
Figure 6.10: These points represent the coexistence curve for bulk neon as determined from acoustic resonance experiments. They have also been re-plotted, shifted by +145mK to agree with the accepted bulk coexistence curve. The solid line is the coexistence curve determined by Pestak and Chan[19].

was impossible to see equilibration within the two-phase region. This reality set the limit on my resolution – with only one or two dozen points along an isochore, the transition temperature could at best be determined within a 10mK window.

The addition of aerogel to the system also drastically affected the form of the resonance spectra. Since the system became a more complex, fluid-porous medium, acoustic resonator, the resonance frequencies were no longer simple harmonics. Also, with the aerogel backbone to help support acoustic modes, the transition did not appear as distinct as in the pure fluid system. In fact, at times it became downright undetectable. This was most strongly manifested by the low density isochores – at best, the transition appeared as a slight inflection of the curve instead of a sharp kink.

Another major complication added by the aerogel was the appearance of peak splitting in many of the spectra. There appeared to be frequency windows in which the resonator did not support a fluid resonance even though one would be expected there. In later experiments it was not uncommon to encounter many such windows, and the windows shifted with density. These are discussed in more detail in the

153

section on helium in aerogel B51, where they were the most obvious. Ironically, this particular complication became worse as my skills in machining and assembling resonators improved, implying that the complication is not due to poor cell assembly or bulk fluid in the resonator. Indeed, this problem increased in severity as the experimental setup became cleaner.

This behavior suggests that some fundamental mode is interfering with my simple longitudinal resonance. It is probably not an external resonance (such as a membrane) since it shifts monotonically with density, but exactly what internal mode is interfering is not clear. The most obvious candidate is a simple torsional mode; the resonant torsional frequency of a cylinder with free ends[135] is:

$$\nu = \frac{n}{2L}\sqrt{\frac{G}{\rho}}$$

However, plugging in some representative values from my cells shows that the fundamental torsional frequency is too high to account for the multiple windows as higher torsional harmonics. While the mode that caused the problem is not quite that simple to explain, it is most likely some sort of mode with a largely shear character which will be addressed later. Similar peak splitting has been seen in resonance experiments with superfluid ^{4}He in aerogel[53].

6.5 Neon in 95% Aerogel

There were two complete data runs completed for what was nominally neon in 95% silica aerogel. Actually, the first data run used a cell that included a significant volume that was not occupied by the aerogel ($\text{Vol}_{gel} \sim 0.8*\text{Vol}_{total}$), and the gel was about 94% porous. These results were used in preliminary reports, and I include the final coexistence curve from that run here, but all of these data are superseded by the second data set. The second set, neon in aerogel B110, represent my highest precision resonator results.

6.5.1 Preliminary results

Our early resonator experiments were plagued by the presence of large quantities of bulk fluid in the cell. This problem was remedied by changing the approach to cell construction. Originally aerogels were grown to fit an experimental cell that had already been constructed. Since aerogels usually shrink slightly during the aging

154

or supercritical drying stages of production, it took many tries to find the correct mould size in which to grow the gel. Even then only a small percentage of the dried gels were in good enough shape to use in an experiment. The first data set was taken when I finally managed to manufacture a gel that was monolithic and close to the size of the resonator cavity, although even then it was a loose fit. After data collection, when the aerogel was removed it had shrunk somewhat – when it was first placed in the cell it filled over 80% of the volume, but when it was removed it filled less than 80%.

The isochores resembled those of bulk neon, although the transition was rounded instead of a sharp dip or kink. An isochore is included as Figure 6.11, for a neon density of 527kg/m^3. The isochore includes curves tracking the frequency of the first and second resonant modes; the phase transition appears as a feature at exactly the same position in both curves. A third curve has been overlaid, showing a much denser data set taken near to the transition temperature in an effort to more precisely fix the transition temperature.

From a series of these isochores a coexistence curve was constructed, Figure 6.12. The error bars reflect the degree of difficulty in choosing a single transition temperature from a smoothed feature in the isochore. The data on the high density side of the curve are truncated because the high filling pressures necessary to achieve higher densities endangered the resonator. The filling pressure was restricted by the strength of the thin acoustic membranes at the ends of the resonator.

The coexistence curve is narrowed and shifted towards the high density side of the bulk coexistence curve as expected. The curve appears to be shifted to lower temperatures, but much of that shift may simply be an error in thermometer calibration as discussed in the section 6.2.4. The temperatures have not been shifted to account for this calibration error. The shape of the curve looks like it could be described by a critical exponent *higher* than the bulk curve, but the behavior of the fluid in the aerogel is no doubt obscured by the presence of so much fluid outside the aerogel. For this reason, no detailed analysis of this curve was performed.

6.5.2 Final results

A much better data run was completed in aerogel B110 after a couple of years of practice and some partially successful attempts. In fact, these data form the highest quality set of resonator results collected for this thesis. Compared to the helium

155
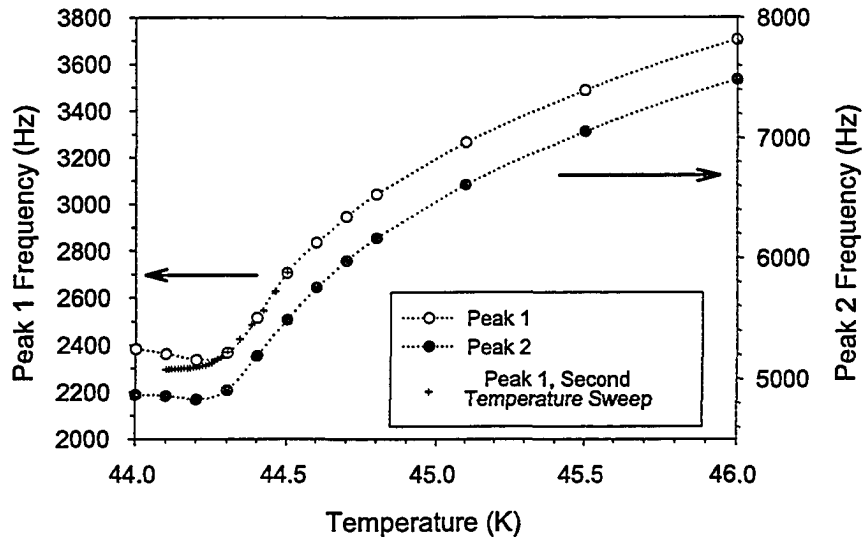
Figure 6.11: Isochore for neon ($\rho = 527 kg/m^3$) in $\sim 95\%$ porous aerogel from the early resonator; only the cooling runs are shown here.
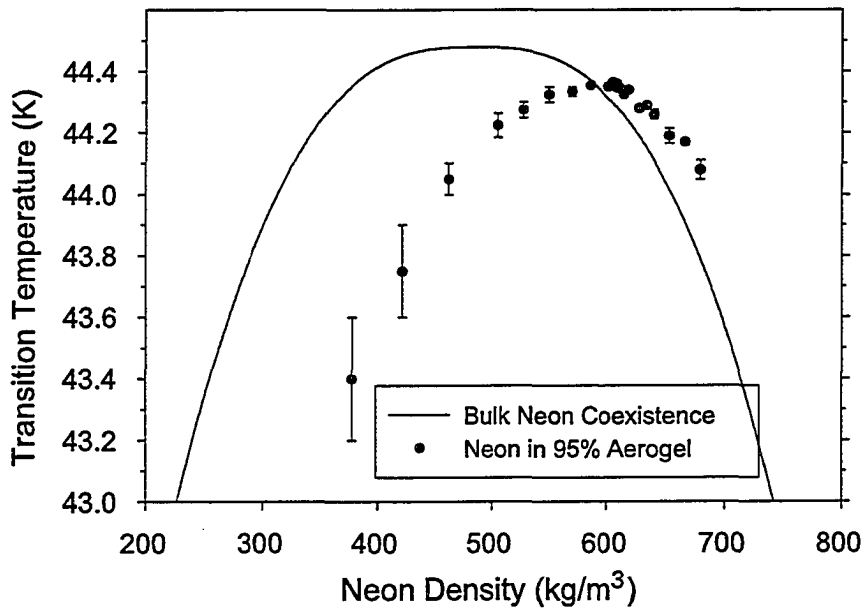
Figure 6.12: Coexistence curve of neon in 95% aerogel as we published in preliminary reports, constructed from isochores like that shown in Figure 6.11. The solid line is the accepted curve for bulk neon. The data plotted here *have not* been adjusted to account for the thermometer calibration.

156
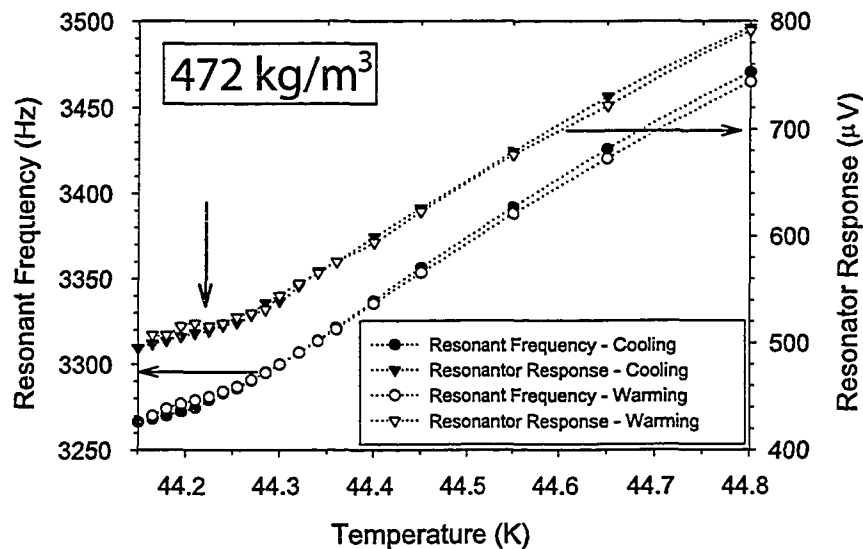
Figure 6.13: This isochore shows the low density behavior $(\rho = 472\frac{kg}{m^3})$ of the first resonance peak of neon in aerogel B110. The horizontal arrows link the frequency and amplitude data to their respective axes, while the vertical arrow denotes the transition temperature.

data that follow, the neon data are denser and have smaller uncertainties.

The liquid-vapor transition still did not appear as a sharp kink in the isochore for low densities – it appeared as a gentle inflection or as a slight jump. It is difficult to discern a feature which represents a phase transition – even hysteresis between cooling and warming runs falls below the resolution of the acoustic resonator. These difficulties restrict the data to densities near the critical density (and, consequently, to temperatures close to the critical temperature).

For the denser isochores the transition was more obvious, although exactly which feature of the isochore corresponds to the transition is not immediately evident and it changes with density. The highest density used in this experiment corresponded to the highest filling pressure I was sure the cell could withstand before breaking. Some representative isochores are included as Figures 6.13, 6.14 and 6.15. Each figure includes information on the frequency and amplitude of the acoustic resonance as read from a lock-in amplifier. As such, absolute values of the amplitude have little meaning, but relative amplitudes along an isochore give information on attenuation of the acoustic signal.

From these three representative curves one can see that there is no single feature which marks the liquid-vapor transition, but that signs of the transition become

157
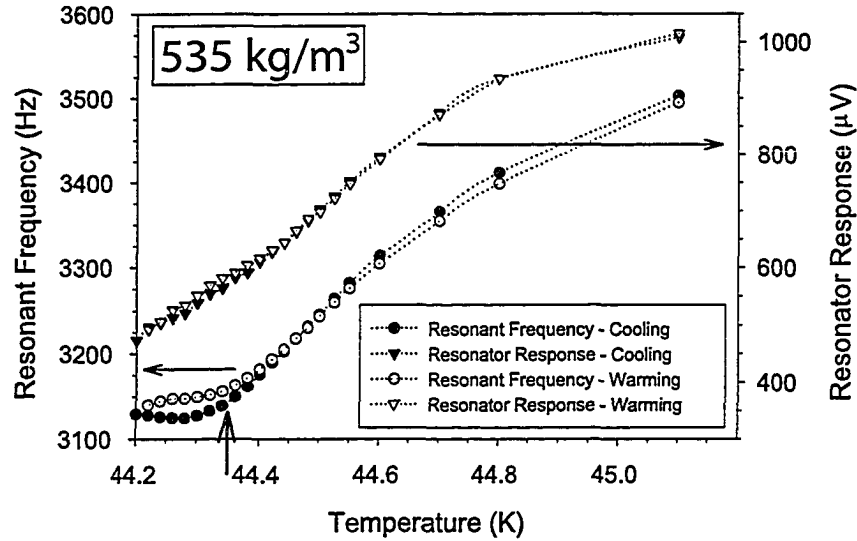
Figure 6.14: This isochore shows the behavior of neon near its critical density in aerogel B110 ($\rho = 535\frac{kg}{m^3}$). The horizontal arrows link the frequency and amplitude data to their respective axes, while the vertical arrow denotes the transition temperature.

Figure 6.15: This isochore shows the high density behavior ($\rho = 641\frac{kg}{m^3}$) of neon in aerogel B110. The horizontal arrows link the frequency and amplitude data to their respective axes, while the vertical arrow denotes the transition temperature.

more distinct as the density increases. On the low density curve it is difficult to discern any significant feature on the scale of the figure, although the slope does obviously change at some point. By the density shown in the second figure the change of slope is more obvious, and hysteresis becomes visible. Finally, at high densities there is a significant, and sharp, change in resonant frequency at the transition. Hysteresis in these isochores is usually a sign of non-equilibrium behavior – below the liquid-vapor transition equilibration times stretched into hours. Each point was taken after waiting a specified time so that before the appearance of two phases each point had adequate time to equilibrate, but after the appearance of distinct liquid and vapor phases equilibration within that time was not guaranteed.

For each sharp feature in the resonant frequency there should be a corresponding feature in the peak amplitude. At the transition you expect to see a sharp increase in attenuation, and consequently a sharp decrease in amplitude. In the lower density curves (Figure 6.13 and Figure 6.14), no such sharp decrease is seen, although in both cases a careful examination of the amplitude curves turns up slight indications of a transition at the same temperature as seen in the frequency curves (i.e. change of slope or appearance of hysteresis). In the high density curve (Figure 6.15) however, there is a sharp decrease in amplitude at the same temperature as the sharp drop in resonant frequency, although it is somewhat obscured since the resonant frequency appears to remain virtually constant above 44.2K. In fact the resonance is split between a peak near 3450Hz and another at 3600Hz. As the temperature was lowered, weight shifted from the higher frequency peak to the lower frequency one without a peak ever moving through the frequency space in between. This behavior is reflected in the *increase* in amplitude as temperature decreases until 44.2K; then the amplitude decreases again because of the condensation of neon. This type of behavior was also obvious in the data for the helium resonators in the next sections and is probably indicative of mode crossing behavior.

Both cooling and warming runs are included in the isochores, and both show the liquid-vapor transition, but often at slightly different temperatures. Since the warming runs start in the two phase region where latent heat may be released or absorbed as the temperature is changed, thermal equilibrium is not established as quickly as in the single phase system *above* the transition. This may result in the warming runs showing an apparent transition temperature higher than the true temperature. When choosing the transition temperature for each isochore, the

159
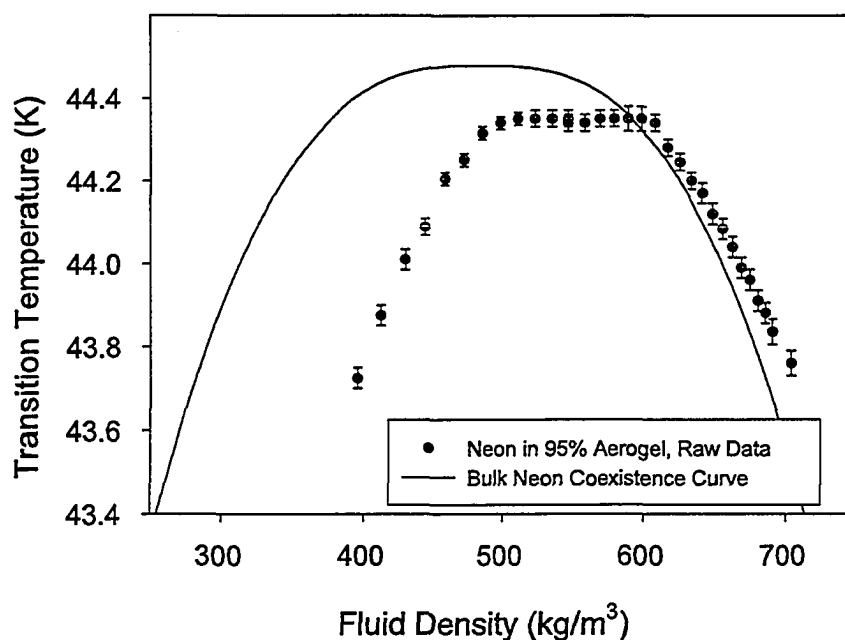
Figure 6.16: The coexistence curve of neon in aerogel B110. This raw data does not take into account the error in the thermometer calibration. The solid line in the accepted coexistence curve of bulk neon.

warming data can be used as a guide, but the precise choice was always made using the cooling data.

The final coexistence curve is shown in Figure 6.16. There are three important differences between the bulk neon coexistence curve (shown by the solid line) and the data for neon in aerogel. The first is that the curve has been narrowed, the second is that the center of the curve has been shifted to higher density, and the third is that the shape of the the coexistence region seems to include a plateau in the center. There is also a shift in transition temperature, although with the uncertainty about the calibration of the thermometer, it difficult to say much about that shift.

If the adjusted temperatures are correct, then the coexistence curve has only been depressed by 0.02K, or 0.05%. This very small shift is an order of magnitude smaller than the shift seen for nitrogen (0.6%) in Apollo Wong's experiments[54, 11]. Although without a fit to the coexistence curve a quantitative analysis of its width is not possible, cursory examination of the curve indicates only slight narrowing($\sim$ 25%). This narrowing is significantly less than that reported in helium but only slightly narrower than nitrogen[54, 11]. The odd plateau seen at the top of

160

the curve is also a new feature. If we ignore the data along the plateau for now, and focus on the low and high density sides of the coexistence curve for neon in aerogel, we can evaluate the critical exponent β. This should be equal to ~ 0.33 for a bulk system close to the critical point, and can be easily extracted from a log-log plot of reduced density versus reduced temperature as:

$$\log \left| \frac{T_c - T}{T} \right| = \beta \left(\log \left| \frac{\rho_c - \rho}{\rho_c} \right| \right)$$

Such a plot is included as Fig 6.17. The figure includes two fits, in which the effective critical temperature is allowed to vary. One curve is the best fit possible assuming Ising behavior (i.e. setting $\beta \sim 0.33$); this is a poor quality fit which shows two distinct regions with different slopes rather than simple linear behavior. A better overall fit is obtained assuming the mean field exponent of $\beta = 0.5$; this also implies a critical temperature near the *bulk* T_c before the thermometer correction (which would further increase it to $T_c = 44.54K$). The apparent mean-field like behavior of this "transition" may simply be a coincidence – it is certainly not behavior we expected, nor is it obvious how we can explain it. In fact we need to remember that there is some doubt about the validity of treating this transition as a regular liquid-vapor transition, especially given the sometimes ambiguous transition markers.

161
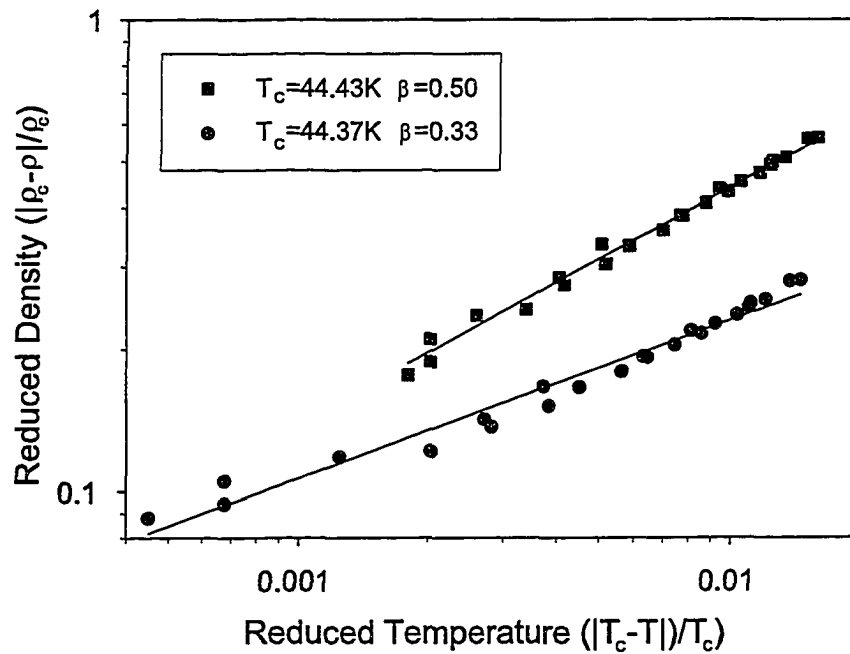
Figure 6.17: The coexistence curve of neon in aerogel plotted in log-log form, in terms of reduced variables. Raw data were used for these plots, with points along the plateau removed. The two fits show the best fits if T_c is allowed to vary while β is either set to an Ising-like value (0.33) or the mean field value (0.50). Note that the Ising like fit is fairly poor – showing systematic variations throughout the temperature range.

162

6.6 Helium in Aerogel B110

There were two attempts at collecting data on helium in aerogel B110 which yielded useful data. The first attempt ended when the cell was accidentally warmed during a helium transfer (not by me) and broke the piezoelectric transducers before a complete data set could be collected. This incomplete data set was started at high density and ended, prematurely, just as the transition was becoming indistinct. The second data set was more complete, but since there was less bulk fluid in the second cell the spectra were plagued by the problems mentioned above; the data presented here is from the second, more complete, data run.

As for the neon data, I have included three isochores from the helium resonator (Figure 6.18, 6.19 and 6.20). Notice how difficult it is to discern an unambiguous transition temperature. To pick a sensible transition temperature one must find a relatively sharp feature that is present in both the first and second harmonic, and preferably one that appears in both the frequency and amplitude of the resonance. Figure 6.18 illustrates very well the effect of those regions where a resonant peak cannot exist – the resonant peak changes positions in discrete jumps as well as gradual shifts. The entire data set for the second peak has been eliminated from Figure 6.20 since the transition is utterly obscured by shifting peak heights that have little to do with the phase of the fluid in the aerogel pores. Most points within this data set were collected after a 15 minute equilibration time – this was sufficient time for points above the transition to equilibrate; points below the transition did not always have time to equilibrate, leading to hysteresis at lower temperatures.

These isochores were used to construct the coexistence curve shown in Fig 6.21. The error bars reflect both the uncertainty in picking a transition temperature from a rounded feature and the uncertainty caused by slight differences in transition temperature determined from the first and second peaks in the isochore.

There is simply not enough precision in the data to draw many conclusions from this curve but some important observations may be made. The curve is narrowed by a factor of two from bulk and it is shifted toward the higher density side of the bulk helium coexistence curve. The data are not precise enough to make any meaningful fits to determine effective critical exponents, but are not inconsistent with an Ising-like fit. They are also not precise enough to state confidently that there is a plateau at the center of the curve as seen in the neon curve, but the curve does seem to
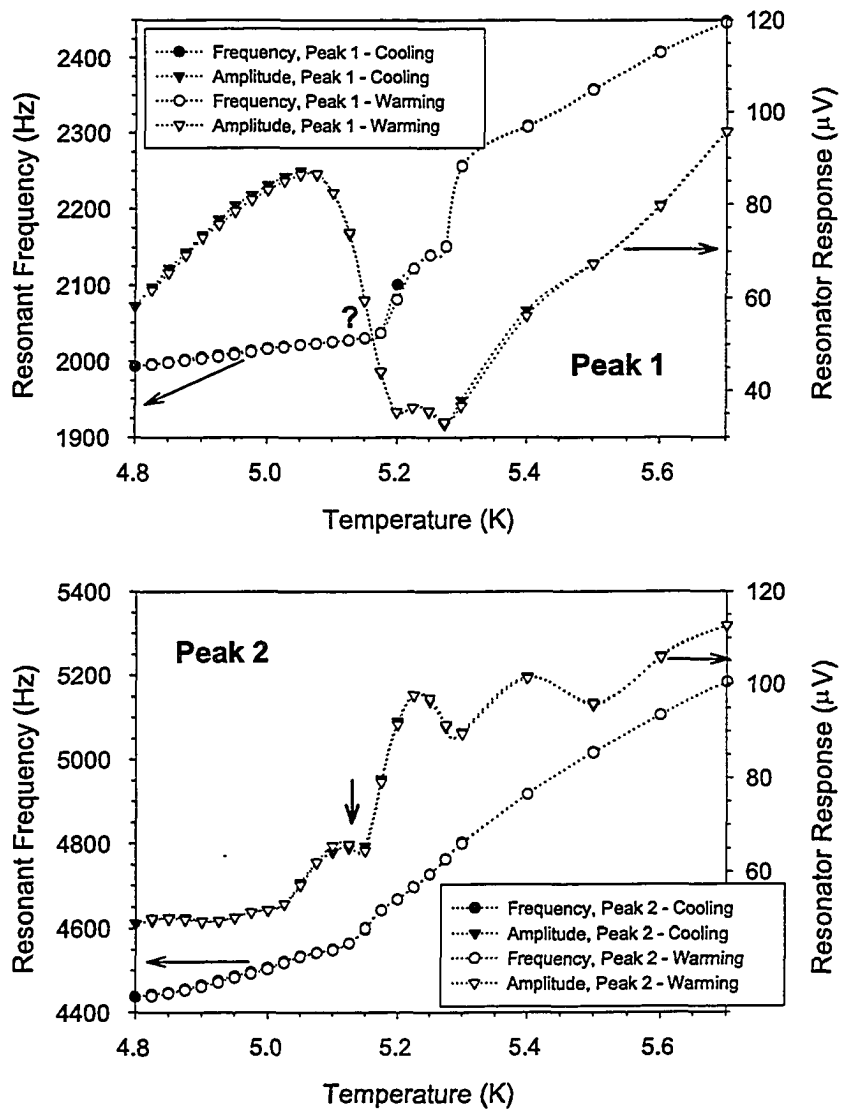
Figure 6.18: This isochore shows the low density behavior ($\rho = 70.0\frac{kg}{m^3}$) of helium in aerogel B110. The two panels track the behavior of the first and second resonant peaks respectively. The horizontal arrows link the frequency and amplitude data to their respective axes, 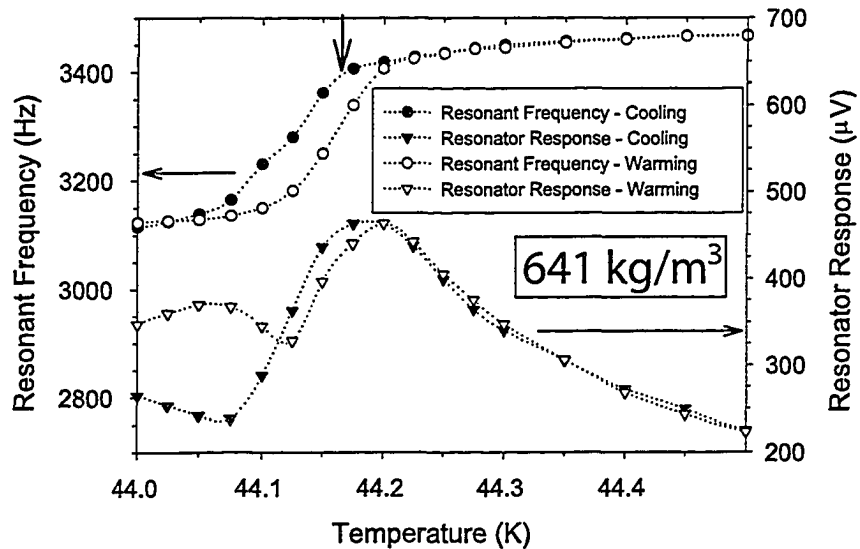while the vertical arrow denotes the transition temperature. The behavior of the first peak is a little unclear near the transition, denoted by a "?".
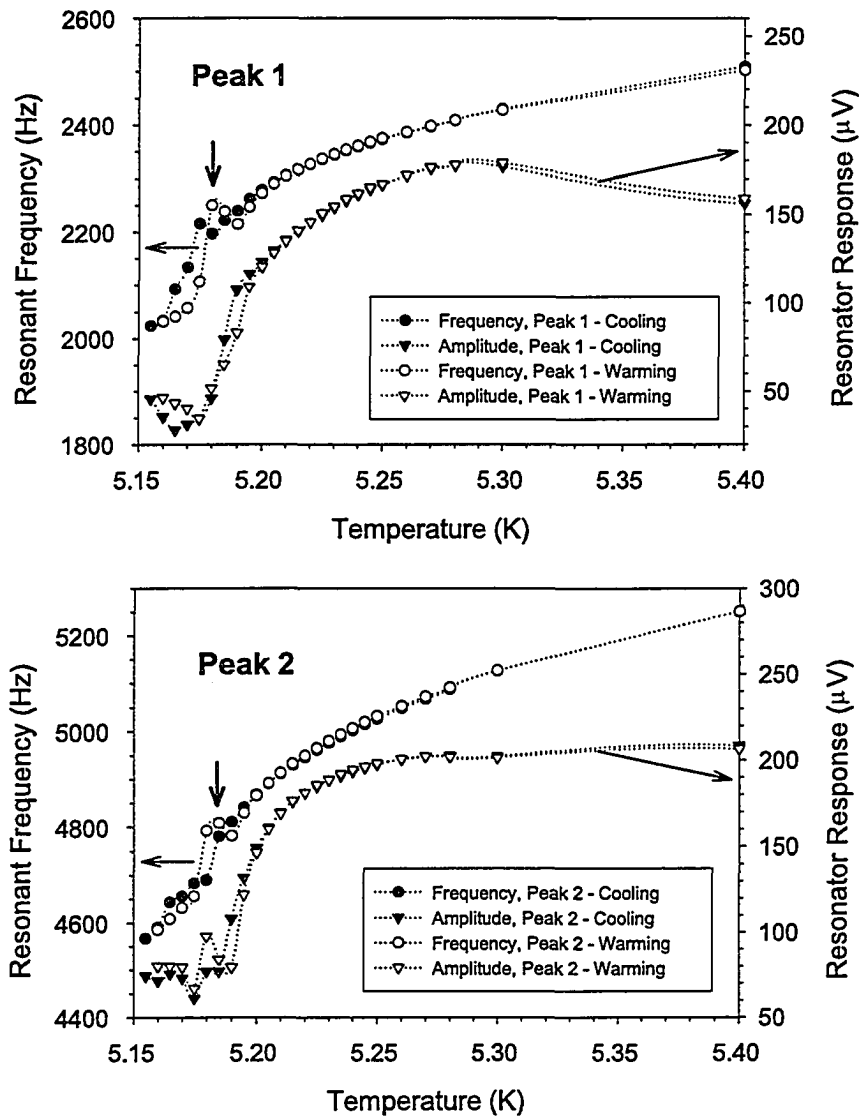
Figure 6.19: This isochore shows the behavior of helium near the critical density in aerogel B110 ($\rho = 88.6\frac{kg}{m^3}$). The two panels track the behavior of the first and second resonant peaks respectively. The horizontal arrows link the frequency and amplitude data to their respective axes, while the vertical arrow denotes the transition temperature.

165
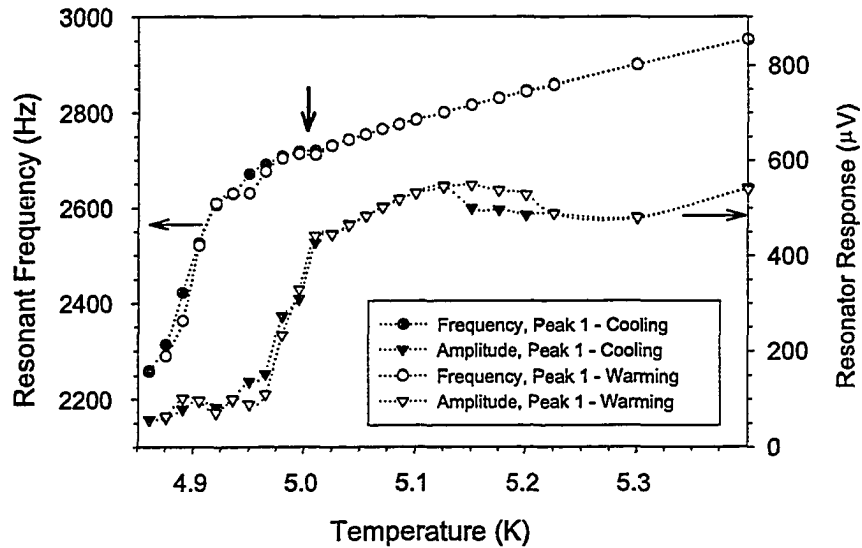
Figure 6.20: This isochore shows the high density behavior $(\rho = 102.5\frac{kg}{m^3})$ of helium in aerogel B110. The second resonant peak has been obscured in the vicinity of the transition and has not been included in this figure. The horizontal arrows link the frequency and amplitude data to their respective axes, while the vertical arrow denotes the transition temperature.
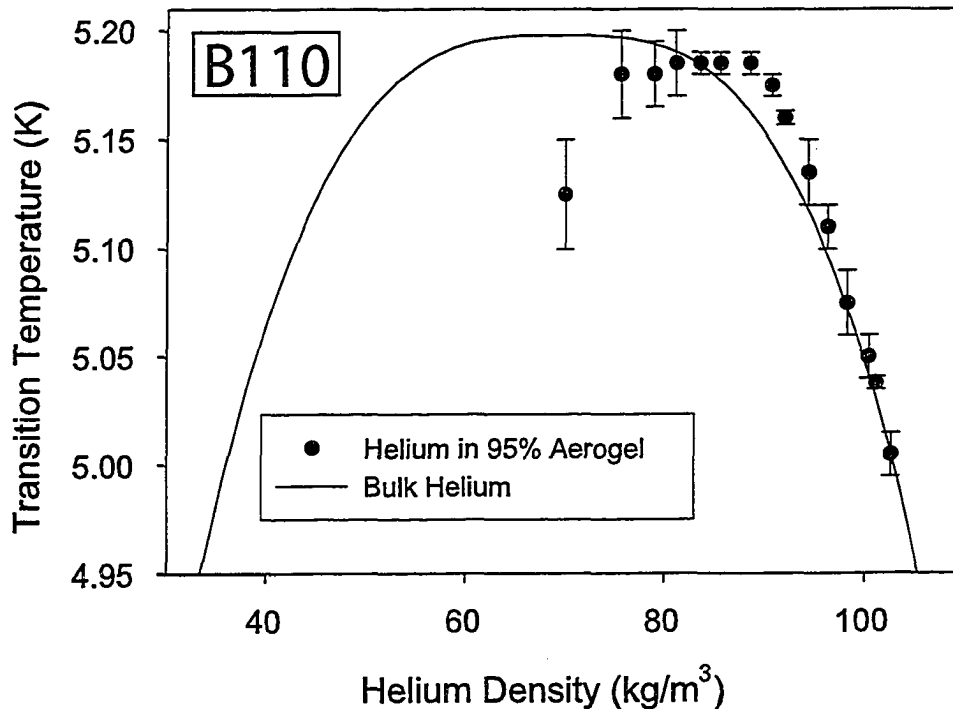
Figure 6.21: Coexistence curve for helium in aerogel B110. As expected it is narrowed and shifted towards higher densities. The large error bars make it difficult to state whether or not the shape of the curve is significant.

166

share that qualitative feature with the neon curve from the previous section. The high density side of the curve also looks steeper than the bulk coexistence curve, which differs from the neon resonator where the curve for neon in aerogel B110 had a high density leg which had a shallower slope than bulk.

The thermometer used for these experiments is much more reliable than that used in the neon experiments – it has been checked against the thermometer used in the capacitive measurements of Chapter 5 and found to agree within a millikelvin over the relevant temperature range. That thermometer in turn has been checked by determining the critical temperature of ^{4}He. The density calibrations for this experiment and the following one (helium in aerogel B51) are probably more reliable than in the neon experiment; they were measured directly, while the neon calibration was constructed from successive dosing, which may have led to a systematic error that grew as the density increased.
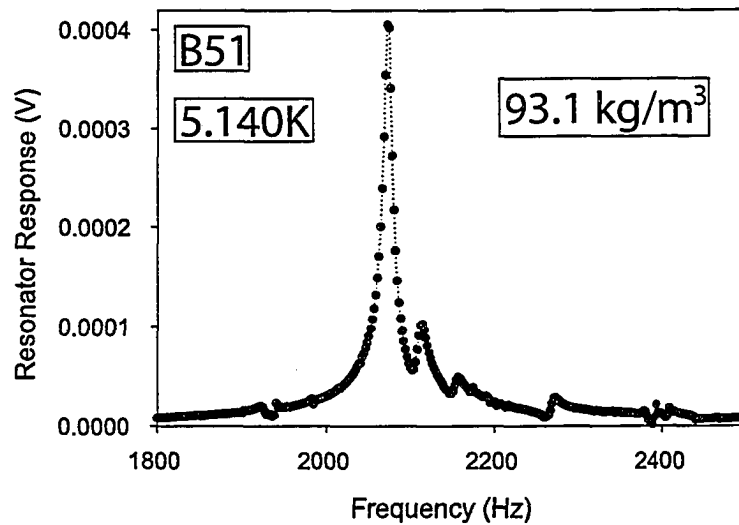
Figure 6.22: This is a single spectrum of the B51 aerogel-helium resonator corresponding to T=5.140K and $\rho = 93.1\frac{kg}{m^3}$. There are a number of distinct peaks, although this frequency range should only show a single peak because it corresponds to the fundamental resonance of a cylindrical cavity filled with helium and aerogel. As the temperature is changed, the positions of the peaks shift slightly, but mostly the weight of the signal (i.e. the area under each peak) shifts from one peak to another. For instance, at this density there is a distinct peak about 2500Hz when the cell is at 5.700K; by 5.140K this peak has shrunk, but is still present at about 2400Hz if one looks carefully. The presence of these oddly behaving modes obfuscates any signature of the phase transition. For some isochores it was impossible to locate a transition at all because of this behavior.

6.7 Helium in Aerogel B51

The results for the resonator experiments on helium in aerogel B51 resemble those for helium in aerogel B110. However, the resonant peaks were even more difficult to track, with more interference (see Figure 6.22 for an example). The resonant frequencies were lower, because of the lower elastic constants of the more porous aerogel, and any signal above about 5kHz was swamped by interference between lower frequency resonances.

The overwhelming nature of the interference present in this data set provides an excellent opportunity to analyze this behavior and its possible origin. As I mentioned before, there were problems with interference in both the neon and helium data sets in B110, however in neither case was the problem as severe. In all three cases the origin of the multiple peaks is probably due to a phenomenon known as "mode crossing." In the most general of terms, this occurs when two different

168

types of resonance occur at similar frequencies – it is possible for energy supplied to one resonant mode to shift to the other, affecting the response amplitude of either resonance. In the case of the aerogel resonators the two modes must be acoustic in nature. In other resonance techniques, such as torsional oscillators used for precise measurements of superfluid density in helium at low temperatures, the modes may be much less similar – in the case of the torsional oscillator acoustic resonances may interfere with the torsional resonance which the researchers are monitoring.

In Figure 6.23 an isochore of helium in aerogel B51 is shown to emphasize the effects of these interfering resonances. In the plot of the resonant peak positions as a function of temperature we can see four distinct regions; as the simple cylindrical cavity acoustic resonance shifts to lower frequencies (because the compressibility of the fluid is increasing as temperature falls) it encounters three frequency regions in which no peak exists. These regions, near 1300Hz, 1600Hz, and 1925Hz respectively, probably represent frequencies at which mode crossing occurs. If so, the dependence of these frequencies on density should give a hint as to the form of the other resonance present in the cell. The spacing between modes ($\sim 300Hz$) implies that they are governed by very low elastic constants; since we are already probing the lowest longitudinal acoustic mode of the aerogel-filled cavity the obvious candidates are shear modes. These modes involve oscillations of the entire aerogel-fluid systems, but with only the shear modulus of the aerogel as the restoring force. A simple torsional oscillation of a solid cylinder is likely not the culprit, since using values of the shear modulus of aerogel[123] the resonance should be near 1000Hz, with higher modes separated by more than the 300Hz we see. However, if the modes responsible are more complicated modes which are mostly shear in nature, then the restoring force is unaffected by the density of fluid in the cell and the frequency should be inversely proportional to the root of the system density ($f \propto \sqrt{\frac{\mu}{\rho}} \propto \rho^{-\frac{1}{2}}$). In Figure 6.24 the frequencies of mode crossings are plotted as a function of system density (i.e. the sum of the densities of the fluid and the aerogel).

The density dependence of the interfering modes is consistent with them being mostly shear in character, although with the current data set there is no way to state with confidence what the form of these resonances actually was. The large number of modes wreaks havoc with choosing transition temperatures from the isochores; while in the isochores in aerogel B110 there were a couple of regions of density where the transition was obscured, here every isochore shows at least some

169
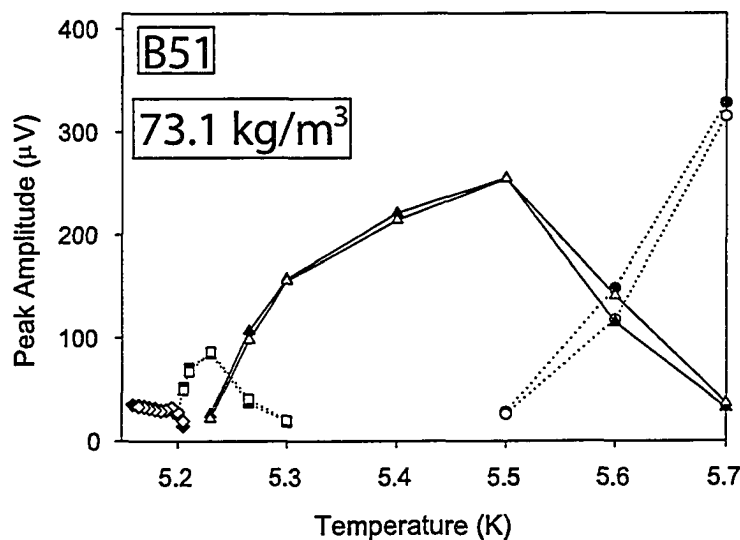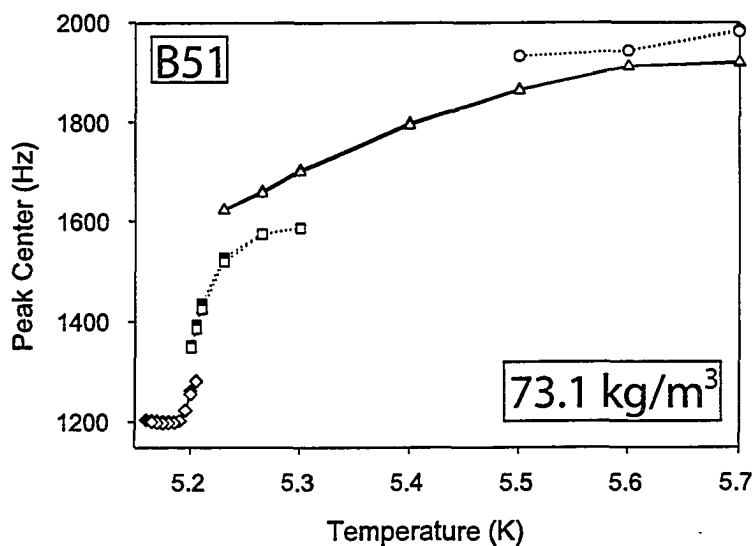
Figure 6.23: This isochore shows the low density behavior ($\rho = 73.1\frac{kg}{m^3}$) of helium in aerogel B51. Cooling data are shown by solid symbols (e.g. ◆) while warming data is indicated by open symbols (e.g. ◊). The two panes track the peak position and amplitude for the fundamental longitudinal resonance. Each spectrum may contain a number of distinct peaks, but they all correspond to the fundamental resonance (affected by some sort of other resonance). Notice how there are distinct frequencies at which peaks cannot occur, such as 1925Hz, 1600Hz and 1300Hz.

170
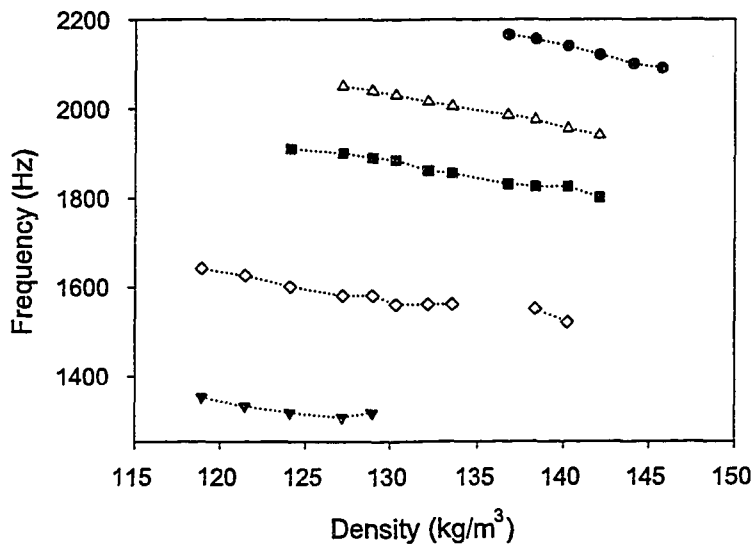
Figure 6.24: Density dependence of the mode crossing frequencies in the helium in aerogel B51 isochores. While this density range is too small to make definitive statements about the form of density dependence seen here, the frequencies are definitely decreasing as density increases, and are consistent with the inverse square root relationship one expects from shear modes.

evidence of mode crossing near the transition. Representative isochores are included as Figures 6.25 to 6.27; in all these figures closed symbols represent data taken along a cooling run while open symbols indicate a warming run. Again, no single feature presented itself as an obvious marker of a transition – as the density changes so does the character of the transition. In isochores which show obvious hysteresis, there was usually a problem with slow equilibration below the transition – in such a case the cooling data should be taken as being closest to equilibrium near the transition. Most isochores were collected with a 30 minute equilibration period at each point.

Combining the isochores, the coexistence curve for helium in aerogel B51 is shown in Figure 6.28. The curve is only well defined on the high density side, although the lowest density point seems to indicate that the transition temperature is starting to move to lower values. This would imply that the low density branch of the curve was shifted significantly from the bulk curve, but not as much as in helium in aerogel B110; certainly the curve is wider than in B110. The lack of a clear marker for the transition on the low density side is consistent with results from the other resonators, and with the gradual transition seen on the low density side of the capillary condensation curve of the adsorption isotherms in Chapter 5. The top of the curve is consistent with a plateau, but it is too noisy to draw any conclusions.

171
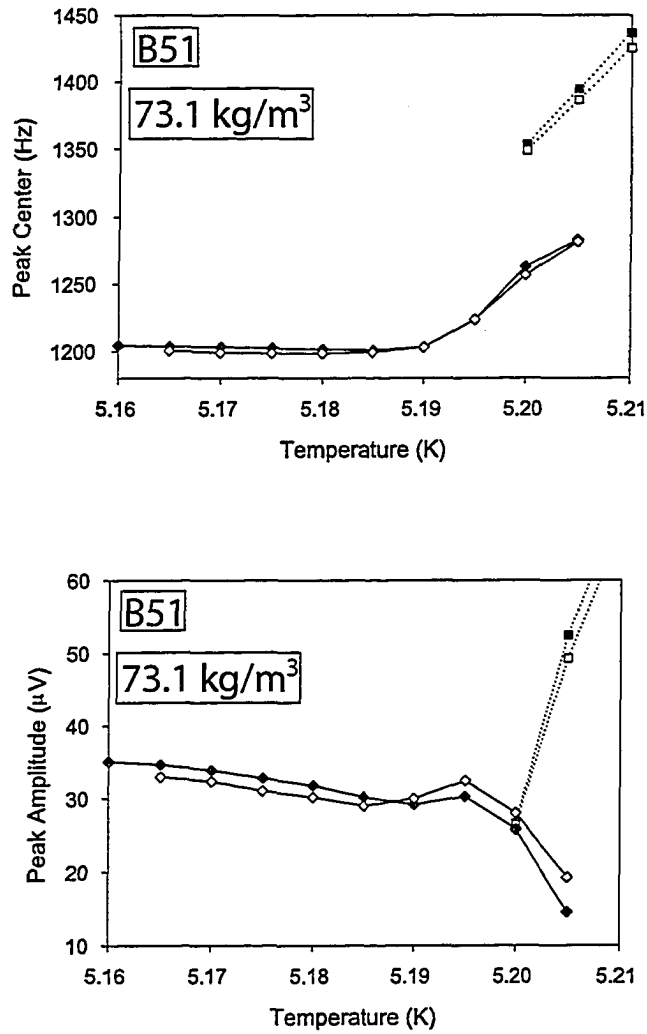
Figure 6.25: This isochore shows the low density behavior ($\rho = 73.1\frac{kg}{m^3}$) of helium in aerogel B51. The two panes track the peak position and amplitude for the fundamental resonance, but are zoomed in from Figure 6.23 so that we can see the transition more clearly; in this case at $5.190K \pm 0.005K$. Cooling points are shown as closed symbols while warming is indicated by open symbols.

172
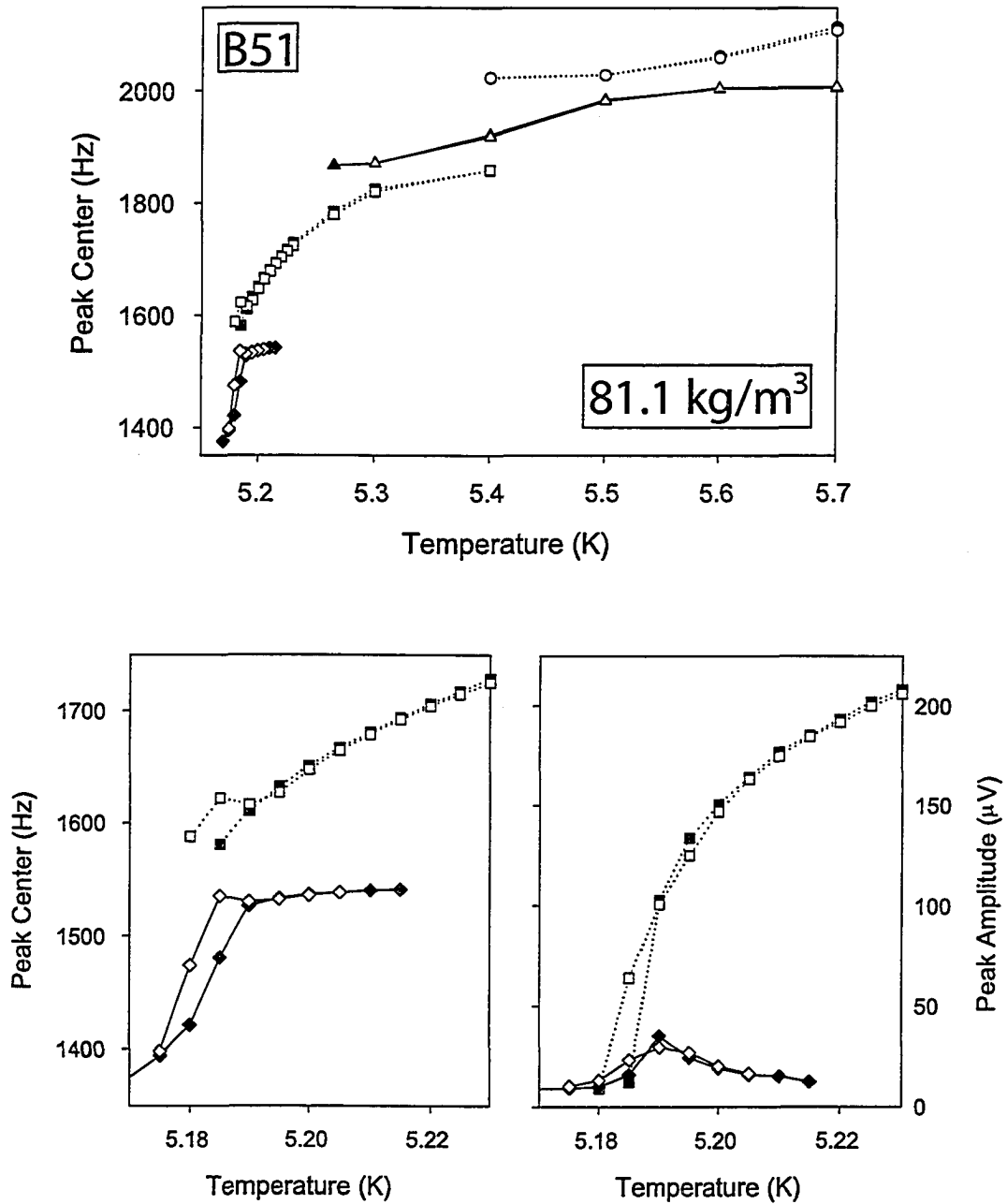
Figure 6.26: This isochore shows behavior for an intermediate density $(\rho = 81.1\frac{kg}{m^3})$ of helium in aerogel B51. The upper panel shows the positions of resonance peaks over the entire temperature range of the isochore, while the bottom two panes zoom in on the transition, at $5.190K \pm 0.005K$. Cooling points are shown as closed symbols while warming is indicated by open symbols.
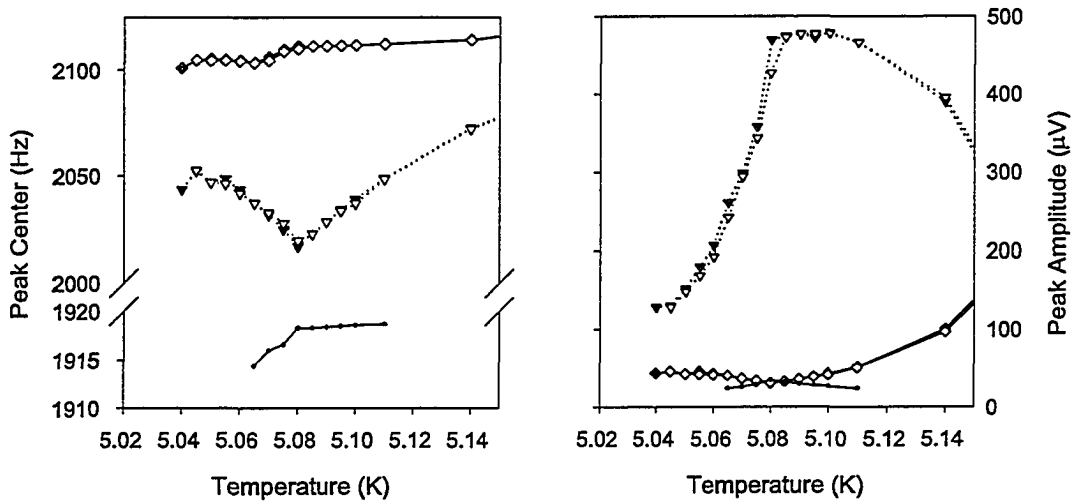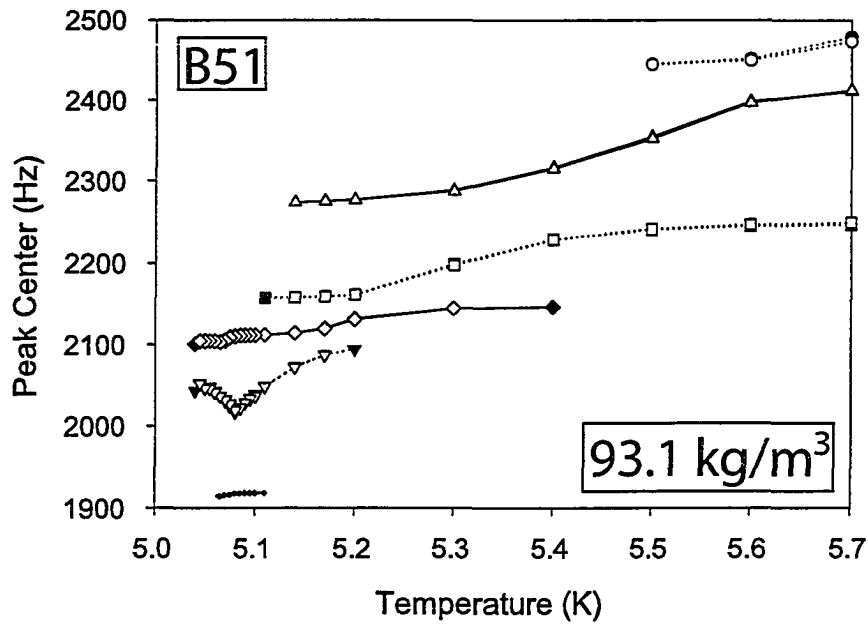
Figure 6.27: This isochore shows the high density behavior ($\rho = 93.1\frac{kg}{m^3}$) of helium in aerogel B51. The format is identical to Figure 6.26, with the transition in this case occurring at $5.080K \pm 0.010K$. Cooling points are shown as closed symbols while warming is indicated by open symbols.

174
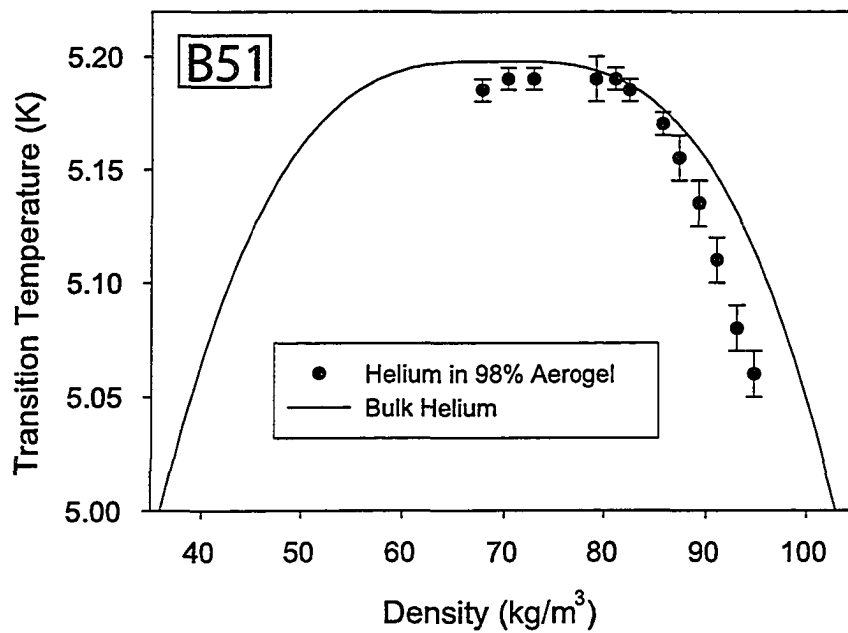
Figure 6.28: Coexistence curve for helium in aerogel B51. Again we see that the curve is close to the high density side of the bulk coexistence curve, however no low density transitions could be located using the acoustic resonator. With no low density points it is impossible to make conclusions about the shape or width of the resultant curve, although the top of the curve is again consistent with the existence of a plateau and the curve is obviously wider than the curve for helium in aerogel B110.

The high density leg is steeper than the bulk curve, similar to the curve seen for helium in aerogel B110. No attempts to fit the curve to critical exponents have been made since the data do not cover a large enough range or have high enough precision to draw any real conclusions.

175

6.8 Equilibration of Fluids in Aerogel

As discussed in Chapter 4, aerogels are excellent insulators. The silica skeletons of gels with $\phi \geq 0.95$ are such poor heat conductors that virtually all heat must pass through the fluid in the pores. When this fact is coupled to the small pores of the aerogel, which prevents any significant convection in the fluid, it is easy to see why aerogels work so well as insulators. In experiments, however, this is a major drawback which necessitates very small samples or very slow data collection. Since thermal conduction in aerogels is diffusive, it scales as the square of sample length; thus while samples a millimeter thick may equilibrate in a few minutes, samples a centimeter thick may take hours. While some experiments work well with very thin samples, such as the capacitance measurements on the $\sim \frac{1}{2}mm$ thick discs described in the next chapter, the resonance experiments used large aerogels with their associated long equilibration times.

While the resonant frequencies used to plot isochores were taken from full spectra acquired at each temperature such as that shown in Figure 6.7, the data acquisition software also tracked the position of the largest resonant peak as a function of time. There were problems with the peak tracking method, since the program had no intelligent way of dealing with mode crossing; however, it was a valuable tool for monitoring how the cell relaxed towards equilibrium. The log file was used as a check to ensure that the cell had reached equilibration, but it also sheds light on when the cell has entered the two-phase region of the coexistence curve.

In general, for the aerogels used in these studies, an equilibration time of thirty minutes sufficed for small temperature changes in the single phase region of the phase diagram. Far from the transition the temperature was stepped by hundreds of millikelvin between points, which was too large a step to allow complete equilibration, but this usually only corresponded to an error of a few Hertz for the resonant frequency (this was insignificant when compared to the frequency differences between consecutive points in this region of the isochore). As the temperature was lowered into the region of the transition temperature equilibration slowed. Below the transition equilibration times of hours are the norm, probably because of the release of the latent heat of condensation.

Figure 6.29 displays all the data collected in the log file of a single isochore of neon in aerogel B110 during cooling, $\rho_{neon} = 535\frac{kg}{m^3}$ in this case. The figure
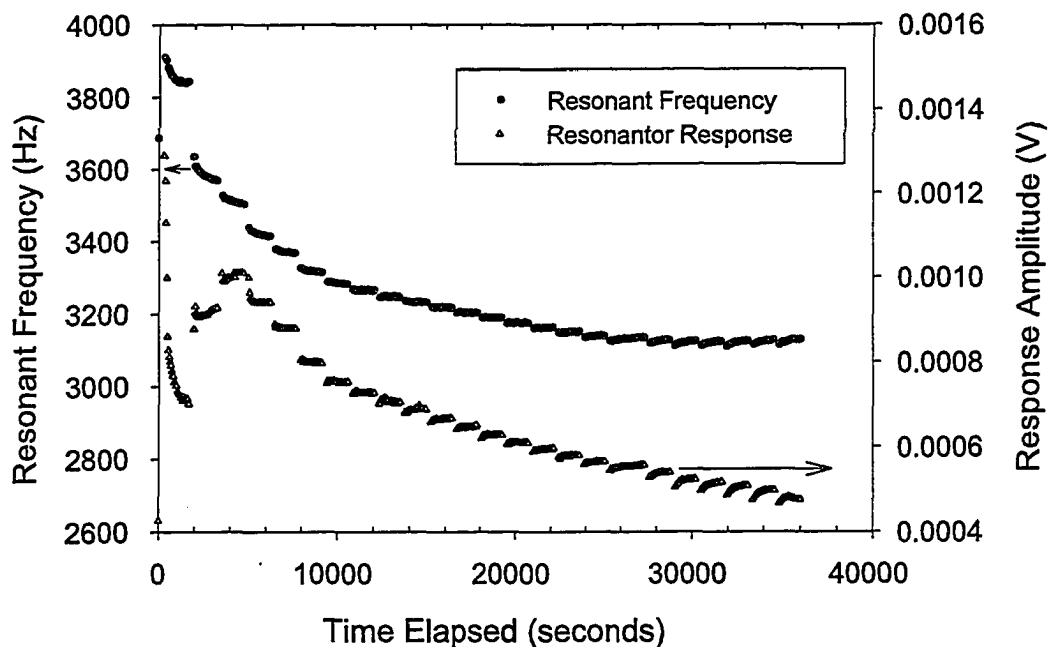
Figure 6.29: The log file for resonance of neon ($\rho_{neon} = 535\frac{kg}{m^3}$) in aerogel B110. Both the resonant frequency and the peak amplitude are shown. Each segment in the figure corresponds to a single temperature step followed by an equilibration period during which the temperature within the aerogel relaxed toward the temperature of the cell. The first few temperature steps were large ($\geq 0.5K$) so that the sample had not quite equilibrated; the next few segments (for smaller temperature steps) show that the sample has equilibrated within the time allowed, but by the final few segments the signal is obviously still drifting after the equilibration period has elapsed. The onset of this slow relaxation behavior corresponds to the same temperature as the kink in the isochore resonance frequency used as a marker of the transition.

177

consists of about two dozen small curves for frequency and amplitude separated by small gaps. Each gap corresponds to a single temperature step, followed by relaxation towards an equilibrium value. For the first few temperatures, changes in frequency and amplitude were large, as expected from large steps in temperature $(\Delta T_{step} \geq 0.5K)$ early in the isochore. During those steps the system has not quite come to equilibrium, although it is close to equilibrium relative to the change in signal. For the data collected between t=10,000 to t=20,000 seconds, the system can be seen to be in equilibrium by the end of each step. For the last half-dozen curves, however, the system has not equilibrated — the amplitude is still drifting by the time the experiment is ready to step onto the next temperature.

Figure 6.30 shows four of the curves from Figure 6.29, but plotted relative to the time when each temperature step was taken. Each curve highlights the behavior in one temperature region. The high temperature curve (T=45.4K) was taken after a 0.6K drop in temperature, so it shows a large change in resonant frequency as the aerogel's internal temperature almost equilibrates in the twenty minute wait time. The second curve (at T=44.4K) shows behavior just above the transition temperature in the isochore — the frequency equilibrates quickly. The last two curves are at lower temperatures, after liquid has begun to condense in the aerogel; neither curve has equilibrated in its allotted time. One of the curves extends longer than the other three — this is because during equilibration the temperature briefly drifted too far from the set point and the program automatically waited for a longer period. By examining the relaxation behavior in the curves it is possible to estimate a transition temperature for this isochore of about 44.36K, which agrees well with the estimate obtained from plotting resonant frequency against temperature $(44.350K \pm 0.020K)$.

178
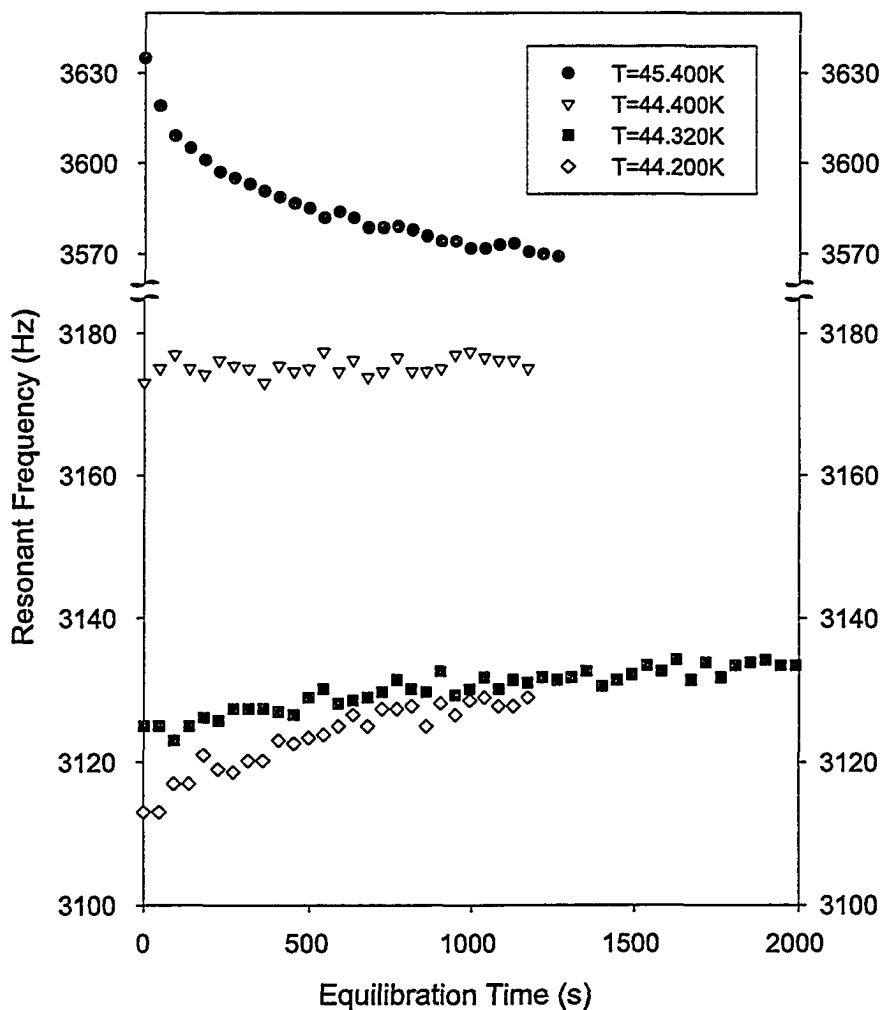
Figure 6.30: These are four of the segments shown in Figure 6.29, shown relative to the first data point collected after that temperature step. The top curve, at 45.400K, shows behavior after a large (0.6K) temperature step – the sample has not quite reached equilibrium by the time the resonance spectrum is taken, but it is close. The second curve, at 44.400K, shows behavior above, but close to, the transition – the temperature steps were smaller and the equilibration very quick. The third and fourth curves show the behavior of the system below the transition; the temperature steps were identical to that before the 44.400K curve above, but both the lower temperature curves show slow relaxation and have not reached equilibrium values by the time the spectrum was collected.

179

Chapter 7

Deformation of Aerogels During Fluid Adsorption and Desorption

Aerogels are very compliant materials – even small stresses can lead to large physical deformations. In chapter 4, I mentioned that the BET method of surface area determination does not work well in porous aerogels because of this deformation; in this chapter I present measurements of the actual deformation of high porosity aerogels during fluid adsorption. Measurements of the linear deformation of aerogels were performed using a Linear Variable Differential Transformer (LVDT) during adsorption of helium in 95% aerogel (B110) and of neon in $\sim$ 98% aerogel (B51). The LVDT allowed a non-contact measurement of position with very high precision. The measurements were all performed at temperatures where the liquid surface tension was much smaller than that of liquid nitrogen at 77K.

While these experiments have produced some results, and promise to provide very interesting data, the study is in its preliminary stages. I constructed a prototype cell and measured the condensation of neon near its liquid vapor critical point, but the thermal equilibration times were prohibitively long. A second cell was constructed to measure smaller samples and incorporated an *in situ* pressure gauge, but even this cell was very slow to equilibrate. Current results include a rough "equilibrated" data set for neon in aerogel B51 and some slightly out-of-equilibrium data sets for helium in aerogel B110. Experiments are currently underway to expand the measurements in aerogel B110.

180

Porosity (ϕ)	Density ($\frac{kg}{m^3}$)	Young's Modulus (Y) (bar)
Quartz	2200	700,000
87%	286	1000
95%	110	25
98%	44	2

Table 7.1: Young's modulus of various silica aerogels. Note how quickly the moduli decrease for higher porosities. From references [27] and [119].

7.1 Capillary Stresses in Aerogels and Adsorption Isotherms

In chapter 2 we discussed the forces present at the triple line (where liquid, vapor, and solid meet). When a liquid-vapor interface is present in a dense porous medium this force creates a curvature of the interface which is related to the depression of the condensation pressure for the fluid. It is assumed that the solid matrix itself is unaffected by the liquid, but for very compressible solids such as aerogel this may not be the case.

The simplest way to quantify the linear compressibility of a solid is with the Young's Modulus, Y, defined by:

$$Y \equiv \frac{Pressure}{\Delta L/L}$$

where pressure has been applied to one face of an object, and L is the length of the object perpendicular to the applied force. The Young's moduli for some silica aerogels are included in Table 7.1; they follow a power law dependence in aerogel density of $Y \propto \rho^{3.7}$ [119].

The Laplace pressure exerted by liquid in a pore can be calculated (assuming that the fluid wets the pore walls) as described much earlier by:

$$P = \frac{2\gamma_{lv}}{R}$$

where γ_{lv} is the surface tension of the fluid and R is the radius of the pore. Since this equation assumes a hemispherical form to the meniscus which is appropriate for cylindrical pores but not appropriate for the diffuse strand-like structure of aerogel, our choice of R is somewhat arbitrary. To get an "order of magnitude" estimate we should choose a value for R which is about the separation between aerogel strands, but must be sure not to read too much into any calculations using that value.

181

Fluid	γ_{lv} $\left(\frac{mN}{m}\right)$	P_{cap} (bar)	$\frac{P_{cap}}{Y}$ (95%)	$\frac{P_{cap}}{Y}$ (98%)
H_2O (295K)	72	58	2.3	29
N_2 (77K)	8.9	7.1	0.28	3.6
Ne (43K)	0.13	0.10	0.004	**0.05**
He (2.2K)	0.29	0.23	0.009	0.12
He (4.2K)	0.089	0.071	**0.003**	0.04
He (5.0K)	0.015	0.012	**0.0005**	0.006

Table 7.2: Predicted distortions caused by surface tension in 95% and 98% porous aerogels. The data for water and N_2 are included for illustrative purposes only – the calculations are not justified for fluids with such high surface tensions. Surface tensions were taken from reference [133].

Assuming $R = 25nm$ allows us to calculate values shown in Table 7.2. The table takes the ratio of calculated capillary pressures to Young's modulus for 95% and 98% aerogels – a rough estimate of the fractional length change of the aerogel sample. Note that this calculation assumes linear elastic behavior, an assumption clearly violated for changes in length of more than a few percent. Thus, the ratio of surface tension to Young's modulus for nitrogen or water in aerogel give nonsensically large numbers. The three numbers shown in bold are estimates for the physical systems measured.

Reichenauer and Scherer measured the shrinkage of some higher density aerogels during nitrogen sorption[138] with a view to incorporating the distortion of the aerogel into existent methods of determining pore sizes from N_2 adsorption isotherms. Their aerogels had Young's moduli of 38 and 214 bar, larger than the aerogels in this study, and showed a *17%* linear compression of the lower density aerogel during emptying. These gels were permanently compressed by about 7% after the adsorption isotherm was completed, indicating severe damage to the structure. Shen and Monson used a Monte Carlo study to model fluid adsorption in a flexible porous network which resembled a high porosity aerogel[139]; they also saw a large volumetric change in their matrix, especially during desorption.

7.2 Measurement Technique

LVDT's provide a high precision, non-contact measure of position of a cylindrical ferromagnetic core. They consist of that core and a set of three coils (a primary coil and two secondary coils) with the axes of all coils aligned in parallel. The secondary coils are actually connected in series in an *antiparallel* fashion, so that when excited by the primary coil they produce no net voltage (i.e. the primary coil and secondary
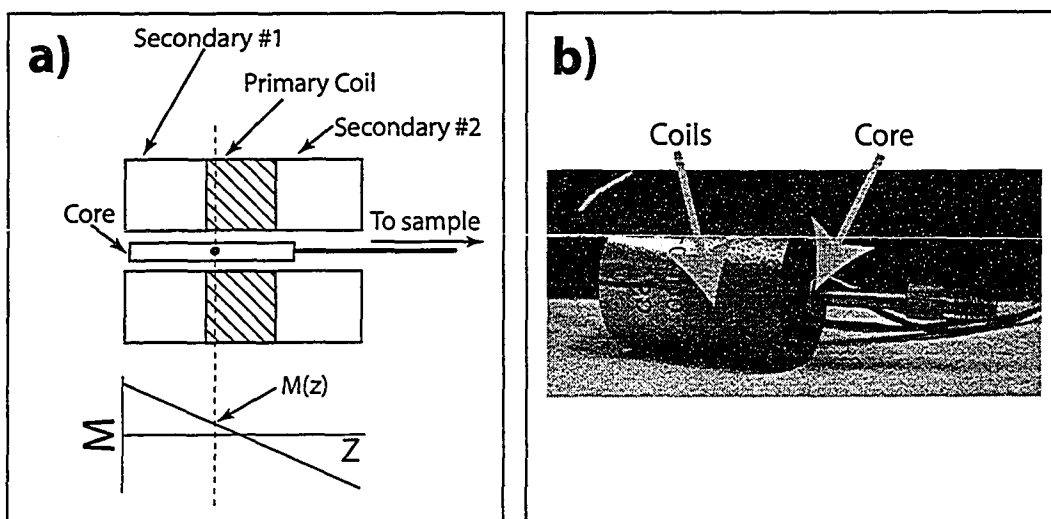
Figure 7.1: a)A cross-section of a LVDT. The dot on the core represents the center of the core, and the graph below it shows how mutual inductance (M) depends on the position of the center relative to the coils. b)A photograph of a commercial LVDT similar to the one used in this experiment.
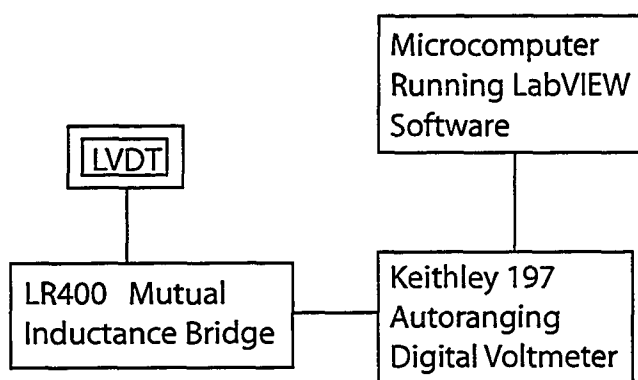
Figure 7.2: The electronics used to measure the LVDT mutual inductance.

coils have a mutual inductance of zero). The presence of a ferromagnetic slug along the axis of the coils greatly perturbs the field generated by the primary coil, such that the mutual inductance measured is highly dependent on the position of the core. This arrangement is shown in Figure 7.1, while Figure 7.2 shows the electronics used in the measurements.

Commercial LVDT's are sold as matched pairs of coils and cores, optimized for linear response to displacement. In reality inductance follows an "S" shaped curve, but when the core is close to the center of the coils the response is effectively linear. In order to accommodate our experimental cells, we required a larger gap between the outer diameter of the core and the inner diameter of the coils than the commercial LVDT's used. This led to a larger non-linearity and smaller useful

183

range. The output from LVDT's are usually measured with much simpler electronics than a mutual inductance bridge, but since we possessed a Linear Research bridge (LR400), that is what was used to measure the inductance.

The gas handling systems (GHS) used in this experiment were borrowed from the neon resonator experiment (for the first LVDT cell) and the helium capacitive measurements of capillary condensation (for the second LVDT cell). Thus, the first GHS had a known volume, and small bursts of neon of well known quantity could be admitted to the cell. The second GHS incorporated a flow meter, so instead of dosing the cell with gas we could flow gas continuously in or out. In the flow isotherms, flow is measured in units of "standard cubic centimeters per minute" or "sccm." As mentioned in an earlier chapter, this is an arbitrary unit, since the flow controller was not meant to regulate helium; it can be used to roughly compare relative rates but is useless in determining the absolute quantity of helium admitted.

7.2.1   Cell Design and Construction

We constructed two experimental cells over the course of this experiment. The first was a prototype used to prove that the experiment could produce useful and interesting data. The second cell included improvements for more precise pressure and displacement measurements, and faster thermal equilibration within the aerogel. Both cells followed the same general layout, shown in Figure 7.3; both cells were made of copper.

Our prototype was a large simple cell including only six mounting flats and a capillary inlet. Pressure measurements were made with a room temperature Mensor 1000psi gauge (Model 4040). The Mensor gauge has an accuracy of 0.01% of full scale (1000psi in this case) but, from experience, has proven to be reproducible and stable to about 0.02psi. The LVDT consisted of hand wound copper coils (~ 1000 turns for the primary and ~ 2000 turns for each secondary, painstakingly wound by Alex Ondrus), and a commercial core. James Day had originally machined a custom core from soft iron, but the core did not behave linearly or reproducibly when used in the LVDT. The entire assembly was mounted on the CTI mini-fridge used in the neon resonator experiments. The cell is shown in Figure 7.4.

Once the first set of measurements was completed it was obvious that we could resolve the deformation of aerogel during condensation of low surface tension fluids, but that the cell we were using did not maximize our precision. The aerogel sample

184
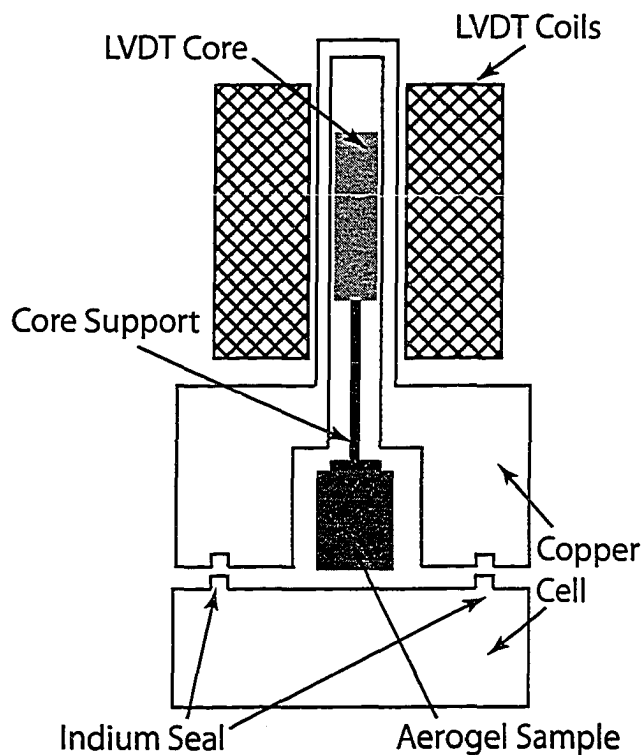
Figure 7.3: Schematic of LVDT cell — the cells were kept vertical so that gravity held the core assembly on top of the aerogel sample. The coils could be adjusted relative to the core by the use of set screws. Flats were machined onto the side of the base for thermometers, heaters, and mounting brackets.
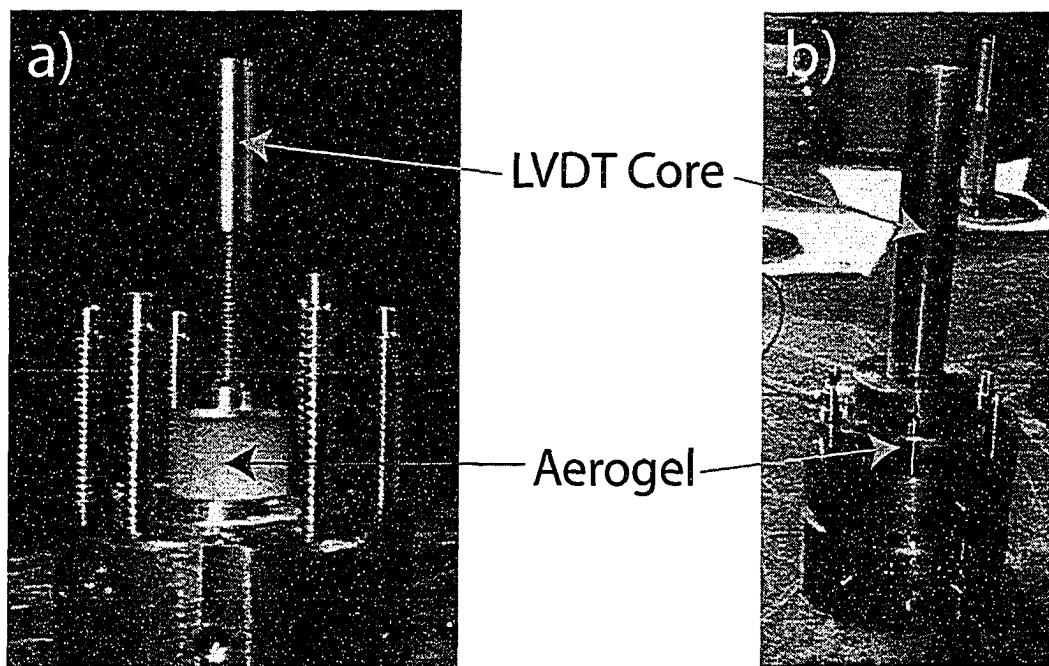
Figure 7.4: Picture of cell #1 both open and closed. The aerogel sample is visible in the open cell, as a 1cm tall cylinder supporting the ferromagnetic LVDT core. The top portion of the cell is slipped over this arrangement as shown to the right. The LVDT coils are then slipped into place over the long copper tongue which encases the core.

185
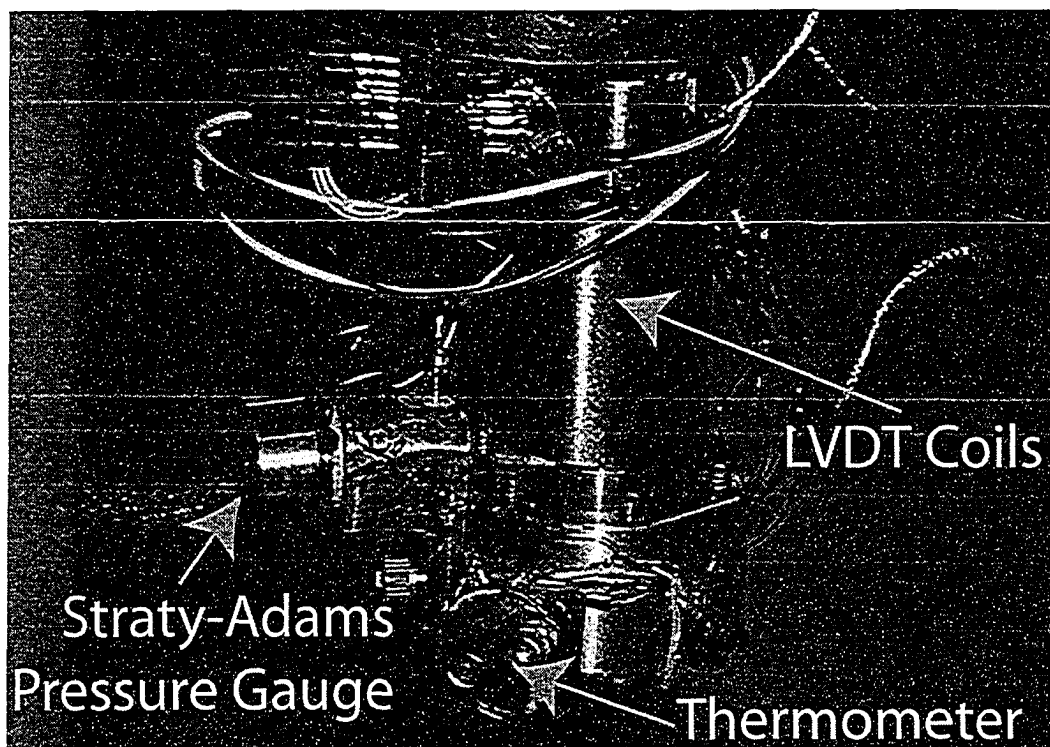
Figure 7.5: Picture of cell #2 mounted on a helium cryostat. This cell is similar to the cell pictured in Figure 7.4, but in this case it is fully assembled.

used in the first experiment was also far too large – it took weeks to measure a single isotherm. Thus, we used a new aerogel mold (4mm NMR tubes) and the new cell was designed around this sample dimension.

Both aerogel samples were cut into cylinders about 1cm (0.400" minus the thickness of saw blade) in length using the same Foredom high speed grinder used to cut the aerogel slices for our capacitive adsorption isotherms. The $\frac{1}{2}$" diameter gel used in the first (neon) cell was cut from a standard ~ 1" long aerogel as used in the resonator and capacitance experiments. The thinner aerogels were grown in NMR tubes held within larger test tubes. The larger test tube was mounted in a lathe and rotated slowly while the high speed grinder gradually cut though it and the aerogels it contained.

The new cell included a second capillary inlet for a Straty-Adams type pressure gauge which could be bolted onto the cell for low temperature *in situ* pressure measurement during filling. It was also designed to fit within a set of commercial LVDT coils (Schevitz HR050), increasing precision by almost an order of magnitude over our custom wound coils.

186
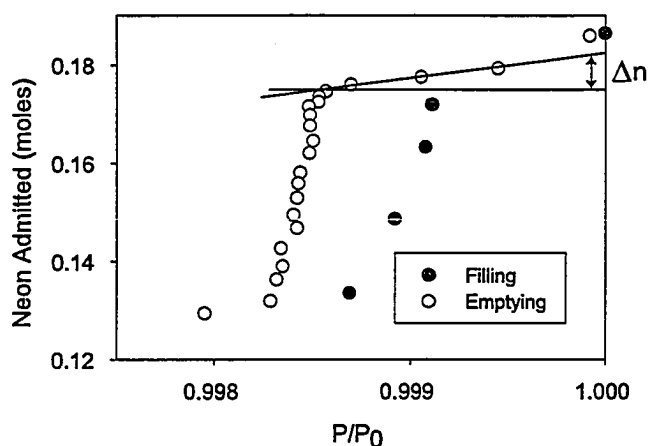
Figure 7.6: An isotherm of neon adsorbed in aerogel B51; the slope of the isotherm after filling is indicative of the compression of the aerogel. We can use Δn to calibrate the LVDT as described in the text and shown in the next figure.

7.3 Neon in "One-Step" Aerogel B51

Three sets of data were collected for neon, progressively farther from the critical point. The first data runs at 44.3K and 44.0K did not show any measurable compression of the aerogel during filling, although there was one point during emptying at 44K that may show some change in sample length. The third run, at 43K, showed a large change in sample length however. Surface tension increases as one moves further from the liquid-vapor critical point by a power law $\gamma = \gamma_0 \, \epsilon^\mu$ where $\mu = 1.26$, so liquid neon at 43K should have a surface tension about four times as large as at 44K.

When designing this experiment we did not foresee the order of magnitude changes observed in LVDT sensitivity as it was cooled. Thus there was no direct way to use our room temperature calibration to make any predictions about the calibration at lower temperatures. It is also experimentally challenging to perform such a calibration at 43K, so we were left with no way to convert changes in inductance into length changes. However, as mentioned by Reichenauer and Scherer[138], it is possible to extract information about the sample shrinkage from the adsorption isotherm itself.

If we assume that the liquid is incompressible, and that the high density corner of the adsorption isotherm corresponds to the aerogel matrix being full of liquid, but compressed, then we can estimate the volume change of the aerogel at maximum compression. Once this is is known, and assuming linear response from the LVDT, we have our calibration. So, referring to the adsorption isotherm in Figures 7.6 and 7.7, we can determine the change in aerogel volume by:

187
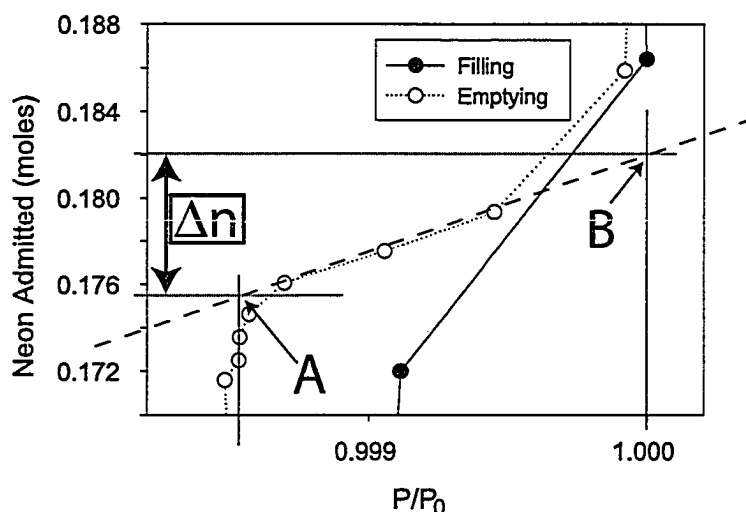
Figure 7.7: This is a blow-up of Figure 7.7. The linear portion of the emptying branch (highlighted by the dashed line) represents compression of the aerogel without the formation of liquid-vapor interfaces within it. By extrapolating this section from the corner of the desorption isotherm ("A") to saturated bulk vapor pressure ("B") we get a measure of the number of moles removed while compressing the gel. By calculating "B-A" by can determine the amount of neon removed from the gel, and thus how much it was compressed.

$$\Delta V = V \left(1 - \frac{\Delta L}{L} \right)^3 = \frac{\Delta n}{\rho_{neon}}$$

"Δn" is labelled in the figures – it is difference between the amount of neon adsorbed by the aerogel when at saturated vapor pressure and when it is still full but about to start draining. Since there is a large volume of bulk neon vapor present in the cell the absolute value of moles admitted is meaningless – one must only consider relative changes in the quantity of neon in the cell. While this technique is not very precise, it does give us an estimate of the aerogel shrinkage which should be correct within about 20%. From Figure 7.7 we can see that $\Delta n \approx 0.0065$ moles; this also corresponded to a change of about $7.7*10^{-7}$ H in mutual inductance, giving us a way of relating M to length change. Incidentally, when the LVDT was properly centered our inductance bridge could resolve about $10^{-8} Henrys$, giving us an instrumental resolution of $\sim 10\mu m$.

Using the calibration just discussed, we can plot the aerogel length change as a function of the amount of neon adsorbed, shown in Figure 7.8. Here we have set zero to be the fully relaxed aerogel, and no deformation is obvious for the first 0.1 or so moles of neon admitted to the cell. In this regime, a thin film is collecting on the

188
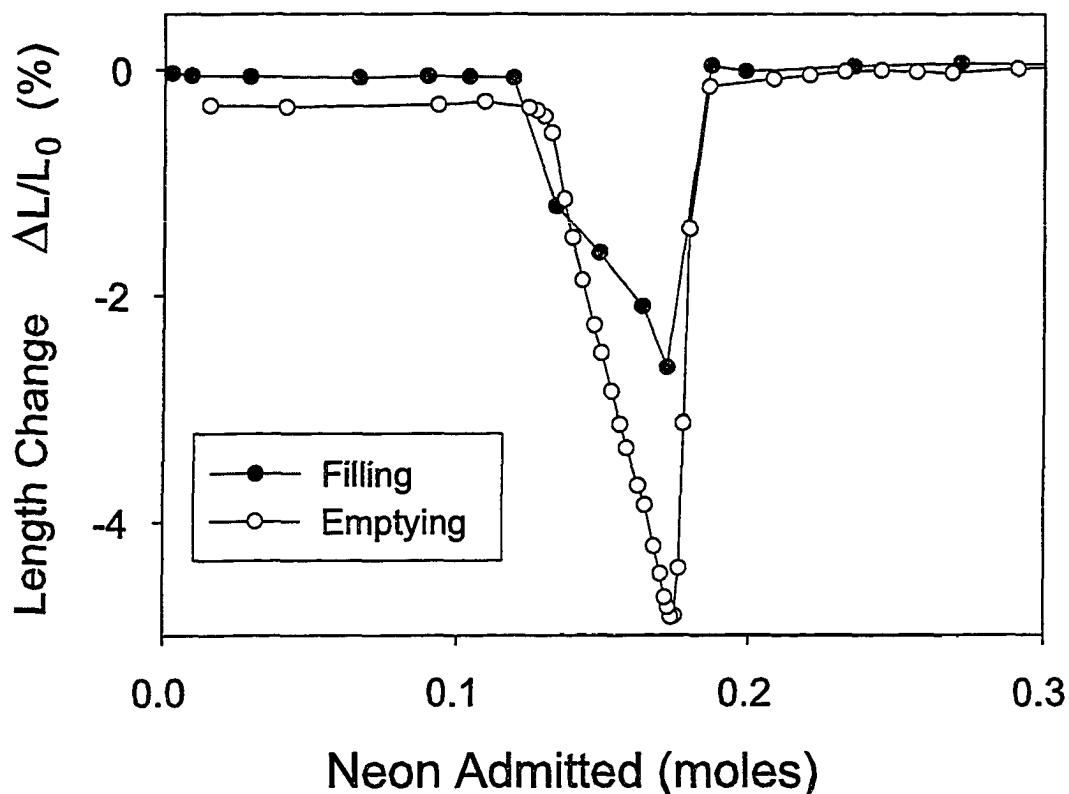
Figure 7.8: Using the calibration calculated from Figure 7.6 we can determine how much the gel has compressed at various points along the isotherm. The offset after emptying might be due to drift, but is probably due to a slight permanent deformation of the aerogel sample.

aerogel strands, and the rest of the neon is present in the cell as vapor (remember that close to the critical point the density of bulk neon vapor can be quite large). Then, as neon begins to condense into the aerogel, the aerogel contracts, reaching a maximum linear change of about 2.5%. Once the gel is full (at $n_{neon} \approx 0.2moles$), there are no longer any liquid-vapor interfaces causing stress in the aerogel and it re-expands to its original size. Upon removal of the neon, the same process occurs in reverse. However, since the pressure difference across the interface is greater during desorption the aerogel is compressed even more – almost 5%.

To highlight the behavior of aerogel along the isotherm, Figure 7.9 shows the deformation of aerogel B51 along an isotherm next to the actual pressure-density adsorption isotherm itself. In this figure points are labelled on both plots showing how the compression of the aerogel relates to the position along the adsorption isotherm. Perhaps most importantly, the much larger pressure depression during
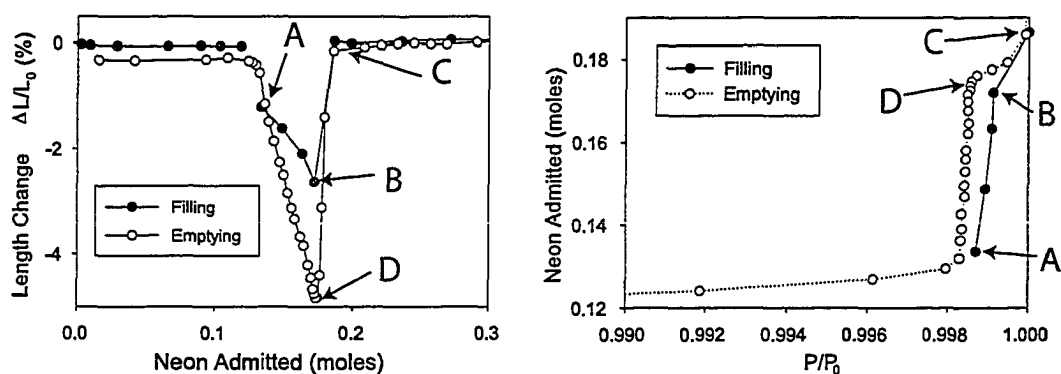
Figure 7.9: This figure shows the contraction of the aerogel during the adsorption isotherm next to the adsorption isotherm itself. Solid symbols refer to data taken during filling while empty symbols refer to data taken while emptying the cell. Points "A" and "B" refer to the beginning and end of capillary condensation during filling. Points "C" and "D" refer to the gel when completely full of liquid – at point "C" the gel is completely relaxed while at point "D" the gel is still full but the skeleton has been compressed.

emptying than during filling (i.e. $|P_D - P_0| > |P_B - P_0|$ explains the much larger compression of the aerogel seen at point "D."

7.4 Helium in Aerogel B110

7.4.1 Cell Differences and Sensor Calibration

The cell used in the second set of measurements, made with helium as the condensing fluid, had a number of improvements which were described above. It allowed us to make much more precise measurements and was easier to control. It also allowed us to make direct calibrations for the LVDT instead of using the adsorption isotherms to calibrate the LVDT. However, because the sample used was thinner, the pressure exerted by the weight of the ferromagnetic core is larger than the same core would exert on the larger diameter gel used in the neon experiment. For this reason we have used a 95% aerogel (B110) in this experiment rather than a 98% gel (B51) as used in the neon work. If we wish to extend this work to 98% aerogel, a lighter core (i.e. less than the 3 gram core used here) must be substituted, or a new method must be used. The 95% gel is compressed only about 0.1% by the weight of the core, but a 98% gel would be compressed by about 1.5%.

To show what the signal from this LVDT looks like as a function of core position, I have included our room temperature calibration here as Figure 7.10. Note the slight

190
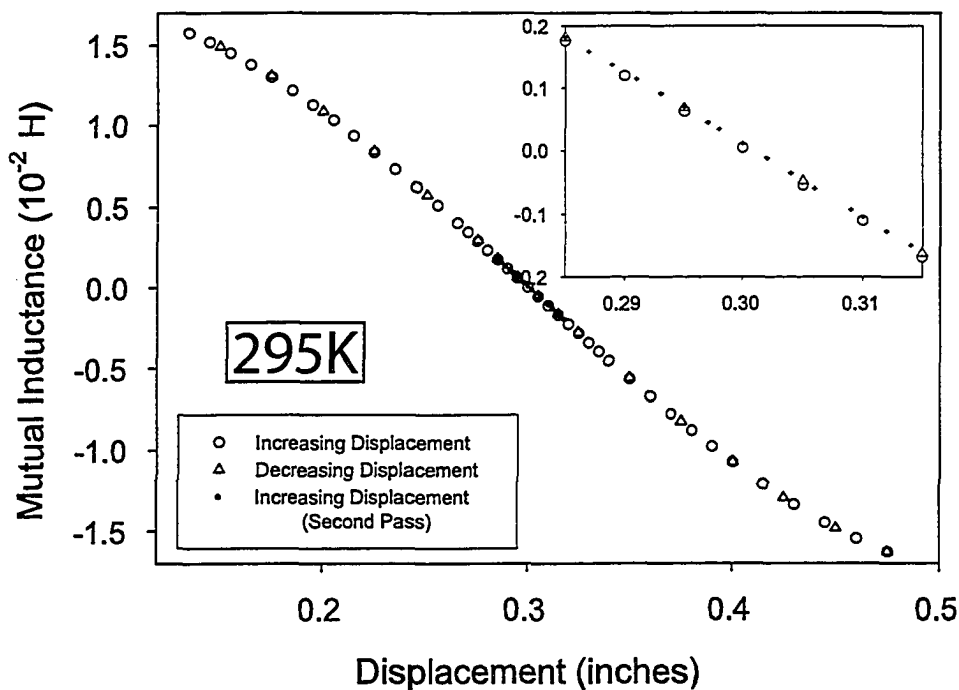
Figure 7.10: This calibration curve of the LVDT was made at 295K. It includes a large linear region near M=0, with slight deviations from linearity growing as the core moves further from the center. Any deviation from reproducibility is probably due to mechanical backlash in the micrometer.

"S" shape to the curve, with a very linear region near the M=0 point highlighted in the inset. Resolution is set by the inductance bridge, so near M=0, displacement can be resolved down to tens of nanometers. The scale for displacement in this figure is simply the reading from a small manual micrometer.

At low temperatures several major changes occur, as one can see by comparing the low temperature calibration shown in Figure 7.11 to the room temperature calibration shown in Figure 7.10. First, the sensitivity plummets – by 4.2K our resolution has fallen to a few micrometers rather than nanometers, although this is still plenty of resolution for our purposes. The second major change is in the polarity of the response; as the LVDT is cooled, a positive signal will decrease through zero before settling on a negative number. Where a movement at room temperature might have caused "M" to increase, at 4.2K it will cause "M" to *decrease*! However, while unexpected, the behavior is reproducible, so a calibration can still be performed. Also, since the signal has fallen by a couple of orders of magnitude from the room temperature signal, the LVDT is much more sensitive to its environment. This can be seen in the offset of its linear region (i.e. where $M \propto position$). Whereas the

191
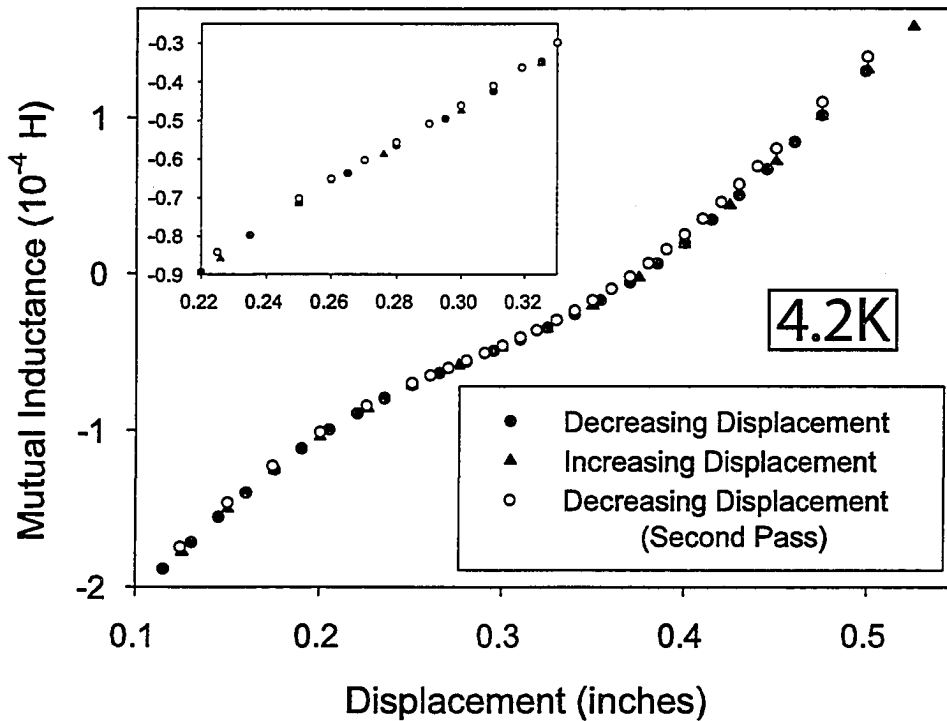
Figure 7.11: Calibrations of the LVDT at 4.2K were made using a micrometer. Note that the small linear region at the center of the LVDT has been offset from zero by remnant magnetization around the LVDT. The two calibration scans give slopes that agree within a few percent – this sets the accuracy of the technique.

linear region at room temperature occurred around M=0, at 4.2K it occurs near to $M = -5*10^{-5} Henrys$. This small offset was probably present but unresolvable at room temperature.

However, despite these changes in the LVDT behavior, it is still a sensitive non-contact probe of position and its response is very reproducible. The 4.2K calibration (Figure 7.11) includes two data sets, with the LVDT warmed to room temperature between them. Slopes of the best fit lines in the linear regions were 0.482 and $0.484 \frac{mH}{inch}$ respectively, so the response is reproducible to within about 1%.

7.4.2 Isothermal Aerogel Deformation Data

In chapter 2 I mentioned that there is a solid-vapor interfacial energy in the same sense that there is liquid-vapor interfacial energy – both result in surface tensions. Since solids are much more difficult to distort than liquids we do not normally think of deformations at the interface between solid and vapor, however they do occur. In aerogel we have a very compressible solid which may show an easily resolvable

192
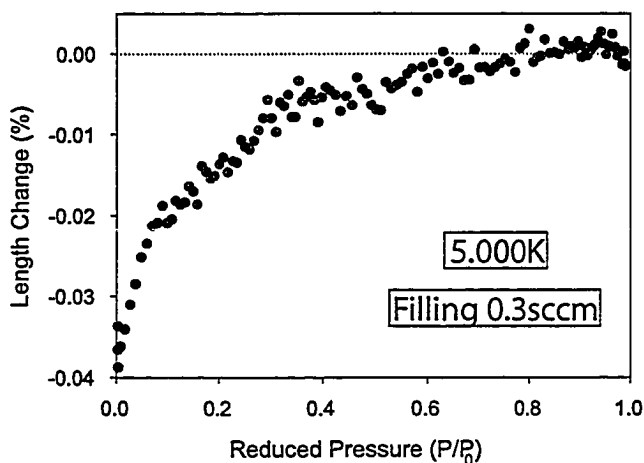
Figure 7.12: Relaxation of aerogel B110 during adsorption of helium at 5K and low reduced pressures. Zero has been set as the maximum length, so when empty the gel appears somewhat compressed. The cell was not completely empty at the beginning of this experiment, so the length of the completely "dry" aerogel is not known.

deformation caused by the silica-vacuum interfacial energy. As a liquid film collects on the aerogel strands, if the interfacial energy between silica and liquid helium is less than that between silica and vacuum (which it is), the aerogel may relax and expand. Indeed this is exactly what was seen; during filling at 4.2K the aerogel expanded by about 0.08%. We do not have a comparable measurement at 5.0K because the 4.2K isotherm was performed first and we could not completely remove the helium film from the surface before starting the 5.0K isotherm.

Unfortunately I do not have good low pressure data along a 4.2K isotherm, but I do have data along the 5.0K isotherm (except for the initial very thin film of helium adsorbed at very low pressures) and have included it as Figure 7.12. The data shown do not include the high pressure region where one sees capillary condensation – the figure is only meant to show the aerogel dilation as a helium film is adsorbed on the strands. The "zero" of length change is set equal to the maximum value of length; this differs from the 4.2K isotherm where we have an actual reading for "zero" before *any* helium is added.

Low temperature (4.200K) isotherms for helium adsorption in aerogel B110 are shown in Figure 7.13. The plot differs somewhat from the neon data above; since the helium was admitted through a flow controller I cannot state with confidence exactly how much is present in the cell. Instead the isotherm is plotted as length change as a function of cell pressure. The maximum change in length occurs during emptying and is equal to about 0.4% of total length; this is close to the estimate of 0.3% made in Table 7.2.

Isotherms collected using four different filling rates are included on the figure. The filling branch is indicated by solid circles, triangles, and squares while the emp-

193
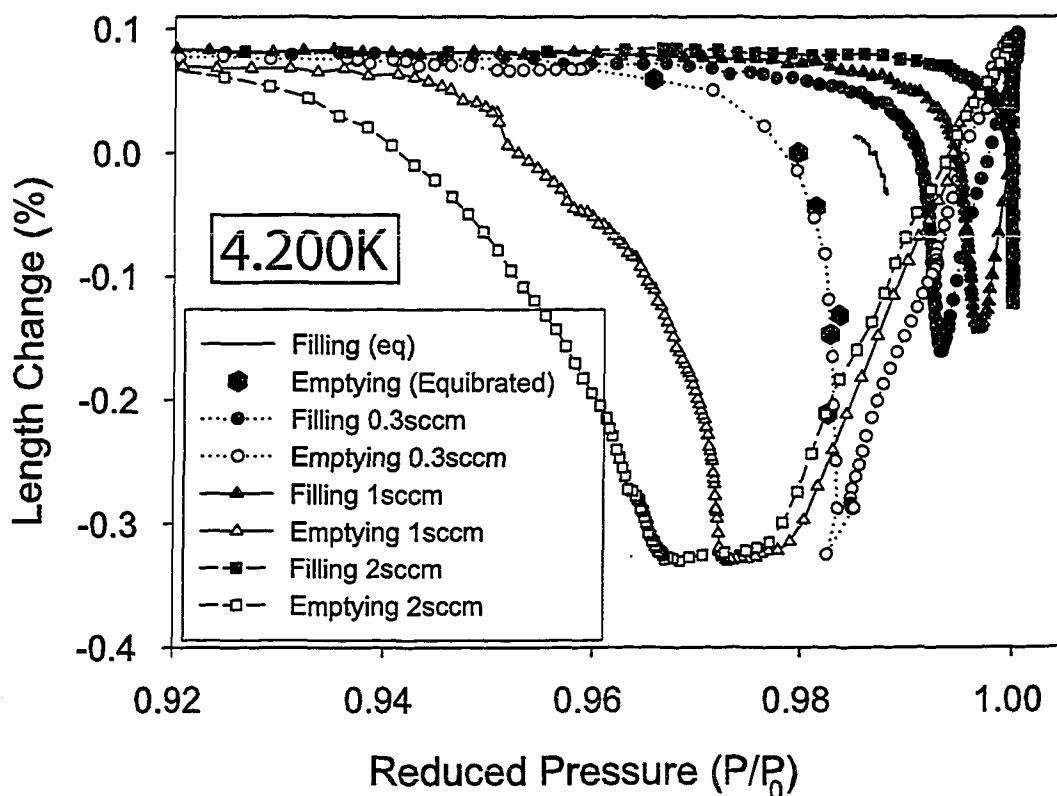
Figure 7.13: Deformation of aerogel B110 during adsorption of helium at 4.2K. The isotherms were highly rate dependent, with even the slowest rates of filling too fast for equilibration.

tying branch is indicated by the corresponding empty symbols. Two portions of very slow scans are included as a thin solid line (filling) and large solid hexagons (emptying). Looking first at the emptying branches, there are two important observations to make. First, the magnitude of the deformation does not depend on the rate at which the cell is emptied although the *pressure* does depend on that rate. Second, the 0.3sccm points agree roughly with the six equilibrated emptying points, implying that the 0.3sccm isotherm shows the rate independent behavior of the aerogel. The filling data do not show either of these characteristics: the degree of compression depends on the rate of filling, and none of the filling isotherms agree with the slowest data taken so we have not resolved the rate independent behavior yet.

While we do not have information on the exact quantity of helium in the cell using our setup, by examining the log files we can see evidence that the maximum deformation of the aerogel corresponds to the end of capillary condensation or the

194

beginning of capillary evaporation. The deformation of the aerogel along the high pressure side of the isotherm occurs about twenty times faster than on the lower pressure side – corresponding to a large deformation associated with relatively little mass transfer. In addition, the cell seems to respond much more slowly to changes during the low pressure portion of the deformation which is consistent with the sample being within the hysteresis loop of the isotherm. Our assumption that the maximum deformation along the helium isotherms corresponds to the complete filling of the aerogel pore space seems reasonable from these observations; it is also supported by the neon results where it we were able to verify that point of maximum deformation did indeed correspond to the last point before the aerogel pores began to empty.

The portion of the isotherms closest to P_0 should have identical slope for the emptying and filling branches of the isotherm; in this region the gel is full of liquid and the aerogel matrix is simply responding to the pressure difference across the liquid-vapor interface present at the aerogel surface. The fact that the slope of the two branches differ in Figure 7.13 as they approach saturated vapor pressure indicates a system out of equilibrium. Hopefully with slower data collection the two branches of the isotherm will overlap in this pressure range. The different behavior of the filling and emptying branches at lower pressures indicates that the mechanisms of capillary condensation and of capillary "evaporation" are probably very different.

Isotherms were also collected at two rates at 5.0K, shown in Figure 7.14. Here the compression is much smaller (because surface tension is much smaller) but still resolvable. This near to the critical point we are probably not liberating as much latent heat during capillary condensation, so equilibration is faster – for this sample the 0.3sccm data is probably very close to the rate independent behavior.

Finally, Figure 7.15 presents a comparison of the 0.3sccm data for isotherms taken at 4.2K and 5.0K. This is simply to highlight the different degree of compression and the higher capillary condensation pressure at 5.0K.

195
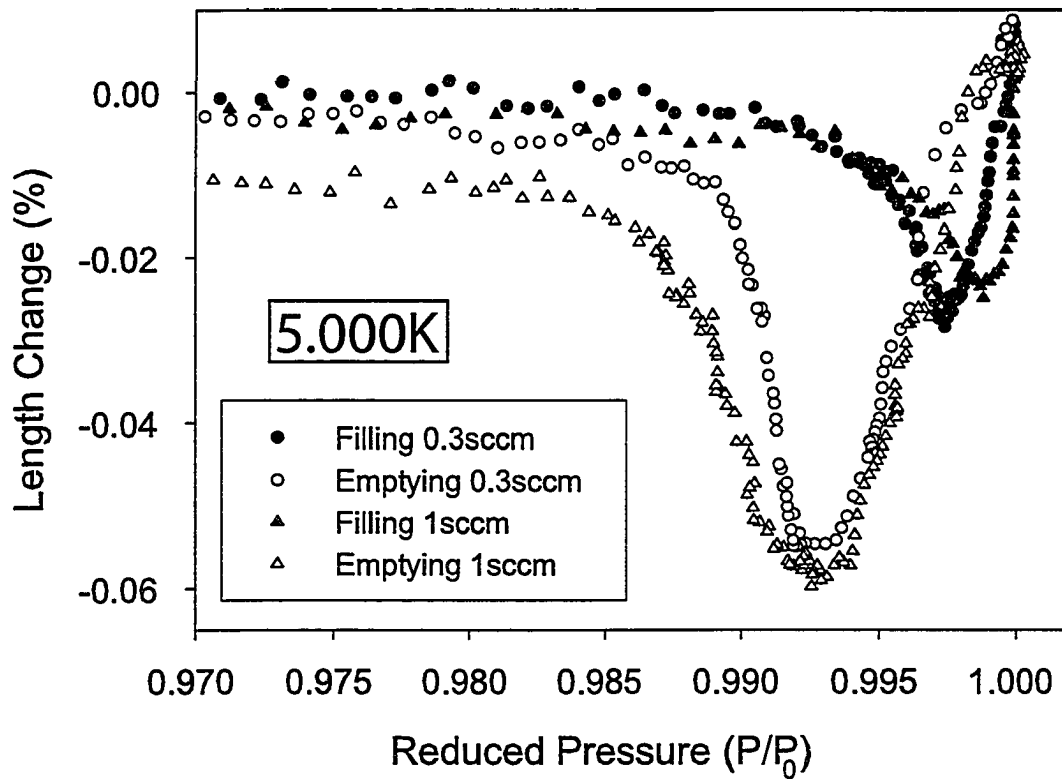
Figure 7.14: Deformation of aerogel B110 during adsorption of helium at 5.0K. These isotherms are better equilibrated than those at 4.2K, with the slowest filling rate almost equal to the limiting (i.e. rate independent) behavior.
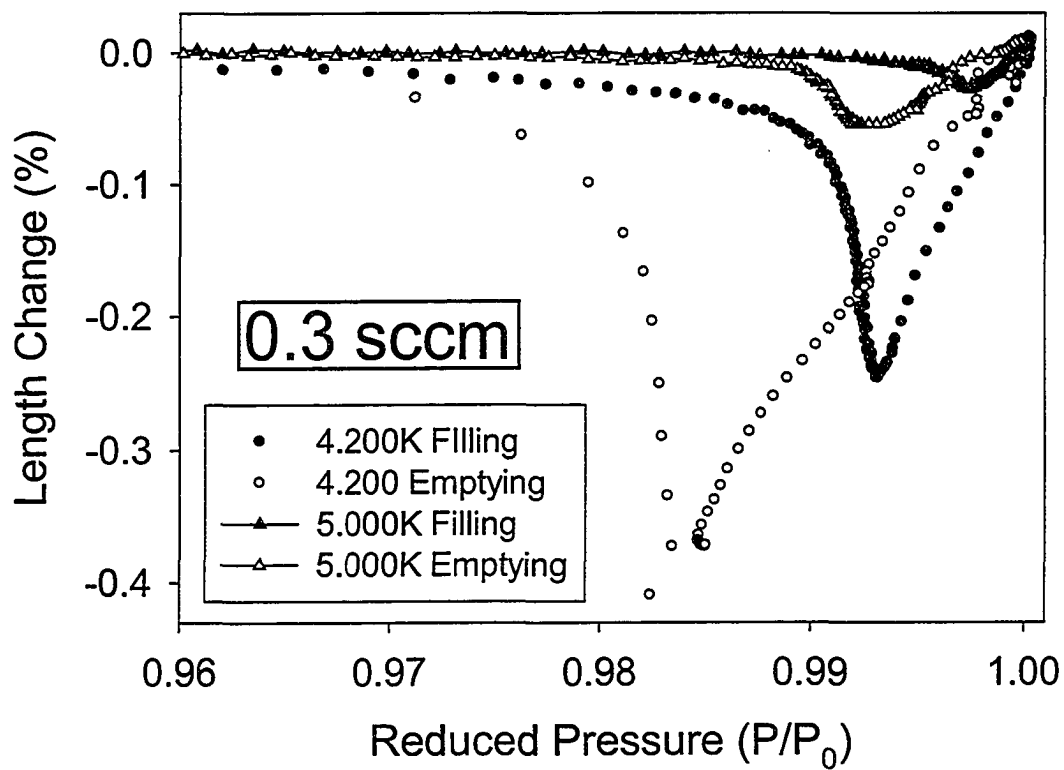
Figure 7.15: A comparison between the slowest filling rate (0.3sccm) scans at 5K and 4.2K, plotted relative to their fully expanded length. The two important differences are the higher capillary condensation pressure and smaller deformation of the aerogel at 5K, both related to the lower surface tension of helium at this temperature.

197

Chapter 8

Discussion and Interpretation of Results

This thesis began with an introduction to liquid-vapor critical behavior and capillary condensation. Experimental data were then presented for condensation of helium and of neon in highly porous silica aerogel at temperatures close to their respective critical points. In this, the final chapter of my thesis, I will try to bring together these concepts with the results of our experiments.

8.1 Summary of Background Material

In restricted geometries (e.g. pores or channels) fluids tend to condense more readily than in bulk – liquid forming in pores or channels at pressures lower than condensation in bulk volumes. This behavior is usually well described by taking into account the energetics of liquid-vapor and liquid-solid interfaces, known as surface tension. The energy gained by adsorbing liquid onto the surface of pores outweighs the loss in entropy in the fluid during condensation, and once a film has formed its curvature can act to depress the adsorbate's vapor pressure. In general this behavior is fairly well understood – the depression of condensation pressure has been shown to follow the Kelvin Equation down to very small sizes of pores. Capillary condensation in *real* porous media still requires extensive modelling to interpret with any accuracy because of the highly variable nature of pores, but there is general agreement that the fundamental aspects of capillary condensation are well explained.

Near the liquid-vapor critical point of the adsorbed fluid, on the other hand, there is no general agreement about what happens to fluids in pores. As the critical temperature is approached thermal fluctuations in fluid density grow from atomic

scales to macroscopic scales; close to the critical point these fluctuations may exceed the size of the pores in which the fluid is confined. Along with the growth of fluctuation size, other thermodynamic properties diverge (or tend to zero) as the critical point is approached. How these variables respond to confinement near the critical point is an open question.

Measurement of the critical behavior of confined fluids probes equilibrium thermodynamic properties such as density, compressibility or heat capacity. To speak meaningfully of these quantities we must presuppose a system in equilibrium (i.e. not one governed by metastable states and hysteresis). Furthermore, our interest is in phase transitions of the system as a whole, not individual pores – while we might meaningfully speak of transitions in a single pore, we are only interested in transitions within the entire *aerogel-fluid* system. Thus, we are probing changes in thermodynamic variables which occur throughout the macroscopic sample – if a macroscopic equilibrium transition is indeed present, then close to the critical point behavior should be governed by thermal fluctuations.

In essence that leaves us with two conflicting pictures of near critical fluids in porous media – one governed by surface tension and the other by thermal fluctuations. The two interpretations do not necessarily meet smoothly at some intermediate value of reduced temperature because each interpretation is too simple in some way. Capillary condensation assumes a very simple form of surface tension which may not be appropriate when the wavelength of capillary waves caused by thermal fluctuations approaches the size of the pores. On the other hand, simply assuming that thermal fluctuations in the pore-fluid follow the same relationships as those in pure fluids may not be valid either.

Researchers have discussed the behavior of fluids in pores near the liquid-vapor critical point in terms of a "capillary critical point" but definitions of this point are as varied as the studies that have investigated it. It is treated as anything from the temperature coinciding with the disappearance of hysteresis loops in adsorption isotherms, to a more fundamental thermodynamic point which plays the same role as the true liquid-vapor critical point does for bulk fluids. In the former case, all properties of the fluid are assumed to remain bulk-like (e.g. the surface tension will have bulk-like values for all temperatures) despite the perturbing effect of the matrix. In the latter case, equilibrium thermodynamic properties such as surface tension may exhibit power law behavior as they approach the capillary critical point.

199

At low temperatures the differences between these interpretations are negligible, but as one approaches the critical point they diverge.

A variety of work has been performed on fluids in dense porous glasses such as CPG (controlled pore glass) where the question of fluid behavior near the critical point has the complications explained above and there is no general agreement about how to picture this behavior. Work on fluids in aerogels throws yet another variable into this mix. In describing the capillary condensation of a fluid one needs to assume a distinct liquid-vapor interface with some sort of well defined curvature. This is usually assumed to be a hemispherical meniscus for cylindrical pores or hemi-cylindrical for slit pores, but aerogels do not have a well defined pore shape. Instead, aerogels with their diffuse network of silica strands show little evidence for favoring a single curvature of the meniscus of adsorbed fluids. Thus, as temperatures and filling fractions change so too does the pressure difference across the liquid-vapor interfaces within the aerogel. In fact, with such a diffuse network of strands we considered that it was possible that close to the critical point thermal fluctuations dominate the fluid behavior just as they do in bulk.

Early experiments at Penn State[10, 11] saw no hysteresis in adsorption isotherms in aerogel, and an apparent discontinuous jump in density at temperatures below the critical point, just as one sees in the bulk liquid-vapor transition. Their work used heat capacity and optical scattering methods to map out "coexistence curves" for helium and nitrogen in 95% porous aerogel and they could fit those curves with critical exponents consistent with bulk fluid behavior. In the late 1990's we were beginning our measurements using low frequency acoustic resonators, and the Grenoble group were taking data using their very low frequency mechanical pendulum. The Grenoble results[15] on helium in 95% aerogel were consistent with capillary condensation like behavior, with little evidence of the macroscopic equilibrium transition necessary to meaningfully discuss critical exponents. Recently computer models of fluid condensation in aerogel have also reached a level of complexity which helps us interpret our experimental data and they favor a picture without a macroscopic equilibrium phase transition near the bulk critical point. Finally, direct measurement of density fluctuations of near critical carbon dioxide in aerogel[59] showed little evidence for a divergence in correlation length. The lack of this divergence, while far from conclusive, supports a view of fluid behavior in aerogel being controlled by factors other than critical fluctuations.

8.2 "Equilibrium" of Fluids in Aerogels

When describing our experiments on condensation of fluids in aerogel, there are some pitfalls in the language that are hard to avoid. Specifically the words "equilibrium" and "equilibration" are used in a few different senses in this thesis. First, the most common use is "thermal equilibrium": the point where the temperature within the system is uniform, and any spontaneous processes which liberate or adsorb heat have already occurred. To reach thermal equilibrium we must wait minutes to hours after stepping the sample temperature or the density of fluid in the aerogel, while heat slowly flows into or out of the system. However, once thermal equilibrium has been reached, that does not necessarily imply that the lowest energy state for the system has been reached – it could be stuck in a metastable state.

In the adsorption isotherms "equilibrium" takes on its most confusing mix of meanings. In the hysteretic region, the shape of adsorption isotherms in aerogel depends sensitively on the rate at which the gel is filled or emptied. If the isotherm is performed slowly enough the shape will eventually adopt a rate-independent shape (any slower data collection will not change the shape of the hysteresis loop). In our experiments we mapped out the rate-independent hysteresis loops of helium in aerogel by stepping the pressure in the system and letting the gel come to thermal equilibrium. This hysteresis loop is almost certainly composed of very deep metastable states – somewhere within the hysteresis loop true "equilibrium" (i.e. lowest energy) states exist but are not experimentally accessible. In this case "equilibrium" refers to the microscopically defined lowest energy state of the system, not just its temperature. When no hysteresis loop exists, we can assume that the system is really in an equilibrium state.

Thirdly, we may speak of an "equilibrium (first order) phase transition." Such a liquid-vapor transition requires two things: first, the transition must be between coexisting equilibrium states (i.e. not between two metastable states) and second, the two states must have a chemical potential that does not depend on the presence or proportions of the two phases. In other words we are searching for macroscopic two-phase coexistence – not simply the existence of liquid and vapor phases, but for phases whose chemical potential is not affected by average system density.

To clarify the idea of the equilibrium phase transition, we consider the basic thermodynamic behavior of fluids. For a simple system at constant temperature,

201
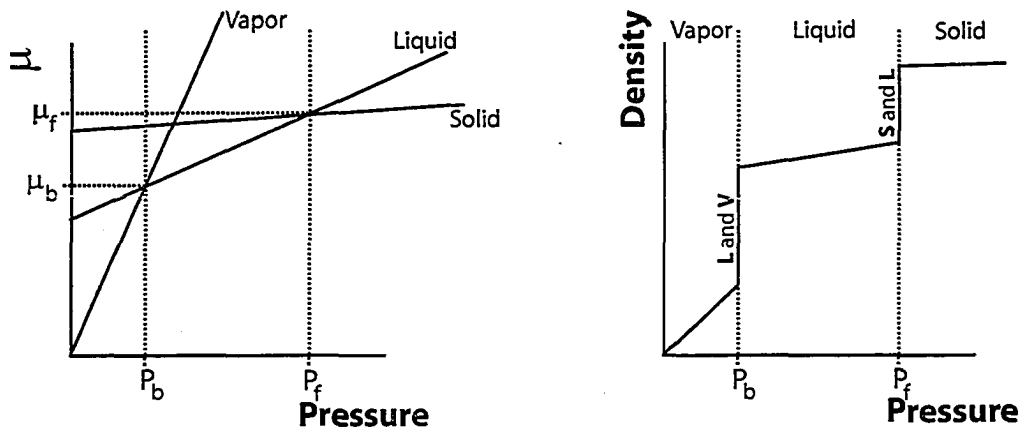
Figure 8.1: Two projections of the thermodynamic phase diagram for a simple fluid. In the left-hand panel the chemical potential is shown as a function of pressure for all three phases. The phase with the lowest potential is thermodynamically stable – when two chemical potentials are equal these phases can coexist. The right-hand panel displays the average density for the system as a function of pressure – when two phases are in coexistence the system density can change dramatically with no change in pressure (or, equivalently, chemical potential).

but variable pressure, there are at most three phases – solid, liquid, and vapor (if one neglects crystallographic transitions and the like). Each of those phases has a chemical potential that varies with pressure, and at every pressure one phase will have the lowest chemical potential – that will be the stable phase for those thermodynamic conditions. There can exist points where the chemical potentials of two or three phases intersect and those points correspond to phase transitions; at those points two phases can coexist without the chemical potential of the system changing. This is shown schematically in Figure 8.1, where the left-hand panel shows the chemical potentials of solid, liquid and vapor and the other panel plots the average density of the system as the pressure is varied. The same concepts are illustrated pictorially in Figure 8.2, along with corresponding states of the fluid-aerogel system studied in this thesis. In bulk, as long as there are two phases present the chemical potential is fixed at a constant value, which in turn fixes the pressure at a constant value. If fluid in aerogel exhibits macroscopic coexistence and an equilibrium phase transition there must exist a region where density changes without any change in pressure – a plateau in the adsorption isotherm.

This will be discussed in more detail in the section on adsorption isotherms later in this chapter, but there were no plateaus in any of the non-hysteretic isotherms.

202
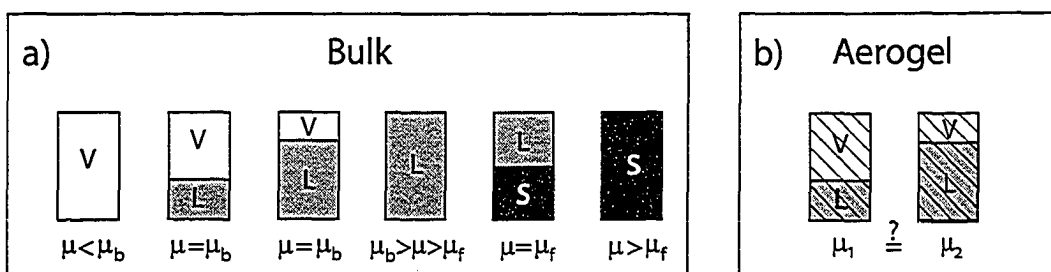
Figure 8.2: a)As the pressure (and hence the chemical potential μ) of a fluid system is increased, it transforms from vapor to liquid, and then to solid. When only a single component is present, pressure and chemical potential can vary but during coexistence they are set at constant values. For instance when vapor and liquid are both present the system has a chemical potential of μ_b, independent of the proportions of the two phases. b)In aerogel, for there to exist an equilibrium phase transition exhibiting macroscopic coexistence the chemical potential cannot depend on the proportions of liquid and vapor in the sample; in terms of the figure, μ_1 must equal μ_2 or there is no true coexistence.

This precludes the existence of macroscopic coexistence as described above. There is the possibility of an underlying equilibrium transition existing inside some of the hysteresis loops of the lower temperature isotherms, but if so it is difficult, or impossible, to access experimentally.

8.3 Summary of Experimental Results

The three experiments described in this thesis offer three different views of fluid condensation in aerogel. The overall picture that emerges from these views is one in which capillary condensation of fluids in aerogel can be very well described by surface tension until close to the critical point. Even quite close to the bulk critical point we see no evidence for macroscopic coexistence. Both near to the critical point and far from it there are indications that some very interesting behaviors may be occuring during condensation.

8.3.1 Acoustic Resonator

Chronologically, the acoustic resonator experiments were started before our capacitive measurements of fluid density in aerogel. The resonators were designed because a low frequency signal would be attenuated less by the aerogel than the ultrasonic signals previously used in Dr. Beamish's laboratory[137], and the resonance technique would allow us to pinpoint a liquid-transition fairly precisely along an isochore.

Indeed, for bulk fluids the resonator could reproducibly pinpoint the liquid-vapor transition temperature to within a few millikelvin along any isochore. However, the first few attempts at mapping out the neon-aerogel coexistence curve showed rounded transitions and presented some experimental difficulties. Since each cell had to be built to fit a specific sample, creating the the cells was a slow process. In addition, once the cell was assembled, there were often problems with leaks or with signal transducers coming off as the cell was cooled.

Our early resonators yielded incomplete or poor quality data sets; it was assumed that as the quality of the cells improved, so too would the data. However, the final resonators used, and described in this thesis, show that this was not to be the case. Instead, as dead volume was eliminated and data collection became more efficient the transition became more and more difficult to see – as if by cleaning up the system we were eliminating the transition that we wanted to make clearer. Still, all resonator data sets show some sort of feature that might be associated with a liquid-vapor transition along isochores. The nature of this feature changes with density, and disappears at lower densities. If the transition detected by the resonator was true liquid-vapor coexistence, one would expect a signature that evolved in a sensible way – perhaps evolving from a kink to a dip and back to a kink. However, our data shows a spectrum of behaviors which does not resemble the bulk resonator data at all. Perhaps the resonator is registering the appearance of inhomogeneous density distribution within the aerogel, but not a true liquid-vapor coexistence. In that case, as soon as the fluid began to exhibit regions of lower or higher density the acoustic response would change, but there would be no restrictions on how the signal would change – in fact one would expect it to change in a non-symmetric way with density.

Since our original intention was to use the resonator to map out the liquid-vapor coexistence curves inside aerogel, I have plotted the location of the "phase transition" feature in each aerogel-fluid system as a function of temperature and density. These plots may only be considered "coexistence curves" in the true sense of the word if we are dealing with a macroscopic equilibrium transition, and the sense one gets from these experiments is that we are *not* seeing this behavior. However, it is common to produce such plots when discussing fluid condensation in porous media so they do allow us to compare general features to other studies, even if the precise meaning and origin of those features is a little nebulous.

Our coexistence curve for neon closely resembled the coexistence curve for nitrogen in aerogel found by Apollo Wong[11]. Perhaps Wong's light scattering results probed the appearance of an inhomogeneous density distribution in the same way as our resonator. Our helium curve did not resemble Wong's[10] helium coexistence curve at all – in fact our helium results were much more similar to the neon and nitrogen curves. Wong's helium curve was mapped out using an AC heat capacity technique – our experiences suggest that the frequency of the oscillating heat current was probably not slow enough to allow the entire sample to come to equilibrium. Our isotherms from chapter 5 clearly show thermal relaxation times on the order of one hundred minutes for a sample 0.5mm thick. The Penn State sample was 0.25mm thick, so one would expect a thermal time constant no more than four times faster. Their AC heat capacity technique applied a sinusoidally varying heater current with a frequency on the order of 0.1 - 1 Hertz – although the precise frequency is not given in Wong's thesis[54], the external time constant of the cell was about 100 seconds, which places a lower limit on the excitation frequency. Our results tend to indicate that the internal time constant of the sample was then at least an order of magnitude *larger* than their external time constant – not a desirable relationship in AC calorimetry. If we assume that their sample was similar to ours except in thickness, then we would expect a time constant of about 25 minutes. If a sinusoidal heating current was applied at 0.1Hz, then it would probably have penetrated less than 5% of the sample. Thus, they may have been probing the aerogel's response to local heating, rather than it's equilibrium thermal properties, leading to confusion about the meaning of their heat capacity signatures.

All of the resonator curves share characteristics of "coexistence curves" of fluids in denser porous media – the curve is somewhat narrowed and displaced to higher density and lower temperatures than the bulk fluid. It can not be stressed enough that these results can only be interpreted as a coexistence curve if we are certain that the transition in the aerogel is an equilibrium one which leads to macroscopic variations in fluid density. While we can not rule this out based solely on the resonator experiments, our isothermal capacitive measurements of helium density during condensation in aerogel do not support such an interpretation in the temperature range of the resonator coexistence curves.

8.3.2 Capacitive Measurement of Helium Adsorption in Aerogel

In a set of measurements complementary to the resonators we monitored the density of helium adsorbed in aerogel along a series of isotherms from 4.400K (well below T_c) to 5.700K (well above T_c), with the highest concentration of data just below T_c. If helium condensation in aerogel were analogous to the condensation of liquid helium in bulk, then the adsorption isotherms should have shown a flat region where density changed discontinuously from that of the pore vapor to that of the pore liquid without pressure changing at all. The corners of that plateau (where it met the sloped sections of the isotherm corresponding to the compressible vapor and liquid phases respectively) would mark the onset of coexistence and allow one to map out the coexistence curve. These isotherms would then "cut" through the coexistence curve horizontally, rather than the vertical "cuts" made by the resonator isochores – the two independent measurements might have then coincided, giving us two independent mappings of the coexistence curve.

While such a result would have been tidy, and a powerful argument for true coexistence, that is simply not what we saw. Instead, adsorption isotherms below 5.155K (in aerogel B110) and below 5.180K (in aerogel B51) showed distinct hysteresis loops which showed a rate dependent behavior but appeared to reach a limiting hysteresis that corresponded to metastable filling and emptying states. While the hysteresis loops were flatter than those seen in most dense porous media (with the possible exception of MCM-41 and similar materials, which are designed to have incredibly narrow pore size distributions), they all have measurable slopes in aerogel B110. There are a few isotherms in aerogel B51 which have regions with slopes below our resolution – they may in fact be flat in this region.

Furthermore, the "corner" of the isotherm marking the onset of capillary condensation is not distinct enough to unambiguously assign a value to the density of the "pore vapor," as one would assign a value to the density of the bulk vapor. The completion of capillary condensation is more distinct, and easier to use in analysis, but it is also not as sharp as one would expect in a straightforward transition. Furthermore, the transition temperatures deduced from our resonator data occur well above the disappearance of hysteresis loops in the adsorption isotherms, in a temperature range where none of the isotherms exhibit a zero slope region (i.e. the chemical potential of the fluid phases is changing as fluid accumulates in the

206

aerogel).

While we did not see evidence of the equilibrium transition for which we went searching, there are some very interesting results that emerged form these isotherms. We have good data on the thermal relaxation of the aerogel samples following a pressure step, which suggests that all but the slowest experiments on non-superfluid filled aerogels will be out of thermal equilibrium. We also mapped out hysteresis curves to temperatures within a hair's breadth of the critical temperature; hysteresis disappears from B110 40mK below T_c and disappears from B51 20mK below T_c. In this region surface tension becomes small, and any liquid-vapor interface can support significant distortion from thermal fluctuations. The isotherms become flatter as the temperature is reduced, and the hysteresis loops change from roughly triangular at high temperatures to more rectangular at low temperatures.

Most papers published on the liquid-vapor transition in porous media include plots of "coexistence" curves, although these curves are not necessarily given great weight in any analysis of the results. Exactly what features to plot, and even how to define those features, is a somewhat arbitrary decision; however, once the plot is constructed it does allow for quick comparison between experiments and between the pore fluid and bulk fluid. To this end, plots of the "coexistence curves" for helium in aerogels B110 and B51 are included here as Figures 8.3 and 8.4. When hysteresis loops are present, the closure points of the loops, which are always within the accompanying uncertainty of any "kink" in the adsorption isotherm, are used to mark the onset and completion of condensation in the aerogel. When no loops are present, there is no distinct low density feature in the adsorption isotherms, but the existence of a sharp corner on the high density side of the isotherm is used to mark the high density side of "coexistence" in aerogel B110 (Figure 8.3). For easy comparison, the resonator data for these two samples are also included on the curves.

In both figures, points from the resonator and capacitance measurements tend to agree at higher densities. However, as the density falls, so does the quality of agreement between the curves determined by these two methods. While they may be probing the same thing at high average fluid densities in the aerogel, clearly they are probing different things at lower densities. That said, they do show some qualitative similarities – most importantly, that the width of the "coexistence curve" determined by both methods is similar, and many times larger than seen by Wong
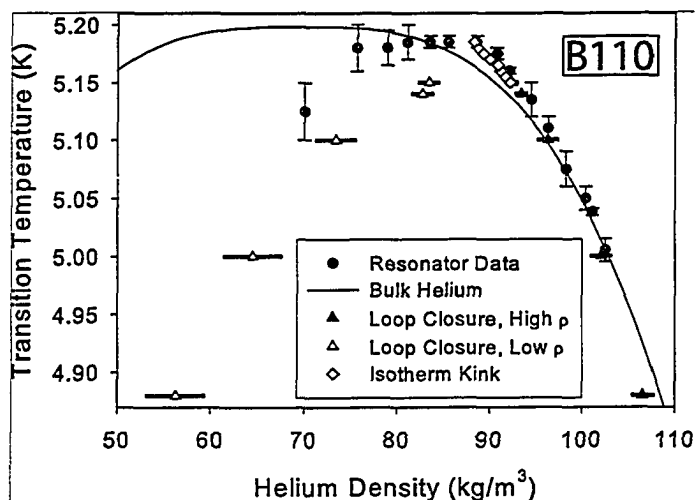
Figure 8.3: Data from the resonator and isotherm experiments for aerogel B110 plotted together with the behavior of bulk helium. There are three sets of data from the isotherms: the first two show the points at which the hysteresis loop closes while the third set maps out the position of the kink in the isotherm that shows the completion of capillary condensation.
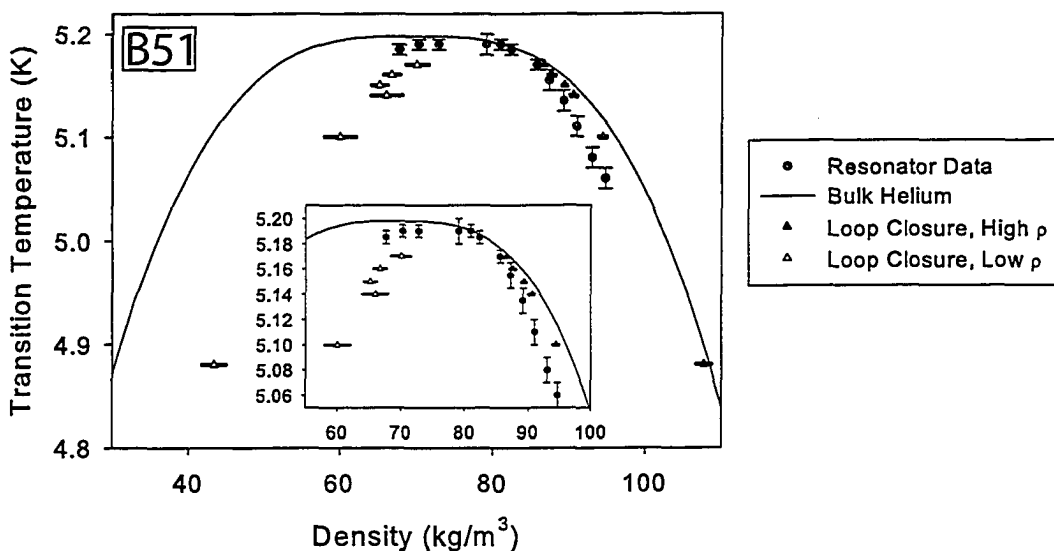
Figure 8.4: Data from the resonator and isotherm experiments for aerogel B51 plotted together with the behavior of bulk helium. This is similar to the previous figure but only includes two sets of data since no high quality isotherms were taken that exhibited a kink above the disappearance of hysteresis. The features of this graph are similar to that of Figure 8.3.

208

and Chan in their study of helium in aerogel[10]. The differences between the two data sets (resonance data and capacitance data) underscore the shortcomings of interpreting our data in terms of an equilibrium transition – if we were probing a simple liquid-vapor transition the data collected by these two methods should agree within error.

8.3.3 Aerogel Compression by Fluid Surface Tension

Our last set of measurements is only peripherally related to the first two experiments. Spurred on by the miniscule elastic constants of low density aerogels and the non-zero magnitude of the surface tension of liquid helium, we measured significant distortion during filling and emptying of the aerogel below the critical point of the fluid. Primarily, this should be taken as a note of warning to anyone condensing fluids into monolithic low density aerogel samples – while near the critical point there may be small distortions which spring back once the gel is completely filled or completely emptied, at low temperatures the strain may be great enough to permanently compress the aerogel.

Some researchers have claimed to see a small region of anomalous slope at the beginning of capillary evaporation in low density aerogel which may be explained by distortion – the effective pore size will change with compression and re-expansion, causing a change in the capillary pressure. We certainly see such a feature in our capacitively measured isotherms, although it is difficult to interpret in our case since distortion of the gel changes both the area of our electrodes and their separation. We can predict the degree of compression during emptying with surprising accuracy from an estimate of the aerogel Young's modulus and the surface tension of the fluid. While this does not give us insight into the mechanisms of capillary condensation when the gel is partially filled, it is consistent with desorption occurring by the penetration into the gel of vapor menisci with a characteristic radius, which does not depend heavily on temperature. However, it is also possible that desorption occurs by the homogeneous nucleation within the pore-space.

8.4 Interpretation of Fluid Condensation in Aerogel Results

8.4.1 Resonator Coexistence Curves

Since we began the resonator experiments assuming an equilibrium phase transition, and others before us have interpreted results in terms of the shape of their "coexistence curves," we will begin by trying to interpret the shape of the resultant coexistence curve using power law critical behavior. This is difficult to do for the helium curves where only the high density side can be easily distinguished, but is possible for the neon in aerogel B110. Afterwards we will backtrack a little and, without assuming that the final coexistence curve has any specific meaning, try to gain insight into the character of the transition itself.

First let us discuss the shape of the "coexistence curve" assuming that it represents a sensible phase transition. Experimentally, the bulk liquid-vapor coexistence curve is usually described by an effective critical exponent of $\beta \approx 0.35$, slightly larger than the Ising model value of $\beta \approx 0.33$ because of corrections to that asymptotic value. Our neon in aerogel coexistence curve (Figure 6.16) clearly has two distinct regions: a curve at lower temperatures and a plateau at higher temperatures. One critical exponent cannot describe this sort of behavior, so we must describe the two regions separately. There are three values for the critical exponent which are worth considering with respect to our curve: Ising model ($\beta \approx 0.33$), random-field Ising model ($\beta \approx 0$), and mean field ($\beta = 0.5$).

The signature of random-field behavior would be a very flat-topped coexistence with steep sides. This is consistent with the plateau-like region of the neon-aerogel coexistence curve, but not with the "legs" of the curve. Since random-field behavior results in a near-zero critical exponent, the traditional log-log plot to extract a critical exponent is of little use. However, a log-log plot of transition temperature against density for points away from the plateau allows us to evaluate the shape of the rest of the coexistence curve. Fixing the value of β and allowing the value for the critical temperature to vary allows us to try to fit the data into either Ising or mean-field behavior; the best fits for the data to each of those models were shown in Figure 6.17. Clearly the Ising model does not describe the data well, although naively fitting an Ising-like curve to the raw data intersects almost all the points within error (only missing a couple near the plateau region).

On the other hand, fitting the data to a mean-field exponent results in a much better fit; the data are scattered, but fall roughly along a line in the log-log plot rather than the kinked form seen in the Ising fit. If the critical exponent is allowed to vary, the best looking fits occur near $\beta \approx 0.55$, but the data is noisy enough that this fit is nearly indistinguishable from the mean field fit – to find a reliable and precise exponent one really needs more data points than acquired in this experiment. This sort of behavior seems somewhat odd though – in most other studies of near-critical fluids in porous media (see Chapter 3) the shape of the coexistence curves resembled the Ising model behavior. However, most of those studies used methods involving measuring excess adsorption which are more akin to our isothermal studies than to the resonator work; their indication of capillary condensation is the closure of hysteresis loops or a kink in the excess adsorption rather than a direct probe of the appearance of an inhomogeneous density distribution within the medium.

The most tempting inference to be made from the neon-aerogel coexistence curve would be that plateau in the center of the curve reflects a cross-over to a near-zero critical exponent, such as exhibited by the random field Ising model. While there is nothing within the neon resonator experiment to gainsay this explanation, and the helium resonator experiments also suggest a plateau at the top of the coexistence curve, there are some doubts raised about this interpretation from the isothermal data for helium in aerogel. Since any critical behavior seen in neon in aerogel should be universal enough to show up in the helium experiments, any questions raised by the helium isothermal results are applicable to the neon experiments as well. Specifically, the isotherms close to the critical point of helium all exhibit finite slopes and no hysteresis – the finite slope indicates that the system does not contain macroscopic phases in equilibrium with each another. So, speaking of our curve in terms of critical exponents is intriguing but probably not scientifically rigorous.

There is precedent for crossover to random field behavior in models, with behavior away from the critical point described by the Ising model and a sharp crossover to random field behavior near the critical point[25]. In a renormalization group calculation on the random field Ising model Falicov et al. saw a magnetization curve (analogous to the liquid-vapor coexistence curve) which exhibited a plateau which depended on the strength of the random fields[140]. However, both these examples presuppose a true equilibrium phase transition.

With all of the equivocation in the preceding paragraphs about the nature of

the liquid-vapor transition in aerogel, I would like to address some of the reasons to doubt that it is a true equilibrium in the sense of the bulk liquid-vapor transition. In bulk fluid, the compressibility diverges near the critical point. This results in a sharp dip in sound speed at the liquid-vapor transition when the fluid density is close to critical. Further from the critical density the transition appears as a sharp kink in sound speed, sometimes appearing as a dip (for lower densities) and sometimes as a shoulder (for higher densities). In either case the feature smoothly evolves with density and the transition remains distinct. This is not the case for fluid in aerogel: the signature of the transition changes dramatically with density in a much larger way than bulk fluid. If we were dealing with true macroscopic coexistence of liquid and vapor within the aerogel, there is no reason to expect such dramatic changes in the signature – to the contrary one might sensibly expect the signature of the transition to remain roughly constant, with gradual changes as the density is altered. The inclusion of aerogel will certainly wash out the changes in fluid compressibility near the critical point, but it should not affect different densities in different ways if the fluid response remains bulk-like in character.

The transition along the low density side of the coexistence curve is at best difficult to see, and at worst completely indistinct. The transition appeared as a smoothed out kink in the resonant frequency as a function of temperature. It was not accompanied by hysteresis between cooling and warming along the isochores, and the kink was gradual enough that the mode crossing present in most of the experiments obscured the signal too much to unambiguously pick a sign of the transition in any of the helium runs, and even made it difficult to assign a transition temperature in the neon resonator experiments. As density was increased the transition became more distinct, with the gradual change in slope eventually replaced by a distinct kink, often followed by a sharp drop in resonant frequency. These isochores usually exhibited hysteresis below the assigned transition temperature. The hysteresis only appeared in higher density isochores, and at temperatures consistent with the appearance of hysteresis in the capacitively measured isotherms.

The change in the transition marker indicates that the transition is changing, suggesting a more complicated choice of phases (perhaps including such things as films or bridges). This may fit in with the SAXS studies of ^{4}He condensation and ^{4}He-^{3}He phase separation [52, 53] which show that there are two distinct regions towards the low density side of the adsorption isotherm. As helium condenses a film

212

grows out to a significant distance and then collapses, as the fluid redistributes into larger "blobs" distributed throughout the aerogel.

8.4.2 Capacitive Isotherms

While the resonator experiments were predicated on the assumption that there was an underlying equilibrium macroscopic phase transition, and thus have less utility for studying out-of-equilibrium transitions, one may more directly interpret the adsorption isotherm results. Since there is evidence that there is not an equilibrium phase transition at the transition temperatures determined from the resonator, we can apply our knowledge of single-pore models of fluid condensation to studying the capacitively collected isotherms. Remember that we incorporated the Laplace pressure across a curved interface into a thermodynamic treatment of condensation in pores and derived the Kelvin Equation.

Using the second form of the Kelvin equation derived in Appendix A, and assuming a hemispherical meniscus we have:

$$p_0 - p_v = \frac{2\gamma}{r} \left(\frac{v_l}{v_v - v_l} \right)$$

Where the surface tension of the fluid and the the molar volumes of the liquid and vapor are all temperature dependent.

While real porous media do not exhibit exactly the magnitude of response expected from the model pore, they are consistent with this picture – the capillary condensation pressure gives a sensitive probe of pore size. Adsorption and desorption isotherms may occur at different pressures because of the different meniscus shapes during the two processes. For dense porous media it makes sense to envision archetypal meniscus shapes, but for capillary condensation in aerogel the picture is not at all clear. There is no evidence that the condensing fluid forms any structure any larger than a thin film on the aerogel strands. Attempts to describe the condensation of helium in terms of "constant curvature bubbles"[134], while explaining the shape of the adsorption isotherms, have no direct evidence supporting them. In fact, in the mean field calculations by Detcheverry *et al.* the condensed fluid is distributed in a disordered manner with regions of fluid that exhibit a wide range of interface curvatures[82].

If condensation in aerogel is well described by the Kelvin equation then it should be possible to extract information on the dominant size scales involved in capillary

213
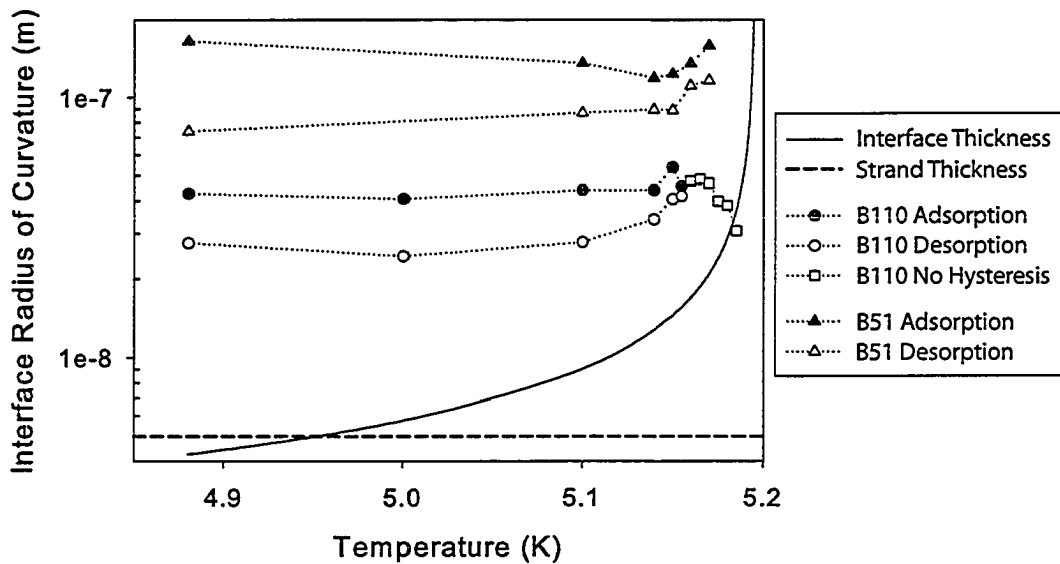
Figure 8.5: Effective radii of curvature for the helium liquid-vapor interfaces during adsorption and desorption in aerogels B110 and B51 from the Kelvin equation. We can see that such an interpretation works relatively well for lower temperatures but produces quickly changing values above 5.150K. The approximate thickness of the aerogel strands and the liquid-vapor interface thickness are also included on the plot.

condensation by calculating the curvature of the interface as described by the Kelvin equation. This value should remain relatively insensitive to temperature, since the temperature dependence of the adsorption isotherms should be accounted for by the temperature dependence of surface tension and molar volume. If we assume that helium in aerogel has a bulk-like surface tension, the density of adsorbed helium is equal to bulk helium, and the sharp corner at the high density end of the adsorption isotherm represents the pressure of capillary condensation, then we can extract a value for the curvature C. This value can then be converted to a pore size if we assume a well defined meniscus of a given shape. These calculations are shown in Figure 8.5 assuming a hemispherical meniscus. Also included in the figure are lines showing the size of the silica particles that make up the aerogel strands and the liquid-vapor interface thickness.

The interface thickness is calculated assuming the fluid is bulk-like, and is given by the equation[141]:

$$L = 3.64\xi$$

where L is the interface thickness and ξ is the fluid correlation length calculated from

214

$\xi = \xi_0 t^{-0.63}$ where ξ_0 is an amplitude which depends on the fluid ($\xi_0(^4He) = (1.8 \pm 0.3) * 10^{-10}m$ [38]). The interface thickness is only an estimate, since the presence of aerogel in the real system will certainly affect the density profile drastically at the liquid-vapor interface. When discussing capillary condensation in dense porous media the walls are assumed to be solid and uniform but in aerogel the "walls" are actually strands and once the interface thickness exceeds the strand thickness it is not sensible to treat the strands as uniform, smooth walls.

Above 5K the liquid-vapor interface is thicker than the aerogel strands, removing any sensible version of a smooth uniform wall which is often pictured in model pores. Similarly, as one approaches T_c the interface thickness eventually becomes comparable to the effective "r" calculated for B110 from the Kelvin equation. This behavior is not usually of concern in denser media where the capillary condensation pressure is displaced to lower partial pressure and disappears before one can get too near to the bulk liquid-vapor critical point. It does not make sense for the radius of curvature of an interface to be less than the thickness of the interface since that would preclude the existence of a distinct phase within that radius. In this regime it is probably better to picture the aerogel as contributing to the system as a perturbation affecting the fluid phases in some averaged way. In such a regime, the use of the Kelvin equation to extract an effective radius of curvature becomes tricky.

The low temperature values (i.e. less than 5.150K) for "r" extracted from the Kelvin equation are roughly constant and, within a few percent, can be summarized as:

Sample	Branch	r
B110	Filling	43nm
	Emptying	28nm
B51	Filling	135nm
	Emptying	85nm

So we can see that by assuming that the shape of the interface is identical during filling and emptying we extract a radius of curvature for that interface which is roughly 50% larger on filling than emptying. This could simply point to different shapes of the liquid-vapor interface during adsorption and desorption.

Near and above 5.150K, the radii extracted for helium condensation in sample B110 change rapidly. This may mean that the liquid-vapor interface has a shape

215

that is highly temperature dependent, but could also be an indication that there is an additional energetic concern affecting the system near the critical point (i.e. other than bulk surface tension).

It is interesting to compare the length scale extracted from the Kelvin equation with the correlation length of the aerogels themselves. For a base catalyzed aerogel with a density near $90\frac{mg}{cm^3}$, just less than our sample B110, the correlation length(ξ) was measured to be a little less than 10nm[113]. Furthermore, simulation studies deduced a relation between the correlation length and the fractal dimension of gels[112] which allows us to calculate the density dependence of the correlation length. For base catalyzed gels, with a fractal dimension of about 1.9, we would expect:

$$\xi \propto \rho^{-0.9}$$

From this relation we can estimate that $\xi_{B51}/\xi_{B110} \approx 2$. So, assuming that the structure of our base catalyzed gel resembles that of the gels on which scattering data has been collected, our two samples should have correlation lengths of just under 10nm (B110) and just under 20nm (B51). This length is of the same order, but much less than than radius of curvature extracted from the Kelvin equation above. Furthermore, while correlation length increases by a factor of about two between samples, the interface radius of curvature appears to change by about a factor of three. So, while there may be a relation between r and ξ one is not simply proportional to the other.

Near the critical point, where surface tension does not dominate the energetics of the system, one might expect to find equilibrium phase transitions resembling the bulk liquid-vapor transition. However this does not appear to be the case – the adsorption isotherms in this region all exhibit finite slopes (even in B51 – see Figure 5.47). It is only at lower temperatures that the isotherms in B51 have hysteresis loops which have vanishingly small slopes on both the adsorption and desorption branches.

8.5 Possible extensions of projects

The results of these studies leave little room to interpret the behavior of near-critical fluids in aerogels as a realization of the random-field Ising model, but there are some possible extensions to the projects described here. The capacitive measurements of

helium adsorption have proven to be precise and reproducible; the system can easily be used for any porosity of aerogel and also for denser porous glasses. In fact it may be interesting to repeat some of our measurements in aerogels with similar porosities but different synthesis conditions (i.e. acid catalyzed or neutrally reacted).

It would certainly be interesting to extend our measurements of aerogel compression during fluid adsorption to helium in 98% porous aerogel. To do this we will need to eliminate the large weight of the ferromagnetic core used in the LVDT – possibly the entire LVDT could be replaced with a different measurement technique. If a coaxial capacitor was constructed with the inner and outer plates moveable with respect to one another it would be possible to estimate relative linear displacement by measuring capacitance of the system. The inner plate could then rest on top of the aerogel cylinder, as the LVDT core does now, and would move as the aerogel expanded or contracted. We would need to ensure that the capacitor plates could not move laterally, only along the central axis, and would need to subtract any contribution from changes in the dielectric between the plates (i.e. changes in helium density). Such a system would allow us to reduce the weight on the aerogel sample to a fraction of a gram, and with careful calibration should provide at least as much sensitivity as the LVDT currently does.

8.6 Final Words

Fluid adsorption in aerogel is a process which exists in between the more classical picture of capillary condensation and the equilibrium first order transition characteristic of condensation in bulk fluids. The low elastic constants of aerogels restrict study to fluids with low surface tensions in order to avoid permanent deformation of the gel, which means that we are restricted to helium or other fluids near their liquid-vapor critical points. This, in turn, leads to very small temperature and pressure shifts for the liquid-vapor transition.

Furthermore, the open structure of aerogels does not seem to support the simple constant curvature menisci assumed by analyses such as the Kelvin equation. Instead, from scattering[52] and simulation[82] studies, liquid seems to be adsorbed along the strands and at intersections with no distinct shape to the liquid-vapor interface.

As the temperature of the sample is raised towards the liquid-vapor critical point the assumption that a distinct liquid-vapor interface exists begins to decay.

In helium, above 5K the liquid-vapor interface already exceeds the diameter of the aerogel silica strands so that the energy of the liquid-vapor interface may include contributions from the underlying silica but may be governed by thermal fluctuations. At temperatures close to the disappearance of hysteresis in the adsorption isotherms the interface thickness exceeds the correlation length of the gel; at this point the fluid cannot effectively sample small regions of the aerogel – it simply sees a homogenous background.

Our work probed the regimes from a well defined liquid-vapor interface at temperatures below 5K through to temperatures where thermal fluctuations probably cause the fluid to sense the aerogel as an isotropic background. Nowhere in these data did we see signs of an equilibrium first order transition. Isothermal pressure-density scans and isochoric temperature-compressibility scans allowed us to map out effective "coexistence curves," but the two methods yielded different curves – another sign of the lack of an equilibrium transition. Without strong evidence for a true thermodynamic phase transition it is inappropriate to interpret the resultant data in terms of critical behavior as we hoped to do at the outset of this work. Some of the hysteresis loops in aerogel B51 were exceptionally flat, which may indicate an underlying equilibrium phase transition in this system which we cannot access experimentally because of metastable filling and emptying states. Even if such a transition exists we simply cannot interpret our results in terms of an equilibrium transition because we cannot access the equilibrium states.

Fluid adsorption in aerogel does allow us to investigate capillary condensation as one approaches the liquid-vapor critical point. This is an interesting problem in itself, and with better understanding of the microscopic structure of the liquid-vapor interface in aerogel we may be able to resolve how thermal fluctuations near the critical point affect adsorption. This microscopic information will have to come from studies such as the SAXS work done at Argonne[52] and the simulations performed at Université Pierre et Marie Curie[82]. Furthermore, the tunable density and structure of aerogel provides researchers with control over exactly how much they wish to perturb the adsorbed fluid, and with a tool to probe how slightly different microstructures can affect fluid adsorption. While we have a large quantity of data, it is limited to two well understood samples; better understanding of this system may have to wait until there is a wider range of data taken in a more varied set of aerogels.

218

While the critical behavior that helped to motivate this project was never found, we have seen some behavior of helium near its liquid-vapor critical point in aerogel that is not well described by a simple application of the Kelvin equation either. So, although we have not gained another system which can be added to the random-field universality class, these results open exciting possibilities for general studies of capillary condensation in a regime where the liquid-vapor interface may not be the most significant energetic concern.

Bibliography

[1] P. G. de Gennes. Liquid-liquid demixing inside a rigid network. qualitative features. *Journal of Physical Chemistry*, 88:6469, 1984.

[2] M. H. W. Chan, K. I. Blum, S. Q. Murphy, G. K. S. Wong, and J. D. Reppy. Disorder and the superfluid transition in liquid ^{4}He. *Physical Review Letters*, 61(17):1950–1953, 1988.

[3] Norbert Mulders, Ravi Mehrotra, Lori S. Goldner, and Guenter Ahlers. Superfluid density from heat-pulse propogation near the λ line in ^{4}He-aerogel systems. *Physical Review Letters*, 67(6):695–698, 1991.

[4] G. K. S. Wong, P. A. Crowell, H. A. Cho, and J. D. Reppy. Superfluid critical behavior in ^{4}He-filled porous media. *Physical Review Letters*, 65(19):2410–2413, 1990.

[5] N. David Mermin and David M. Lee. Superfluid helium 3. *Scientific American*, 235(12):56–71, 1976.

[6] J. V. Porto and J. M. Parpia. Correlated disorder in a p-wave superfluid. *Physical Review B*, 59(22):14583–14592, 1999.

[7] G. Gervais, K. Yawata, N. Mulders, and W. P. Halperin. Nucleation and interfacial coupling between pure and dirty superfluid phases of ^{3}He. *Physical Review Letters*, 88(4):art. no.-045505, 2002.

[8] Th. Hohenberger, R. König, and F. Pobell. Phase separation of liquid ^{3}He-^{4}He mixtures in porous Vycor glass. *Journal of Low Temperature Physics*, 110(1/2):579–584, 1998.

[9] Norbert Mulders and M. H. W. Chan. Heat capacity measurements of ^{3}He-^{4}He mixtures in aerogel. *Physical Review Letters*, 75(20):3705–3708, 1995.

[10] Apollo P. Y. Wong and M. H. W. Chan. Liquid-vapor critical point of ^{4}He in aerogel. *Physical Review Letters*, 65(20):2567–2570, 1990.

[11] A. P. Y. Wong, S. B. Kim, W. I. Goldburg, and M. H. W. Chan. Phase separation, density fluctuation, and critical dynamics of N_2 in aerogel. *Physical Review Letters*, 70(7):954–957, 1993.

[12] B. J. Frisken, Fabio Ferri, and David S. Cannell. Effect of dilute silica gel on phase separation of a binary mixture. *Physical Review Letters*, 66(21):2754–2757, 1991.

[13] B. J. Frisken, Fabio Ferri, and David S. Cannell. Critical behavior in the presence of a disordered environment. *Physical Review E*, 51(6):5922–5943, 1995.

[14] C. Gabay, F. Despetis, P. E. Wolf, and L. Puech. Measurements of helium density in aerogel near the liquid-vapor critical point. *Journal of Low Temperature Physics*, 121(5/6):585–590, 2000.

[15] Claude Gabay. *Transitions de phases de l'hélium dans les aérogels de silice.* PhD thesis, CNRS - Grenoble, 2001.

[16] Michael E. Fisher. Renormalization group theory: Its basis and formulation in statistical physics. *Reviews of Modern Physics*, 70(2):653–681, 1998.

[17] Leo P. Kadanoff, Wolfgang Gö, David Hamblen, Robert Hecht, E. A. S. Lewis, V. V. Palciauskas, Martin Rayl, J. Swift, David Aspnes, and Joseph Kane. Static phenomena near critical points: Theory and experiment. *Reviews of Modern Physics*, 39(2):395–431, 1967.

[18] R. Guida and J. Zinn-Justin. Critical exponents of the N-vector model. *Journal of Physics A: Mathematical and General Physics*, 31:8103–8121, 1998.

[19] M. W. Pestak and M. H. W. Chan. Equation of state of N_2 and Ne near their critical points. Scaling, corrections to scaling, and amplitude ratios. *Physical Review B*, 30(1):274–288, 1984.

[20] Erik Luijten and Horst Meyer. Crossover behavior in ^{3}He and Xe near their liquid-vapor critical point. *Physical Review E*, 62(3):3257–3261, 2000.

[21] Charles Pittman, Theodore Doiron, and Horst Meyer. Equation of state and critical exponents of ^{3}He and a ^{3}He-^{4}He mixture near their liquid-vapour critical point. *Physical Review B*, 20(9):3678–3689, 1979.

[22] Daniel S. Fisher, Geoffrey M. Grinstein, and Anil Khurana. Theory of random magnets. *Physics Today*, 41(12):56–67, 1988.

[23] F. Brochard and P. G. de Gennes. Phase transitions of binary mixtures in random media. *Journal de Physique - Lettres*, 44:L785–L791, 1983.

[24] Heiko Rieger. Critical behavior of the three-dimensional random-field ising model: Two-exponent scaling and discontinuous transition. *Physical Review B*, 52(9):6659, 1995.

[25] M. S. Cao and J. Machta. Migdal-Kadanoff study of the random-field ising model. *Physical Review B*, 48(5):3177–3182, 1993.

[26] Pierre-Gilles de Gennes, Françoise Brochard-Wyart, and David Quéré. *Capillarity and Wetting Phenomena.* Springer-Verlag, 2004.

[27] Robert C. Weast, editor. *CRC Handbook of Chemistry and Physics, 56th Edition.* CRC Press, 1975.

[28] Jacob N. Israelachvili. *Intermolecular and Surface Forces.* Academic Press, Ltd., 1992.

[29] S. J. Gregg and Sing K. S. W. *Adsorption, Surface Area and Porosity.* Academic Press, 1967.

[30] L. D. Gelb and K. E. Gubbins. Characterization of porous glasses: Simulation models, adsorption isotherms, and the Brunauer-Emmett-Teller analysis method. *Langmuir*, 14(8):2097–2111, 1998.

[31] R. J. Dombrowski, C. M. Lastoskie, and D. R. Hyduke. The Horvath-Kawazoe method revisited. *Colloids and Surfaces a-Physicochemical and Engineering Aspects*, 187:23–39, 2001.

221

[32] Po-Zen Wong, editor. *Methods in the Physics of Porous Media*. Academic Press, 1999.

[33] Ralf Schmidt, Eddy Walther Hansen, Michael Stöcker, and Ole Henrik Akporiaye, Duncan Ellestad. Pore size determination of MCM-41 mesoporous materials by means of ^{1}H NMR spectroscopy, N_2 adsorption, and HREM. A preliminary study. *Journal of the American Chemical Society*, 117:4049–4056, 1995.

[34] E. D. Adams, Y. H. Yang, K. Uhlig, and G. E. Haas. Thermodynamics of freezing and melting in ^{4}He in vycor. *Journal of Low Temperature Physics*, 66(1/2):85–98, 1987.

[35] Eric Molz and John Beamish. Freezing and melting of helium in different porous media. *Journal of Low Temperature Physics*, 101(5/6):1055–1077, 1995.

[36] Katsumi Kaneko, Ayumi Watanabe, Taku Iiyama, Ravi Radhakrishan, and Keith E. Gubbins. A remarkable elevation of freezing temperature of CCl_4 in graphitic micropores. *The Journal of Physical Chemistry B*, 103(34):7061–7063, 1999.

[37] J. V. Sengers and J. M. H. Levelt Sengers. Thermodynamic behavior of fluids near the critical point. *Annual Review of Physical Chemistry*, 37:189–222, 1987.

[38] David B. Roe and Horst Meyer. Ultrasonic dispersion and attenuation near the liquid-gas critical point in ^{3}He. *Journal of Low Temperature Physics*, 30(1/2):91–115, 1978.

[39] M. R. Moldover. Interfacial tension of fluids near critical points and two-scale-factor universality. *Physical Review A*, 31(2):1022–1033, 1985.

[40] Liza Monette, Andrea J. Liu, and Gary S. Grest. Wetting and domain-growth kinetics in confined geometries. *Physical Review A*, 46(12):7664–7679, 1992.

[41] Zhiming Zhuang, Arturo G. Casielles, and David S. Cannell. Phase diagram of isobutyric acid and water in dilute silica gel. *Physical Review Letters*, 77(14):2969–2972, 1996.

[42] K. Morishige and M. Shikimi. Adsorption hysteresis and pore critical temperature in a single cylindrical pore. *Journal of Chemical Physics*, 108(18):7821–7824, 1998.

[43] P. Huber and K. Knorr. Adsorption-desorption isotherms and x-ray diffraction of Ar condensed into a porous glass matrix. *Physical Review B*, 60(18):12657–12665, 1999.

[44] William D. Machin. Properties of three capillary fluids in the critical region. *Langmuir*, 15:169–173, 1999.

[45] P. I. Ravikovitch, S. C. O. Domhnaill, A. V. Neimark, F. Schüth, and K. K. Unger. Capillary hysteresis in nanopores: Theoretical and experimental studies of nitrogen adsorption on MCM-41. *Langmuir*, 11:4765–4772, 1995.

[46] Matthias Thommes and Gerhard Findenegg. Pore condensation and critical-point shift of a fluid in controlled-pore glass. *Langmuir*, 10:4270–4277, 1994.

[47] Thomas Michalski, Anke Benini, and Gerhard H. Findenegg. A study of multilayer adsorption and pore condensation of pure fluids in graphite substrates on approaching the bulk critical point. *Langmuir*, 7:185–190, 1991.

222

[48] Matthias Thommes, Gerhard H. Findenegg, and Martin Schoen. Critical depletion of a pure fluid in controlled-pore glass. Experimental results and Grand Canonical ensemble Monte Carlo simulation. *Langmuir*, 11:2137–2142, 1995.

[49] Nigel B. Wilding and Martin Schoen. Absence of simulation evidence for critical depletion in slit pores. *Physical Review E*, 60(1):1081–1083, 1999.

[50] Arvind Rajendran, Thomas Hocker, Orazia Di Giovanni, and Marcus Mazzotti. Experimental observation of critical depletion: Nitrous oxide adsorption on silica gel. *Langmuir*, 18:9726–9734, 2002.

[51] A. Maciolek, R. Evans, and N. B. Wilding. Effects of confinement on critical adsorption: Absence of critical depletion for fluids in slit pores. *Physical Review E*, 60(6):7105–7119, 1999.

[52] L. B. Lurio, Norbert Mulders, M. Paetkau, M. Lee, S. G. J. Mochrie, and M. H. W. Chan. X-ray scattering measurements of helium adsorption into silica aerogel. *Journal of Low Temperature Physcis*, 121(5-6):591–596, 2000.

[53] Norbert Mulders. Personal communication.

[54] Pak yeung Apollo Wong. *Liquid-Vapor Critical Point of Fluids in Porous Glasses*. PhD thesis, The Pennsylvania State University, 1992.

[55] M. H. W. Chan. Unpublished data.

[56] M. H. W. Chan. Personal communication.

[57] C. Gabay, P. E. Wolf, and L. Puech. A very low-frequency pendulum for measurements of helium density in aerogel. *Physica B*, 284:99–100, 2000.

[58] T. Lambert, C. Gabay, L. Puech, and P. E. Wolf. Optical study of ^{4}He condensation into a silica aerogel. *Journal of Low Temperature Physics*, 134(1):293–302, 2004.

[59] Y. B. Melnichenko, G. D. Wignall, D. R. Cole, and H. Frielinghaus. Density fluctuations near the liquid-gas critcal point of a confined fluid. *Physical Review E*, 69(5):057102, 2004.

[60] B. J. Frisken and David S. Cannell. Critical dynamics in the presence of a silica gel. *Physical Review Letters*, 69(4):632–635, 1992.

[61] B. J. Frisken, David S. Cannell, M. Y. Lin, and S. K. Sinha. Neutron-scattering studies of binary mixtures in silica gels. *Physical Review E*, 51(6):5866–5879, 1995.

[62] Arthur E. Bailey, B. J. Frisken, and David S. Cannell. Domain growth in the presence of quenched disorder. *Physical Review E*, 56(3):3112–3118, 1997.

[63] N. B. Wilding. Computer simulation of fluid phase transitions. *American Journal of Physics*, 69(11):1147–1155, 2001.

[64] S. M. Gatica, M. M. Calbi, and M. W. Cole. Simple model of capillary condensation in porous media. *Physical Review E*, 65:1–4, 2002.

[65] Andrea J. Liu, D. J. Durian, Eric Herbolzheimer, and S. A. Safran. Wetting transitions in a cylindrical pore. *Physical Review Letters*, 65(15):1897–1900, 1990.

[66] Andrea J. Liu and Gary S. Grest. Wetting in a confined geometry: A Monte Carlo study. *Physical Review A*, 44(12):7894–7897, 1991.

[67] James P. Donley and Andrea J. Liu. Phase behavior of near-critical fluids confined in periodic gels. *Physical Review E*, 55(1):539–543, 1997.

[68] R. Evans. Fluids adsorbed in narrow pores - Phase-equilibria and structure. *Journal of Physics-Condensed Matter*, 2(46):8989–9007, 1990.

[69] William G. Madden and Eduardo D. Glandt. Distribution functions for fluids in random media. *Journal of Statistical Physics*, 51(3/4):537–558, 1988.

[70] William G. Madden. Fluid distributions in random media: Arbitrary matrices. *Journal of Chemical Physics*, 96(7):5422, 1992.

[71] David M. Ford and Eduardo D. Glandt. Vapor-liquid phase equilibrium in random microporous matrices. *Physical Review E*, 50:1280, 1994.

[72] E. Pitard, M. L. Rosinberg, G. Stell, and G. Tarjus. Critical behavior in a disordered porous matrix: An Ornstein-Zernike approach. *Physical Review Letters*, 74(22):4361–4364, 1995.

[73] K. S. Page and P. A. Monson. Monte carlo calculations of phase diagrams for a fluid confined in a disordered porous material. *Physical Review E*, 54(6):6557–6564, 1996.

[74] L. Sarkisov and P. A. Monson. Computer simulations of phase equilibrium for a fluid confined in a disordered porous structure. *Physical Review E*, 61(6):7231–7234, 2000.

[75] L. Sarkisov and P. A. Monson. Lattice model of adsorption in disordered porous materials: Mean-field density functional theory and Monte Carlo simulations. *Physical Review E*, 65(1):011202, 2002.

[76] E. Kierlik, P. A. Monson, M. L. Rosinberg, L. Sarkisov, and G. Tarjus. Capillary condensation in disordered porous materials: Hysteresis versus equilibrium behavior. *Physical Review Letters*, 87:055701, 2001.

[77] J. K. Brennan and W. Dong. Phase transitions of one-component fluids adsorbed in random porous media: Monte Carlo simulations. *Journal of Chemical Physics*, 116(20):8948–8958, 2002.

[78] W. Rzysko, J. J. de Pablo, and S. Sokolowski. Critical behavior of simple fluids confined by microporous materials. *Journal of Chemical Physics*, 113(21):9772, 2000.

[79] Linghui Zhang, Songyin Cheng, and Paul R. Van Tassel. Effect of templated quenched disorder on fluid phase equilibrium. *Physical Review E*, 64:042101, 2001.

[80] Anna Lopatnikova and A. Nihat Berker. Renormatlization-group study of superfluidity and phase separation of helium mixtures immersed in a disordered porous medium. *Physical Review B*, 56(18):11865–11871, 1997.

[81] V. Krakoviack, E. Kierlik, M.-L. Rosinberg, and G. Tarjus. Adsorption of a fluid in an aerogel: Integral equation approach. *Journal of Chemical Physics*, 115(24):11289–11298, 2001.

[82] F. Detcheverry, E. Kierlik, M. L. Rosinberg, and G. Tarjus. Mechanism for gas adsorption and desorption in silica aerogels: The effect of temperature. *Langmuir*, 20:8006–8014, 2004.

[83] F. Detcheverry, E. Kierlik, M. L. Rosinberg, and G. Tarjus. Local mean-field study of capillary condensation in silica aerogels. *Physical Review E*, 68:061504, 2003.

[84] S. S. Kistler. Coherent expanded aerogels and jellies. *Nature*, 127:741, 1931.

[85] S. J. Teichner. Aerogels of inorganic oxides. In J Fricke, editor, *Aerogels*, pages 22–30. Springer-Verlag, 1986.

[86] G. Poelz. Aerogel in high energy physics. In J Fricke, editor, *Aerogels*, pages 176–187. Springer-Verlag, 1986.

[87] Ioannis Michalou(di)s. Nephele. http://web.mit.edu/%7Emichalou/www/index.html.

[88] J. Fricke and T. Tillotson. Aerogels: production, characterization, and applications. *Thin Solid Films*, 297:212–223, 1997.

[89] Nicola Hüsing and Ulrich Schubert. Aerogels – airy materials: Chemistry, structure, and properties. *Angewandte Chemie International Edition*, 37:22–45, 1998.

[90] J. Fricke and A. Emmerling. Aerogels – Recent progress in production techniques and novel applications. *Journal of Sol-Gel Science and Technology*, 13:299–303, 1998.

[91] Yu. K. Akimov. Fields of application of aerogels (review). *Instruments and Experimental Techniques*, 46(3):5–19, 2003.

[92] Peter Tsou. Silica aerogel captures cosmic dust intact. *Journal of Non-Crystalline Solids*, 186:415–427, 1995.

[93] H. D. Gesser and P. C. Goswami. Aerogels and related porous materials. *Chemical Reviews*, 89:765–788, 1989.

[94] R. W. Pekala, S. T. Mayer, J. L. Kascmitter, and F. M. Kong. Carbon aerogels: An update on structure, properties, and applications. In Y A Attia, editor, *Sol-Gel Processing and Apllications*, pages 369–377. Plenum Press, New York, 1994.

[95] John D. Wright and Nico A. J. M. Sommerdijk. *Sol Gel Materials*. Gordon and Breach Science Publishers, 2001.

[96] H. Tamon, T. Sone, and M. Okazaki. Control of mesoporous structure of silica aerogel prepared from TMOS. *Journal of Colloid and Interface Science*, 188(1):162–167, 1997.

[97] B. E. Yoldas, M. J. Annen, and J. Bostaph. Chemical engineering of aerogel morphology formed under nonsupercritical conditions for thermal insulation. *Chemistry of Materials*, 12:2475–2484, 2000.

[98] W. Lenhard, A. Emmerling, and J. Fricke. Investigations of isothermal sintering of silica aerogels. In Y A Attia, editor, *Sol-Gel Processing and Apllications*, pages 257–265. Plenum Press, New York, 1994.

[99] A. Hafidi Alaoui, T. Woignier, J. Phalippou, and G. W. Scherer. Room temperature densification of aerogel by isostatic compression. *Journal of Sol-Gel Science and Technology*, 13:365–369, 1998.

[100] T. M. Tillotson and L. W. Hrubesh. Transparent ultralow-density silica aerogels prepared by a two-step sol-gel process. *Journal of Non-Crystalline Solids*, 145:44–50, 1992.

[101] A. Venkateswara Rao, G. M. Pajonk, N. N. Parvathy, and E. Elaloui. Influence of sol-gel parameters on the transparancy and monolithicity of silica aerogels. In Y A Attia, editor, *Sol-Gel Processing and Apllications*, pages 237–256. Plenum Press, New York, 1994.

[102] M. Prassas, J. Phalippou, and J. Zarzycki. Synthesis of monolithic silica aerogels by hypercritical solvent evacuation. *Journal of Materials Science*, 19:1656, 1984.

[103] G. Poelz and R. Riethmüller. Preparation of silica aerogel for Cherenkov counters. *Nuclear Instruments and Methods*, 195:491–503, 1982.

[104] Ph. Dieudonne, P. Delord, S. Calas, A. Hafidi-Alaoui, and J. Phalippou. Silica dissolution-redeposition in gels and aerogels. *Journal of Sol-Gel Science and Technology*, 19:657–660, 2000.

[105] Douglas A. Loy, Edward M. Russick, Stacey A. Yamanaka, and Brigitta M. Baugher. Direct formation of aerogels by sol-gel polymerizations of alkoxysilanes in supercritical carbon dioxide. *Chemistry of Materials*, 9:2264–2268, 1997.

[106] K. Tajiri, K. Igarashi, and T. Nishio. Effects of supercritical drying media on structure and properties of silica aerogel. *Journal of Non-Crystalline Solids*, 186:83–87, 1995.

[107] G. M. Pajonk, A. Venkateswara Rao, B. M. Sawant, and N. N. Parvathy. Dependence of monolithicity and physical properties of TMOS silica aerogels on gel aging and drying conditions. *Journal of Non-crystalline solids*, 209:40–50, 1997.

[108] S. Henning. Large-scale production of airglass. In J Fricke, editor, *Aerogels*, pages 38–41. Springer-Verlag, 1986.

[109] George W. Scherer. Stress development during supercritical drying. *Journal of Non-Crystalline Solids*, 145:33–40, 1992.

[110] George C. Ruben, L. W. Hrubesh, and T. M. Tillotson. High resolution transmission electron microscopy nanostructure of condensed-silica aerogels. *Journal of Non-Crystalline Solids*, 186:209–218, 1995.

[111] Renè Vacher, Thierry Woignier, Jacques Pelous, and Eric Courtens. Structure and self-similarity of silica aerogels. *Physical Review B*, 37(11):6500, 1988.

[112] Anwar Hasmy, Eric Anglaret, Marie Foret, Jacques Pelous, and Rèmi Jullien. Small-angle neutron-scattering investigation of long-range correlations in silica aerogels: Simulations and experiments. *Physical Review B*, 50(9):6006–6016, 1994.

[113] Dale W. Schaefer and Keith D. Keefer. Structure of random porous materials: Silica aerogels. *Physical Review Letters*, 56(20):2199, 1986.

[114] F. Devreux, J. P. Boilot, F. Chaput, and B. Sapoval. NMR determination of the fractal dimension in silica aerogels. *Physical Review Letters*, 65(5):614–617, 1990.

[115] Fabio Ferri, B. J. Frisken, and David S. Cannell. Structure of silica gels. *Physical Review Letters*, 67(25):3626–3629, 1991.

[116] J. Gross, J. Fricke, R. W. Pekala, and L. W. Hrubesh. Elastic nonlinearity of aerogels. *Physical Review B*, 45(22):12774–12777, 1992.

[117] Joachim Gross, R. Goswin, R. Gerlach, and Jochen Fricke. Mechanical properties of SiO_2-aerogels. *Journal de Physique (Paris)*, 50(C-4):C4185–C4190, 1989.

[118] Ying Xie and John R. Beamish. Ultrasonic properties of silica aerogels at low temperatures. *Physical Review B*, 57(6):3406–3410, 1998.

226

[119] T. Woignier and J. Phalippou. Scaling law variation of the mechanical properties of silica aerogels. *Journal de Physique (Paris)*, 50(C-4).

[120] George W. Scherer, Douglas M. Smith, Xiaomei Qiu, and Julie M. Anderson. Compression of aerogels. *Journal of Non-Crystalline Solids*, 186:316–320, 1995.

[121] L. Duffours, T. Woignier, and J. Phalippou. Plastic behavior of aerogels under isotatic pressure. *Journal of Non-Crystalline Solids*, 186:321–327, 1995.

[122] M. Moner-Girona, A. Roig, E. Molins, E. Martines, and J. Esteve. Micromechanical properties of silica aerogels. *Applied Physics Letters*, 75(5):653–655, 1999.

[123] David R. Daughton, James MacDonald, and Norbert Mulders. Acoustic properties of silica aerogels from 400mK to 400k. *Physica B*, 329-333:1233–1234, 2003.

[124] M. A. Biot. Theory of propagation of elastic waves in a fluid-saturated porous solid. I. Low-frequency range. *The Journal of the Acoustical Society of America*, 28(2):168–178, 1956.

[125] M. A. Biot. Theory of propagation of elastic waves in a fluid-saturated porous solid. II. Higher-frequency range. *The Journal of the Acoustical Society of America*, 28(2):179–191, 1956.

[126] L. Forest, V. Gibiat, and T. Woignier. Biot's theory of acoustic propagation in porous media applied to aerogels and alcogels. *Journal of Non-Crystalline Solids*, 225:287–292, 1998.

[127] A. M. de Goer, R. Calemczuk, B. Salce, J. Bon, E. Bonjour, and R. Maynard. Low-temperature excitations and thermal properties of silica aerogels. *Physical Review B*, 40(12):8327–8335, 1989.

[128] A. Bernasconi, T. Sleator, D. Posselt, J. K. Kjems, and H. R. Ott. Dynamic properties of silica aerogels as deduced from specific-heat and thermal-conductivity measurements. *Physical Review B*, 45(18):10363–10376, 1992.

[129] T. M. Haard, G. Gervais, R. Nomura, and W. P. Halperin. The pathlength distribution of simulated aerogels. *Physica B*, 284-288:289–290, 2000.

[130] W. Chr. Heerens and F. C. Vermeulen. Capacitance of kelvin guard-ring capacitors with modified edge geometry. *Journal of Applied Physics*, 46(6):2486–2490, 1975.

[131] G. C. Straty and E. D. Adams. Highly sensitive capacitive pressure gauge. *Review of Scientific Instruments*, 40(11):1393–1397, 1969.

[132] www.ansoft.com.

[133] E. W. Lemmon, M. O. McLinden, and D. G. Friend. Thermophysical properties of fluid systems. In P. J. Linstrom and W. G. Mallard, editors, *NIST Chemistry WebBook, NIST Standard Reference Database Number 69*. National Institute of Standards and Technology, Gaithersburg MD, 20899 (http://webbook.nist.gov), 2003.

[134] Jongsoo Yoon and Moses H. W. Chan. Superfuid transition of ^{4}He in porous gold. *Physical Review Letters*, 78(25):4801–4804, 1997.

[135] Y. C. Wang and R. S. Lakes. Resonant ultrasound spectroscopy in shear mode. *Review of Scientific Instruments*, 74(3):1371–1373, 2003.

227

[136] J. L. Kline and E. F. Carome. Low frequency sound velocity measurements in xenon in the critical region. *Journal of Chemical Physics*, 58(11):4962–4967, 1973.

[137] Hong Wee Tan. Neon in porous glass samples and aerogels. Master's thesis, University of Alberta, 1998.

[138] G. Reichenauer and G. W. Scherer. Extracting the pore size distribution of compliant materials from nitrogen adsorption. *Colloids and Surfaces a-Physicochemical and Engineering Aspects*, 187:41–50, 2001.

[139] J. Shen and P. A. Monson. A molecular model of adsorption in a dilute semiflexible porous network. *Molecular Physics*, 100(13):2031–2039, 2002.

[140] Alexis Falicov, A. Nihat Berker, and Susan R. McKay. Renormalization-group theory of the random-field Ising model in three dimensions. *Physical Review B*, 51(13):8266–8269, 1995.

[141] D. Bonn and G. H. Wegdam. Capillary waves and ellipsometry experiments. *Journal de Physique I*, 2(9):1755–1764, 1992.

[142] R. J. Hunter. *Introduction to Modern Colloid Science*, chapter 5. Oxford University Press, New York, 1999.

[143] Janet A. W. Elliott. On the complete kelvin equation. *Chemical Engineering Education*, 35(4):274–278, 2001.

[144] L. D. Landau and E. M. Lifshitz. *Statistical Physics*, chapter 15. Pergamon Press, 1958.

[145] T. J. Barton, L. M. Bull, W. G. Klemperer, D. A. Loy, B. McEnaney, M. Misono, P. A. Monson, G. Pez, G. W. Scherer, J. C. Vartuli, and O. M. Yaghi. Tailored porous materials. *Chemistry of Materials*, 11(10):2633–2656, 1999.

[146] P. Wiltzius, F. S. Bates, S. B. Dierker, and G. D. Wignall. Structure of porous Vycor glass. *Physical Review A*, 36(6):2991, 1987.

[147] K. Sing. The use of nitrogen adsorption for the characterisation of porous materials. *Colloids and Surfaces a-Physicochemical and Engineering Aspects*, 187:3–9, 2001.

[148] P. I. Ravikovitch and A. V. Neimark. Characterization of nanoporous materials from adsorption and desorption isotherms. *Colloids and Surfaces a-Physicochemical and Engineering Aspects*, 187:11–21, 2001.

[149] J. Y. Ying, C. P. Mehnert, and M. S. Wong. Synthesis and applications of supramolecular-templated mesoporous materials. *Angewandte Chemie-International Edition*, 38(1-2):56–77, 1999.

[150] A. Corma. From microporous to mesoporous molecular sieve materials and their use in catalysis. *Chemical Reviews*, 97(6):2373–2419, 1997.

[151] D. R. Tilley and J. Tilley. *Superfluidity and Superconductivity*. Adam Hilger, Ltd, Bristol, 1986.

[152] E. G. Syskakis, F. Pobell, and H. Ullmaier. Superfluidity of ^{4}He confined in microscopic bubbles in copper. *Physical Review Letters*, 55(27):2964–2967, 1985.

[153] L. Smart and E. Moore. *Solid State Chemistry*. Stanely Thornes Ltd., 1998.

[154] S. Miyamoto and Y. Takano. Dehydration of large zeolite crystals for a study of He-4 in confined geometries. *Physica B*, 194:163–164, 1994.

228

[155] A. Dyer. *An Introduction to Zeolite Molecular Sieves*. John Wiley and Sons, 1988.

[156] R. M. Barrer. *Zeolites and Clay Minerals as Sorbants and Molecular Sieves*. Academic Press, London, 1978.

[157] K. Ohtsuka. Preparation and properties of two-dimensional microporous pillared interlayered solids. *Chemistry of Materials*, 9(10):2039–2050, 1997.

[158] M. J. Hernando, C. Pesquera, C. Blanco, I. Benito, and F. Gonzalez. Differences in structural, textural, and catalytic properties of montmorillonite pillared with (GaAl₁2) and (AlAl₁2) polyoxycations. *Chemistry of Materials*, 8(1):76–82, 1996.

[159] T. Mandalia, M. Crespin, D. Messad, and F. Bergaya. Large interlayer repeat distances observed for montmorillonites treated by mixed Al-Fe and Fe pillaring solutions. *Chemical Communications*, (19):2111–2112, 1998.

[160] D. T. Karamanis, X. A. Aslanoglou, P. A. Assimakopoulos, and N. H. Gangas. PIGE and XRF analysis of a nano-composite pillared layered clay material for nuclear waste applications. *Nuclear Instruments and Methods in Physics Research Section B- Beam Interactions with Materials and Atoms*, 181:616–621, 2001.

[161] Y. S. Han and J. H. Choy. Modification of the interlayer pore structure of silica iron oxide sol pillared clay using organic templates. *Journal of Materials Chemistry*, 8(6):1459–1463, 1998.

[162] T. L. Porter, M. P. Eastman, M. E. Hagerman, J. L. Attuso, and E. D. Bain. Scanning force microscopy and polymerization studies on cast thin films of hectorite and montmorillonite. *Journal of Vacuum Science and Technology a- Vacuum Surfaces and Films*, 14(3):1488–1493, 1996.

[163] F. Kooli, T. Sasaki, V. Rives, and M. Watanabe. Synthesis and characterization of a new mesoporous alumina- pillared titanate with a double-layer arrangement structure. *Journal of Materials Chemistry*, 10(2):497–501, 2000.

[164] F. Kooli, T. Sasaki, M. Watanabe, C. Martin, and V. Rives. Microporosity and acidity properties of alumina pillared titanates. *Langmuir*, 15(4):1090–1095, 1999.

[165] J. H. Choy, H. C. Lee, H. Jung, and S. J. Hwang. A novel synthetic route to TiO₂-pillared layered titanate with enhanced photocatalytic activity. *Journal of Materials Chemistry*, 11(9):2232–2234, 2001.

[166] M. Mamak, N. Coombs, and G. A. Ozin. Mesoporous nickel-yttria-zirconia fuel cell materials. *Chemistry of Materials*, 13(10):3564–3570, 2001.

[167] M. J. MacLachlan, N. Coombs, R. L. Bedard, S. White, L. K. Thompson, and G. A. Ozin. Mesostructured metal germanium sulfides. *Journal of the American Chemical Society*, 121(51):12005–12017, 1999.

[168] P. N. Trikalitis, K. K. Rangan, T. Bakas, and M. G. Kanatzidis. Varied pore organization in mesostructured semiconductors based on the [SnSe₄] (4-) anion. *Nature*, 410(6829):671–675, 2001.

[169] W. Cheng, E. Baudrin, B. Dunn, and J. I. Zink. Synthesis and electrochromic properties of mesoporous tungsten oxide. *Journal of Materials Chemistry*, 11(1):92–97, 2001.

[170] R. Ryoo, S. H. Joo, M. Kruk, and M. Jaroniec. Ordered mesoporous carbons. *Advanced Materials*, 13(9):677–681, 2001.

[171] N. K. Raman, M. T. Anderson, and C. J. Brinker. Template-based approaches to the preparation of amorphous, nanoporous silicas. *Chemistry of Materials*, 8(8):1682–1701, 1996.

[172] Neeraj and C. N. R. Rao. Phase transformations of mesoporous zirconia. *Journal of Materials Chemistry*, 8(7):1631–1634, 1998.

[173] S. Obrien, R. J. Francis, S. J. Price, D. Ohare, S. M. Clark, N. Okazaki, and K. Kuroda. Formation of silica-surfactant mesophases studied by real-time in-situ x-ray-powder diffraction. *Journal of the Chemical Society-Chemical Communications*, (23):2423–2424, 1995.

[174] D. Y. Zhao, J. L. Feng, Q. S. Huo, N. Melosh, G. H. Fredrickson, B. F. Chmelka, and G. D. Stucky. Triblock copolymer syntheses of mesoporous silica with periodic 50 to 300 angstrom pores. *Science*, 279(5350):548–552, 1998.

[175] D. Kumar, K. Schumacher, C. D. F. von Hohenesche, M. Grun, and K. K. Unger. MCM-41, MCM-48 and related mesoporous adsorbents: their synthesis and characterisation. *Colloids and Surfaces a-Physicochemical and Engineering Aspects*, 187:109–116, 2001.

[176] Q. S. Huo, J. L. Feng, F. Schuth, and G. D. Stucky. Preparation of hard mesoporous silica spheres. *Chemistry of Materials*, 9(1):14–17, 1997.

[177] H. Yang, G. Vovk, N. Coombs, I. Sokolov, and G. A. Ozin. Synthesis of mesoporous silica spheres under quiescent aqueous acidic conditions. *Journal of Materials Chemistry*, 8(3):743–750, 1998.

[178] H. Yang, N. Coombs, O. Dag, I. Sokolov, and G. A. Ozin. Free-standing mesoporous silica films; morphogenesis of channel and surface patterns. *Journal of Materials Chemistry*, 7(9):1755–1761, 1997.

[179] H. Yang, N. Coombs, I. Sokolov, and G. A. Ozin. Registered growth of mesoporous silica films on graphite. *Journal of Materials Chemistry*, 7(7):1285–1290, 1997.

[180] H. Yang, N. Coombs, and G. A. Ozin. Thickness control and defects in oriented mesoporous silica films. *Journal of Materials Chemistry*, 8(5):1205–1211, 1998.

[181] Y. Sato, K. Nakanishi, K. Hirao, H. Jinnai, M. Shibayama, Y. B. Melnichenko, and G. D. Wignall. Formation of ordered macropores and templated nanopores in silica sol-gel system incorporated with EO-PO-EO triblock copolymer. *Colloids and Surfaces a-Physicochemical and Engineering Aspects*, 187:117–122, 2001.

[182] S. H. Tolbert, A. Firouzi, G. D. Stucky, and B. F. Chmelka. Magnetic field alignment of ordered silicate-surfactant composites and mesoporous silica. *Science*, 278(5336):264–268, 1997.

[183] S. Inagaki, Y. Fukushima, and K. Kuroda. Synthesis of highly ordered mesoporous materials from a layered polysilicate. *Journal of the Chemical Society-Chemical Communications*, (8):680–682, 1993.

[184] Q. B. Kan, V. Fornes, F. Rey, and A. Corma. Transformation of layered aluminosilicates and gallosilicates with kanemite structure into mesoporous materials. *Journal of Materials Chemistry*, 10(4):993–1000, 2000.

[185] A. Walcarius and J. Bessiere. Electrochemistry with mesoporous silica: Selective mercury(II) binding. *Chemistry of Materials*, 11(11):3009–3011, 1999.

[186] D. T. On and S. Kaliaguine. Large-pore mesoporous materials with semi-crystalline zeolitic frameworks. *Angewandte Chemie-International Edition*, 40(17):3248–3251, 2001.

[187] Chibing Tan, Bing M. Fung, Jerry K. Newman, and Chilan Vu. Organic aerogels with very high impact strength. *Advanced Materials*, 13(9):644–646, 2001.

[188] C. J. Brinker and G. W. Scherer. Sol-gel glass. 1. gelation and gel structure. *Journal of Non-Crystalline Solids*, 70(3):301–322, 1985.

[189] Thomas H. Elmer. Porous and reconstructed glasses. In *Ceramics and Glasses*, volume 4 of *Engineered Materials Handbook*, pages 427–432. ASM International, 1992.

[190] Wolfgang Haller. Rearrangement kinetics of the liquid-liquid immiscible microphases in alkali borosilicate melts. *Journal of Chemical Physics*, 42(2):686–693, 1965.

[191] R. Li and K. Sieradzki. Ductile-brittle transition in random porous Au. *Physical Review Letters*, 68(8):1168–1171, 1992.

[192] Grard Frey. Microporous solids: From organically templated inorganic skeletons to hybrid frameworks ... Ecumenism in chemistry. *Chemistry of Materials*, 13:3084–3098, 2001.

[193] G. P. Crawford, L. M. Steele, R. Ondriscrawford, G. S. Iannacchione, C. J. Yeager, J. W. Doane, and D. Finotello. Characterization of the cylindrical cavities of Anopore and Nucleopore membranes. *Journal of Chemical Physics*, 96(10):7788–7796, 1992.

[194] M. P. Lilly and R. B. Hallock. Probing the internal structure of nuclepore with hysteretic capillary condensation. *Physical Review B*, 6317(17), 2001.

[195] L. D. Gelb, K. E. Gubbins, R. Radhakrishnan, and M. Sliwinska-Bartkowiak. Phase separation in confined systems. *Reports on Progress in Physics*, 62(12):1573–1659, 1999.

[196] M. Rall, J. P. Brison, and N. S. Sullivan. Supercooling of molecular-hydrogen in zeolite. *Physical Review B*, 44(17):9639–9642, 1991.

[197] N. S. Sullivan, M. Rall, and J. P. Brison. NMR-studies of molecular-hydrogen in zeolite. *Journal of Low Temperature Physics*, 98(5-6):383–401, 1995.

[198] N. Wada, H. Kato, and T. Watanabe. Formation of layers and gas and liquid states of helium in 8-13 angstrom diameter pores of Y-zeolites. *Journal of Low Temperature Physics*, 95(3-4):507–523, 1994.

[199] J. Wilks. *The Properties of Liquid and Solid Helium*. Clarendon Press, Oxford, 1967.

[200] K. Konishi, H. Deguchi, and K. Takeda. Heat-capacities of helium in one-dimensional and 3-dimensional channels at low-temperatures. *Journal of Physics-Condensed Matter*, 5(11):1619–1632, 1993.

[201] K. Konishi, T. Hattori, H. Deguchi, and K. Takeda. Heat-capacities of neon in one-dimensional and 3-dimensional channels at low-temperatures. *Journal of Physics-Condensed Matter*, 6(12):2341–2346, 1994.

[202] G. M. Zassenhaus and J. D. Reppy. Lambda point in the ^{4}He-Vycor system: A test of hyperuniversality. *Physical Review Letters*, 83(23):4800–4803, 1999.

[203] D. W. Brown, P. E. Sokol, and S. N. Ehrlich. New disorder induced phase transitions of classical rare gases in porous Vycor glass. *Physical Review Letters*, 81(5):1019–1022, 1998.

[204] M. Y. Lin, S. K. Sinha, J. M. Drake, X. I. Wu, P. Thiyagarajan, and H. B. Stanley. Study of phase-separation of a binary-fluid mixture in confined geometry. *Physical Review Letters*, 72(14):2207–2210, 1994.

[205] M. Sliwinska-Bartkowiak, G. Dudziak, R. Sikorski, R. Gras, R. Radhakrishnan, and K. E. Gubbins. Melting/freezing behavior of a fluid confined in porous glasses and MCM-41: Dielectric spectroscopy and molecular simulation. *Journal of Chemical Physics*, 114(2):950–962, 2001.

[206] S. B. Kim, J. Ma, and M. H. W. Chan. Phase diagram of ^{3}He-^{4}He mixture in aerogel. *Physical Review Letters*, 71(14):2268–2271, 1993.

[207] D. D. Awschalom, J. Warnock, and M. W. Shafer. Liquid-film instabilities in confined geometries. *Physical Review Letters*, 57(13):1607–1610, 1986.

[208] D. D. Awschalom and J. Warnock. Supercooled liquids and solids in porous-glass. *Physical Review B*, 35(13):6779–6785, 1987.

[209] K. Morishige and K. Kawano. Freezing and melting of water in a single cylindrical pore: The pore-size dependence of freezing and melting behavior. *Journal of Chemical Physics*, 110(10):4867–4872, 1999.

[210] K. Morishige and K. Kawano. Freezing and melting of methanol in a single cylindrical pore: Dynamical supercooling and vitrification of methanol. *Journal of Chemical Physics*, 112(24):11023–11029, 2000.

[211] K. Morishige and Y. Ogisu. Liquid-solid and solid-solid phase transitions of oxygen in a single cylindrical pore. *Journal of Chemical Physics*, 114(16):7166–7173, 2001.

[212] K. Morishige and K. Kawano. Freezing and melting of nitrogen, carbon monoxide, and krypton in a single cylindrical pore. *Journal of Physical Chemistry B*, 104(13):2894–2900, 2000.

[213] K. Morishige, K. Kawano, and T. Hayashigi. Adsorption isotherm and freezing of Kr in a single cylindrical pore. *Journal of Physical Chemistry B*, 104(44):10298–10303, 2000.

[214] Nobuo Wada, Junko Taniguchi, Hiroki Ikegami, Shinji Inagaki, and Yoshiaki Fukushima. Helium-4 bose fluids formed in one-dimensional 18Å diameter pores. *Physical Review Letters*, 86(19):4322, 2001.

[215] Nobuo Wada, Atsuo Inoue, Hideo Yano, and Kazuo Torii. Registered state and a two-dimensional bose liquid of ^{4}He in mesopores of hectorite. *Physical Review B*, 52(2):1167–1175, 1995.

[216] M. Hieda, M. Suzuki, H. Yano, N. Wada, and K. Torii. Interfacial slippage of helium films on 2D mesoporous hectorite. *Physica B*, 284:125–126, 2000.

[217] Daryl Tulimieri, Jongsoo Yoon, and Moses H. W. Chan. Ordering of helium mixtures in porous gold. *Physical Review Letters*, 82(1):121, 1999.

[218] D. T. Smith, K. M. Godshalk, and R. B. Hallock. Adsorption and capillary condensation of ^{4}He on Nuclepore - 3rd-sound and capacitance measurements. *Physical Review B*, 36(1):202–216, 1987.

[219] E. Chomski and G. A. Ozin. Panoscopic silicon - a material for "all" length scales. *Advanced Materials*, 12(14):1071–1078, 2000.

[220] R. Pelster. Dielectric spectroscopy of confinement effects in polar materials. *Physical Review B*, 59(14):9214–9228, 1999.

233

Appendix A

Derivation of the Kelvin Equation

Rigorous derivations of the Kelvin equation can be found in the literature[142, 143, 144]. Here I will simply outline the derivation – for details one should consult the above references.

Our starting points are the Laplace equation and chemical equilibrium. The Laplace equation (equation 2.5) gives the pressure difference across a curved liquid vapor interface as

$$p_l - p_v = \gamma C$$

Meanwhile, the fact that the system is in chemical equilibrium means that the two phases must have the same chemical potential: $\mu_l = \mu_v$. Actually the equality of the chemical potentials must be true no matter what the shape of the interface, so we may write out the chemical potentials above a flat interface and above a curved interface respectively:

$$\mu_l(T, p_0) = \mu_v(T, p_0)$$
$$\mu_l(T, p_l) = \mu_v(T, p_v)$$

Notice that the existence of the curved liquid-vapor interfaces shifts the chemical potentials of both phases. In order to derive the Kelvin equation in one of its forms, assumptions can be made about the form of the chemical potential. Usually the liquid is assumed to be incompressible, which means

$$\mu_l(T, p_0) - \mu_l(T, p_l) = v_l(p_0 - p_l)$$

while the vapor is assumed to behave like an ideal gas, giving

$$\mu_v(T, p_0) - \mu_v(T, p_v) = -RT \ln \frac{p_v}{p_0}$$

234

Setting the liquid and vapor potentials equal gives us

$$-RT \ln \frac{p_v}{p_0} = v_l(p_0 - p_l)$$

which, when combined with the Laplace pressure, gives the Kelvin equation:

$$-RT \ln \frac{p_v}{p_0} = -v_l C \gamma + v_l(p_0 - p_v) \tag{A.1}$$

If we are describing capillary condensation of a fluid in a pore of radius "r," the walls of which it wets completely, then the curvature ("C") can be replaced by $\frac{-1}{r}$ for a cylindrical meniscus or $\frac{-2}{r}$ for a hemispherical one. In the latter case equation A.1 attains a more recognizable form

$$-RT \ln \frac{p_v}{p_0} = \frac{2 v_l \gamma}{r} + v_l(p_0 - p_v)$$

Alternatively, if the changes in pressure are small (either because of a small curvature, small surface tension, or both) we can treat both the liquid and vapor phases as incompressible. This is an attractive approach when the assumption of ideal gas behavior is not justified. Making the assumption of incompressibility we find that

$$\mu_l(T, p_0) - \mu_l(T, p_l) = v_l(p_0 - p_l)$$
$$\mu_v(T, p_0) - \mu_v(T, p_v) = v_v(p_0 - p_v)$$

Now, substituting in the Laplace pressure, we can derive a different form of the Kelvin equation:

$$p_0 - p_v = -\gamma C \left(\frac{v_l}{v_v - v_l} \right) \tag{A.2}$$

which, for a hemispherical meniscus in a pore becomes:

$$p_0 - p_v = \frac{2\gamma}{r_{cap}} \left(\frac{v_l}{v_v - v_l} \right)$$

We also know that the coexistence curve has a shape described by the Clausius-Clapeyron equation:

$$\frac{d \ln p}{dT} = \frac{\Delta H}{RT^2}$$

where ΔH can be the heat of vaporization or the heat of fusion depending on what transition we are interested in. If we restrict ourselves to small temperature ranges over which ΔH may be treated as a constant then this may be integrated to give:

$$\ln \left(\frac{p}{p_0} \right) = -\frac{\Delta H}{R} \left(\frac{1}{T} - \frac{1}{T_0} \right) \approx -\frac{\Delta H}{R T_0^2} \Delta T$$

235

where p_0 and T_0 are the values for the bulk transition. Combining this relation with the Kelvin equation we can estimate the temperature depression of the condensation of fluid inside a pore of radius r:

$$\Delta T = \frac{2\gamma_{lv} v_l T_0}{r \, \Delta H} \qquad (A.3)$$

236

Appendix B

Porous Media for the Study of Fluid Transitions in Confined Geometries

This review describes the synthesis and structure of materials useful in investigations of fluid phase transitions in confined geometries. Porous media have uses throughout the physical sciences and industry, mostly due to their high surface area-to-volume ratio and the confinement afforded by the small volume inside each pore. Any review of porous media can only scratch the surface of this multifaceted topic; while this paper mentions other applications of the porous materials described within, it concentrates on utility in studies of fluid behavior. References are provided should the reader wish to investigate applications or materials in more detail. This review will begin with an introduction to the concept of a porous medium and briefly justify interest in fluid phase transitions within porous media. Synthetic approaches to the construction of various mesoporous materials will be covered and the review will conclude with a brief overview of what sorts of phase transitions have been studied.

B.1 Introduction

A porous medium is a solid which contains open spaces within its structure. For instance, a sponge or a loaf of bread may be described as a porous medium. In these cases, the pores are roughly spherical and embedded in a solid fibrous network. A jar of marbles is also a porous medium, although this time the solid is a network of spherical particles and the pores consist of the interstices between the spheres. Pore systems can have many morphologies, from unconnected spheres embedded in a solid matrix to an open volume with thin threads of solid forming a skeleton

through mostly empty space.

Porous materials can be divided into the somewhat arbitrary categories of "microporous," "mesoporous," and "macroporous" on the basis of their average pore size[145]. If most pores are 5-20Å(large enough to accommodate a small molecule but small enough to exclude large molecules) the material is classified as microporous. Mesopores are larger than most single molecules (20-500Å), while macropores are large enough that the walls are effectively flat open surfaces (>500Å). While chemists have constructed microporous materials for many years, only in the last twenty years or so have we used rational synthetic approaches to control structure in mesoporous materials.

The porosity of the medium may be described as the volume of pore-space divided by the total system volume (if the marbles described above were hexagonally close packed they would leave 26% of the volume open, thus the porosity would be 26%). Alternatively it may be described as the volume of the pore-space divided by the total system mass, a more experimentally accessible quantity (the glass marbles above would have a pore volume of $0.16cm^3/g$). Porosity can vary from zero, in the case of dense solid materials, to greater than 99%, as seen in some aerogels (described in section IV.4).

The techniques used to characterize porous materials differ from those used to characterize many other solid state compounds because the properties of interest are so different. Whereas the structure of the unit cell and bulk electronic properties are of paramount importance in a crystal, the size, shape and connectivity of the pores are most important in a porous medium.

Some porous materials crystallize into very regular structures, but most contain at least some disorder or are completely amorphous. For this reason X-ray diffraction (XRD) is much less powerful in the characterization of porous media. It is still an extremely important tool, but growing good quality single crystals is difficult to impossible. Powder X-ray diffraction (PXRD) gives information about pore sizes in ordered materials, but the important peaks can be located in the small angle region (as low as 1°) which requires the use of a specialized small-angle diffractometer. For amorphous samples such as porous glasses, small angle x-ray[113] or neutron[146] scattering (SAXS or SANS) can be used. These techniques can probe for structural correlations at various length scales and SANS can give information on phonon dynamics in the glass.

238
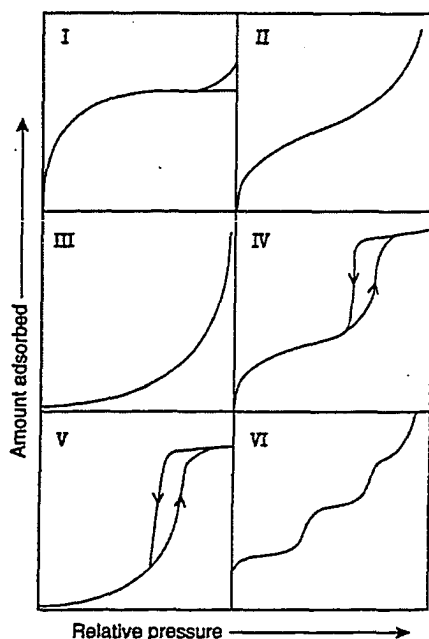
Figure B.1: The six types of adsorption isotherms in the IU-PAC classification. Type I corresponds to microporous materials, Types II, III and VI correspond to nonporous (or macroporous) materials, and Types IV and V correspond to mesoporous materials.[145]

Transmission electron microscopy (TEM) can provide important information about structure, especially when dealing with mesoporous materials (whose characteristic dimensions are within the resolution of even mediocre or outdated TEM systems). Scanning electron microscopy is used to probe the morphology of the material on a larger scale, but can rarely resolve features as small as the pores. Unfortunately, both of these techniques are most effective on conducting samples, while most of the porous materials described here are insulators.

The most important technique, without which no paper on porous materials should be published, is the adsorption isotherm. In this technique a gas is slowly admitted to a cell containing the porous material and pressure is monitored as a function of the volume of gas admitted. There are six general types of adsorption isotherm, as seen in Figure B.1. The shape of the isotherm is dependent on the shape of the pores, their connectivity (how often the pores intersect and the structure of the openings at each intersection), and the pore size.

The surface area of a material can be deduced from the adsorption isotherm using the Brunauer-Emmett-Teller (BET) method[147], by assuming that at low pressure all adsorbed molecules form a close packed monolayer on the pore surfaces. The position and shape of any hysteresis in the adsorption isotherm gives information about the pore structure and the amount of variation in pore size or "pore size distribution" (PSD). Materials with disordered pores, a wide pore size distribution,

239

or pores which contain narrow "necks" between them, will usually exhibit large hysteresis. This non-equilibrium behavior is rooted in kinetic barriers and metastability. For instance liquid plugs formed in the smaller pores within the structure may inhibit evaporation, or the nucleation of a denser phase may be difficult and condensation does not occur. From the shape of the isotherm and an assumption that all pores are cylindrical (the Barrett-Joiner-Halenda method) or slit shaped (the Hovath-Kawazoe method), pore size distributions can be derived[147, 31, 148].

B.2 Fluids in Porous Media

Porous media have found widespread use in chemistry and in industry because of their exceptional catalytic activity and their selective adsorption of fluids[145, 149, 150]. However, this review is focused on their utility for studying the effect of pore-fluid interactions on fluid phase transitions. There are a variety of transitions which may be studied, including condensation and freezing in most fluids, and superfluid transitions in ^{4}He (a manifestation of Bose condensation) and in ^{3}He (a condensation of weakly bound quasi-particles analogous to superconductivity in metals)[151]. Each transition gives slightly different information about the effect of the porous medium on fluids, because each is affected in a different way by the medium.

Microporous materials have pore diameters comparable in size to atomic bonds, so the adsorption of fluids is generally dominated by very strong substrate-fluid interactions which cause molecules to be adsorbed into specific sites and remain localized. Thus microporous materials change transitions quite drastically. Mesoporous media have large enough pore radii (>20Å) that the substrate-fluid and fluid-fluid interactions can both contribute to the fluid behavior. Hence, the pore walls will perturb the fluid in a manner that can be tuned by changing the size of the pore and the constituents of the pore wall. While this perturbation is the most important effect of confining fluids to porous media, it is not the only effect. Since phase transitions require the growth of domains in the fluid, the size and shape of the individual pores will limit the size of the domains. The connectivity of the pores is also important to the relation between separate domains within the medium. As it turns out, a network of parallel and nonintersecting cylindrical pores affects transitions in a very different manner than a network of randomly connected pores even though their average diameter can be quite similar. In fact the effect of confinement in small nonintersecting spherical pores[152] is well explained by finite size effects,

240

although this structure has little in common with most porous media.

To provide a good substrate for the study of fluid phase transitions, a material must have a well characterized structure, with most pores having the same structure. For this reason materials such as porous carbon and packed powders are not as useful, and will not be covered in this review.

While studies of fluid phase transitions may seem dry, esoteric, or even boring to those accustomed to the excitement and applicability of fields such as catalysis, they are necessary to understand the fundamental behavior of matter in confined spaces and the effect of impurities and disorder on fluid behavior. In fact, we will need a better understanding of fluid behavior just to properly classify micro- and mesoporous media. Currently, very basic theories of gas adsorption on surfaces are used to classify porous materials and determine pore sizes. These theories are inadequate for pores with diameters of only a few nanometers, but there are no alternative methods except cumbersome density functional calculations.

B.3   Synthetic Approaches to Porosity

Most materials of interest for the study of fluid phase transitions are mesoporous, but there are also some microporous materials that have been studied. Synthesis of micropores is finicky, but has been successfully accomplished for many years. Mesopores are more difficult to construct because they are too large to build out of simple inter-linked coordination polyhedra, but are too small to manufacture using physical techniques such as lithography. Most synthetic approaches to mesoporosity require multiple steps and fall into two broad categories. In one approach large building blocks are constructed and then assembled into a superstructure containing mesoscopic pores. Thus, the structure is best thought of in terms of these "secondary building units" rather than actual ions. Examples of this approach include pillared layered clays and heteropolyanion salts. The second approach involves forming a material from two or more phases, freezing in the structure, and then removing all but one of the phases. Examples of this approach include sol-gel syntheses of glasses and template-directed synthesis of ordered mesoporous silica. Both of these approaches lead to structures with more disorder than in most solid state materials.

241

B.4 Porous Materials

There is a plethora of porous media, but this review is restricted to a few types of microporous and mesoporous materials. The categories covered include: zeolites, pillared layered solids, organic templated materials, sol-gel derived glasses and a few other materials included as "miscellaneous materials."

B.4.1 Zeolites

Zeolites are microporous alumino-silicate crystals, made up of interconnected $[AlO_4]$ and $[SiO_4]$ tetrahedra. The largest zeolite channels and pores seldom exceed 10Å in diameter[153]; although larger pores have been synthesized, the channels between pores remain quite restrictive. The tetrahedra form a negatively charged framework, with regular pockets that hold a large number of water molecules solvating the cations necessary to balance the electronegative skeleton. The water in zeolite pores can be reversibly removed without altering their structure, leaving behind a network of pores. In fact the name zeolite comes from the Greek roots *zeo*, boil, and *lithos*, stone, because of the water produced upon heating the crystals. The dehydration of zeolites tends to break large zeolites apart into powder because of the generation of large internal steam pressure, but they can be carefully dehydrated to yield large monolithic samples ($\sim 0.5cm$ long) while maintaining the open pore system[154].

There is a large variety of naturally occurring zeolites and the range of possible synthetic zeolites is practically endless. Zeolites are usually formed in the laboratory by crystallisation from a mixed silica-alumina gel under hydrothermal conditions; details can be found in more specialised books[156, 155]. Examples of zeolites are shown in Figure B.2 - the polyhedral representation highlights the structure of the pore, while the connectivity of the pores is best visualised by smoothing out the walls and representing the pores as balls and cylinders. The fact that zeolite crystals are built up using $[SiO_4]$ and $[AlO_4]$ tetrahedra means that a large pore must consist of an ordered arrangement of dozens of these relatively small building blocks. It is not surprising that large pore structures are seldom encountered (a manifestation of Pauling's Parsimony Principle).

It is possible to introduce much larger pores into zeolites after synthesis, but they do not have the same structure as the micropores described above. Mesopores can be formed through dealumination of the zeolite skeleton using steam or $SiCl_4$;

242
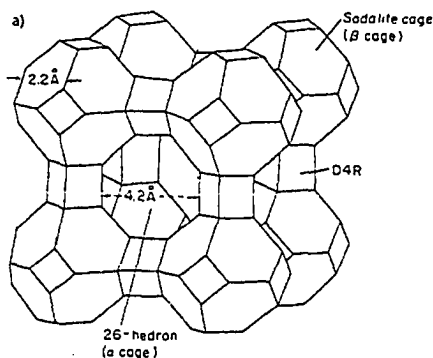
Figure B.2: Two examples of zeolite structures, a)zeolite A and b)zeolite ZSM-5. These two structures use different representations to emphasise the pore structure and pore-channel connectivity respectively.[155]
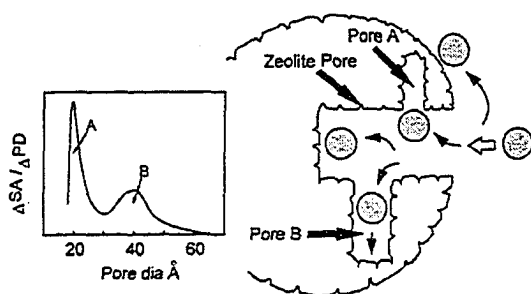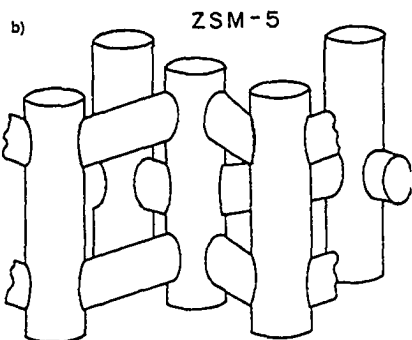
Figure B.3: Mesopores can be formed in zeolites through dealumination. Steam dissolves aluminium rich areas, leaving relatively large open volumes (pores A and B above) within the zeolite. Zeolite micropores line the walls and provide catalytic sites, while the "large" mesopores provide easy access for large molecules.[150]

the resultant structure is shown schematically in Figure B.3. These pores (labed A and B in Figure B.3) have a much broader size distribution than the micropores in the zeolite framework. They allow increased accessibility of larger molecules to the zeolite pores, which should increase catalytic properties of the zeolites. However, this odd pore size distribution - a sharp peak in the micropore region and one or two relatively sharp peaks in the mesopore region - makes this an unlikely substrate for the study of phase transitions in fluids. Because of the many distinct size scales, any observed fluid behavior in these mesoporous zeolites would be difficult to ascribe to a particular type of substrate-fluid interaction.
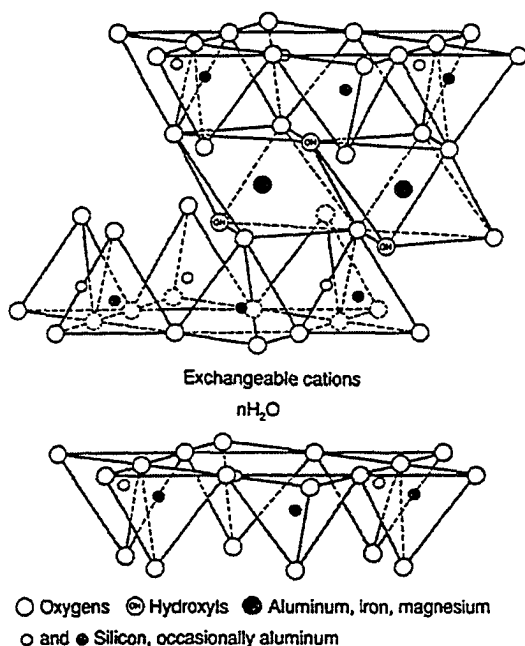
Figure B.4: The structure of a generic smectite clay, one octahedral oxide layer sandwiched between two tetrahedral oxide layers. This composite layer is separated from the next by a layer of hydrated cations.[157]

Exchangeable cations
nH₂O

O Oxygens ⊕ Hydroxyls ● Aluminum, Iron, magnesium
○ and ◉ Silicon, occasionally aluminum

B.4.2 Pillared Layered Solids

Layered clays have a history in chemistry as long and almost as illustrious as zeolites. These naturally occurring compounds consist of two-dimensional layers of metal oxide polyhedra separated by open layers containing hydrated cations (usually sodium or calcium) to counter the electronegative oxide layers. The composition and structure of the oxide layers are used to classify layered clays into broad categories. Many clays have a 2:1 layer structure, meaning one octahedrally coordinated oxide layer (often aluminum or magnesium) is sandwiched between two tetrahedrally coordinated oxide layers (silicon and aluminum), although 1:1 clays and fibrous clays are also common[156]. The 2:1 clays are categorized by layer charge into: smectites (electrostatic layer charge=0.2-0.6), vermiculites (layer charge=0.6-0.9), micas (layer charge~ 1) and brittle micas (layer charge~ 2). The type of ions contained in the coordination sites identifies the members of each class. A schematic of a smectite clay is shown in Figure B.4. While these clays have "pores" in the sense of open spaces between the layers filled with water, once dehydrated these pores tend to collapse. If rehydrated, the layers will expand to adsorb multiple layers of water between oxide layers. While this makes smectites powerful absorbents, it means that there is no characteristic size to the pores and they are unsuitable for applications that require stable structures and easy access to the surface. Layered clays have been used as catalysts, but zeolites tend to perform the same job better

244

(a)

(b)
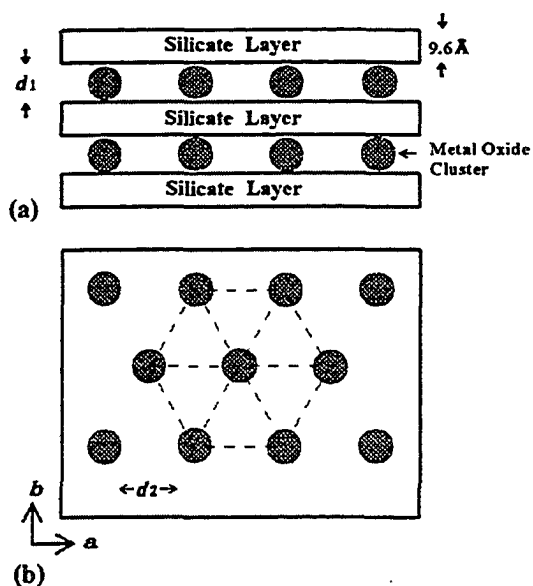
Figure B.5: Schematic representation of a pillared clay consisting of silicate layers (usually smectite layers as shown in Figure B.4) and metal oxide pillars (see Figure B.6 for an example). d_1 is referred to as the "gallery height." [157]
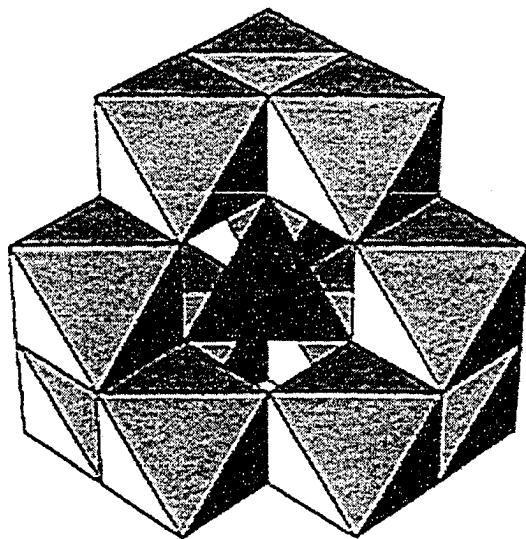
Figure B.6: $[Al_{13}O_4(OH)_{24}(HO)_{12}]^{7+}$, a complex cation used as a pillar in layered clays.[157]

because of their well defined structure and pore distribution.

It is possible to synthesize layered clays with a regular pore structure unaffected by the quantity of water adsorbed if the interlayer structure is modified. Carefully designed chemical structures can be used to bridge the interlayer gap. These "pillars" balance the charge of the electronegative layers and by binding to the layers they prop open the structure if it is dehydrated, and prevent it from swelling if it is exposed to water. Pillars come in an assortment of shapes, sizes and charges that allow control of the interlayer spacing. They can be incorporated into a variety of clays, with the smectite group clays providing the most promising hosts due to their low layer charge. Most articles on these "pillared interlayered clays" (PILCs)

245

describe work on montmorillonite[158, 159, 160, 161], although work has been done on other smectites[157].

The simplest way to visualize the PILC structure is as a stack of solid sheets supported by arrays of pillars as shown in Figure B.5. Of course, these "solid sheets" actually have a complex surface structure which has important effects on the behavior of adsorbed fluids. Similarly, the pillars are not simply support sticks but rather massive complexes that take up a significant portion of the interlayer volume.

Powder X-ray diffraction (PXRD) results from PILCs show one or two broad peaks indexable to (n00) planes characteristic of materials with long range order along one axis only. The silicate layer in a smectite is about 10Åthick and the interlayer spacing, called the "gallery height," is determined by the size of the pillar. Although the spacing between silicate layers is quite regular in PILCs, the orientation of the layers is random and there appears to be no long range order in the position of the pillars. The spacing between pillars depends on the system details, but is on the order of 35Å(much larger than the 5Åspacing of available binding sites on the layers). It is experimentally difficult to engineer structures with gallery heights above about 15Å. For gallery heights smaller than 15Å, simple spacers such as Keggin ions (an example is shown in Figure B.6) can be incorporated into the structure as pillars. For larger separations an auxiliary swelling agent must be used in the synthesis to hold the layers apart while pillars are constructed between them. PILCs with gallery heights of 15Åor less tend to fall into the microporous category, but there are promising results in the search for larger gallery heights. For instance a structure with a spacing of about 60Åhas been synthesized[159], but characterization on this length scale is somewhat challenging.

One difficulty which is not often mentioned when discussing these substrates in the lack of agreement between gallery spacing determined from interlayer separation in PXRD results and pore size determined from adsorption isotherms using Barrett-Joiner-Halenda or Horvath-Kawazoe models. Often the "average pore size" will be larger than the gallery height, implying that the most important characteristic dimension for fluid adsorption is not the gallery height at all. Some interpret this as a measure of the lateral distance between pillars within the layer, while others attribute it to the small gaps between microscopic PILC particles. Unfortunately, PILCs are difficult to image with transmission or scanning electron microscopy be-

246
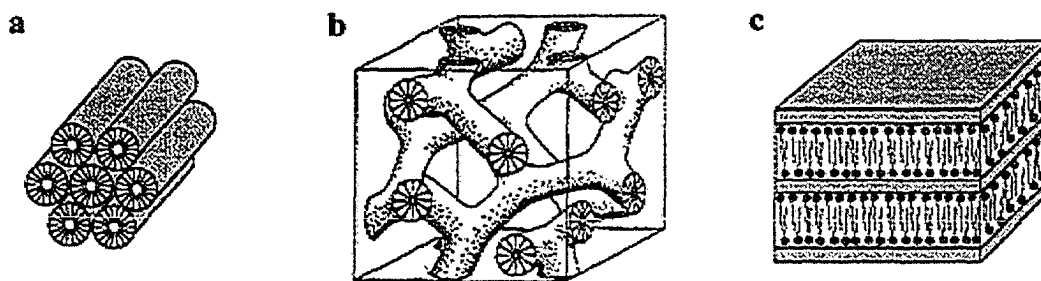
Figure B.7: Surfactant structure within the MCM family of materials before calcination: a)hexagonal (MCM-41); b)cubic bicontinuous, Ia3d (MCM-48); c)and lamellar (MCM-50 or MCM-L).[171]

cause of their insulating character and small pore sizes. Scanning force microscopy can be used on smectites[162], but the images do not have the resolution to solve this problem. While this lack of agreement in the interpretation of pore size distribution does not in any way hamper investigation of catalytic and molecular sieving properties of PILCs, it needs to be resolved before PILCs can become important substrates for the investigation of fluid phase transitions.

Pillared layered solids can be constructed from materials other than layered clays as well. For instance layered titanate has been used to create very ordered pillared structures which exhibit small angle PXRD peaks out to the (500) reflection[163]. These layered titanates have gallery heights of 10Åor larger[163, 164, 165]. The actual pillaring technique is very similar to that used in PILCs.

B.4.3 Organic Templated Materials

As we move further and further from the traditional domain of solid state chemists, we reach the burgeoning field of organically templated materials. These compounds begin life in a solution state chemical reaction, but their isolation, work-up and characterization is very much in the realm of the solid state chemist. This section will concentrate on the preparation of mesoporous silicate materials, but if the reader is interested there is currently an explosion of literature underway on template mediated synthesis of mesostructured inorganic compounds for electronic and optical applications[166, 167, 168, 169]. Mesoporous carbons can also be synthesized by using polymer impregnated mesoporous silica as a starting point[170].

While zeolites and PLSs are microcrystalline, templated silicas are prepared from a mixture of liquids which physically separate to form some sort of ordered

247

A Precursor solutions

Micelles and isolated cationic   Inorganic silicate anions
surfactant molecules   (for example, D4R oligomers)

B Ion exchange

or

C SLC assembly

Phase transformation

Lamellar SLC   Hexagonal SLC
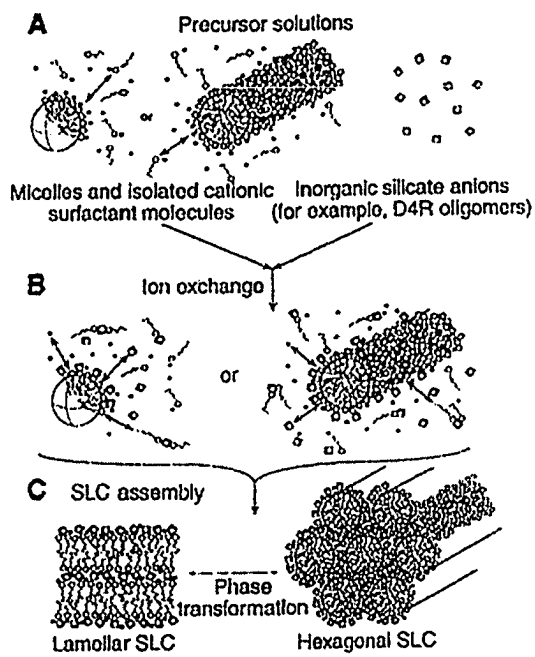
Figure B.8: The formation of MCM-41.[150]

hkl	d /Å
100	36.0
200	17.8
300	11.9

MCM-L

hkl	d /Å	hkl	d /Å
211	37.6	421	20.2
220	32.6	332	19.7
321	24.5	422	18.8
400	23.1	431	18.0
420	20.6	333	17.7

MCM-48

hkl	d /Å
100	39.2
110	22.7
200	19.6
210	14.8

MCM-41

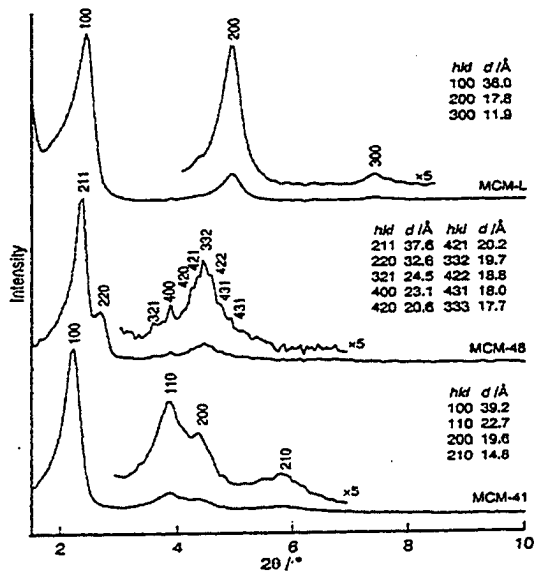$2\theta /°$

Figure B.9:   PXRD   of   MCM materials[150]

248

large scale structure. This structure is solidified through condensation of a silica backbone, and once this condensation is complete the other phases are removed leaving an ordered array of open pores. The symmetry and scale of the resulting material is sensitive to the structure of the directing template and to the relative concentrations of the reactants.

This field is derived from the procedures developed at Mobil in the early 1990's for the synthesis of mesoscopically ordered silica[149]. The process of producing amorphous high purity silica by the condensation of a pure silica source, such as tetraethyl orthosilicate (TEOS), has been used for decades. However, by condensing TEOS in a basic aqueous environment in the presence of a long chain surfactant, an ordered hexagonal array of surfactant filled rods encased in silica was formed. By varying the concentration of surfactant it is also possible to obtain a cubic lattice of micelle tubes or a layered phase (referred to as MCM-41, MCM-48 and MCM-50 respectively, shown in Figure B.7).

The formation of MCM-41 is shown schematically in Figure B.8; the small silicate precursors gather around micelles and rods of the long chain, amphiphilic, template. The formation of these encased micelles continues until the silica source is exhausted. This structured gel is allowed to age for a few days as the silica polymerizes. It is then calcined at a few hundred degrees centigrade to drive off the solvent and surfactant and to reinforce the silica backbone. The resultant micrometer to millimeter sized particles have a supra-molecular lattice of open cylindrical pores with long range order, as seen from the PXRD results shown in Figure B.9. The evolution of these phases from solution is well characterized in zirconia[172] as well as silica[173].

In recent years an enormous variety of materials have been synthesized using this general approach. By varying the size of the surfactant, the pore size can be altered from 20Åto 100Å. Even larger pores can be created in acid catalyzed materials (labeled SBA). These materials also have hexagonal phases like MCM-41 (e.g. SBA-3 and SBA-15) and a number of other phases with different symmetries[150]. One advantage of using SBA type materials is that neutral polymers can be used to form the template for large pores, up to 300Å[174].

The best studied group of mesoporous silicas are hexagonal arrays of open cylinders such as MCM-41. In calcined samples of MCM-41 PRXD often shows a few peaks, although the first (100) peak is much better resolved than subsequent peaks. The lack of many higher order peaks can be interpreted as moderate disorder in the

superlattice; PXRD of SBA materials usually only shows one peak, indicating more disorder. Although the pore superlattice is well ordered, the walls of individual pores are composed of amorphous silica and the microscopic hexagonal structure is not often reflected in the macroscopic structure of these materials. When allowed to react under quiescent conditions MCM-41 forms a powder[175], but by stirring the mixture as it reacts various morphologies are found. For some conditions, small spheres[176] are the product, while under other conditions small gyroids (shapes with cylindrical symmetry, which have points at the end, instead of flat surfaces) are synthesized[177]. While the gyroids do not show hexagonal symmetry, they do have a unique axis that is aligned with the axis of the silica cylinders. Films of ordered mesoporous silica have also been studied[178, 179, 180], but most experiments on fluids in porous media require bulk samples so thin films will be of limited utility.

Mesoporous ordered silica has been prepared in large monoliths in a couple of ways. Using a sol-gel technique similar to that describe in the next section a disordered agglomeration of micrometer size spheres containing ~ 3nm pores was prepared by Sato, et al.[181] Tolbert, et al., prepared a large (~ 1cm) sample of MCM-41 with pores throughout the sample oriented in the same direction by synthesizing the sample in a high magnetic field[182].

There is another templating method that can be used to synthesize a hexagonal array of cylindrical pores. Kanemite, a layered silicate, can be transformed to the mesoporous silicate FSM-16 through the use of cationic surfactant molecules in a basic solution. The surfactant is absorbed between the layers, and then the layers begin to cross-link, giving a hexagonal lattice of one dimensional pores about 2nm in diameter[183]. Similar substrates can be prepared from layered aluminosilicates and gallosilicates[184].

Applications of mesoporous ordered silica particles are beginning to be explored. Walcarius and Bessire showed its electrochemical utility as a highly selective electrode[185]. Small zeolitic areas can be incorporated into mesopore walls[186], creating a promising catalyst which combines the huge surface area and easy access of mesoporous materials with the acidic binding sites that make zeolites so useful.

B.4.4 Sol-Gel Derived Glasses

As mentioned above, very pure silica glass is best produced from a purified precursor such as TEOS ($Si(OCH_2CH_3)_4$). When combined with water and a basic or acidic

250

catalyst TEOS will quickly polymerize to form a gel that yields a porous glass when dried. If monolithic, nonporous, silica is needed this porous glass can be sintered at higher temperatures to eliminate the empty volume. However, for our purposes the dried gels are perfect as is. Sol-gel derived glasses are by no means restricted to silica - they are easily synthesized from a variety of oxides (e.g. alumina, titania, zirconia, and tungsten oxides) and from a number of interesting organic systems[187].

These structures are amorphous on small length scales, although longer range correlations may be present[113]. They may be described in terms of pore size and volume, or in terms of the thickness of the silica skeleton, but they do not have the regular structure seen in the first three classes of materials. In the formation of these gels the solvent acts as a template, encouraging the densification of the silica skeleton while leaving large volumes with nothing but solvent. Since the solvent has characteristic dimensions much smaller than any feature in the gel these voids have random size and shape - the structure is a result of the kinetics of polymerization and aggregation of silica particles in suspension. The condensation can be acid or base catalyzed[188]. The acid catalyzed gels show a mixture of micropores and mesopores; base catalyzed gels are usually used in studies of fluid confinement because they have little microporosity - all voids are within the mesoporous range.

Since condensation of TEOS to SiO_2 releases four moles of ethanol for every mole of silica formed, the silica gel is quite dilute - by adding more ethanol to the reactant solution they can be further diluted. These wet gels (or "alcogels") can vary in porosity from $\sim 85\%$ to $\sim 99.8\%$ depending on the initial alcohol concentration. If not dried slowly, these very dilute gels shrink and fall apart into powder. This shrinkage is due to the surface tension of the alcohol. As ethanol evaporates, the surface tension of the remaining solvent pulls on the walls of the pores in the glass and collapses any large pores that do not have proper support. If an alcogel is dried over a period of weeks it will retain its macroscopic shape while shrinking in size. Larger pores collapse to become smaller pores, leaving a relatively narrow pore size distribution. These are known as "xerogels."

The large pores can be preserved if the solvent is removed without a liquid-vapor interface ever passing through the gel; in order to accomplish this the gel is pressurized and heated above the liquid-vapor critical point of the solvent. Once the solvent has become a supercritical fluid it can be gradually released from the gel without introducing any surface tension[103]. Gels dried in this manner retain
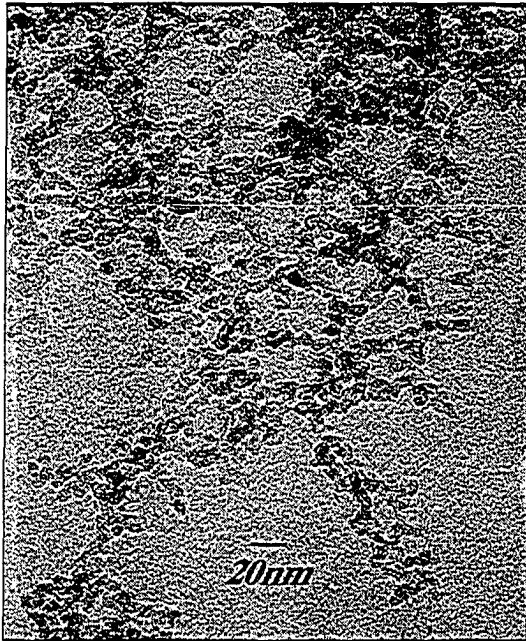
251

Figure B.10: Transmission electron micrograph of 95% porous silica aerogel taken with the JEOL-2010 TEM in the University of Alberta Physics Department.

the porosity and size of their alcogel precursor and have an incredibly broad pore size distribution reaching into hundreds of angstroms. In fact, the structure of these silica "aerogels" with porosity greater than 95% is so open that the concept of a "pore" does not really apply; instead one should visualize these as structures consisting of interconnected strands of silica of varying diameter and length. A picture of an aerogel is included as Figure B.10.

B.4.5 Miscellaneous Materials

There are a variety of interesting mesoporous materials that do not fit neatly into any of the previously mentioned categories - this section addresses a few of them.

Materials can be prepared from phase separated solids. An example is porous Vycor glass, which has been available from Corning for decades. It is a Borosilicate glass with about a 30:70 B:Si ratio which has been cooled below its spinodal decomposition temperature (where it separates into regions of higher and lower boron concentration). When leached by dilute acid, the boron rich regions dissolve leaving a complex system of interconnected pores[146, 189]. The pore diameters are determined by the degree of spinodal decomposition and the period that the glass is exposed to the acid leaching solution - they are on the order of 50Å. The silica glass left retains the macroscopic shape and size of the original sample, but is about 30% porous. "Controlled pore glasses" are made in a similar manner. By varying the initial concentration of boron, the development temperature (the temperature
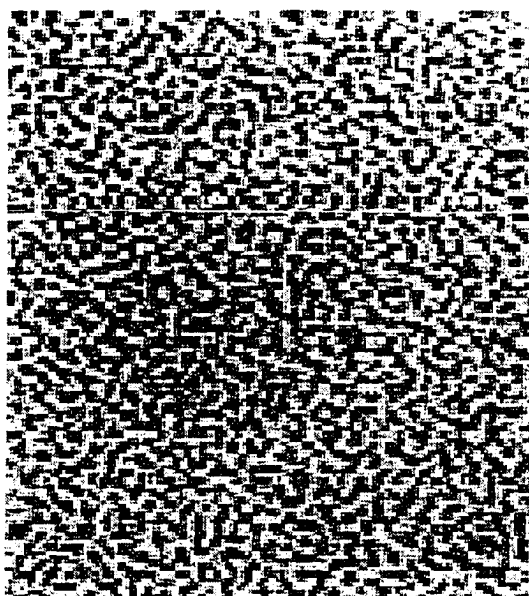
252

Figure B.11: Scanning electron micrograph of porous gold annealed at 100°C.[191]

at which the glass separates) and the developing time, a wide range of pore sizes are possible[190].

Porous gold has a structure similar to Vycor, but is prepared in a very different manner. An alloy of about 70:30 Ag:Au is made from stoichiometric quantities of the two metals. The sample is then immersed in acid for about twelve hours to leach out the silver. The remaining gold is annealed, leaving a sample of gold that is about 70% porous and retains the macroscopic shape and size of the original. The pores in porous gold are disordered and worm-like with many interconnections (see Figure B.11). Their pore size is determined by the annealing temperature - samples annealed at 100°C have very fine (200Å) interconnected voids while those annealed above 500°C are macroporous with voids on the order of micrometers[191].

Porous heteropolyanion salts (HPSs) are crystalline, solid state compounds with interesting chemistry that may develop in the near future. Currently there are few salts approaching mesoporous scales, although a number of microporous salts have been made. A HPS has multiple levels of structure and is best described by reference to Figure B.12. The primary building block is a large anionic complex (similar to a Keggin ion, as used to pillar the PLSs described above); these nonporous primary blocks assemble to form a nonporous secondary building block. Finally, a number of these secondary building blocks coalesce to form a final, tertiary, structure that has large pores between secondary building blocks.

253
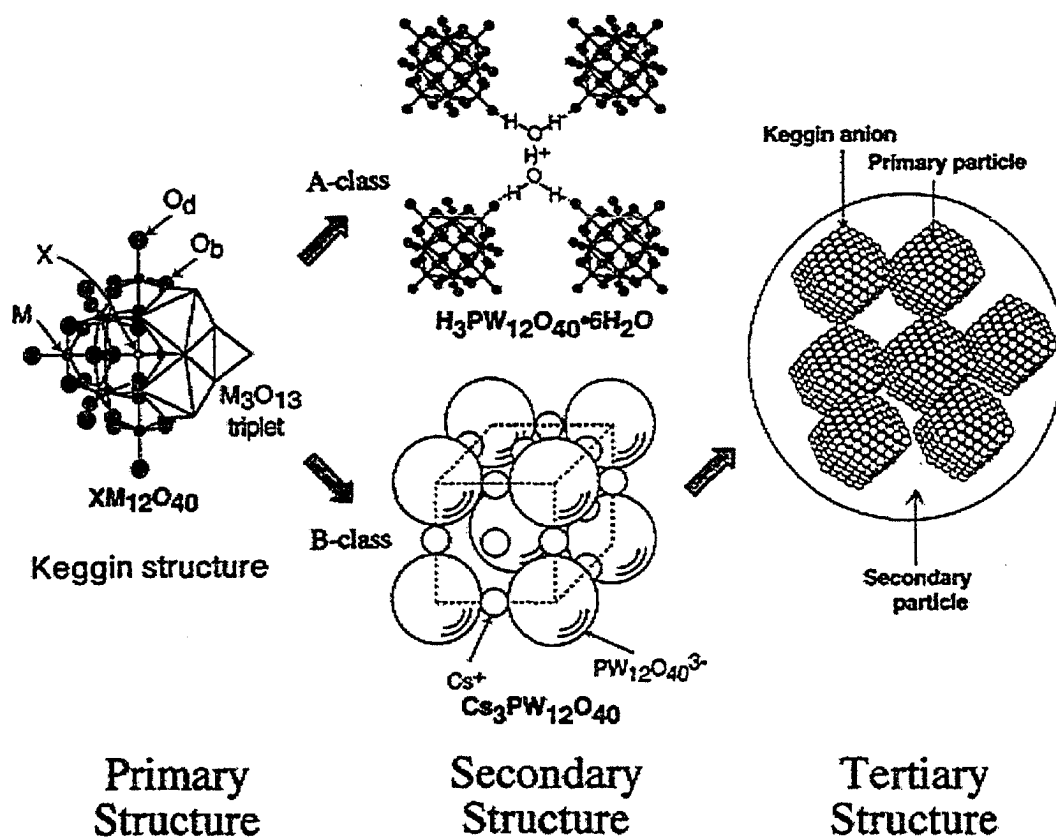
Figure B.12: Structure of a porous heteropolyanion salt, showing the importance of multiple levels of structure.[145]

A similar sort of "secondary building unit" approach with tetrahedral complexes has been used to create "supertetrahedra" with open pores about 2nm in size[192] as shown in Figure B.13. None of these materials have large pore sizes or macroscopic particle sizes so they not likely to be used in studies of fluid phase transitions until larger structures can be engineered.

One of the most important applications of mesoporous materials has traditionally been as sieves and filters. One very creative filter, with holes from 150Å to a few micrometers in diameter[193], is called Nucleopore, produced by exposing a thin disc of polycarbonate to a radioactive source. Where radioactive particles pass through the polymer they create damaged tracks that can be etched out, leaving cylindrical holes passing through the disc. The pores reflect the particle trajectories, so they are relatively straight but not necessarily perpendicular to the surface. Depending on the density of pores, they may intersect a few other pores on their way through the filter[194].

254

Figure B.13: Structure of ASU-13, composed of supertetrahedra.[192]

B.5 Fluid Phase Transitions in Pores

While chemists have lost no time in investigating the catalytic and molecular sieving possibilities of many novel mesoporous media, physicists and physical chemists have done less work on fluid phase transitions within these structures. Part of this stems from the quantity 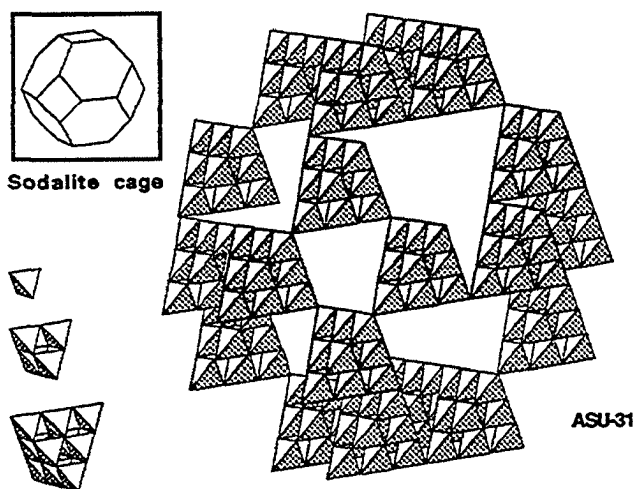of substrate used in many physics experiments; while a chemist may be happy to work with a few milligrams of sample or with a sample consisting of very fine powder, physicists often use large monolithic samples of millimeter to centimeter dimensions. Another valid reason to hold back use of these materials in experiments is the lack of agreement on details of structure. In order to interpret the results of phase transition investigations the structure needs to be very well characterized - otherwise the experiment will shed no light on the effect of confinement, fluid-wall interactions or pore connectivity on the transition.

Ironically, our lack of understanding of fluid-pore interactions makes it difficult to interpret the structure of mesoporous media; our methods for evaluating pore size distributions and surface areas are often based on naive theories of gas adsorption developed in the first half of the twentieth century. The only exact way to investigate fluid-wall interactions is with molecular simulation, a technique that is far too computationally intense to use regularly. Density functional methods can be used to evaluate adsorption isotherms and give information about pore size and shape, but they are also computationally intense and are not as useful near critical points. To characterize media and understand fluid-pore behavior we will need a suite of well chosen experiments and simulations on a variety of substrates. Unfortunately, the substrates available are not always as well understood and characterized as we

255

need.

There is well developed literature on fluids in zeolites and Vycor but literature is sparse to absent on transitions in the more recent materials derived from PILCs and templated silica. Much of the literature on phase transitions concerns helium and hydrogen because the low temperature of their transitions lead to low noise measurements. In addition, the presence of the superfluid transition in helium provides an extra tool with which to probe the effect of substrates on phase transitions. The details of fluid phase transitions in porous media are beyond the purview of the present report and have been reviewed elsewhere[195], but a short list of what sorts of systems have been studied is included.

Work on fluids in zeolites indicates that the micropores have a strong perturbative effect on the adsorbed fluids. The freezing point of hydrogen is significantly lowered by confinement in zeolites[196, 197]. For partially filled pores in Silica-Y and Na-Y zeolites, a solid first layer of adsorbed helium will form on the surface and a partly liquid second layer will form on top[198]. Pores full of helium freeze before it reaches a superfluid transition (pure helium never freezes at atmospheric pressure[199]). In ZSM-23 and ZSM-5 zeolites, helium appears to remain fluid but there is no indication of superfluidity[200]. In fact, low temperature heat capacity of helium[200] and neon[201] in ZSM-23 and ZSM-5 can be modelled as atoms confined to individual pores with a certain activation energy - there is no fluid flow between pores, just activated transport.

Work on helium in Vycor shows a slight depression of the superfluid transition temperature by the pores, but otherwise the transition remains the same as seen in bulk helium[202]. The freezing of fluids such as hydrogen, oxygen, and argon[203] in Vycor have been well studied. Vycor tends to lower the freezing temperature and to induce disorder in the solid and may stabilize a different structure than that of the bulk solid. Phase separations in binary fluids have also been studied in Vycor[204, 8]. Capillary condensation and freezing in controlled pore glasses have also been studied[205, 46, 48].

Transitions in aerogels are currently a topic of interest in the low temperature physics community. While aerogels have a very open structure and do not seem to shift fluid transition temperatures much, the very nature of the transitions can change. Both the ^{4}He and ^{3}He superfluid transitions[2, 6] in aerogels exhibit behaviors different than seen in bulk, as does binary fluid separation[206]. Some work on

256

the liquid-vapor critical point in aerogels has also been done[10, 14] although there is some disagreement about interpretation of the results. Work on fluids in xerogels has also been done[207, 208].

There are some results on condensation in MCM-41 type templated silicas and some work on freezing in the same substrate. Fluids used include water[209], methanol[210], oxygen[211], Krypton[212, 213], and nitrobenzene[205]. ^{4}He seems to undergo a transition to a 1-D Bose superfluid when confined to 18Å cylindrical pores in FSM-16[214]. MCM-41 like materials provide an especially important test system since many models of fluid adsorption assume cylindrical nonintersecting pores - a structure not exhibited by any other type of substrate. Behavior of fluids in MCM-41 is fairly well explained and more work on this system will help nail down important parameters and benchmark fluid behavior for other pore structures.

The ^{4}He superfluid transition in a PLS[215, 216] has been studied. All of the interesting behavior seen is attributed to the two dimensional nature of the pores, but the hectorite substrate, like other PLSs, is not completely characterized. More work on these substrates is promising, especially if a series of PLSs with varying gallery heights can be investigated.

Work on helium in porous gold[134, 217] and Nucleopore[218] shows essentially bulk behavior; it seems that random porous media with pore sizes larger than 100Åcan be well described using the models developed for bulk fluids and for wetting of flat surfaces.

B.6   Conclusion

The field of mesoporous materials is rapidly growing as these materials are becoming widely used in areas or research from optics to catalysis. They already enjoy widespread use as molecular sieves and for sorption. Advances in material chemistry have allowed the tailoring of structures an order of magnitude larger than possible a decade ago, and they are reaching the scale where physical processes can assist in the design and manufacture of intricate and versatile structures[219]. As a spin-off, these novel materials provide us with a panoply of environments in which to watch phase transitions. Subtle changes in the size, shape and connectivity of the fluid domains within these substrates allow us to see how perturbations affect transitions, which in turn helps to elucidate the fundamental physics behind fluid behavior. In addition to its fundamental importance, elucidation of the effect of pores on fluid

behavior will lead to better characterization of substrates used in applied fields. Chemistry has provided a wonderful variety of experimental possibilities, and once these new structures have been well characterized there will be a great deal of physics waiting to be discovered.

258

Appendix C

Linearity of Aerogel Capacitor Response to Helium Density

C.1 Aerogel with Single Phase Fluid

We need to justify using capacitance as a direct measure of fluid density in aerogel. Although it is well accepted that a uniform fluid will have a dielectric constant that is roughly proportional to fluid density, it is not necessarily true that the dielectric constant of a fluid filled aerogel is linear in fluid density. We will use the assumption of an effective dielectric constant which is a volume average over the entire sample, using the machinery described by R. Pelster [220]. For our work I define the liquid as the matrix with silica as a dilute inclusion. We will start with some definitions and then move on to some approximations.

Symbol	Definition	Restrictions
ϕ	Porosity	≥ 0.95
δ	$1 - \phi$	≤ 0.05
ϵ_{eff}	effective dielectric constant	unknown
ϵ_{fluid}	ϵ of helium $= 1 + x$	$\epsilon_{fluid} \leq 1.05$ $x \leq 0.05$
ϵ_{gel}	ϵ of silica strands	$\approx 3.9 \ at \ 1kHz$
$\langle E \rangle_{fluid}$	Electric field in helium	
$\langle E \rangle_{gel}$	Electric field in silica	
e_{gel}	$(\langle E \rangle_{gel}) / (\langle E \rangle_{fluid})$	

For dilute inclusions of phase i in a matrix we can assume a uniform field and we only need worry about dipole moments. This allows as to use (Pelster[220], Eq. 5):

$$e_i = \frac{\epsilon_{matrix}}{A \left(\epsilon_i - \epsilon_{matrix} \right) + \epsilon_{matrix}} \tag{C.1}$$

259

The aerogel certainly is a dilute inclusion for porosities above 95%, so we can certainly use Eq. C.1. Thus, for silica strands (where $A = 1/3$ for randomly oriented cylinders), and expanding around $x = 0$:

$$e_{gel} = \frac{\epsilon_{fluid}}{\frac{1}{3}\left(\epsilon_{gel} - \epsilon_{fluid}\right) + \epsilon_{fluid}} = \frac{1+x}{\frac{1}{3}(3.9) + \frac{2}{3}(1+x)} \approx 0.5085 + 0.336x \qquad (C.2)$$

Now we can start in earnest. From Pelster[220] Eq. 1, assuming that the wavelength of the electric field is greater than any feature in our system, we can express the dielectric constant of the system as a volume average. We are measuring capacitance at 1kHz, so we will certainly see a volume averaged dielectric constant.

$$\epsilon_{eff} = \epsilon = \frac{(1 - \delta)\epsilon_{fluid} + \delta\epsilon_{gel}e_{gel}}{(1 - \delta) + \delta e_{gel}} \qquad (C.3)$$

Since we are dealing with very porous aerogels, we will expand around $(\delta = 0)$.

$$\epsilon \approx \epsilon_{fluid} + \delta\, e_{gel}(\epsilon_{gel} - \epsilon_{fluid}) + \delta^2 e_{gel}(1 - e_{gel})(\epsilon_{gel} - \epsilon_{fluid}) \qquad (C.4)$$

Substituting back in our values for ϵ_{gel}, e_{gel}, and $\epsilon_{fluid} = (1 + x)$ we get:

$$
\begin{aligned}
\epsilon \;\approx\;& (1 + x) + \delta\, e_{gel}(\epsilon_{gel} - (1 + x)) + \delta^2 e_{gel}(1 - e_{gel})(\epsilon_{gel} - (1 + x)) \\
=\;& (1 + x) + \delta\,(0.5085 + 0.336x)(3.9 - (1 + x)) \\
+\;& \delta^2(0.5085 + 0.336x)(1 - (0.5085 + 0.336x))(3.9 - (1 + x))
\end{aligned}
$$

We are interested in how linear our capacitor response is with respect to a change in helium density. We know that $(\epsilon_{helium} - 1) \propto \rho_{helium}$ so $x \propto \rho_{helium}$, therefore consider:

$$\frac{\Delta C}{C_0} \propto \Delta\epsilon_{fluid} = \frac{d\epsilon}{dx}\Delta x \propto \Delta\rho_{helium} \qquad (C.5)$$

We are assuming the relationship is linear (i.e. $\frac{d\epsilon}{dx}$ has no dependence on x), so we want to verify that any deviations from this are small enough to ignore.

$$
\begin{aligned}
\frac{d\epsilon}{dx} \;=\;& 1 + 0.467\delta + 0.226\delta^2 & (C.6) \\
-\;& x\left\{0.672\delta + 0.643\delta^2\right\} + x^2\, 0.114\delta^2 & (C.7)
\end{aligned}
$$

The terms shown above on line C.6 are independent of "x;" in other words they reflect the linear behavior we would like to assume. Since $\delta \leq 0.05$, the magnitude of the slope is close to 1. To judge how significant the nonlinearities are, we must compare them to that magnitude. Since both δ and x are small, we can neglect all but the leading term of the non-linear terms shown in line C.7, which leaves us with:

$$Non - linearity \approx -0.672\delta x \qquad (C.8)$$

We can assume that $x \leq 0.05$ since that dielectric constant ($\epsilon = 1.05$) would correspond to a helium density of $\sim 130\frac{kg}{m^3}$, the liquid density at about 4K. Plugging values into Equation C.8, that leaves us with:

$\phi = 0.95$	Non-linearity $\leq 0.2\%$
$\phi = 0.98$	Non-linearity $= \leq 0.1\%$

Obviously, this deviation from linearity is small enough to ignore since it is comparable to, or smaller than, experimental reproducibility.

C.2 Aerogel with Two Phase Fluid

To generalize the work of the previous section we must consider the case where the helium in the gel exists in two phases separated by well defined interfaces. This three phase system (liquid, vapor, and silica) will be treated as a liquid helium matrix with vapor as an inclusion which might not be dilute and silica as an inclusion which is dilute. To begin with we will define some terms again:

Symbol	Definition	Restrictions
f	filling fraction	$0 \leq f \leq 1$
ϕ	Porosity	≥ 0.95
ϵ_{eff}	effective dielectric constant	unknown
ϵ_{liq}	ϵ of liquid helium	$1.025 \leq \epsilon_l \leq 1.05$
	$= 1 + y$	$y \leq 0.05$
ϵ_{vap}	ϵ of helium vapor	$1.000 \leq \epsilon_v \leq 1.025$
	$= 1 + x$	$x \leq 0.025$
ϵ_{gel}	ϵ of silica strands	$\approx 3.9\ at\ 1kHz$
$\langle E \rangle_l$	Electric field in liquid helium	
$\langle E \rangle_v$	Electric field in helium vapor	
$\langle E \rangle_{gel}$	Electric field in silica	
e_{vap}	$(\langle E \rangle_v) / (\langle E \rangle_l)$	
e_{gel}	$(\langle E \rangle_{gel}) / (\langle E \rangle_l)$	
z	$(1 - \phi)e_{gel}$	$z < 0.05$

For dilute inclusions of a phase i in a matrix we can assume a uniform field and we only need worry about dipole moments. This allows as to use (Pelster, Eq. 5)[220]:

$$e_i = \frac{\epsilon_{matrix}}{A\left(\epsilon_i - \epsilon_{matrix}\right) + \epsilon_{matrix}} \tag{C.9}$$

From the previous chapter we have an expanded form of e_{gel}:

$$e_{gel} \approx 0.5085 + 0.336y \tag{C.10}$$

Inclusions of vapor are not necessarily dilute, but Eq. C.9 provides values close to correct for filling fractions less than 0.3, and this may be improved by allowing A to vary during filling (i.e. not making any assumptions about the geometric effect of the vapor). When the majority phase is vapor rather than liquid, this whole derivation can be flipped around so that vapor plays the role of the matrix with liquid as the inclusions. So, with the caveat that this expression is not great right at half filling we have, expanding around $x = 0$:

$$
\begin{aligned}
e_{vap} &= \frac{\epsilon_{liq}}{A\left(\epsilon_{vap} - \epsilon_{liq}\right) + \epsilon_{liq}} = \frac{1+y}{1 + Ax + (1-A)y} \\
&\approx \left[\frac{(1+y)}{1+(1-A)y} - \frac{Ax(1+y)}{(1+(1-A)y)^2} + \frac{A^2x^2(1+y)}{(1+(1-A)y)^3}\right]
\end{aligned}
$$

Furthermore, each of those terms can be expanded around $y = 0$, dropping all terms that are more than second order in x and y, to give:

$$e_{vap} \approx (1+y)\left[1 + A(y - x)\right] + A^2(y - x)^2 \tag{C.11}$$

Now we can start the messy stuff. From Pelster's Eq. 1[220], assuming that the wavelength of the electric field is greater than any feature in our system, we can express the dielectric constant of the system as a volume average. We are measuring capacitance at 1kHz, so we will certainly see a volume averaged dielectric constant. In our case we have three components, so the form of the equation is slightly different:

262

$$\epsilon_{eff} = \epsilon = \frac{f\phi\epsilon_{liq} + (1-f)\,\phi\epsilon_{vap}e_{vap} + (1-\phi)\,\epsilon_{gel}e_{gel}}{f\phi + (1-f)\,\phi e_{vap} + (1-\phi)\,e_{gel}}$$

$$= \frac{f\phi(1+y) + (1-f)\,\phi(1+x)e_{vap} + z\epsilon_{gel}}{f\phi + (1-f)\,\phi e_{vap} + z} \tag{C.12}$$

We are interested in the change in dielectric constant with a change in density. So let's get all the filling dependent terms (i.e. f and A) out of the denominator by expanding Equation C.12 around $e_{vap} = 1$.

$$\epsilon \approx \frac{\phi\,(1 + x + f(y-x)) + z\epsilon_{gel}}{\phi + z}$$
$$+ \left(y + (y+1)A(y-x) + A^2\,(y-x)^2\right)\frac{\phi(1-f)}{\phi+z}\left(1 + x - \frac{\phi\,(1+x+f(y-x)) + z\epsilon_{gel}}{\phi+z}\right)$$
$$+ \left(A(y-x) + y\right)^2 \left(\frac{\phi^2(1-f)^2}{(\phi+z)^2}\right)\left(\frac{\phi}{\phi+z} - 1\right) \tag{C.13}$$

At a given temperature (i.e. along an isotherm) that density change is essentially a change in filling fraction, Δf, during capillary condensation. So, with x and y held constant (i.e. the densities of the phases are not changing, just their relative quantities) how does the dielectric constant respond to filling? Taking the derivative of Eq. C.13 and removing higher order terms we get:

$$\frac{d\epsilon_{eff}}{df} \propto (y-x) + y\left[\frac{z\,(\epsilon_{gel}-1)}{\phi+z}\right]$$
$$+ \frac{(A(y-x)+y)\,\phi f(y-x) + A(y-x)z(\epsilon_{gel}-1)}{\phi+z}$$
$$- (1-f)(y-x)\left[\frac{\phi f(y-x) + z\,(\epsilon_{gel}-1)}{\phi+z}\right]\frac{dA}{df}$$

Here, the first line presents the magnitude of the linear response to change in filling. It has a magnitude of about (y-x), the difference in dielectric constants of the two phases, as one would expect. The nonlinear terms are more complex, but lets plug in some value we know. Because we can choose to use either the liquid or vapor as the matrix, we know $f < 0.5$. We know that $\epsilon_{gel} = 3.9$. We can assume $x \approx 0$ and $y \approx 0.05$, which are close to the values assumed by gaseous and liquid helium in coexistence at 4K. Thus we can calculate e_{gel} so that $z = 0.525(1 - \phi)$. The nonlinear terms then reduce to about:

263

$$error \leq 0.08 \left[0.5\frac{dA}{df} - A \right] \quad (for\ 95\%\ aerogel)$$

$$error \leq 0.05 \left[0.5\frac{dA}{df} - A \right] \quad (for\ 98\%\ aerogel)$$

If we assume that A does not change much with filling, which is reasonable barring a sudden phase change to a new adsorbate geometry, and that $A \approx 0.33$, which is the value used for both spheres and randomly oriented cylinders, then the errors reduce to $\leq 3\%$ for 95% aerogel and to $\leq 2\%$ for 98% aerogel.

264